Cranfield
UNIVERSITY

JEFFREY JOHN ROPER

AN INVESTIGATION OF COMPUTATIONAL TECHNIQUES FOR THE PREDICTION OF SUPERSONIC DYNAMIC FLOWS

CRANFIELD COLLEGE OF AERONAUTICS

PhD THESIS

Cranfield
UNIVERSITY

Cranfield College Of Aeronautics

Department Of Flow Control And Prediction

PhD Thesis
Academic Year 1999-2000

Jeffrey John Roper

INVESTIGATION OF COMPUTATIONAL TECHNIQUES FOR THE PREDICTION OF SUPERSONIC DYNAMIC FLOWS

Supervisor: Professor John A Edwards

December 1999

Abstract

A computational investigation was undertaken to examine techniques for predicting supersonic dynamic flows, involving unsteadiness over fixed and moving surfaces. The fixed geometries examined were cylinder-flares and compression ramps, and the moving body geometries a pitching aerofoil and a rapidly deployed flap.

Investigation into the characteristics of incipient separation of a supersonic cylinder-flare flow revealed that the separated length varied with a power of the flare angle and that the variation in height of the separated region varies in a bi-modal manner with flare angle. For small-scale separations (flare angles less than those which would traditionally have been expected to induce separation) the height of the separated region was seen to vary slowly with flare angle. For larger flare angles, the separation bubble was found to grow rapidly in height and length with increasing flare angle and produce significant deflection of the external flow.

Computations of a Mach 5 compression ramp induced unsteady shock boundary layer interaction exhibited self-sustained oscillations at frequencies and amplitudes consistent with experimental data. Large dynamic structures (up to 1.7 boundary layer thicknesses in extent) were observed, and their production, propagation and deformation illustrated.

By modifying the turbulent viscosities produced by a non-dimensional implementation of the Baldwin-Lomax turbulence model (using under-relaxation) a turbulence model was produced which accurately predicted separation lengths for a series of Mach 6.85 compression ramp flows encompassing laminar, transitional and turbulent flow regimes (dependent on ramp angle).

A technique was developed to enable efficient computation of dynamically moving and/or deforming body flows. This technique was based on hierarchical, adaptive mesh refinement coupled with automatic generation of body surfaces, in which mesh adaption was used to capture the body geometry to within a specified accuracy. This, in conjunction with automatic cell creation and destruction, enabled the derivation of steady and unsteady, time accurate, conservative boundary conditions. This algorithm was used to compute a quasi-steady laminar supersonic pitching aerofoil flow, and an unsteady turbulent supersonic flap deployment. In both cases agreement with experiment was found to be good.

Acknowledgements

I am indebted to my supervisor, Professor John Edwards for his support, guidance and encouragement during my forays into computational hypersonic aerodynamics. I would like to thank him for helping to align my DERA work programme with my PhD work programme and hence making my part-time PhD possible, and for the significant resources he placed at my disposal.

A massive debt of thanks must go to my incredibly accommodating wife Jayne, who humoured me when I was raving about my success, consoled me when I was bewailing my woes, and tolerated me when I was trying to explain to her just how interestingly unique was another shock separated flow!

I would like to thank my parents, Stan and Anita, and my brother Stan for their endless support over the years and for believing in my abilities.

I would also like to thank Emeritus Professor John Stollery for his continued interest in my work and for providing guidance and help whenever we met.

Thanks to Professor Rob East for discussions concerning the flow physics and modelling of rapidly deployed flap flows.

I am grateful to DERA and the Ministry of Defence for sponsoring my entire undergraduate and post graduate education.

List of Figures

0. Nomenclature

U	Streamwise velocity
δ	Boundary layer thickness
T	Temperature
p or P	Pressure
M	Mach number
γ	Ratio of specific heats or intermittency depending on context
Re	Reynolds number
H(=δ^*/θ)	Shape factor
Cf	Skin friction coefficient
e	Internal energy
ρ	Density
θ	Momentum thickness
Π	Wake parameter
C_μ, $Cx_{,\varepsilon}$	Constants for k-ε turbulence model
$c_1 \ldots c_6$	Constants used to calculate boundary layer profile
C_{kleb}	Constant for calculating Klebanoff intermittency factor
Cp	Pressure coefficient
F or f	Frequency
k	Turbulent kinetic energy
$k_a \ldots k_f$	Constants used to calculate boundary layer profile
N	Number of cells in y direction within mesh
Pr	Laminar Prandtl number
q	Heat transfer
R	Universal Gas constant ($287 JK^{-1}kg^{-1}$)
Re	Reynolds number
$Re_{\delta L}$	Reynolds number based on boundary layer thickness
r	Recovery factor
S	Geometric cell scalar
t	Time
T	Temperature
V or v	Flow velocity in y direction (or cell volume)
W or w	Flow velocity in z direction
y	Distance of a point or cell from the wall
y^+	Cell Reynolds number
α	Flap angle used in computations
ε	Turbulent dissipation rate
ζ	y normalised with respect to boundary layer thickness
γ	Ratio of specific heats
κ	Thermal Conductivity
σ_κ, σ_ε	Constants for k-ε turbulence model
ξ	Error term, or vorticity vector depending on context
τ	Shear stress
θ	Shock angle

μ	Viscosity
Ω	Discrete value of flap angle from experimental data
ψ	Discrete value of time from experimental data

Subscripts

∞	Freestream
0	Total
99	Based on 99% of freestream parameter
char	Characteristic
e	At the boundary layer edge
i,j, k	In the appropriate computational direction
lam	Laminar
N	Normal
T	Tangential
pit	Pitot
ref	Reference value
f	Fundamental
t	Turbulent or total
w	At the wall
x,y, z	In the appropriate physical direction
c	Chord length
E_t	Total Energy
I	Moment of inertia
p	Static pressure
t	Time or body surface tangent
α	Body incidence
ε, η	Computational co-ordinates
λ	Moment arm
θ	Momentum thickness
ρ	Static density
τ	Total pitching moment
ω	Angular velocity
start	At the commencement of the flap motion

Superscripts

*	Displacement
'	Post condition
$\bar{}$	Non-dimensional
•	Time derivative
~	Estimate
(n)	At iteration n

1. Introduction

One of the many factors considered when designing new supersonic and hypersonic airframes/projectiles is that of aerothermal heating which can result in aeroshell ablation (particularly of fins, flares and other aerodynamic stabilisation and control surfaces). Dynamic modification of the projectile geometry (via ablation) can cause unforeseen and unpredictable changes in vehicles' overall aerodynamic performance. It has been shown [1] during a series of sea level flights of a finned projectile, that two fundamentally different modes of fin ablation occurred and it was suggested that such modes of failure might be non-deterministic. If such failures are non-deterministic, then, by definition, they cannot be predicted, and for the aerodynamics of the projectile to be known, such ablation must be avoided. The avoidance of ablation, in conjunction with other drivers (for example, avoiding the amplification of infrared signature, damage to guidance, navigation and control systems, and other thermal difficulties) make the ability to predict, if not to control, excessive localised heating at the body surface a highly desirable technology. As the requirement for parasitic mass[1] to decrease becomes more stringent (to facilitate greater launch and hence impact velocities) lower density materials are being used in minimal quantities to provide stability and/or control. This exacerbates ablation problems since smaller masses of lower melting point materials are being used at higher and higher Mach numbers. For example, pure aluminium has a melting point of 932°K, and the stagnation temperature of a Mach 5 flow with static temperature 300°K is 1800°K. Ablation can occur in regions of high localised heat transfer, typically where the flow stagnates, for example, at the base of a fin, where the flow separates and reattaches. Separation typically occurs in regions of rapid pressure rises, for example in strong adverse pressure gradients (for example: due to surface geometry, shock impingement and transverse rocket plumes).

This thesis examines shock boundary layer interactions in three distinct regimes to assess the efficacy of current predictive techniques, and to examine computational results in the context of the current understanding of such flows. The three configurations are:

i. Axisymmetric cylinder-flare induced turbulent interactions (as used for flare stabilisation of projectiles) – these are necessarily two dimensional and can include no edge effects.

ii. Flat plate – flap induced turbulent interactions (as used

[1] mass which is accelerated or launched, other than the projectile itself – typically a sabot is used to transmit driving forces to projectiles such as fin stabilised munitions which would be destroyed without such packaging.

for control surfaces) – these can potentially include three dimensional effects for example lateral spillage. Both steady and unsteady turbulent interactions are examined.

iii. Dynamically deployed flaps – as (ii), but with the flap being rapidly deployed.

In the context of this thesis, shock boundary layer interactions are taken to be either compression ramp or cylinder-flare flows (unless otherwise stated). A schematic of a typical separated supersonic cylinder-flare flow is given in Figure 1.1, with a typical computational flowfield for the flow over a cylinder flare in Figure 1.2 (details of the computation are presented in §2.2). The pressure rise resulting from the shockwave caused by the flow deflection over the ramp or flare propagates upstream through the subsonic portion of the boundary layer, causing a distributed loss of momentum which can result in flow stagnation and separation. At the point at which the boundary layer separates, the external flow immediately adjacent to the boundary layer is deflected and hence a weak separation shock is produced. The recirculatory region beneath the separated boundary layer is referred to as the 'separated region' or the 'separation bubble'. Downstream of the shock-boundary layer interaction, the separated boundary layer reattaches to the surface. This configuration results in increases in heat transfer at (or near) separation and reattachment. Unsteady shock-boundary layer interactions are turbulent shock-boundary layer interactions, for which the flow is no longer steady, but undergoing oscillatory motion. This motion typically affects the location and magnitude of the separated region and the location and strength of the separation and ramp or flare shock waves. Unsteady shock-boundary layer interactions for compression ramp and flare shock separated flows are poorly understood and the causative mechanisms underlying such phenomena are contentious. Whilst experimental data have proved invaluable in the search for underlying causative mechanisms and for the validation of computational models used to attempt to predict such flows, the mechanisms are still not fully understood, and hence effective, reliable prediction techniques have not yet been developed. Until the mechanisms are understood and/or accurate and reliable prediction methods become available, avoidance and control of issues such as ablation will be difficult.

1.1 Incipient Separation

Separation of supersonic and hypersonic flows has been widely researched over many years, yet recent results [2][3][4][5] suggest that the aerodynamic community does not yet fully understand the mechanisms involved. With the advancement of modern experimental techniques (e.g. liquid crystal thermography) high resolution results (spatially) are being obtained, which are suggesting that very small regions of separated flow are occurring for smaller flow deflection angles than would previously have been expected to induce boundary layer separation. An example of this is given in Figure 1.3 [2], which shows an experimentally obtained thermograph showing the heat transfer to a

cylinder-20° flare. For this configuration, at the experimental flow conditions (given in §2), separation would not be expected (on the basis of the traditional empirical prediction techniques, presented in §2) yet peaks in heat transfer, upstream and downstream of the cylinder-flare junction, suggest the presence of a small separated region. For small regions of separated flow, the effects may only be observable in heat transfer and skin friction. (factors which are governed by the 'near-wall' flow), and not in parameters such as surface pressure distribution (which is dominated by bulk flow characteristics) which are more commonly examined by experimental aerodynamicists to determine the presence and location of separation. It was therefore suggested that separation may be occurring in circumstances which have been overlooked to date[2].

In the early 1960's Kuehn [6][7] conducted a comprehensive series of wind tunnel tests at Mach numbers between 1.6 and 4.2 with Reynolds numbers (based on undisturbed boundary layer thickness) of $1.5x10^4$ to $7.5x10^4$ to investigate flows over two dimensional compression corners and various curved surfaces. Three different forebodies were examined: a 20° sharp cone, a 45° blunt cone, and a hemisphere. It was found that the tendency of both two dimensional and three dimensional boundary layers to separate decreased with: increasing Mach number, decreasing Reynolds number, decreasing pressure rise and decreasing adverse pressure gradient.

It was discovered that for axisymmetric flows, the larger the ratio of the radius (of the cylinder) to the undisturbed boundary layer thickness, the more readily the flow separated. Extracting heat from the boundary layer (via a cooled model) decreased the tendency of the boundary layer to separate (also reported by[141][142]).

To assess the onset of separation, flow visualisation was performed with continuous and spark shadowgraph. Incipient separation was located by examining wall pressure distributions for the first appearance of a 'hump' (a three-point inflection), with increasing flow deflection. By varying Mach number, Reynolds number and pressure gradient (via flow deflection) a variation in the magnitude of the mixing between the outer flow and the dissipative flow near the wall (Crocco-Lees[8]) was effected. The rate of momentum transfer to the boundary layer determines the maximum pressure rise that can be sustained by a boundary layer before separation will occur. The rate of momentum transfer to the boundary layer is proportional to the rate of boundary layer growth, and the rate of momentum loss from the boundary layer is determined by the magnitudes of the adverse pressure gradient and the viscous shear at the wall. In all cases it is seen that after the pressure rise required to induce incipient separation was exceeded, the extent of the separated region increased rapidly with further increases in pressure rise.

Kuehn [6][7] observed that turbulent flows over two-dimensional compression corners with minimal flow deflection were attached and steady. For larger

flow deflection angles, the boundary layer separated (and for separated lengths up to five boundary layer thicknesses, the flowfields were steady). For flow deflections resulting in separated lengths in excess of five boundary layer thicknesses the flow was unsteady, with the magnitude of the unsteadiness increasing with the magnitude of the separated region.

A slowly varying flap angle (initially increasing and subsequently decreasing) and hence flow deflection, resulted in the formation of a separated region, its growth, diminution and disappearance. Throughout the incidence range there was no evidence of hysteresis in the appearance, magnitude and disappearance of separated region.

Using experimentally obtained variation in separated length with flare angle, Coleman and Stollery [9] correlated the onset of separation with respect to Mach number and Reynolds number, based on the undisturbed boundary layer thickness for turbulent axisymmetric flows. A reconstruction of the correlation presented in [9] is given in Figure 1.4.

Park, et al [117] simulated a dynamically deployed flap (with reduced angular frequencies of 0.001, 0.01, 0.1 and 1.0) for an *inviscid* Mach 2 flow with a uniform body fitted grid (60x60 was proved to be sufficient). The reference length was taken to be the length of the flap (1m). It was discovered that for reduced angular frequencies of up to 0.01 the flows are quasi-steady. For reduced angular frequencies of >0.1 dynamic effects were observed.

Reduced angular frequency ($0.5\omega cu^{-1}$) is often used to determine whether or not a system is quasi-steady (the dynamic system is in essence a succession of equivalent steady flows). Reduced angular frequency is the ratio of the maximum linear velocity of the moving boundary (ωc) to the flow velocity and if the reduced angular frequency is of order one or more then the system is likely to be unsteady (if the order is less than one the system is likely to be quasi-steady). Assessing steadiness on the basis of reduced angular frequency assumes inviscid flow physics and takes no account of viscous phenomena, which can take significantly more time to establish. Hence for viscous flows, unsteady effects can be found with flows having reduced angular frequencies of order less than 1 (for example Smith [67]).

1.2 Flowfield Unsteadiness

Whilst it is widely known that laminar shock boundary layer interactions are steady [10], this is not necessarily the case for turbulent shock boundary-layer interactions. In the 1950's flow visualisation experiments [6][7] revealed that shock wave turbulent boundary-layer interactions can result in unsteady separated flows. Kistler [11] was possibly the first experimental aerodynamicist to obtain detailed measurements of the fluctuations characteristic of such unsteady shock boundary layer interactions. The magnitude of the oscillations associated with these interactions can be large (in excess of 185dB) with peak amplitudes occurring near separation and reattachment (and to a lesser extent beneath the outgoing boundary layer)

which result from fluctuations in the instantaneous positions of separation and reattachment [12]. The largest amplitudes typically occur at frequencies of several hundred Hz to several kHz, which Pozefsky et al. [13] suggest could destroy conventional aerostructures within minutes.

Many researchers have investigated unsteady shock boundary layer interactions over the past four decades and the work of Dolling and his many co-authors [10][12][14][15][16][17][20][22][27][85][107][25][29][47][81][90][91][92][97][99][104][109][115][120][125][127][129][130] is used here to illustrate the salient features of a typical unsteady shock turbulent boundary layer interaction produced supersonic flow over an unswept two-dimensional compression ramp. For the majority of these experiments, the Mach number was between 4.92 and 5.00, Reynolds number between $49.9 \times 10^6 m^{-1}$ and $66.8 \times 10^6 m^{-1}$ and the undisturbed boundary layer thickness at the hingeline between 15.0mm and 19.3mm. In all cases, the data was obtained for flow over a 28° unswept compression ramp. At the end of this section, selected experiments by other researchers are presented to highlight flow phenomena not covered by the work of Dolling et al.

When examining the causes of unsteadiness it is important to quantify sources of 'noise' and hence the pressure fluctuations in the freestream need to be quantified. Dolling et al undertook their research in an experimental facility with turbulent freestream noise measured to be ±0.6% ($\bar{p}/p_\infty$) of the freestream total pressure [15].

An instantaneous 'snapshot' of an unsteady shock turbulent boundary layer interaction would appear similar in nature to that of a steady analogous flow. The nature of the unsteadiness is in the motion of the separation and reattachment shock waves, the position of the locations of separation and reattachment (and hence the separated length), the height of the separated region and the effects on the wall and near wall parameters of these dynamic changes.

The dynamic nature of these flowfields result in differences with their steady analogous counterparts – for example, the motion of the shock waves will affects its shock Mach number and hence the change in pressure, density, and Mach number across the shock wave.

Whilst periodicity in unsteady flowfields is often reported in wall pressure fluctuations measured under unsteady shock turbulent boundary layer interactions, this is not always the case. For example, Boitnott [18] reports the presence of unsteady shock boundary layer interactions, but with no obvious or repetitive patterns (flow conditions in Table 1.1, set 15).

Dolling and Murphy [22][97] examined a Mach 2.95 flow over a 24° compression ramp (flow conditions in Table 1.1 Set 5) and reported that they were unable to find any periodicity in the wall pressure fluctuations. Despite the apparent lack of periodicity, Dolling and Murphy chose an arbitrary

pressure threshold to be indicative of shock passage and inferred a shock crossing frequency. From spectral distributions there was evidence of broadband amplification of pressure fluctuations under 10kHz, corresponding to a non-dimensional frequency ($\bar{f} = \frac{f\delta}{u_\infty}$) of $\bar{f} = 0.22$.

Experiments by Marshall et al [104] revealed rippling of the shock wave in a spanwise direction with amplitude 0.17δ, and wavelength 0.3δ-2.0δ. Surface pressure fluctuations were measured up to 2.5δ upstream of the interaction. Preliminary computational analysis revealed that the stationary shock was stronger than the unsteady shock seen in the experiments (resulting in a larger separated region). Flow conditions are presented in Table 1.1, set 16.

Unalmis and Dolling [16] observed a thickening and thinning of the boundary layer at relatively low frequencies. Large scale structures were seen to be present within the boundary layer of between 1 and 4 boundary layer thicknesses in extent. The streamwise decay of these structures was over 15-20 boundary layer thicknesses. For an incoming zero pressure gradient turbulent boundary layer, the RMS wall pressure fluctuations can be computed. Unalmis and Dolling compute this value to be approximately 89Pa.

Dolling and Brusniak [85] report shock crossing frequencies for a Mach 5 flow over 16°, 20° and 24° degree ramps (flow conditions in Table 1.1, set 9) which decrease with flow deflection (0.3kHz-0.4kHz ($\bar{f} = 6.9\times10^{-3} - 9.2\times10^{-3}$) for 24° ramp, 0.5kHz-1.8kHz ($\bar{f} = 1.15\times10^{-2} - 4.12\times10^{-2}$) for 20° ramp and 1kHz-3kHz ($\bar{f} = 2.29\times10^{-2} - 6.87\times10^{-2}$) for 16° ramp). This trend may be expected if one were to assert that the subsonic portion of the separation bubble is responsible for convecting acoustically propagated disturbances. If this were the mechanism underlying the oscillations then one would expect the frequency to be inversely proportional to the magnitude of the separated region. The separated region is reported to be very elongated and embedded within the boundary layer. The near wall contra-stream convective velocity was measured to be approximately one tenth of the freestream velocity.

Erengil and Dolling [107] report wall pressure fluctuations of 0.3kHz-0.5kHz ($\bar{f} = 5.8\times10^{-3} - 9.68\times10^{-3}$) for the same flow over a 28° ramp (flow conditions in Table 1.1, set 19).

Unalmis and Dolling [16] showed that during the oscillations the separation and reattachment lines move together and apart causing expansion and contraction of the separation bubble. Similar observations were made previously by Kussoy et al [21]. These oscillations are not related to any non-two dimensionality of the flow, as it was established that the flow was nominally two-dimensional and that any non-two-dimensional effects were due to the three-dimensionality of incoming boundary layer [15].

Dolling et al defined intermittency as the proportion of time that the separation shock is upstream of a specific location and, by assuming that the pressure rise caused by the separation shock is coincident with the separation shock itself, defined an intermittency parameter γ to be:

$$\gamma = \frac{1}{t_{total}} \sum_{i=1}^{N} (t_f - t_r)_i$$

where f denotes fall in wall pressure, r denotes rise in wall pressure, t denotes time, and i denotes interaction. This allows the location of upstream and downstream intermittent boundaries to be selected in an analogous manner to the notional δ_{99}, i.e. γ=1% and γ=99% [15]. Three components of wall pressure fluctuations were identified (as illustrated in Figure 1.5). At $\gamma \approx 0$ and $\gamma \approx 1$ there is little energy in the 100-500Hz ($\bar{f} = 2.29\times10^{-3} - 1.15\times10^{-2}$) region (most is >10kHz ($\bar{f} > 0.23$) from incoming boundary layer). At $\gamma \approx 0.5$ the oscillations are predominantly of type III. Comparing $\gamma \approx 1$ with $\gamma \approx 0$ reveals a larger amplitude of high frequency oscillations due to amplification in the free shear layer. The length of the intermittent region was found to be inversely proportional to the maximum crossing frequency, possibly due to having similar propogation velocities within the separated region with a differing physical distance to traverse. Erengil and Dolling [14] determined the intermittent region to be 1.4 boundary layer thicknesses in length with an upstream influence of nearly three boundary layer thicknesses (upstream of the hingeline). The peak recorded amplitude at the wall had an RMS value of 48% of the freestream static pressure and the maximum zero crossing frequency was 0.86kHz ($\bar{f} = 2.0\times10^{-2}$) with an upper bound ≈1kHz ($\bar{f} = 2.3\times10^{-2}$) [15]. A correlation was discovered between pressure fluctuations in the incoming boundary layer and large-scale downstream sweeps of the shock wave [17]., No corresponding correlation was found, however, for upstream sweeps of the shock wave. A strong correlation between pressure fluctuations in the incoming flow and changes in the direction of the shock wave also became apparent. Whenever the shock wave changes direction specific 'pressure-carrying' structures are seen to enter the interaction and these structures are coincident with the shock foot at the instant of shock turnaround. The pressure signatures for an up-downstream turnaround and a down-upstream turnaround were found to be different. The low broadband frequency of around 1kHz ($\bar{f} = 2.3\times10^{-2}$) results from the shock motion acting over a distance of around an undisturbed boundary layer thickness (17.5mm). Flow conditions are given in Table 1.1, set 17. As noted previously it was shown that the intermittent region is also a region of intermittent separation due to the expansion and contraction of the separated region. McClure [19] showed that the pressure fluctuation 'signatures' convect downstream, through the shock interaction and through the intermittent region. These 'signatures' travel at approximately 75% of the freestream velocity with a temporal extent of 75μs-100μs corresponding to a spatial extent of 3.2-4.3 undisturbed boundary layer thicknesses. Gramann and Dolling [20] detected the pressure 'signatures' for the turbulent flow

structures as far as 20 undisturbed boundary layer thicknesses upstream of the interaction. The interaction region extended to two boundary layer thicknesses upstream of the corner, and the bubble length varied between 1.7 and 3.6 boundary layer thicknesses [10]. The convective velocity was found to be $0.64U_\infty$. Flow conditions are presented in Table 1.1, set 18.

Selig and Smits [23] successfully forced the oscillatory frequency of an unsteady shock boundary-layer interaction by upstream boundary layer blowing at 2.5% and 9% of the freestream mass flux. At frequencies up to 5kHz ($\bar{f} = 2.3\times10^{-2}$)it was demonstrated that complete control over the oscillation frequency could be obtained and that varying the blowing mass flux had little or no effect on either the nature or the magnitude of the unsteady oscillation.

1.3 Mechanisms Underlying Unsteadiness

There has been much conjecture regarding the unsteady shock turbulent boundary layer interactions, with most hypotheses falling into one of three distinct categories:

i. The oscillations are due to large-scale structures in the incoming boundary layer, which are amplified to produce the observed oscillations.
ii. The separated flowfield is inherently unsteady and the oscillations are self-sustaining.
iii. The oscillations are a triggered response to an external stimulus, i.e. the oscillations are not an amplification of the incoming structures, and the incoming structures merely trigger a prescribed oscillation.

Each of these hypotheses has its opponents and proponents together with its supporting and contradictory evidence. A brief discussion of each of the three classes of hypotheses follows.

1.3.1 Hypothesis I - 'Oscillations are amplified incoming structures'

Spina and Smits [103] report the presence of large scale flow structures inclined at 45° to the wall, filling the majority of the boundary layer (flow conditions in Table 1.1, Set 13). These structures convect downstream, retaining much of their shape and character, and pressure identity, for at least one and a half boundary layer thicknesses. The spanwise extent of these structures is very limited.

Andreopolos and Muck [100] (flow conditions in Table 1.1, Set 8) report that the frequency measured for flows over 16°, 20°, and 24° compression ramps are independent of flow conditions downstream of separation. I.e. the form of the oscillations is independent of ramp angle. Similarly it was reported [24] that, on the basis of wall pressure measurements for various Mach 2.84

compression ramp interactions (flow conditions in Table 1.1, Set 6), the mean shock period is independent of ramp angle and the zero crossing frequency was of the same order as the estimated bursting frequency of the incoming boundary layer. It was therefore inferred that since the measured shock speeds are of the same order as the velocity fluctations in the flowfield, the incoming boundary layer is largely responsible for the shock motion. Similar conclusions were reached independantly by Plotkin [65]. For the flow over Muck et al's configuration (a 24° ramp) a convective velocity of $0.6U_\infty$ was reported, corresponding to $0.8U_e$ (where calculation of U_e assumes a 10° flow deflection). Furthermore observations regarding large eddy propogation and pressure signatures were made, which are directly relevant to the ensuing computations. These observations were: "Thus it can be generalised that the convection velocity seems to be associated with the large eddies which travel with U_e in the external part of the boundary layer, which in the present case would be roughly above the separation bubble." and, "Interestingly although we have reverse flow in the separated region, the wall pressure signals are significantly more strongly correlated in the freestream direction than in the reverse direction".

The wavelength of the spanwise 'ripple' is reported as 0.23-0.69 undisturbed boundary layer thicknesses, with separation occurring 1.6 boundary layer thicknesses upstream of the hingeline.

Meyer et al [132] employed laser Doppler velocimetry to quantify levels of turbulent kinetic energy throughout an unsteady shock boundary layer interaction (flow conditions given in Table 1.1, Set 2). It was discovered that there is a significant increase in turbulent kinetic energy and Reynolds stresses in the boundary layer profiles at, and downstream of, the interaction.

Smits and Muck [102] examined Mach 2.8 flows over 8°, 16° and 20° (attached, small scale separation and large scale separation, respectively) compression ramps (flow conditions in Table 1.1, Set 11). They observed a large amplification of turbulence at separation and that the region over which this amplification occurs is 'smeared' by the unsteady shock motion (0.1δ for the 8° ramp and 0.2δ for the 16° case). The pressure rise downstream of the interaction results in compression of the flow and concave curvature of the streamlines, both of which tend to cause an increase in turbulent activity. The maximum amplitude of the RMS quantities was found to be approximately proportional to the overall static pressure rise through the interaction.

This hypothesis is refuted by Erengil and Dolling [17] on the basis that if the previous assertions were true then with a given incoming boundary layer the shock crossing frequency and streamwise extent of its motion would be fixed. It has been shown that for axisymmetric unsteady shock boundary layer interactions with a fixed incoming boundary layer, zero crossing frequency decreases and the extent of shock motion increases with decreasing cylinder radius [25]. It was suggested that the oscillations having a similar frequency to the estimated bursting frequency of the incoming boundary layer could be

purely coincidental. Further evidence to the contrary is found in the dependence of the magnitude and frequency of the oscillations on ramp angle for two-dimensional compression ramp separated flows. If the nature of the oscillations is dictated by the incoming boundary layer, then the magnitude and frequency of the oscillations should be independent of ramp angle, which they are not.

Doubt is cast [17] on the prediction of the crossing frequency used in the original proponents' work [24] suggesting that if the zero crossing frequency had been calculated 'correctly' then the frequency would be approximately halved, removing credence from the alleged correlation.

Examination of wall pressure fluctuations in the absence of a ramp reveals no significant energy at low frequencies (0-3kHz) ($\bar{f} = 0 - 6.87 \times 10^{-2}$), however high energy oscillations at these frequencies are observed in the unsteady interaction flows [17]. If the oscillations are caused by amplification of fluctuations in the incoming boundary layer, then these should be discernible in the absence of the ramp. Following the lack of observable fluctuations in wall pressure under the incoming boundary layer being cited as proof of the lack of incoming boundary layer structures, Unalmis et al [16] computed the likely wall pressure fluctuations due to incoming boundary layer structures. This was found to be approximately 90Pa and it may be that these structures were not seen due to lack of sensitivity.

Thomas et al [52] observed a lower characteristic frequency of approximately one tenth that of the characteristic turbulent frequency of the boundary layer, which is not explained by this hypothesis.

Researches by Beresh et al [131] using PIV and PLS to investigate the flow over a 28° ramp (conditions in Table 1.1, set 1) failed to find any link between incoming structures in the boundary layer and the shock front motion.

Thomas et al [52] present some interesting experimental data employing a 'novel digital signal processing technique' for Mach 1.4 flow over a 6° ramp (flow conditions in Table 1.1, set 3). Following experimental data of Andreoupoulos and Muck (flow conditions in Table 1.1, set 8) [100] alleging unsteady oscillation frequency independence with ramp angle, Thomas et al present spectral analysis of a shock boundary layer interaction. Evidence of broadband amplification is seen downstream of a location 1.5 boundary layer thickness upstream of the hingeline, with peak amplification occurring near the hinge. The predominant frequency is approximately 35kHz ($\bar{f} = 0.81$) which is around the characteristic frequency for this turbulent boundary layer, from which it was assumed that the unsteadiness is due to amplification in structures in the incoming boundary layer. However, it is seen from their data, that the separated region is small (less that five boundary layer thicknesses in streamwise extent), and may be at the limit of steady/unsteady interactions (Keuhn [6][7] reports steady separated flows for streamwise extents up to five

boundary layer thicknesses). No details (other than non-dimensional) are given regarding the magnitude of these perturbations and hence it is impossible to quantify the absolute magnitudes of these perturbations (the amplitudes associated with typical unsteady shock boundary layer interactions are far larger than those associated with incoming boundary layer turbulence). In the plots of spectral energies, it is seen for a small extent (about 43% of a boundary layer thickness) there is a peak in spectral energy around 2kHz ($\bar{f} = 4.6\times10^{-2}$). This is reported to contribute around 40% of the total spectral energy at reattachment and is attributed to 'localised shock oscillation'. According to Thomas et al a very small separation bubble is intermittently present causing intermittent shock displacement. The overall conclusion was that a new mechanism is being effected whereby energy transfer is occurring from small length scale structures to large (the opposite to the norm). On the basis of the references examined for this thesis, it is suggested that in fact it is the intermittence of the separated region that is resulting in an intermittence in unsteady shock boundary layer interaction and that the reason for the predominance in spectral peak at 35Khz ($\bar{f} = 0.81$) relative to the 2kHz($\bar{f} = 4.6\times10^{-2}$) peak is simply due to the magnitude of the separated region (it is known that the amplitude of the oscillations associated with unsteady shock boundary layer interactions increases with separated length). This data, although oft cited, is therefore regarded with caution as a proof of unsteady shock boundary layer interaction through amplification of structures in the incoming boundary layer.

Tran and Bogdonoff [101] reported that for Mach 2.95 flows over 16° and 20° unswept compression ramps, amongst others, the magnitude of the normalised RMS peak increases with shock strength and correlates with product of the initial pressure gradient and the size of the separated region. Flow conditions for these experiments are presented in Table 1.1, set 12.

1.3.2 Hypothesis II - 'Oscillations are a self-sustaining phenomenon.'

Tran [26] concluded that pressure fluctuations in the intermittent region are independent of the large-scale turbulent structures in the upstream boundary layer. If this is the case then the entire mechanism producing the unsteadiness is impervious to upstream influences and must be a closed dynamical system.

Dolling et al. suggest that the unsteady motion is due to unsteadiness inherent within the separated region which is amplified via the shear layer within the large separated portion of the flow. It has been observed by many researchers that the presence of a separated region does not necessarily result in unsteady behaviour, and similarly it has been observed that separated flows increase the effects of unsteady motion, however unsteady motion can also occur without separation.

Dolling [99] examined Mach 2.95 flows over a 24° compression ramp (flow conditions are presented in Table 1.1, set 4) and discovered that unsteady

perturbations are present just upstream of separation. If this is the case, then the unsteady motion cannot be due to incoming structures and the unsteady fluctuations must be as a result of the behaviour of the interaction (or the incoming structures are too small to be measured).

Thomas et al [66] examined a Mach 1.5 flow over 6°, 9° and 12° compression ramps (flow conditions in Table 1.1, set 20) and observed expansion and contraction of the separated region (as per [16]). The temporal results are given in Table 1.2.

Thomas et al [66] concluded that there is a very strong global relationship between the separation bubble motion and shock oscillations; much stronger than any relation to large scale structures in the incoming boundary layer.

Selig and Smits [23] succeeded in forcing the frequency of an unsteady shock boundary-layer interaction ('achieving complete control') by upstream boundary layer blowing, which according to this hypothesis should not have been possible.

1.3.3 Hypothesis III - 'Oscillations are a response to a stimulus'

The control over the unsteady oscillations obtained by Selig and Smits [23] lends credence to this hypothesis (and also that of hypothesis I).

Erengil and Dolling [27] and McClure [19] took simultaneous pressure measurements of wall pressure fluctuations under the incoming boundary layer and in the intermittent region. Through conditional sampling and selective averaging, correlation between specific separation shock motions and pressure fluctuations in the incoming boundary layer was observed. It was suggested that these show a direct link between pressure fluctuations in the incoming boundary layer and separation shock motion. However, Beresh et al [131] failed to find any link between incoming structures in the boundary layer and the shock front motion.

1.3.4 Hypothesis IV - 'A comprehensive model'

Many researchers have avoided speculating as to the causes of unsteadiness on the basis of their limited set of experimental results. For example, Selig et al. [28] report that for a Mach 2.84 flow over a 24° compression ramp the shock "oscillates randomly" in the spanwise direction with an amplitude of the order a boundary layer thickness and a frequency of around 2kHz($\bar{f} = 9.0 \times 10^{-2}$). Flow conditions are given in Table 1.1, Set 14). The separated region was 49mm in length (1.9 boundary layer thicknesses) with a peak height of 6mm (20% of the boundary layer thickness).

Erengil and Dolling [14] produced, via generalisation, a fuller, more encompassing model which incorporates hypotheses I, II, and III:

For the Mach 5 turbulent boundary layer in question, the separation shock

motion is caused by two distinct fundamental phenomena:

i. Perturbation of the ratio of static quantities across the shock e.g. pressure ratio, by fluctuation of either upstream pressure, downstream pressure (or both) will, according to the governing equations, result in an increase or decrease in separation shock Mach number. This in turn will produce a change in the separation shock velocity relative to the freestream, resulting in a change in the position of the separated shock. These fluctuations are alleged to be caused by turbulence (either propagated in the flow or convected by turbulent structures to the vicinity of the separation shock via the subsonic portion of boundary layer downstream of the separation shock). Turbulent fluctuations tend to be high frequency and should be identical for all interactions at these conditions – i.e. no dependence on ramp angle. This corresponds to hypothesis I.

ii. The separation bubble expands and dilates, and the frequency of this expansion and dilation is dependent on the flare angle. This corresponds to hypotheses II and III.

Oscillations of type I are 'jittery' in motion with high frequencies and low amplitudes whilst oscillations of type II are large-scale motions with low frequencies and large amplitudes. This agrees with the experimentally observed frequencies and magnitudes at various locations throughout the interaction as presented in Figure 1.5.

1.4 Modelling Steady and Unsteady Turbulent Separated Flows.

1.4.1 Background

Supersonic separated flows have proved consistently difficult to predict accurately, particularly when the flows are unsteady. Large discrepancies between computational results and unsteady measurements have been attributed to the lack of unsteady models in computational algorithms [29].

Empirical techniques have been developed e.g. [12] which have had a limited degree of success, but are not capable of predicting the majority of required flow parameters and are not sufficiently general in applicability.

It is recognised [30] that turbulence models need only be sufficiently complex to provide those parameters required by the application and no more. For example, in some instances a steady state approximation of the gross flowfield characteristics will suffice; whereas in others detailed simulation of time dependent flow characteristics may be necessary (e.g. for simulation of unsteady shock boundary layer interactions, cavity flows, and other dynamic phenomena).

Turbulence is an inherently three dimensional, time dependent phenomenon, incorporating a considerable range of both length and time scales. As the Navier-Stokes equations (Appendix A) contain all of the physics of a given

continuum flow, it follows that with a sufficiently fine grid and sufficiently small time steps, turbulence should be accurately modelled. It is seen subsequently that solving the Navier-Stokes equations on a 'sufficiently fine grid' with 'sufficiently small time steps' for the compressible supersonic flows examined here is significantly beyond current and immediately foreseeable computing capabilities.

To predict the behaviour of turbulent flows with current computational techniques one must either employ direct numerical simulation (DNS) or a turbulence model. The latter models do not replicate turbulence – they attempt to model the effects of turbulence, and vary greatly in complexity and efficacy. It was shown that for a range of missile bodies and a range of turbulence models that there was no one preferable model [133].

The most commonly used turbulence models fall into one of three classes (listed in order of increasing complexity):

i. Zero order (or algebraic),
ii. First order,
iii. Second order.

1.4.2 Algebraic Turbulence Models

Algebraic (or zero-equation) turbulence models involve minimal additional computational overhead as they simply involve post-processing the flowfield after each time step to provide an estimate of the turbulent eddy-viscosity at each location in the flow.

The Baldwin-Lomax turbulence model [31] (Appendix B) was formulated for use in computations where boundary layer properties (e.g. δ, δ^*, u_e) are difficult or impossible to obtain (as with separated flows and/or flows involving shock waves). Unfortunately algebraic turbulence models frequently prove unreliable for separated flows - for example, it is not uncommon for computed separated lengths to be over-predicted by a factor of two, and for the pressure rise over the separated region to also be over predicted (although to a lesser extent). Similar results are obtained with the Cebeci-Smith turbulence model [34], and these discrepancies are attributed to the omission of upstream turbulent viscous effects. Various modifications to incorporate these effects have been attempted (e.g. by Shang and Hankey [35] and Hung [36]) which produced better agreement with experimental separation position and pressure rise. Unfortunately discrepancies in reattachment location, heat transfer and skin friction coefficient were exacerbated, and thus these modifications were not widely adopted. Another modification to the algebraic turbulence models was formulated by Johnson and King [37], which is regarded as a 'half-equation' model and provides slightly improved predictions of separated flows than the standard Baldwin-Lomax model.

For Baldwin and Lomax's original turbulent boundary layer computations [31]

the turbulence model was evaluated using a thin-layer approximation to the Navier-Stokes equations (neglecting diffusion parallel to the surface of the body). Thin layer approximations were used in preference to classical boundary layer approximations in which the momentum equation normal to the wall is replaced by the assumption of zero pressure gradient through the boundary layer (also neglecting diffusion parallel to the wall) which produces troublesome singularities at the point(s) of separation.

For all of the computations presented herein, the full Navier-Stokes equations were solved (all of the momentum equations were retained) and the problem of singularities at separation could not arise.

Baldwin and Lomax[31] applied their turbulence model to four specific configurations: supersonic turbulent flat plate boundary layer development, a shock wave incident on a turbulent flat plate boundary layer, a turbulent supersonic shock separated compression ramp flow, and transitional aerofoil flows. The Baldwin Lomax turbulence model used for the computations presented in this thesis is a non-dimensional form of the original model by Baldwin and Lomax (Annex B) and is applied to the ramp and flare flows in an identical manner to that employed by Baldwin and Lomax. The non-dimensionalisation maintains numerical accuracy and is consistent with the hierarchical mesh refinement code DRAMR[70].

A précis of Wilcox's summary [30] for algebraic turbulence models is:

> *Algebraic turbulence models only work well with flows for which they have been finely tuned. Algebraic models are simple and hence rarely produce numerical difficulties and* should only be replaced when demonstrably superior alternatives are available. *The Johnson-King model removes some of the inadequacies of the Baldwin-Lomax and Cebeci-Smith models but includes seven ad-hoc closure coefficients and requires iterative solution to produce accurate predictions*[2].

1.4.3 One Equation Turbulence Models

One equation models are incomplete as they are forced to relate turbulent length scales to some arbitrary flow parameter(s). The Reynolds stress tensor is curtailed to produce a simpler incompressible tensor. The dissipation equation[3] is obtained by dimensional analysis and necessitates the formulation of an expression for the length scale. Wilcox [30] notes that one equation turbulence models provide a modest advantage over algebraic mixing length models and developments by Goldberg [38], Baldwin and Barth [39], and Spalart and Allmaras [40] show improved prediction capability. Unfortunately, these modified one-equation turbulence models are not universally applicable and can provide very poor results in certain circumstances.

---

[2] i.e. if the model is finely tuned to a specific problem, the results are good!

[3] The dissipation equation is given as ($\varepsilon \propto \kappa^{\frac{3}{2}} l^{-1}$)

Whilst all of these models have shown improvement for separated flows for certain configurations, the Baldwin-Lomax algebraic turbulence model remains superior for various separated flows (for example [32][33]).

1.4.4 Two Equation Turbulence Models

Two-equation turbulence models include turbulent transport and thus these models are complete, i.e. requiring no a-priori knowledge of the turbulence structure of the flowfield, and represent the simplest complete model of turbulence. In view of this, one may expect two-equation turbulence models to perform significantly better than their one-equation and algebraic counterparts. Unfortunately this is not necessarily true.

Wilcox [30] notes that as with the one equation turbulence models there is no fundamental reason why turbulent viscosity should depend solely upon turbulent parameters such as κ, l, ε or ω. In general the ratio of individual Reynolds stresses to the mean strain rate components depends upon both the mean flow and turbulent scales. Thus two equation turbulence models are no more likely than one-equation models to be universally applicable to turbulent flows, and "*can be expected to be inaccurate for many non-equilibrium turbulent flows*".

It has been shown that most two-equation models cannot accurately predict the constant β in the law of the wall [30] and hence simply applying a no-slip boundary condition at the wall and integrating through the viscous sub-layer produces unsatisfactory results. This can be remedied by applying complex damping functions, although these tend to make the governing equations very stiff. To circumvent this problem, wall functions were developed to enforce the law of the wall near solid surfaces.

There are two fundamental difficulties inherent with in this approach:

i. How far from the wall should the wall function be applied, and how should the non-wall function flow be blended with the wall function flow ?

ii. What happens in the case of flows which are not necessarily attached, wall bounded flows, separated flows, free shear layers, and other flowfields where the wall boundary condition is not valid?

Many poor quality results using the k-ε turbulence model (Appendix C) have been attributed to wall function inadequacy, whereas in fact it is the k-ε model itself that is inapplicable to the application [30]. For example the k-ε turbulence model is recognised as performing poorly for boundary layers with significant adverse pressure gradients, as produced by shock boundary layer interactions.

The k-ω turbulence model [41] (Appendix D) tends to produce better agreement with experimentally determined Cf and Cp than the Baldwin-Lomax turbulence model, for separated flows, although Cp downstream of reattachment is over-predicted.

Despite difficulties with these two equation models, many researchers have employed such models for computing flows, for which the assumptions upon which the models are founded do not hold, and still achieved a reasonable degree of success. For example Dunagan et al [42] computed Mach 3 flows over cylinder-flare and cylinder-flare-cylinder configurations (flow conditions in Table 1.1, set 10) with various flare angles (12.5° for attached flow, 20° for incipient separation, and 30° fully separated flow) and compared the results with experimental data and found them to be in good agreement. Incoming boundary layer profiles were produced by growing a matching boundary layer. Unsteadiness was only apparent for the flow over the 30° flare. Computations were performed using a Reynolds averaged Navier-Stokes code with a k-ε turbulence model. Integration was performed by the explicit second order predictor-corrector finite difference method of MacCormack [43][4]. Agreement in terms of velocity and density profiles was good although the magnitude of the separation was over predicted. It may be that this over prediction of separation length is due to the coarseness of the mesh – it has been seen throughout the computations undertaken for this thesis that insufficient mesh refinement invariably results in excessive separation lengths.

Two equation turbulence models have also successfully predicted unsteadiness for flows known to be unsteady [44]. Detailed experimental data were obtained for Mach 2.85 cylinder-flare flows (flow conditions in Table 1.1, Set 7) with various flare angles via laser Doppler velocimetry, interferometry, oil flow visualisation and wall pressure measurements. Computations were undertaken with a time marching implicit upwind Navier-Stokes code incorporating a q-w turbulence model. The mesh was very coarse (95x95) with stretching towards the wall. No mention of mesh refinement studies is given. The time scale of oscillations (for the 30° flare) is approximately 1ms. Surface pressure measurements for attached flow (12.5° flare) compare favourably with computations, but separated (30.0° flare) flow computations show the correct qualitative trends but are in error quantitatively. The computed separated region is smaller than had been observed experimentally and the predicted decrease in displacement thickness downstream of compression corner is too slow – the experimental thinning is faster – this is attributed to a deficiency in the q-w turbulence model. Computational velocity predictions agree well with experiment as do peak turbulent kinetic energy magnitude and location. Taking separation as corresponding to an intermittency of 0.5 (the separation shock is upstream of this location for the same proportion of time that it is downstream of this location) yields a

---

[4] It is well known that to successfully apply McCormack's predictor-corrector method to these flows it is necessary to use significant amounts of artificial numerical viscosity.

computed separated region of approximately twice the length and twice the height of that observed experimentally. In summary it is concluded that, whilst the mean flow parameters can be predicted reasonably, dynamic effects are difficult to resolve accurately. It was concluded that large scale unsteady motions do not appear to have a critical impact on the ability to compute the mean properties of the flows.

1.4.5 Compressibility Effects

Morkovin's hypothesis [45] states that the effect of density fluctuations on turbulence is small provided they remain small with respect to the mean density. Compressibility effects can be included by Favre averaging [46].

Computations for a Mach 3, 24° compression ramp flow [47] showed that none of the algebraic, one equation or two equation models produced satisfactory results.

Various authors have tried to include the effects of compressibility into turbulence models with differing degrees of success. It is difficult to assess the effectiveness of these modifications, since the cases presented are those for which the modifications have been 'tuned' and hence it is not surprising that their modifications result in significantly enhanced predictions. These modifications are not used to compute other shock-boundary layer interactions or generic flows, and hence the true worth of the modifications remains unqualified.

1.4.6 Limitations of Boussinesq Eddy-Viscosity Relationship

The Boussinesq eddy-viscosity relationship inherently assumes that the principal axes of the Reynolds-stress tensor are coincident with those of the mean strain rate tensor throughout the flow. The Boussinesq relationship assumes that the effects of turbulence can be replicated by the addition of a scalar to the molecular viscosity. It is well known, however, that turbulent effects have many origins, for example surface roughness and freestream turbulence. Arguably the most significant shortfall in this assumption is the lack of flow history - it is known that flow history effects on the Reynolds stress tensor persist for significant distances in turbulent flows. Without these effects it is dubious whether or not such a trivial contrivance as artificially scaling the molecular viscosity could accurately replicate the diverse and subtle effects present in turbulent flows.

There are six categories of flow for which the Boussinesq relationship is not valid and hence significant errors can be expected with prediction techniques employing it [30]. The six categories of flow are:

i. flows with sudden changes in mean strain rate,
ii. flow over curved surfaces,
iii. flow in ducts with secondary motions,
iv. flow in rotating and stratified fluids,
v. three dimensional flows,

vi. flow with boundary layer separation.

It has been shown that turbulence models employing the Boussinesq approximation are generally unreliable for separated flows particularly shock separated flows.

The two main techniques used to remove the inadequacies of the Boussinesq approximation are to use a second order closure model or to use a non-linear constitutive relation [30]. Non-linear constitutive relations are of no use for flows with sudden changes in mean strain rate - for example shock induced boundary layer separation [30]. Second order closure models e.g. Wilcox's multiscale model [159] have recently been shown to produce enhanced results for a limited set of test cases involving flows for which the Boussinesq eddy viscosity approximation is invalid. At present the multiscale turbulence model is still in its infancy and will require significantly more application before it is likely to inspire widespread confidence.

1.4.7 DNS and LES

Direct Numerical Simulation (DNS) involves solving the full Navier Stokes equations directly (in conjunction with the continuity and energy equations) for all turbulent scales (both length and time), and hence requires massive computational resources. Even the smallest length scales in a turbulent flow are typically far larger than the molecular length scales [50], but it has been shown [51] that to undertake a full Navier-Stokes simulation of a pipe flow with Reynolds number of 500,000 (based on pipe diameter) would require computing power of far beyond that available at the present time or within the near future.

Since the turbulence length scale is equivalent to the diameter of a turbulent eddy, the maximum turbulent length scale that can be contained within the boundary layer is the boundary layer thickness itself. LES (Large Eddy Simulation) calculates the effects of the largest eddies, which are computed exactly, and the effects of the smallest eddies are modelled ("with hopefully a non-critical impact on the simulation" [30]).

Neither DNS nor LES rely on the Boussinesq eddy-viscosity relationship and hence the turbulence is not assumed to be aligned with the mean strain rate tensor.

Many proponents of LES seem to ignore the fact that whilst LES is a powerful computational technique, it is a reduced version of DNS and therefore cannot, by definition, produce the same results as DNS in all situations. For example, proponents of the application of LES to unsteady shock boundary layer interactions (e.g. [51]) often rely on the following assertions:

i. The unsteadiness of the separated region is resulting from

unsteadiness in the incoming boundary layer and hence simplified models relying on the Bousinessq eddy-viscosity concept to replicate the effects of turbulence, rather than the turbulence itself, cannot model the oscillations of the separated region.

ii. The only way to accurately model the unsteady oscillations is to model every structure within the incoming boundary layer i.e. to use DNS.

iii. For these high Reynolds number flows DNS is impossible (due to lack of computing power) and hence LES will be used (with the removal of eddies of below a certain length scale).

iv. To compensate for the removal of these sub-grid-scale eddies assume that their only effect was to dissipate turbulent energy with negligible contribution to the Reynolds stresses, and hence apply a sub-grid scale turbulence model.

Since it is impossible to undertake full DNS for these flows, direct comparison between DNS and LES is not possible. If, however, we assume that DNS would replicate the experimental results, then the differences between LES and experiment suggests that replacing the smallest eddies by sub-grid scale artificial viscosity models is having a non-trivial effect.

1.4.8 Summary of Turbulence Modelling

In the context of modelling unsteady shock boundary layer interactions:

i. Zero equation models are computationally inexpensive, numerically stable but can be unreliable for separated flows with a tendency to over-predict the length of the separated region (in extreme cases up to 100% of the experimentally measured length). Zero equation models have a tendency to over-predict the surface pressure rise.

ii. One equation models can offer slight advantages over zero equation models, although these improvements are offset by reduced applicability.

iii. Two equation models "can be expected to be inaccurate for many non-equilibrium flows" [30].

iv. Compressibility effects have been included by many researchers with varying degrees of success, although not generally proven for the classes of flows examined here.

v. The use of the Boussinesque eddy-viscosity relationship assumes that turbulence is isotropic and aligned with the mean strain rate tensor, neither of which is necessarily true. This relationship is not valid for flows with sudden changes in mean strain rate or flows with boundary layer separation, and hence is not valid for unsteady shock boundary layer interactions for which "significant errors can be predicted" [30].

vi. DNS cannot be employed for the flows addressed herein due to lack of computational resources.

vii. LES does not produce the correct results presumably due to inadequacies with sub grid scale models.
viii. More sophisticated and complex non-linear turbulence models employing constitutive relations have been shown only to weakly satisfy physical and mathematical requirements, such as the absence of non-physical flows [140].

Overall, none of the currently available methods will work for high Reynolds number unsteady shock boundary layer interactions. Therefore concentration is focussed on producing correct qualitative results or trying to find a model which is effective for, or can be 'tuned' for, the specific flows under investigation.

Set	Mach	Re (m^{-1})	P_0 (Nm^{-2})	T_0(K)	δ_{99} (mm)	δ^* (mm)	θ (mm)	Π	H	U (ms^{-1})	Ref.
1		$15.x10^6$	335psia	650R	17.8						131
2	2.9	$1.5x10^6$	2.0 atm	294	7.6					603	132
3	1.4	$14x10^6$			13.4						52
4	2.95	$6.5x10^7$	$6.8 x10^5$	265						582	99
5	2.95	$6.5x10^7$	$6.9 x10^5$	265	13+22					582	27,97
6	2.84	$6.5x10^7$	$6.8 x10^5$	265	24	6.4	1.3			575	24
7	2.85	$18x10^6$			11						44
8	2.84				24	6.4	1.3			575	100
9	5		$2.1 x10^6$	327				0.4-0.6			85
10	2.85	$18x10^6$	1.7atm	270	11						42
11	2.79-2.87	$6.3x10^7$	$6.9 x10^5$	252-263	25-26		1.2			562-576	102
12	2.95	$6.7x10^7$	$6.89 x10^5$	255	17	4.5	0.87			565	101
13	2.87	$6.5x10^7$	$6.9 x10^5$	270	28	6.2		0.5	1.2	565	103
14	2.84	$6.5x10^7$	$6.8 x10^5$	265	26	6.4	1.3			575	28
15	4.95	$14.8x10^7$ per foot	314psia	620R	0.7"						18
16	4.95	$5.1 x10^7$	$2.2 x10^6$	344						774	104
17	4.95	$49.6x10^6$	$2.3 x10^6$	350	17.5	6.4	0.53	0.3	12	764	14,15,17
18	4.95	$48.7x10^6$	$2.2 x10^6$	350	17.5					764	10
19	4.95	$15.2x10^{6/ft}$	330psia	647R	14.9	6.6	0.7	0.78		775	107
20	1.5	$12.5x10^6$	$98.6 x10^3$	290	14.3	2.5	1.4		1.8	424	66

Table 1.1 Wind Tunnel Conditions From Referenced Texts

Ramp angle	Average time between shock crossings (ms)	Average shock crossing frequency (Hz)	Mean frequency of shock oscillations (Hz)
6°	0.74	1355	2974
9°	0.87	1150	3570
12°	0.85	1176	3000

Table 1.2. Variation in Temporal Characteristics of a Mach 1.5 Unsteady Shock Boundary Layer Interaction [66]

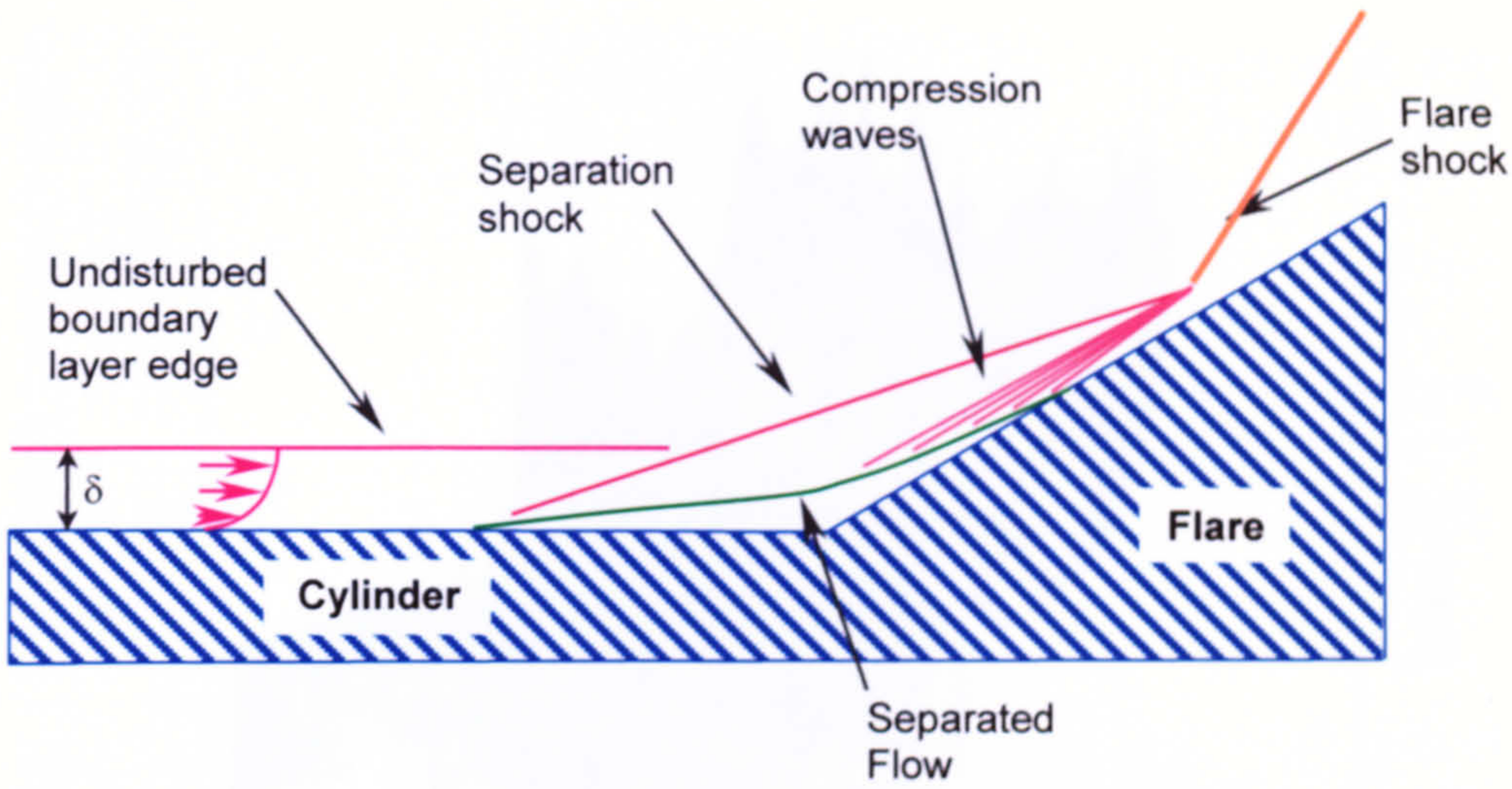

Figure 1.1. Schematic of an Axisymmetric Shock Boundary Layer Interaction

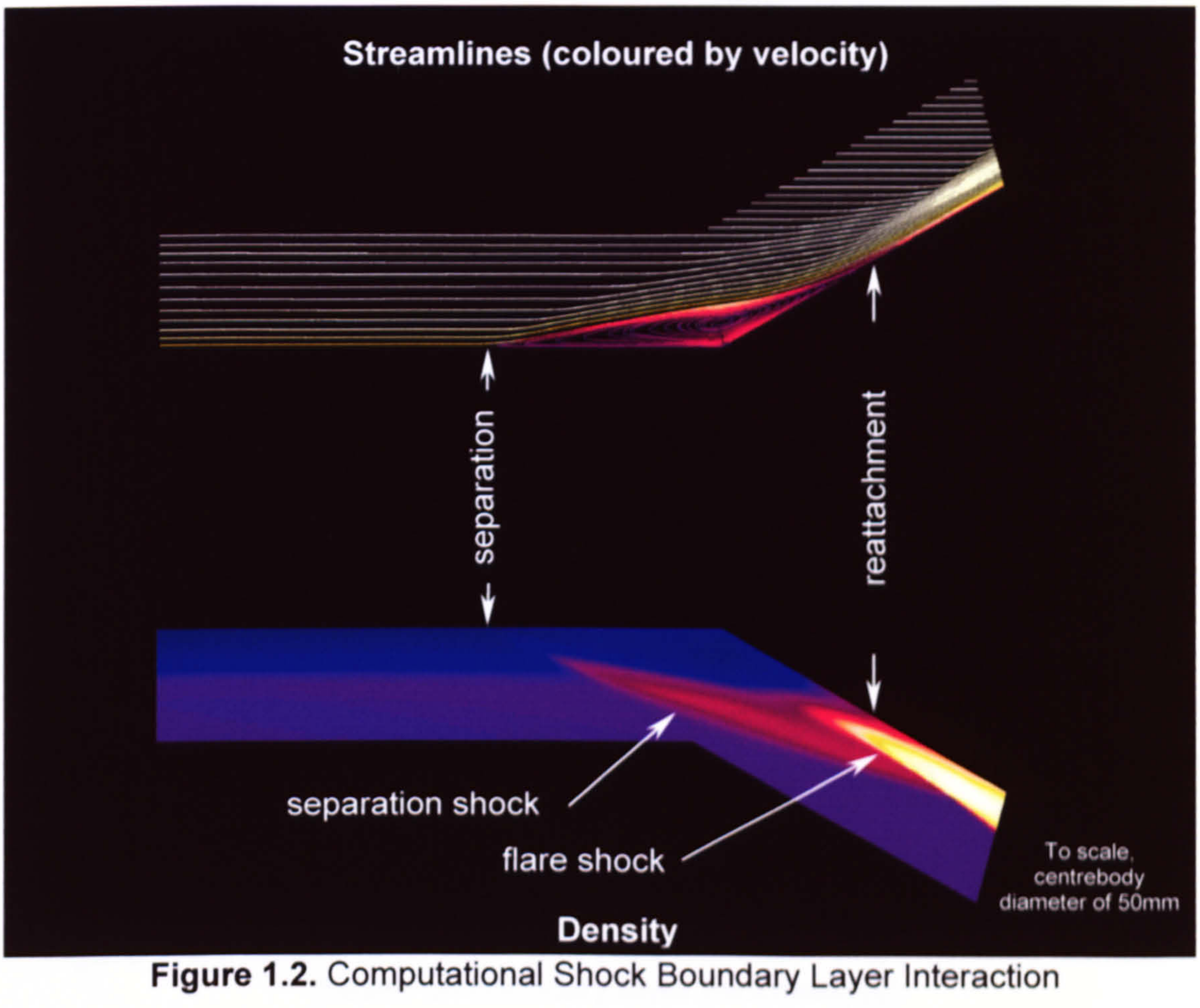

Figure 1.2. Computational Shock Boundary Layer Interaction

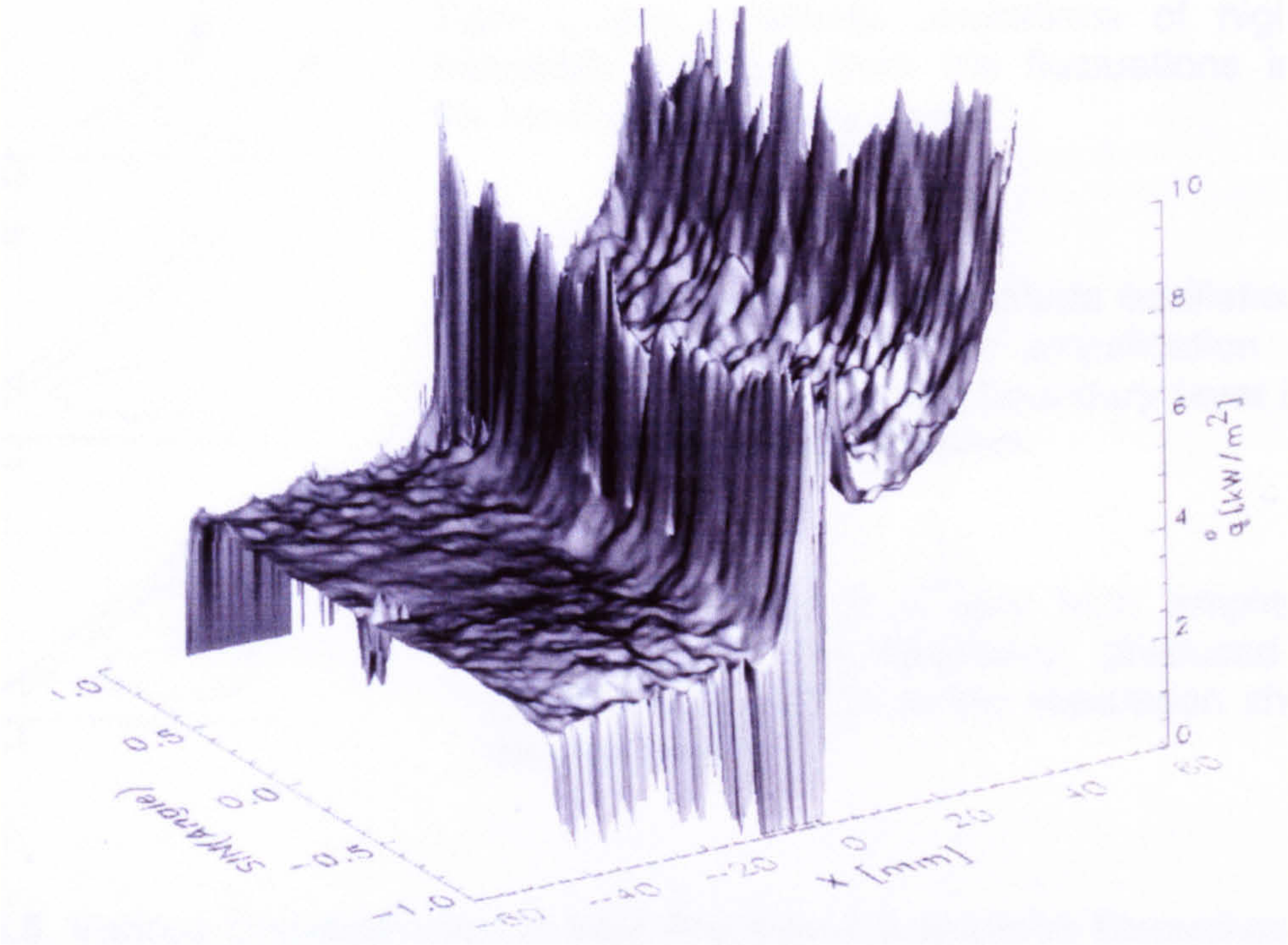

Figure 1.3. Heat Transfer to a Cylinder-Flare (20°) at Mach 5 Measured Using Liquid Crystal Thermography [2].

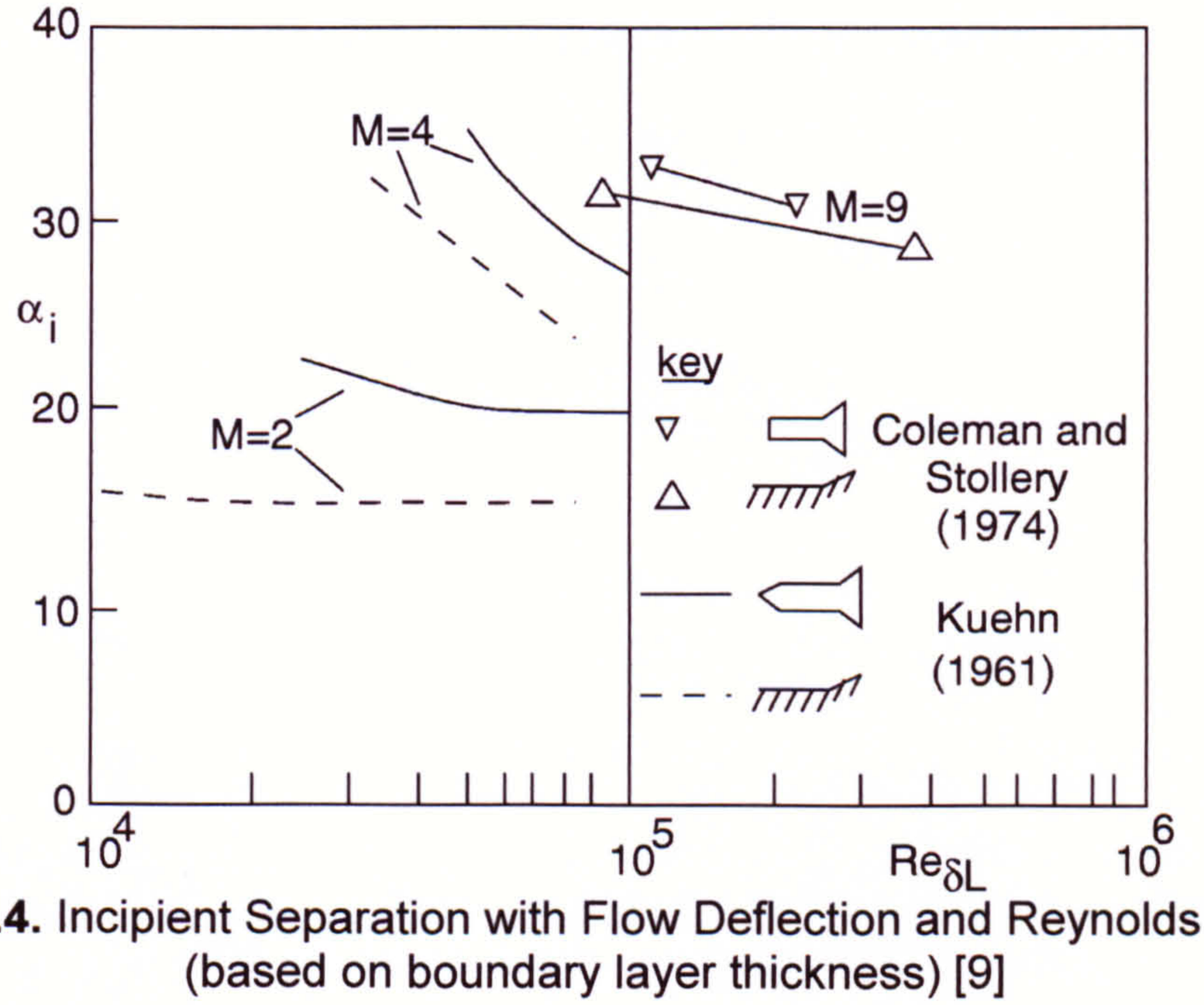

Figure 1.4. Incipient Separation with Flow Deflection and Reynolds Number (based on boundary layer thickness) [9]

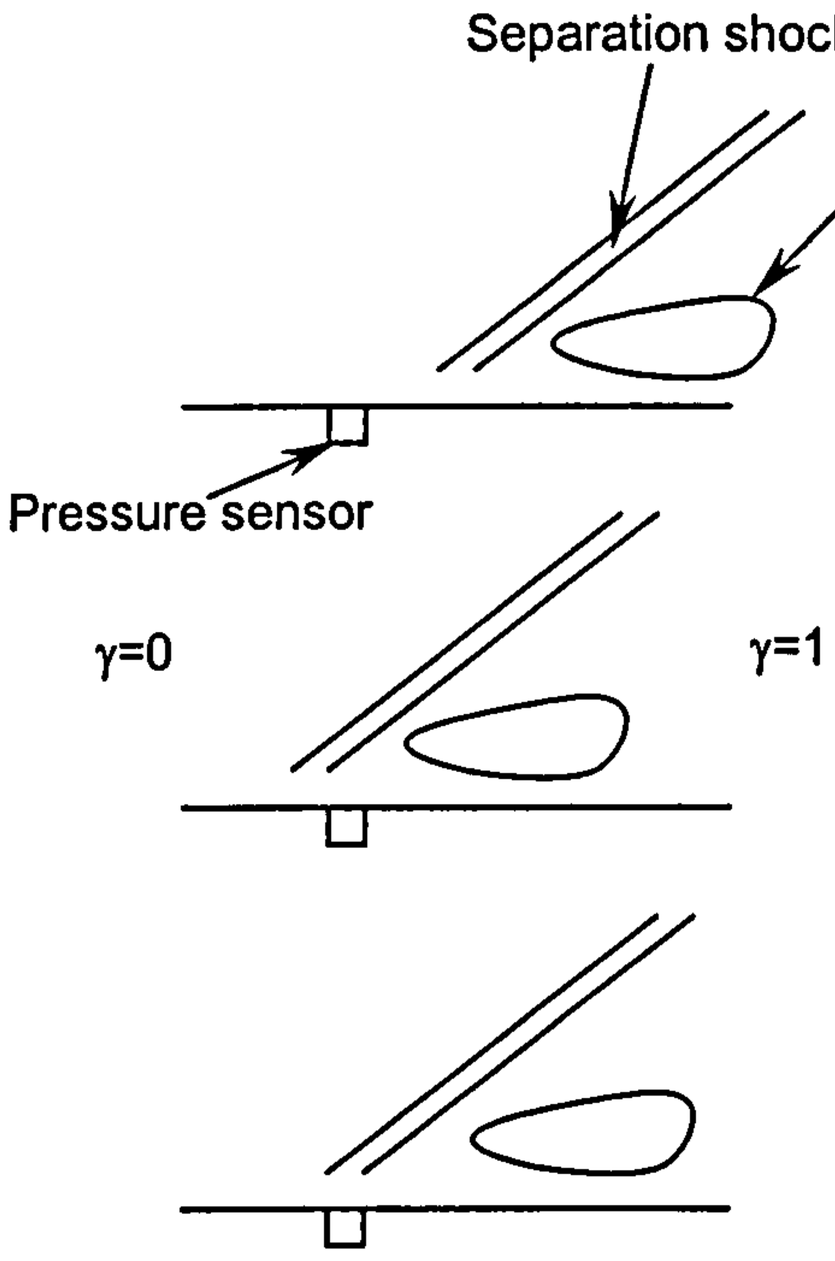

Type I: low amplitude oscillations of high frequency resulting from the fluctuations in the incoming boundary layer.

Type II = Type I + high amplitude oscillations of high frequency due to amplification of turbulence in the incoming boundary layer by the separated free shear layer.

Type III = Type II + very high amplitude oscillations of low frequency, produced by the unsteady motion of the separation shock over the sensor.

Figure 1.5. Various Characteristics of Wall Pressure Fluctuations Throughout an Unsteady Shock Boundary Layer Interaction (as per [15]).

2. Turbulent Axisymmetric Cylinder-Flare Flows

Ascertaining, experimentally, whether or not boundary layer separation is occurring (and if so, where) is not a trivial task to perform accurately and consistently. Three flowfield parameters that are commonly employed to assess the presence and magnitude of separation are:

i. Surface pressure distribution - direct examination of the surface pressure distribution over a body can yield information relating to the location of separation and reattachment by the presence and location of peaks and plateaux.
ii. Shear stress and skin friction - with the advancement of experimental techniques it is possible to use shear stress sensitive skin friction gauges to determine local skin friction coefficients (via shear stress). For the purposes of locating separation and reattachment (and secondary separations) oil flow visualisation is reasonably effective.
iii. Density - optical techniques such as schlieren and interferometry can be used to pinpoint the location of separation shocks and hence the location of separation. This may not necessarily detect the smaller separated regions, if, for example, the deflection, and hence separation shock strength is small, or if the separation shock is embedded in the boundary layer.

These techniques are effective for detecting large scale separation but are less likely to detect the separated regions of small magnitude that are being considered here due to the inherent lack of sensitivity (possibly with the exception of (ii)).

2.1 Experimental Data – Axisymmetric

Babinsky and Edwards [2][3][4][5] undertook comprehensive analysis of various axisymmetric configurations in the DERA HSST (High Speed Supersonic Tunnel) at Mach 5. The HSST is an intermittent pressure-vacuum facility, capable of producing flows of Mach 4 to 6, dependent on nozzle geometry and running conditions. The maximum operating pressure is $1.4 \times 10^6 Nm^{-2}$ and the maximum heater temperature 700°K, with useful flow duration of several seconds. Further details of the facility can be found in [53] from which a reconstructed schematic is presented in Figure 2.1. Throughout these experiments Babinsky and Edwards used a nozzle equipped with a 50mm diameter centrebody and model mount which extends through the nozzle to give a fully turbulent boundary layer at the model attachment location (Figure 2.2). The undisturbed boundary layer thickness at the model mount location is 9.8mm.

High-resolution heat transfer distributions for various cylinder-flare configurations were obtained using liquid crystal thermography via thin coatings of encapsulated liquid crystal applied to the surface of the model

[2][3][4][5]. Changes in hue were recorded using a video camera and heat transfer rates produced by filtering and digital hue analysis. Shear stress sensitive unencapsulated liquid crystals were used for flow visualisation to highlight flow reversal, separation and reattachment. These experiments, produced peaks in heat flux close to the cylinder-flare junction which it was suggested correspond to small scale separation (the flare angles used were smaller than those which would previously have been expected to induce separation).

With the wind tunnel operated at Mach 5, at the model attachment location (the cylinder-flare junction), the undisturbed boundary layer thickness is 9.8mm and the Reynolds number based on this thickness ($Re_{\delta L}$) is 1.19×10^5m[2]. The axisymmetric data of Coleman and Stollery [9] (Figure 1.4) suggests that for $Re_{\delta L}=O(10^5)$ at Mach 5, incipient separation should occur for flow deflections of ≈30°. Separation was seen at 15° and above. Using data from Kuehn[6][7] (Figures 2.3 and 2.4) and extrapolating, incipient separation would be predicted at ≈33°.

2.2 Axisymmetric Computational Results

Computational results were produced using the SPIKE Reynolds averaged, finite volume, cell centred, Navier-Stokes code [54][55][56] based on the ROGER code [57]. SPIKE is a structured, multiple domain, multi-mode CFD code and can be run with various options:

- One, two or three dimensional or axisymmetric,
- Time accurate, explicit, point implicit or alternating direction line implicit,
- Laminar or turbulent (Baldwin-Lomax or k-ε turbulence models),
- Numerical stability control via eigenvalue magnitude limiting (Appendix E), and order and CFL ramping.

2.2.1 Mesh Generation.

To solve the Navier-Stokes equations (to predict the flow over the configurations of interest), some form of spatial discretisation is required (a mesh). The primary considerations are the physical geometry and the mesh extent necessary to capture all of the required flow physics. This is typically performed with a-priori knowledge of the flowfield (e.g. from experimental results) or by theoretical analysis of the problem (for example, the length of plate required to produce a boundary layer of the required thickness and shock positions).

For computations of compression ramp (and flare) separated flows the cell Reynolds number (y^+) required for accurate simulation of the shock boundary layer interaction is small, far smaller than that necessary for undisturbed flat plate (or cylinder) boundary layer growth. To minimise the computational overhead of resolving the flow over a significant length of flat plate with excessively small cells (to provide a sufficiently small y^+ in the interaction region), an inflow boundary condition was added, to enforce the required

boundary layer profile at the appropriate location prior to every iteration (these profiles include the turbulent parameters k and ε where applicable).

INFEMS [62] is a multiple block Index Notation Finite Element MeShing code which produces structured hexahedral multiblock meshes. To enhance convergence and reduce computational cost it is important to ensure that a sufficient but minimal number of cells are placed at every location within the computational domain. The most common methods used to provide minimally sufficient grids involve stretching towards viscous no-slip boundaries (to ensure sufficient spatial resolution within the boundary layer) and in the vicinity of shock waves. Further stretching can be performed, as and where required, for example stretching in a streamwise direction in the proximity of separation (to accurately capture the distributed momentum loss due to the adverse pressure gradient) and reattachment. This stretching can take many forms, the most common being, exponential, geometric, arithmetic, hyperbolic, and trigonometric.

2.2.2 Computation

To obtain optimal convergence with SPIKE the eigenvalue limiter (Appendix E) must be gradually reduced to zero (from an initial value sufficiently large to ensure numerical stability during the preliminary stages of the computation). It is important that the eigenvalue limiter is reduced to zero in order to accurately resolve the thermal boundary layer and unsteady effects[56]. Ascertaining when convergence has been achieved can be problematic due to low frequency or sporadic oscillations in the residuals. To ensure convergence for the steady computations presented here, flowfields are compared as the solution progresses until only negligible changes are occurring and that the changes are not the result of a 'slow drift' towards a different solution.

The smaller the value of the eigenvalue limiter, the less numerical diffusion is induced. Due to the stabilising effect of large eigenvalue limiters, it is usually necessary to start the simulation with a relatively large eigenvalue limiter (0.3) and to progressively decrease the value as the solution approaches convergence and the flowfield fluctuations decrease.

A similar approach is adopted with regard to the 1^{st} and 2^{nd} order terms for the numerical integration, i.e. the computation can be set to start as first order and then apply relaxation to the second order terms to gradually undergo transition to a second-order computation. The CFL number may also be progressively decreased as the solution progresses.

The choice of integration technique is important both in terms of solution validity and convergence rate. For unsteady computations it is more efficient to undertake steady state computations (either with point implicit or alternating direction implicit integration), prior to using a time accurate, explicit solver, than to employ a time accurate explicit solver from the outset. This significantly reduces the computational cost, as the time averaged flow

features are established rapidly due to the use of local time stepping and implicit solution, and produces the majority of the flow features in the unsteady flow. There are five relaxation factors for the inviscid, viscous and k-ε equations, which must be specified according to the integration technique, and requirement for time-accuracy[54][55][56][57].

In an analogous manner, due to the computational expense of solving an additional two equations for the k-ε turbulence model, it is normally advantageous to employ a zero-equation turbulence model (i.e. Baldwin-Lomax) prior to using the k-ε turbulence model. Whilst the changes in solution between Baldwin-Lomax and k-ε are significant, they are, nevertheless, smaller than those between the laminar and k-ε solutions.

2.2.3 Convergence Assessment - Iterative

It was discovered that for shock separated flows, monitoring the residual output from SPIKE was not a very reliable technique for assessing convergence. Due to the amplification of numerical noise and the very slow growth (in computational terms) of the separated region, it can be exceedingly difficult, if not impossible, to assess convergence solely by examining the residuals. An initial test to assess steady state convergence was to output the wall pressure at specified locations and to plot their variation with respect to iteration number and look for a cessation of change. Whilst this proved a better test for convergence than residual analysis, convergence determination was less convincing using a single point, and for multiple point monitoring very large amounts of data were being produced. One technique to circumvent these problems would have been to dump entire pressure distributions at prescribed intervals, although this would require an a-priori estimate as to just how often these dumps should be performed. A far more effective and significantly more sensitive technique was employed. By outputting the locations at which $u_{\tau_i} u_{\tau_{i+1}} \leq 0$, separation and reattachment motion with respect to iteration can be accurately monitored and hence when the region ceases to enlarge, convergence has been reached. By logging the motion of separation and reattachment, the position and magnitude of the separated region can be monitored and solution convergence verified. This is also useful in terms of recording expansion and contraction (and motion) of the separation bubble for subsequent unsteady computations.

2.2.4 Convergence Assessment - Spatial

It is very important that mesh independence is achieved for any computation involving spatial discretisation. For these ramp/flare flows this encompasses two separate issues: sufficiency of spatial resolution, and provision of enough upstream physical domain to allow for the propogation of structures upstream throughout the sub-sonic portion of the boundary layer. The latter is relatively easy to ensure through the addition of computational upstream extent once spatial convergence has been established. The former can hold traps for the

unwary. To assess convergence, and to ensure minimal computational cost, it is necessary to optimise the number of cells in a given direction using grid stretching to relocate/cluster the cells to areas of the flowfield known to require enhanced spatial resolution. Problems can arise due to the non-orthogonality of the meshes (they have been designed for minimum skew for optimal accuracy) – for example: increasing the number of cells in the i direction reduces Δx, and also leads to a reduction in Δy. Thus if the mesh is sufficient in discretisation in the x direction, but not in the y direction, then an increase in the number of cells in the x direction will still produce a different solution. This reduction in Δy is far more gradual than could be achieved by a direct increase in the number of cells in the j direction and hence it is advisable to pursue i and j refinements simultaneously. Subject to these considerations, performing accurate and effective mesh independence analysis is not too onerous. It is imperative, however, that this analysis is undertaken and that the selected mesh is proven to be at least sufficient.

2.2.5 Convergence Assessment - Temporal

Temporal convergence analysis for the time accurate computations presented here is trivial. To ensure time accuracy SPIKE is run using a time accurate explicit solver with global time stepping and thus temporal convergence can be assessed by simply reducing the CFL number and examining the time dependant flowfield for change.

2.2.6 Computational Inflow Production

To model accurately the experimental conditions [2] it is important that the computational inflow matches the experimental freestream and boundary layer flow as accurately as possible. To model the entire flowfield for these configurations it would be necessary to model the boundary layer growth from its inception within a centrebody nozzle in a complex system of pressure gradients through transition to the model attachment location. Obviously this is undesirable and can be avoided since there is sufficient boundary layer data available from these experiments to enable an inflow boundary layer to be constructed without recourse to complete simulation. Experimental data for surface pressure, heat transfer, Stanton number and skin friction coefficient distributions, and boundary layer traverse data for total pressure and static pressure throughout the boundary layer is available [2]. By processing this data it is possible to produce an inflow boundary layer for each of the flow primitives required for the computation. It was shown that such an inflow produces spurious flowfield perturbations when applied with either the Baldwin-Lomax or k-ε turbulence models for boundary layer evolution over a length of centre body [58][59]. Figure 2.5 shows an example of the perturbations in skin friction coefficient resulting from a pressure wave emanating from the wall at the location of the inflow (using the Baldwin-Lomax turbulence model; the results using the k-ε turbulence model were very similar). Over reasonably short distances the growth of this relatively thick boundary layer is slow, and hence the variation in boundary layer profiles can

be assumed to be quasi-one dimensional. Therefore, it is possible to linearly extrapolate through two downstream locations, back to the inflow to produce a Baldwin-Lomax or k-ε compatible inflow [58]. Using this technique, solutions free of spurious pressure waves and skin friction perturbations were produced (Figure 2.6). Similar inflow profile mismatch difficulties have been observed previously e.g. by Zhang and Edwards [60][61]. These profiles do not differ significantly from the original experimentally derived profiles (Figure 2.7). Using the standard subsonic and supersonic Rayleigh-Pitot relationships [143]:

$$P_{ratio} = \frac{P_{pit}}{P_0} = \frac{P_{pit}\left(1+\frac{\gamma-1}{2}M_\infty^2\right)^{\frac{\gamma}{1-\gamma}}}{P_\infty}$$

$$M \geq 1 \Rightarrow P_{pit} = P\frac{\left[\frac{\gamma+1}{2}M^2\right]^{\frac{\gamma}{\gamma-1}}}{\left[\frac{2\gamma}{\gamma+1}M^2 - \frac{\gamma-1}{\gamma+1}\right]^{\frac{1}{\gamma-1}}}$$

$$M \leq 1 \Rightarrow P_{pit} = P\left(1+\frac{\gamma-1}{2}M^2\right)^{\frac{\gamma}{\gamma-1}}$$

direct comparison between experimental and computational pitot pressures through the boundary layer illustrates that the experiment and computation are in good agreement (Figures 2.8 and 2.9).

The overshoot in pitot pressure seen experimentally is due to a weak shock wave produced at the nozzle exit, which impinges into the working section (not present in the computations). Whilst this is not believed to have influenced the results qualitatively, it may influence attempts to make precise quantitative comparisons between computation and experiment. As expected from the quasi-one-dimensional nature of the flow, the pressure, density, Mach number and temperature fields exhibit very little fluctuation over the extent of the cylinder. Further iterations of the extrapolation technique fail to improve the results obtained for a single extrapolation. It transpired that this extrapolation technique could not be used to predict turbulent kinetic energy and specific dissipation rate profiles for k-ε boundary layer profiles (the turbulent kinetic energy was, in places, less than zero). Consequently only results using the Baldwin-Lomax turbulent model are presented here.

2.2.7 Mesh generation

Meshes used for the flared test cases comprised two regions: one upstream and one downstream of the cylinder-flare junction (Figure 2.10). The axisymmetric mesh representing a 2° sector of the flowfield with the inter-region boundary inclined at half the flare angle from the vertical to minimise cell skew. Grid stretching was performed normal to the wall to provide

accurate resolution of the viscous stresses and parallel to the wall to provide better resolution of the flow near to separation and reattachment. The mesh was extended 100mm (10.2δ) upstream of the cylinder-flare junction to ensure that the inflow boundary condition was not affecting the formation and/or behaviour of the separated region. Interior grid point placement was by transfinite interpolation [63] with no mesh smoothing (not deemed to be necessary, as the transfinite interpolation produced neither cell size discontinuities nor high skew).

For each computation, extensive mesh refinement was undertaken to ensure that spatial discretisation had no effect on the solution. To ensure mesh convergence y^+ was reduced from 1 to $2x10^{-3}$ by the addition of cells and increasing the normal grid stretching factor. The mesh details necessary to obtain mesh independence are illustrated in Figure 2.11.

For the results presented here, the same reference point as that of Babinsky[2] was adopted (x=0 is defined to be cylinder-flare junction).

2.2.8 Results

Preliminary results using the Baldwin-Lomax turbulence model (discussed in §1.4.3 and presented in Annex B) predicted a mean value for skin friction coefficient of $1.07x10^{-3}$ which compares favourably with the experimentally measured [2] value of $1.01x10^{-3}$ (an error of 6%). Comparisons of experimental and computational surface pressure distributions are given in Figures 2.12 and 2.13 and agreement is seen to be reasonable. Cylinder-flare flows with the following flare angles were computed and analysed: 0°, 5°, 7.5°, 10°, 15°, 20°, 22.5°, 25°, 27.5°, 30°. An annotated density contour plot for the 30° flowfield is presented in Figure 2.14 to provide an indication as to the magnitude and location of the separated region and the relative positions of salient flow structures. Examination of the streamwise velocity contours (Figure 2.15) clearly shows the presence of a large, well defined separated region. By extracting velocity profiles at the locations marked as 'A', 'B', and 'C' in Figure 2.15, the separation is readily apparent (Figure 2.16) as a reversal in the flow direction near to the surface of the cylinder.

One of the most commonly employed experimental techniques for ascertaining the location of separation and reattachment is to examine the surface pressure distribution for inflections (e.g. [6][7]). The surface pressure coefficient distribution along the cylinder and 30° flare is given in Figure 2.17. The separation and reattachment points are clearly visible ($x\approx$-0.045m (x=-4.6δ) and $x\approx$+0.03m (x=+3.1δ) respectively). Another 'fluctuation' in Cp is visible around x=0 which is more apparent in the skin friction distribution (Figure 2.18). As the flare angle is increased, this increase in skin friction coefficient and the corresponding 'fluctuations' in Cp become more pronounced, as a secondary separation bubble forms under the primary separation bubble.

Using the sign of the skin friction coefficient to indirectly examine the local flow

direction on the surface, separation and reattachment are readily located (the locations at which skin friction changes sign). Locations at which skin friction coefficient is negative must correspond to regions of local flow reversal, i.e. recirculating or separated flow. For the 30° case (Figure 2.18) and larger flare angles, the skin friction coefficient is slightly positive over a small range (around x=0) corresponding to the formation of a secondary separation bubble.

For the 30° case (using skin friction coefficient – Figure 2.18) separation is found to occur 45mm (4.6δ) upstream of the cylinder-flare junction and reattachment 29mm (3.1δ) downstream of the junction, giving a separated region of length of 74.6mm (7.6δ). The maximum excursion of the separated region from the wall is approximately 7.3mm, corresponding to 74.5% of the undisturbed boundary layer thickness.

Whilst examination of surface pressure coefficient can provide relatively accurate positional data for separation and reattachment for large separated regions (for the 30° case the height of the separated region is 75% of the thickness of the undisturbed boundary layer), smaller separated regions produced by lesser adverse pressure gradients have proportionally less effect on the surface pressure distribution and hence these are progressively more difficult to detect and locate. For example, the flow over a 20° flare produces a relatively large separated region (two boundary layer thicknesses in length), but the separated region is very thin (≈9% of the boundary layer thickness) and hence the separated region only produces a slight perturbation to the external flow and thus the surface pressure distribution is not significantly perturbed to allow accurate location of separation and reattachment. This is illustrated in Figure 2.19, from which it is seen that whilst it is difficult to predict, with any certainty or accuracy, the location of separation and reattachment on the basis of surface pressure coefficient (marked as green squares), they are easily located on the basis of skin friction. Similarly, Dolling and Brusniak [85] report the presence of small separated regions embedded within a Mach 5 boundary layer passing over a 16° ramp. These small scale separations are difficult to detect experimentally except via near wall effect sensitive techniques (e.g. liquid crystal thermography). Using liquid crystal thermography small scale separations have been observed experimentally, at these flow conditions, by Babinsky and Edwards[2][3][4][5].

Examining skin friction coefficient shows the reduction in the local flow velocity prior to separation. Figure 2.20 shows the skin friction coefficient distribution for the flow over the cylinder and a 5° flare and it is seen that whilst the flow does not separate, it is retarded significantly at the cylinder-flare junction and that a slight increase in flare angle will result in separation.

Increasing the flare angle increases the flow deflection and hence the strength of the flare shock and consequently the magnitude of the adverse pressure gradient experienced by the approaching boundary layer. The adverse pressure gradient causes a distributed loss of momentum in the boundary

layer and hence the distance upstream of the cylinder-flare junction at which separation occurs is directly related to the flare angle (as reported by Kuehn[6][7]). At each flare angle the qualitative results are identical (excepting the formation of the secondary separation bubble at larger flare angles), and variation in quantitative results is limited, and related, to the position and magnitude of the separated region, the shock waves and their effects.

Table 2.1 summarises the effect of flare angle on the size and location of the separated region produced by computation of the flow over the various flared geometries addressed (obtained directly from skin friction coefficient) and is presented graphically in Figure 2.21.

The variation of separation length with flare angle appears approximately to follow a power law (the power law fit is illustrated as a dotted line in Figure 2.21 and is given by the equation $l = (0.217\alpha - 1.08)^{2.5}$ (l in mm, α in °)).

The height of the computed separated region may be obtained by tracing the dividing streamline from the point of separation to the point of reattachment. Figure 2.22 illustrates the separation of the boundary layer, its passage around the separation bubble via the dividing streamline between the recirculatory flow and the non-recirculatory flow (i.e. the circumscribing streamline). Tracing this streamline through the computational domain is effected by following the path of an imaginary particle through adjacent cells by projecting a uniform velocity vector through each cell to locate the point on the boundary at which the imaginary particle would exit. Repeating this process through consecutive cells chosen on the basis of particle exit boundary, and starting from the cell immediately upstream of separation yields a streamline very close to the dividing streamline. Subtracting the ordinate of each corresponding point on the surface of the cylinder and flare yields the height of the separated region. The separated height distribution for a 30° flare is illustrated in Figure 2.23 (the maximum height being 7.3mm (0.7δ)). Applying this algorithm to each of the test cases produces the variation in height of the separated region with respect to flare angle. The results are given in Table 2.2.

This variation is presented in Figure 2.24. It is noted that as the flare angle is increased above approximately 20° the height of the separated region increases more rapidly with increasing flare angle. Babinsky and Edwards [83] estimated the location and magnitude of a separated region under identical conditions for a 20° flare from their experimental data. Separation was observed 4mm (0.4δ) upstream of the corner (cf. 7mm (0.7δ)) and reattachment 1.5mm (0.2δ) downstream (cf. 12.5mm (1.3δ)) indicating that the computational model is not predicting these locations correctly. These errors are believed to be caused by inadequacies in the Baldwin-Lomax turbulence model (the Baldwin-Lomax turbulence model is known to predict overly large separated regions[30]) or possibly due to the presence of an impinging nozzle

shock. It is also noted that 20° appears to be the angle at which the rate of growth of the separated region becomes significantly more sensitive to flare angle, and hence errors in separated length are likely to be large. Whilst quantitative errors are occurring there is no evidence to suggest that the qualitative data presented here is invalid.

Separation is being predicted at lower angles than would have been expected on the basis of experimental work prior to that of Babinsky and Edwards [83]. This is believed to be due to the separated region being too thin to be observed using traditional experimental techniques (e.g. optical techniques such as shadowgraphs and schlieren or surface pressure distribution analysis). This separated region may be observed using experimental techniques such as liquid crystal thermography or through the application of unencapsulated liquid crystal to highlight variation in shear stress [2], techniques which depend on near wall variations. The presence of separated regions exclusively within the viscous sub-layer are only discernible through skin friction coefficient and heat transfer in a similar manner to the effects of small scale surface roughness.

Small scale separations as observed by Babinsky and Edwards [83] are being predicted computationally. Similar 'two-stage' separation is being observed for which with small flow deflections (much smaller than would ordinarily be expected to induce separation) the magnitude of the separated region varies little with deflection angle. Babinsky and Edwards [83] report a 'sudden increase' in separation length with flare angle, and it has been observed here that whilst the separation length increases rapidly (approximately to the power 2.5 with respect to flare angle) the sudden increase in magnitude of the effects of separation result from the sudden increase in the height of the separated region and its consequent influence on the external flow.

As the flare angle is increased above 20° the height of the separated region increases very rapidly corresponding to the onset of 'traditional' separation for which perturbations to the surface pressure may be used to locate separation and reattachment.

It is noted that whilst very small separated regions are being predicted there is still a minimum angle below which separation does not occur as per [6][7][141][144][145][146][147]. This is entirely consistent with the concept of a loss of momentum necessary to retard the flow to rest or reversal [8].

To examine the characteristics involved in separation, it is necessary to establish that the incoming flow is quasi-one dimensional over the region of interest, i.e. that the boundary layer profiles are self similar. It has been seen previously that the thickness of the boundary layer varies little over the region of interest ($-0.050m \leq x \leq 0.050m$) ($-5.1\delta \leq x \leq 5.1\delta$) as seen in Figure 2.7.

Momentum thicknesses were calculated via numerical integration[5] with the assumption of linear variation between consecutive pairs of cell centred data points. Sample results are presented in Table 2.3.

The variation in momentum thickness between the inflow and the location at which the flares were attached is 5.7%. This is considered a sufficiently small variation that the boundary layer properties may be considered to be independent of position from the inflow to the cylinder-flare junction, i.e. that the flow is quasi-one dimensional.

It is known that the cause of separation is the adverse pressure gradient experienced by the boundary layer, and by applying a one-sided finite difference approximation to the variation of surface pressure coefficient with x between adjacent cells, a first order approximation of the adverse pressure gradient distribution is obtained. The distribution of this gradient along the cylinder surface for various flare angles is illustrated in Figure 2.25. The dotted vertical lines in this figure correspond to the location of separation (obtained by examination of skin friction coefficient) and it is noted that the peak pressure gradient preceding separation (denoted by squares) appears to be insensitive to flare angle and hence insensitive to flare shock pressure rise. It is further noted that the form of the pressure gradient distribution along the cylinder is similarly insensitive to flare angle and thus the integral of the adverse pressure gradient with respect to x must also be independent of flare angle.

The retarding effect on the boundary layer of its passage through the adverse pressure gradient is cumulative in terms of momentum loss[8]. The total momentum loss experienced by the boundary layer at the point at which its velocity becomes zero and separation occurs is the integral of the adverse pressure gradient in the streamwise direction from the inflow to the point of separation. The undisturbed boundary layer results in a surface pressure coefficient of zero (assuming constant pressure through the boundary layer and the lack of external pressure gradients). Applying limits to the integral of adverse pressure gradient suggests that the boundary layer can only sustain a finite adverse pressure gradient prior to separation and that the surface pressure coefficient at the point of separation will be independent of flare angle. This is illustrated in Figure 2.26 in which the horizontal dotted line represents the average surface pressure coefficient at separation (≈0.01378, with deviation of ±2.6%). These results suggest that this specific boundary layer under these specific conditions can only withstand a rise in Cp of ≈0.014 before separating.

The pressure rise necessary to induce separation arises from the compression of the flow through the separation shock wave. Employing a

---

[5] Momentum thickness $\theta = \int_0^{y_1} \frac{\rho u}{\rho_e u_e}\left(1-\frac{u}{u_e}\right)dy$

semi-automated shock location technique, the computational separation shock angles were obtained. For the smaller flare angles the separation shock was partially or totally embedded within the boundary layer and obtaining accurate measurements for ensuing shock angle calculations was difficult. Variation in computational separation shock angle with flare angle is given in Figure 2.27 in which the solid line represents the average angle obtained by repetition of the measurements and the error bars provide an indication as to the probable error (quantified through repetition). It was observed that the separation shock angle was ≈20°±2° over the range of cylinder-flare flows computed. Figure 2.28 correlates flow deflection angle with shock angle from which it is seen that a 20° shock wave will produce flow deflection of ≈11°. To obtain computational flow deflections for the separating boundary layer, two different approaches were employed. The first method obtained an initial estimate of the angle by calculating the inclination of a line projected from the point of separation to the point of reattachment. This produced reasonably constant flow deflection angles for flare angles of 20° and above (deflection angle ≈13.5°). Below 20° the results are less consistent due to mesh discretisation coupled with the limited extent of the separated region. Estimates produced by this technique will overestimate the deflection angle due to the shape of the separated region (Figure 2.29). The second technique produces a distribution of flow deflection angles based on the inclination of the dividing streamline to the horizontal. For low flare angles where the dividing streamline is short in terms of number of cells traversed the approximation to flow deflection angle is less accurate due to the higher inter-cell velocity gradients (the streamline calculations assume uniform flow parameters within each cell). For larger flare angles the dividing streamline corresponds to a flow deflection of ≈11.5° (this is the flow deflection induced by the separation shock, not the flow deflection produced by the flare). A flow deflection of ≈11°-12° is consistent with the observed separation shock angle of ≈20°. From Figure 2.30 the shock wave associated with an 11° flow deflection will produce a rise in Cp of ≈0.12. It was seen that for the test cases where the separated region is large enough to allow the surface pressure coefficient to 'plateau' between the separation shock and the flare shock (25° and above) the plateau has a Cp of ≈0.11 which agrees reasonably well with the pressure rise across the separation shock (Figure 2.31 shows the surface pressure coefficient distribution for a 30° flare).

The agreement in qualitative terms and, to some extent, quantitative terms between experiment and computation is surprising when using the Baldwin-Lomax turbulence model (to accurately predict separation of a turbulent boundary layer, the boundary layer momentum profile must be accurately predicted as well as the adverse pressure gradient distribution).

The Baldwin-Lomax turbulence model does not model the physics of the flowfield[31], merely the physical effects of the turbulence, i.e. there is no explicit laminar sublayer and no boundary layer edge (beyond the edge of the boundary layer the turbulent viscosity does not return to zero). Figure 2.32

shows the inner, outer and selected turbulent eddy viscosities 16.25mm (1.7δ) from the inflow and it is seen that μ_t never returns to zero and hence the undisturbed freestream flow is excessively viscous. Furthermore it is seen that there is a discontinuity in blending between the inner and outer regions.

It has been shown, for these computational models, that an adverse pressure gradient resulting in a Cp rise of approximately 0.014 will induce separation for this flow over these configurations. This value of Cp is independent of position and hence we can assert that with this boundary layer, the separation bubble will extend with increasing applied pressure gradient to ensure that Cp=0.014 at the point of separation. The momentum loss resulting from this adverse pressure gradient produces a separated region with a dividing streamline deflecting the flow through 11°. This flow deflection produces a separation shock inclined at 20° to the cylinder, which in turn produces a rise in Cp of ≈0.1 over the cylinder downstream of separation.

2.3 Axisymmetric Turbulent Unsteady Computations

Due to the quantity of computational data required to log all of the flowfield fluctuations for several cycles of an unsteady motion, preliminary computations were performed whereby 'computational pressure tappings' were selected and the pressure fluctuations at these were recorded. Since the separated region is believed to be integral to the dynamical system, and that the separated region (if present) must span the cylinder-flare junction, this location is an obvious choice for a computational pressure tapping.

Regular, self-sustained oscillations in wall pressure were seen to occur for the flow over both the 20° and 30° flares [58]. Typical pressure histories recorded at the cylinder flare junction is presented in Figures 2.33 and 2.34 and their Fourier spectra in Figures 2.35 and 2.36. The fundamental frequencies obtained by Fourier analysis were 3164Hz ($\bar{f} = 3.8\times10^{-2}$) for the 20° flare (consistent with ramp flow deflections of 20° [85] $\bar{f} = 1.2\times10^{-2} - 4.1\times10^{-2}$)and 2046.1Hz ($\bar{f} = 2.5\times10^{-2}$) for the 30° flare (consistent with ramp flow deflections of 28° [17] $\bar{f} = 2.3\times10^{-2}$). A decrease in frequency of oscillations with an increase in magnitude of separated region (as seen by Dolling et al [15]) can be explained on the basis of acoustic propagation.

Computations were repeated with the value of CFL halved, which, with the global time stepping, halves the timestep throughout the domain, and identical results produced, thus demonstrating temporal convergence.

It was observed [58] that below a certain flare angle (≈20°) a separated region is present, but oscillations are not produced, as reported experimentally by Kuehn [6][7].

Babinsky [2] measured surface pressure fluctuations for a 20° flare using identical conditions with a 200kHz-bandwidth data-logger. Fourier spectra

highlighted a distinct peak at around 25kHz ($\bar{f} = 0.3$), which unfortunately transpired to be caused by mounting vibration of the transducers. Filtering failed to reveal any significant periodic flowfield unsteadiness. It was suggested that this flowfield was unsteady, however no conclusive evidence was produced. It has been seen that for compression ramp flows, broadband amplification of disturbances occurs for $\bar{f} < 0.2$ [22][97] and hence the peak at $\bar{f} = 0.3$ was not considered likely to be produced by this form of flowfield unsteadiness.

Experiments performed by Erengil and Dolling [14] under similar conditions to those of Babinsky [2], albeit for a two-dimensional flow, produced oscillations of similar frequency to those observed computationally ($\bar{f} = 2.4 \times 10^{-2}$ vs $\bar{f} = 2.2 \times 10^{-2}$)

For relatively low Mach numbers and high Reynolds numbers, the pressure rise necessary to induce separation for two-dimensional and three-dimensional flows are similar [7][6] and hence their associated steady characteristics are likewise [148][144][145][146][149]It is not clear as to whether or not this will apply to unsteady flows nor as to whether Mach number or Reynolds number effects are predominant. I.e. whilst the frequencies of oscillations for the CFD simulation of Babinsky's configurations [2] is of the same order as Erengil and Dollings' data [14] it is uncertain as to the validity of such a comparison.

Normalising surface pressure coefficient and skin friction coefficient distributions with respect to time averaged distributions allows identification of the locations of peak amplitude fluctuations (Figures 2.37 and 2.38). These figures were produced by time averaging all of the distributions to generate a time averaged distribution, and then plotting each distribution as a deviation from the average. It is seen that peak fluctuations occur at separation and reattachment, with further fluctuations continuing downstream of the interaction, in qualitative agreement with the experimental data of Kuehn [6][7] and Kistler [11].

Whilst the order of the frequency of the oscillations in pressure terms seems promising, the magnitude of the fluctuations are smaller than would have been expected. Motion of the separation and reattachment locations, as reported by Dolling et al was not apparent. It is known that the pressure rise across the stationary shocks seen here is larger than that across the moving shock waves seen experimentally [104]. This will result in the prediction of a larger separated region, and smaller wall pressure fluctuations – as seen here.

Plotkin [65], amongst others, suggested that the oscillations are caused by unsteadiness in the incoming boundary layer (hypothesis I). The computations undertaken here have no such freestream nor boundary layer unsteadiness. The unsteadiness in an incoming turbulent boundary layer, for this flow, has an approximate characteristic frequency given by:

$$f_{char} \approx \frac{u_\infty}{\delta} \approx \frac{815ms^{-1}}{9.8\times10^{-3}m} \approx 83kHz, \quad (\bar{f}_{char} = 1)$$

Presumably the lack of unsteadiness in the incoming computational boundary layer is responsible for the lack of spectral energy around this frequency.

The difference in the form of oscillations for the 20° and 30° flares suggests different structures or mechanisms between the two cases. This may, in part, be due to the formation of a secondary separation bubble with the 30° flow deflection.

Due to the lack of experimental unsteady turbulent axisymmetric cylinder-flare flow data, the following section continues the investigation of unsteady flows using two-dimensional flat-plate ramp flows.

Flare Angle (α)	$x_{separate}$ (m)	$x_{reattach}$ (m)	Separated Length (mm)
0.0°	N/A - Flow is attached		
5.0°			
7.5°	-0.00015	+0.0001	0.25
10.0°	-0.0013	+0.0008	2.1
15.0°	-0.0033	+0.0025	5.8
20.0°	-0.0071	+0.0125	19.6
22.5°	-0.0112	+0.0158	27.0
25.0°	-0.0188	+0.0196	38.4
27.5°	-0.0288	+0.0242	52.9
30.0°	-0.0454	+0.0292	74.6

Table 2.1. Separation and Reattached Location Variation With Flare Angle

Flare Angle (α)	Separation height (mm)	Separation height (%δ)
0°	0.000	0.0
5.0°	0.000	0.0
7.5°	0.054	0.55
10°	0.176	1.80
15°	0.550	5.61
20°	0.877	8.95
22.5°	1.575	16.07
25°	3.305	33.72
27.5°	5.187	52.92
30°	7.300	74.49

Table 2.2. Variation in Height of the Separated Region with Flare Angle

x(m)	θ (mm)	Re_θ
-0.050	0.436	5146.63
-0.025	0.447	5272.07
0.0	0.462	5441.68
0.025	0.475	5604.41
0.050	0.487	5741.33

Table 2.3. Momentum Thickness Distribution along the Centrebody.

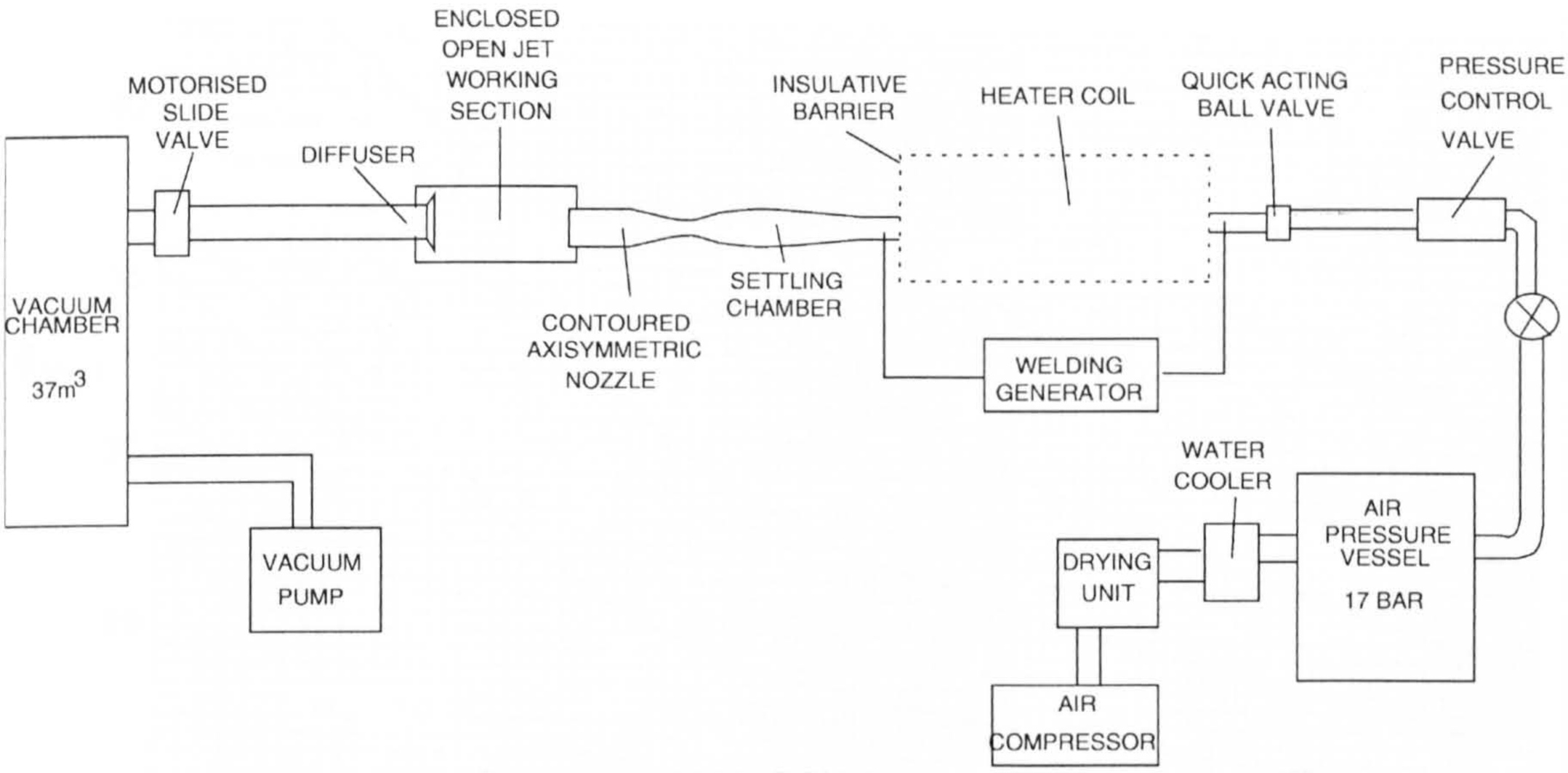

Figure 2.1. Schematic of HSST (reconstruted from [53]).

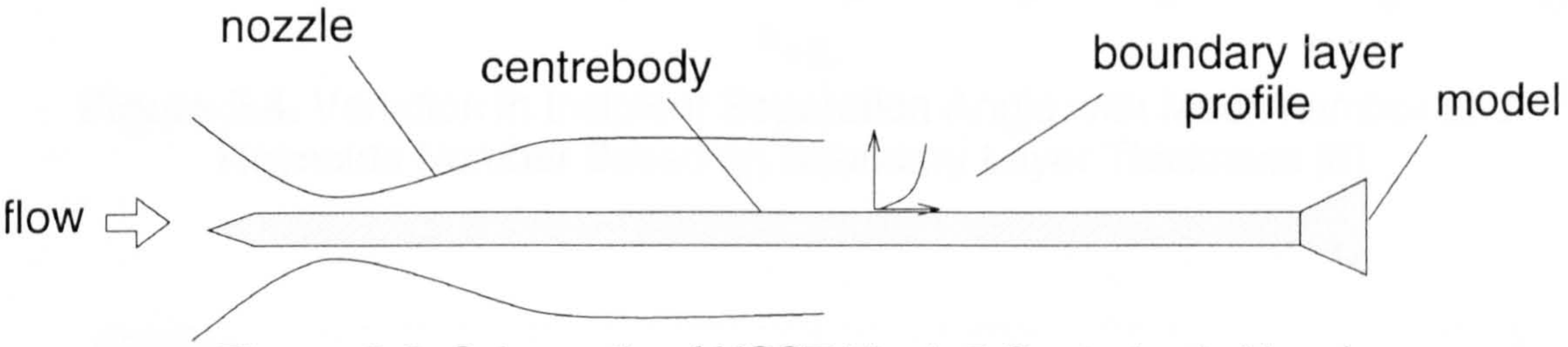

Figure 2.2. Schematic of HSST Mach 5 Centrebody Nozzle

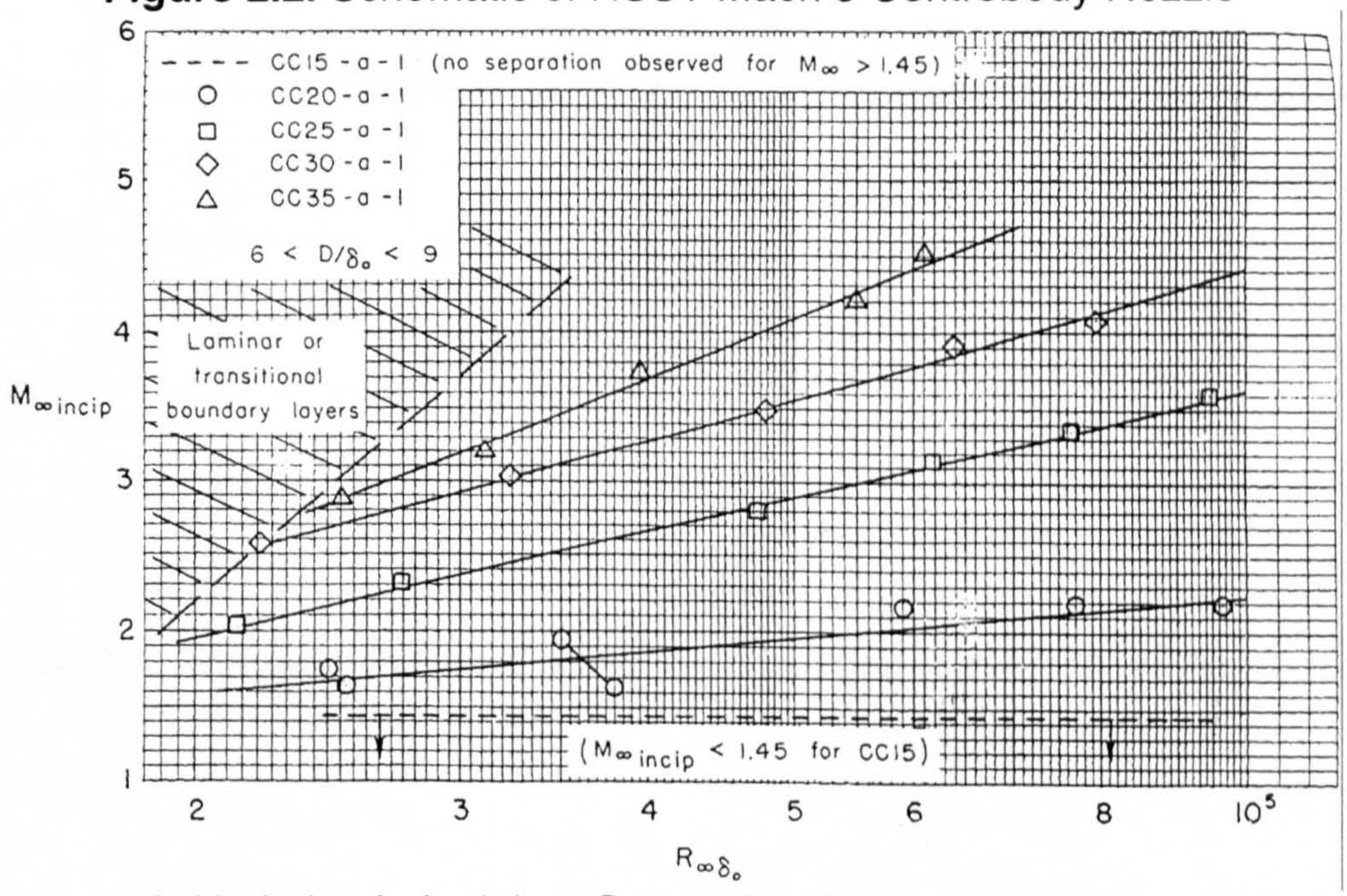

Figure 2.3. Variation in Incipient Separation Angle with Mach number and Reynolds Number Based on Boundary Layer Thickness [6].

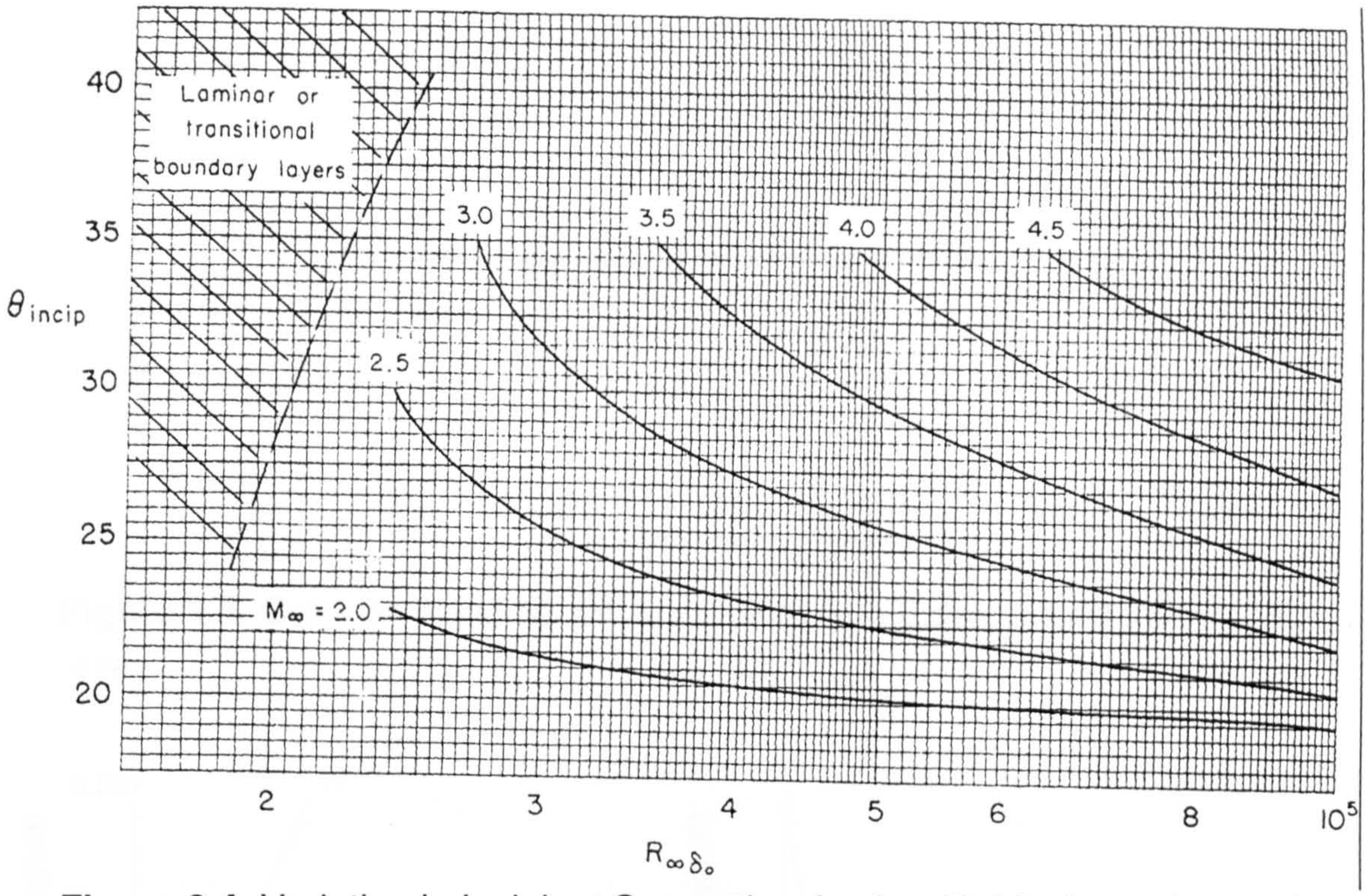

Figure 2.4. Variation in Incipient Separation Angle with Mach number and Reynolds Number Based on Boundary Layer Thickness [6].

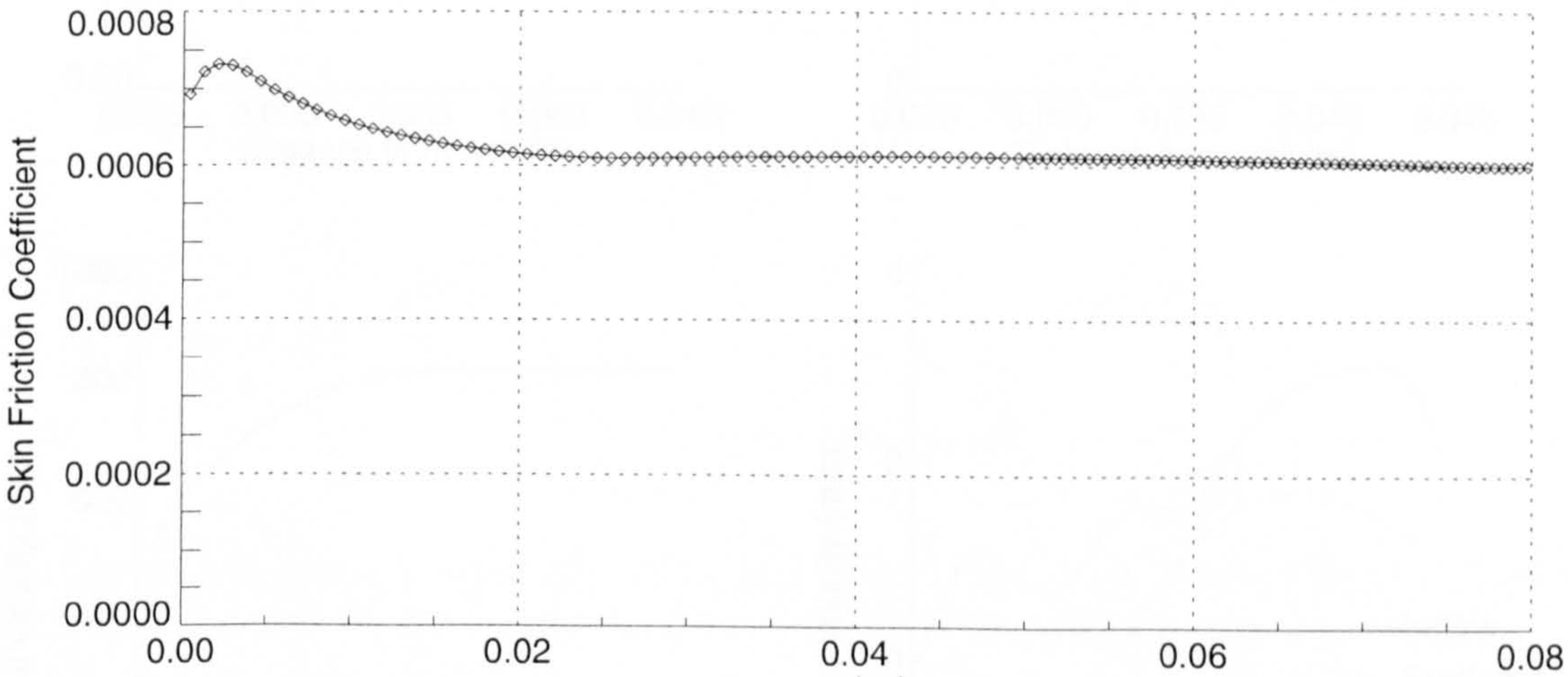

Figure 2.5. Transient in Skin Friction Using Experimental Inflow Profile [58].

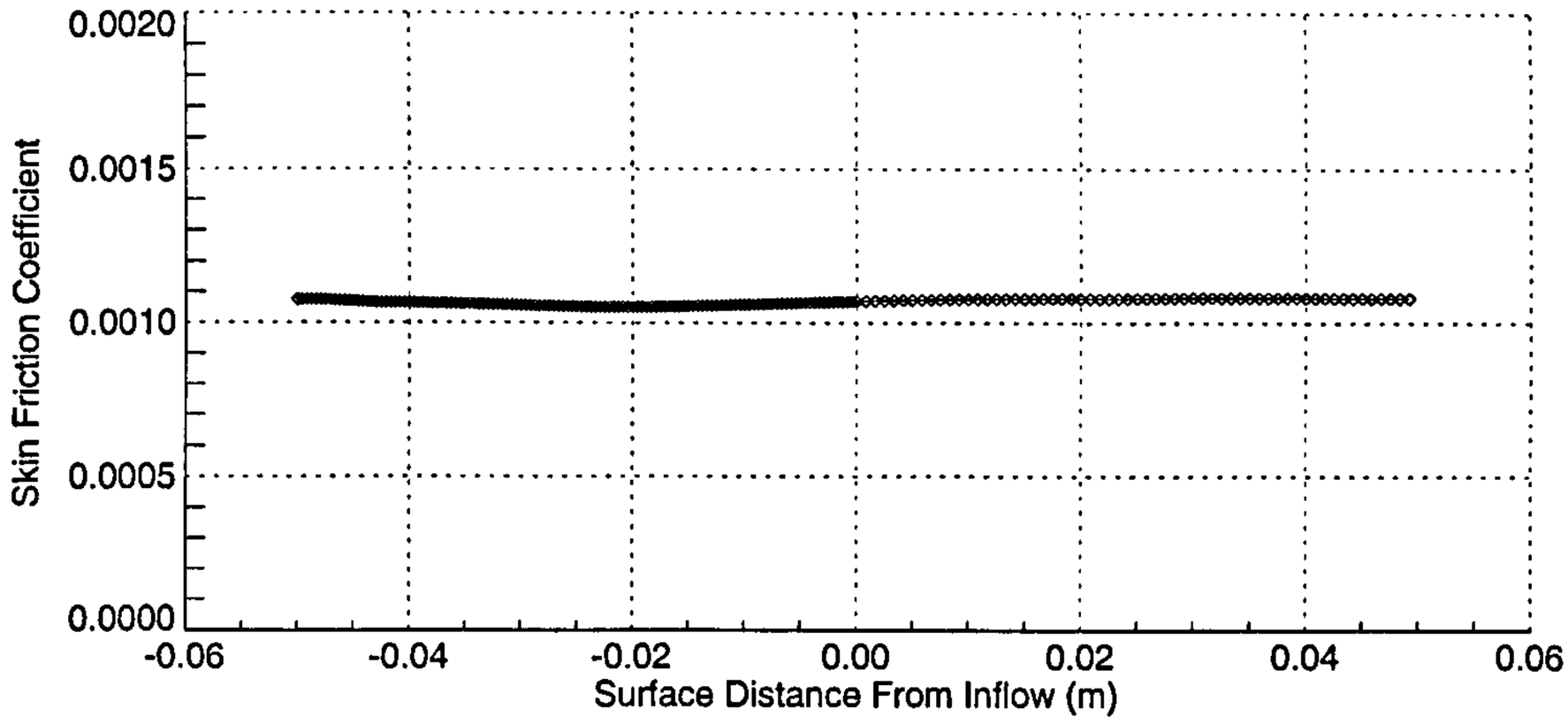

Figure 2.6. Cylinder Skin Friction Coefficient with Extrapolated Inflow [58].

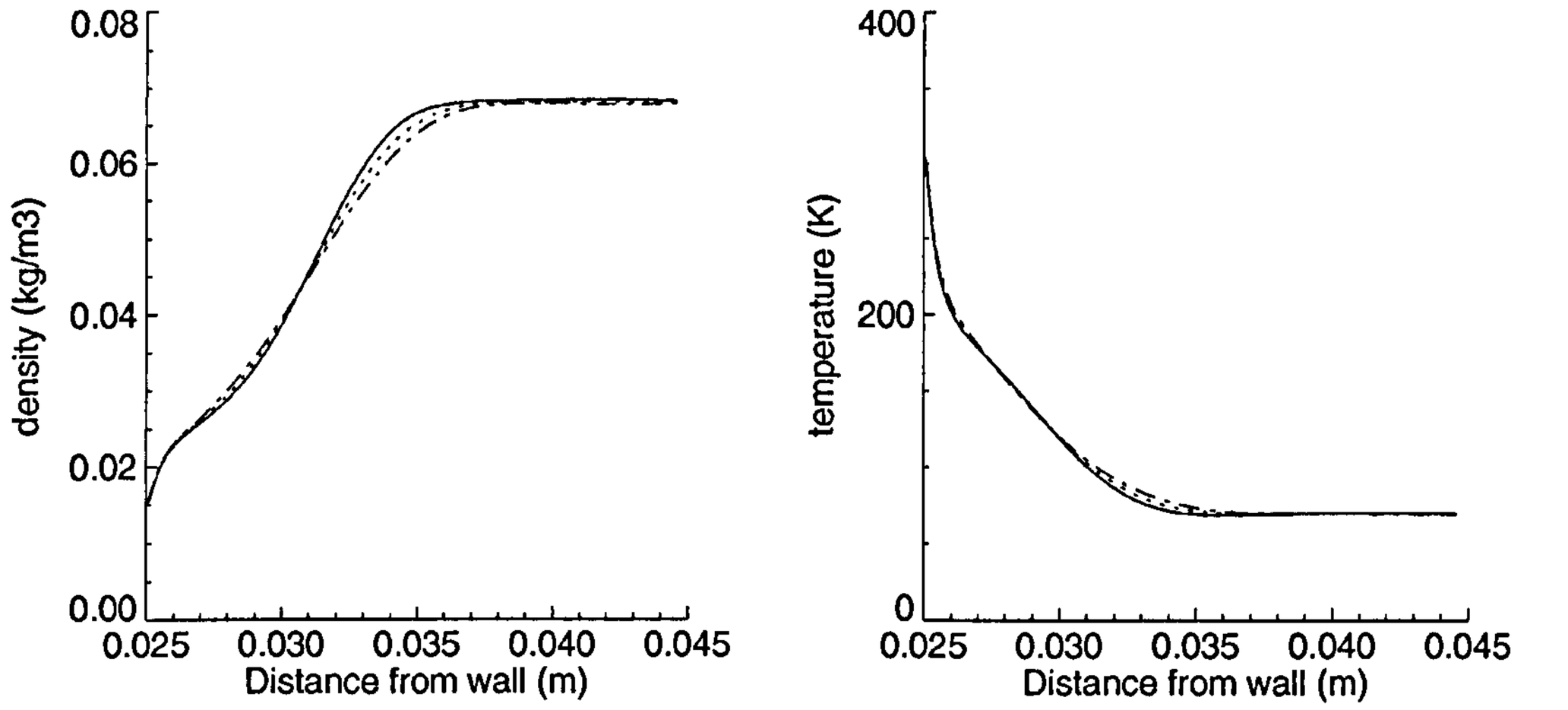

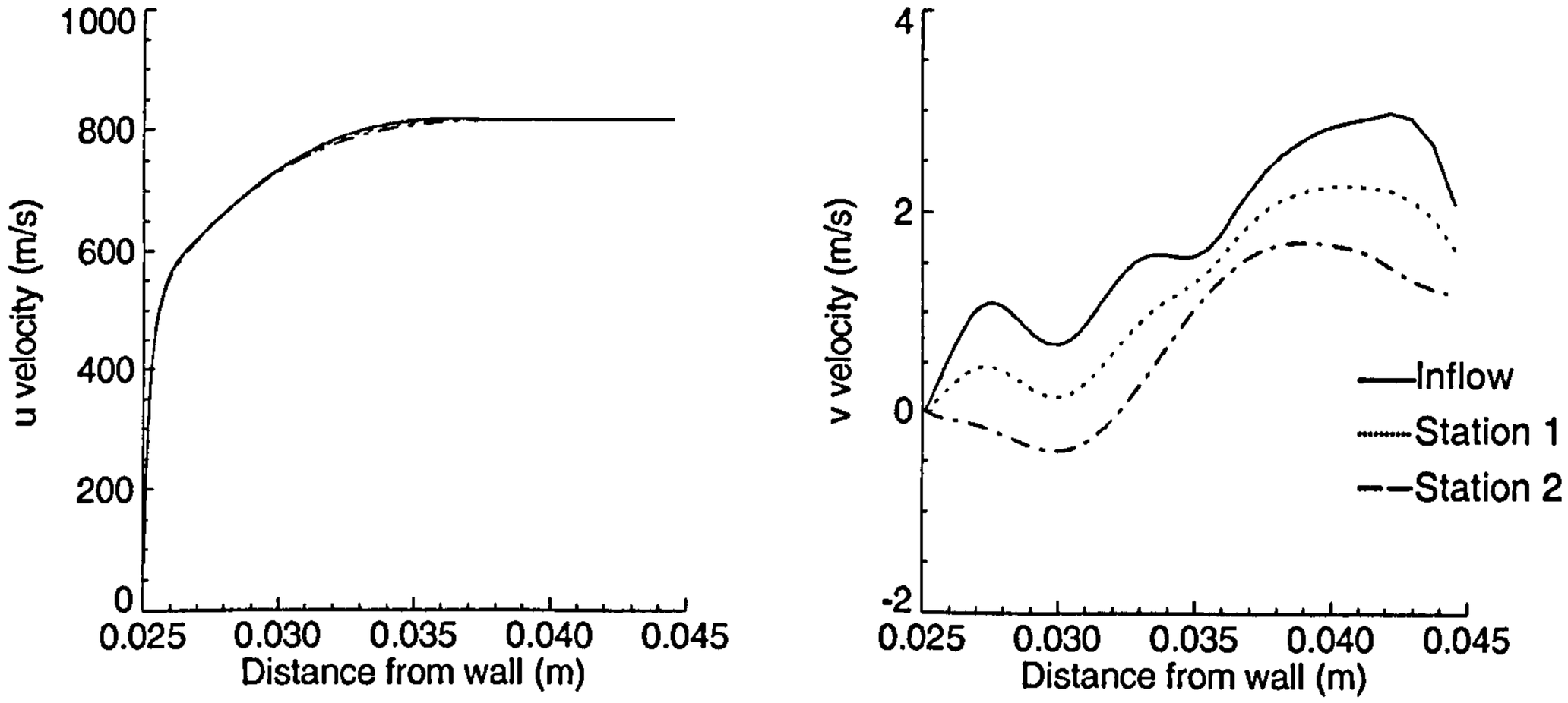

Figure 2.7. Inflow Boundary Layer Profile Extrapolation

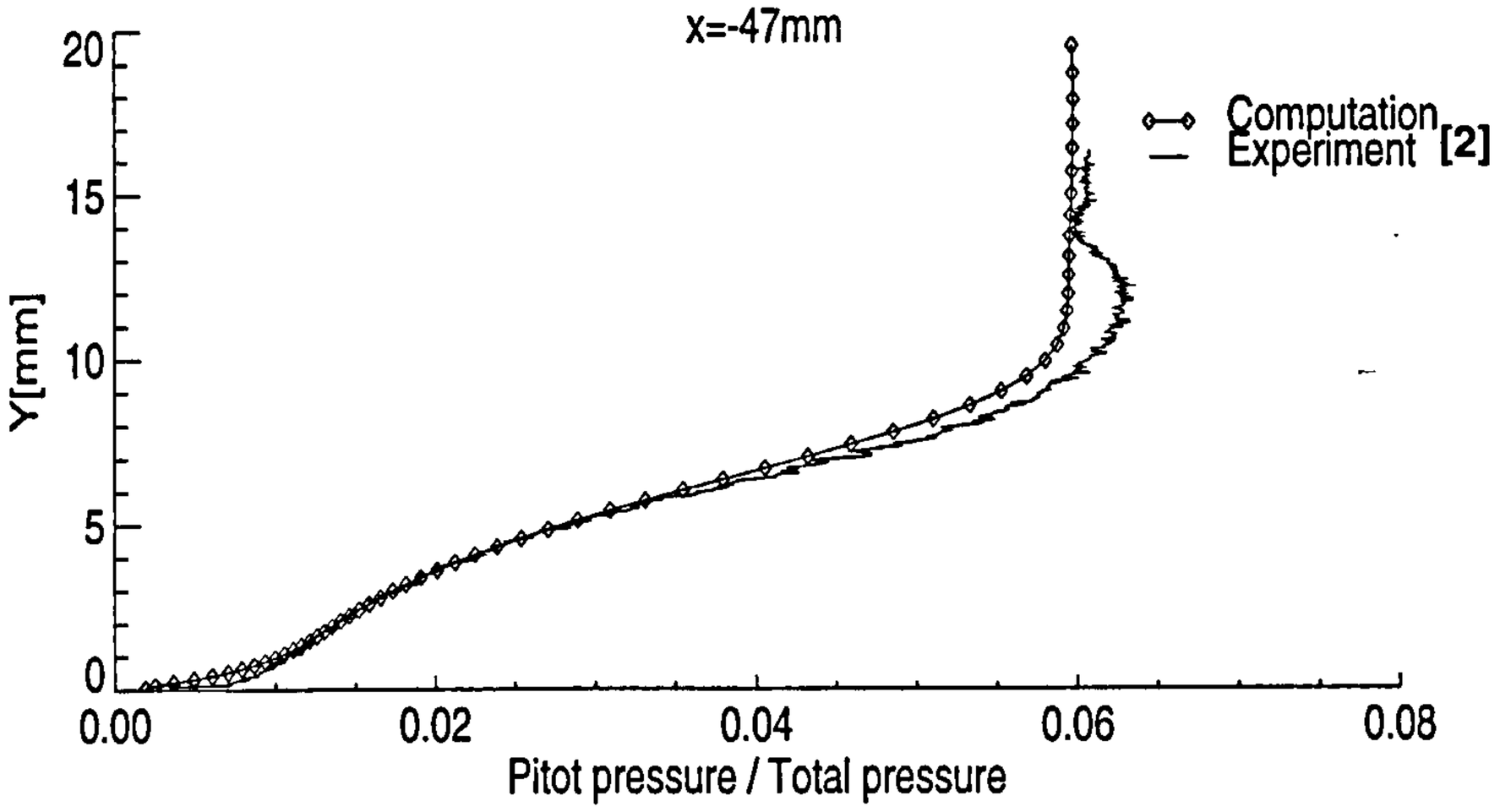

Figure 2.8. Computational and Experimental Boundary Layer Pitot Profiles 47mm Upstream on Cylinder-Flare Junction

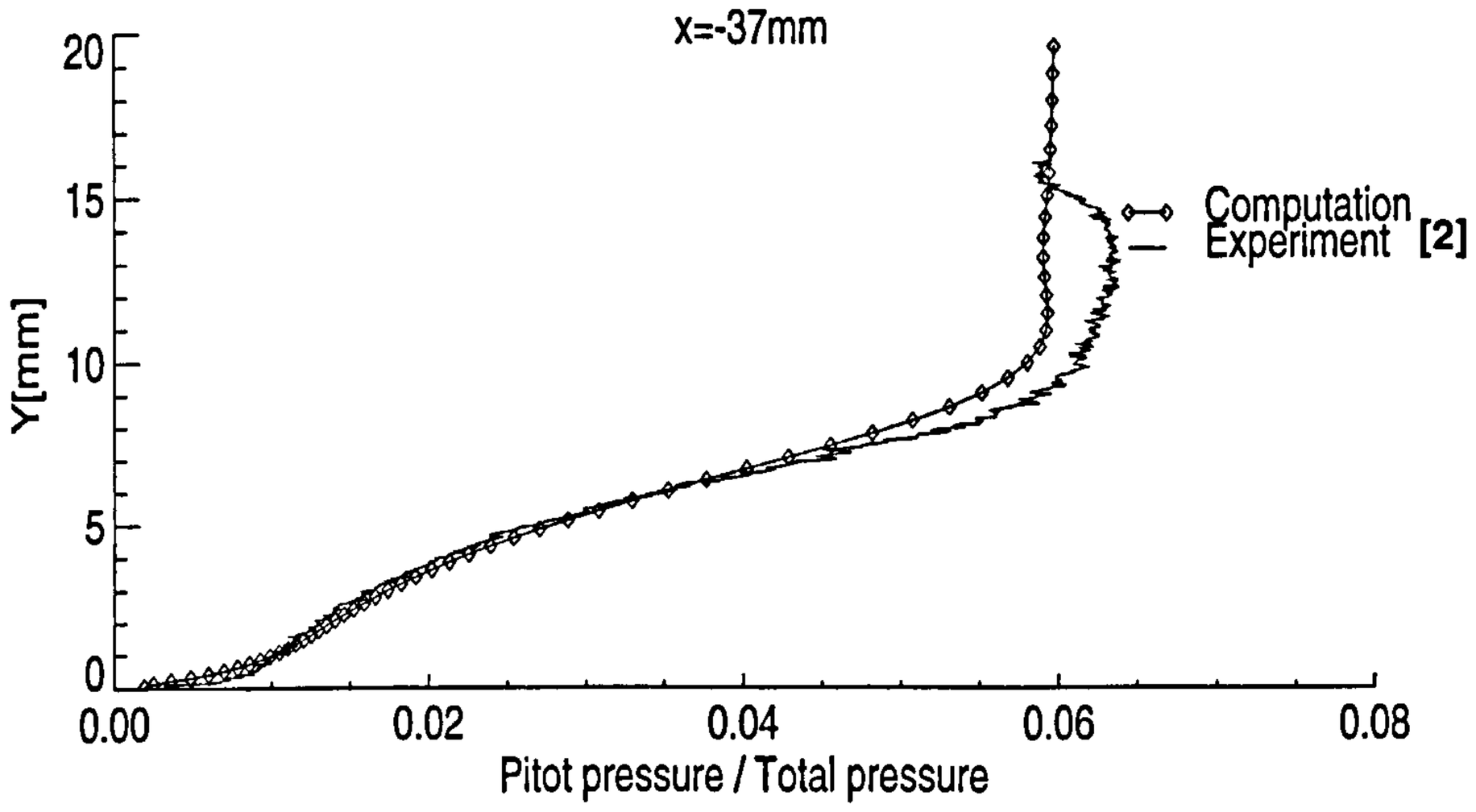

Figure 2.9. Computational and Experimental Boundary Layer Pitot Profiles 37mm Upstream on Cylinder-Flare Junction

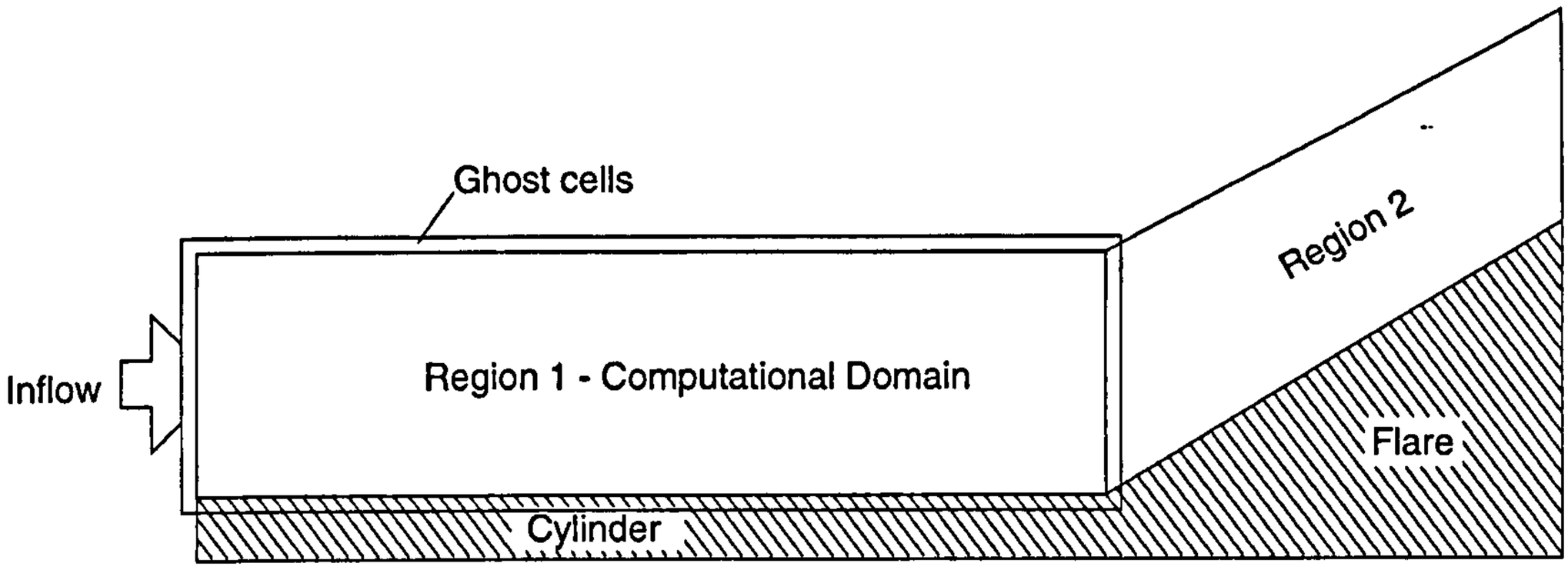

Figure 2.10. Schematic Showing Computational Configuration

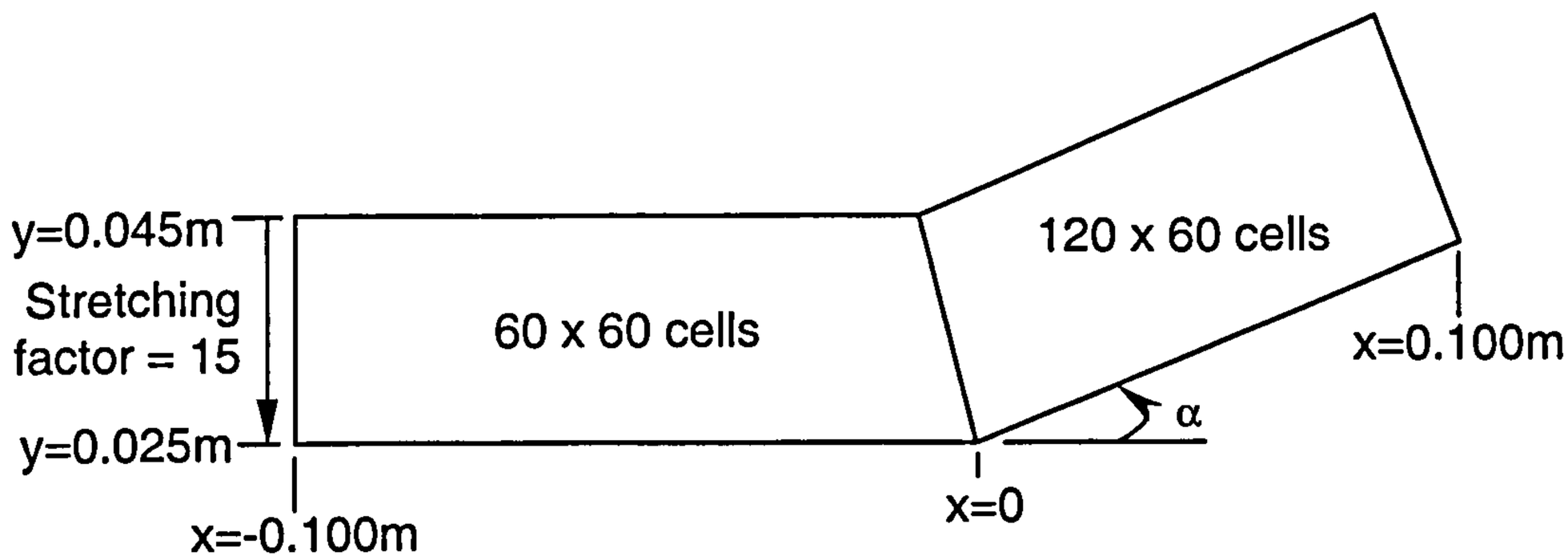

Figure 2.11. Schematic of a Typical Computational Mesh

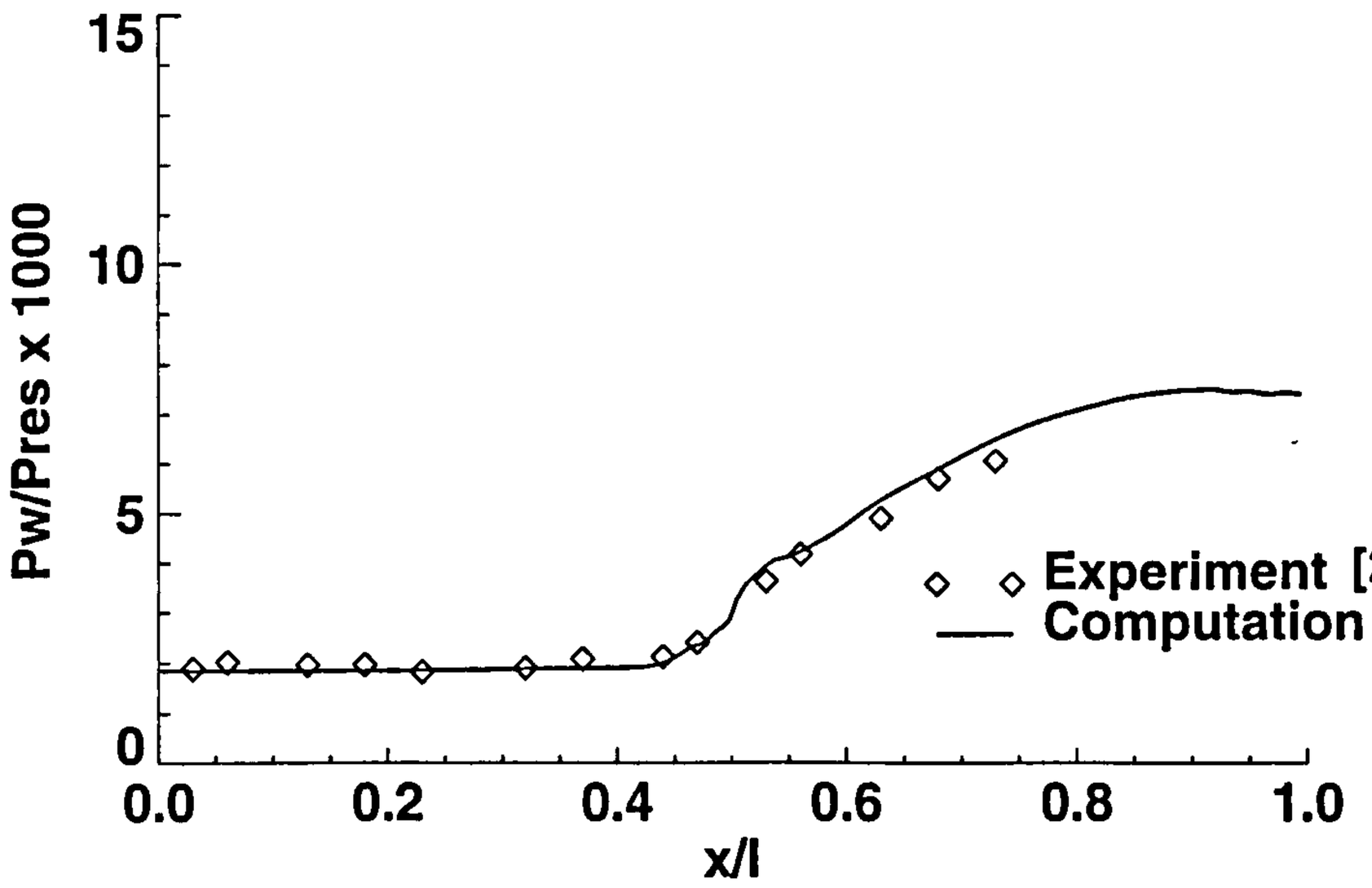

Figure 2.12. Experimental and Computational Surface Pressure Distributions (15° Flare)

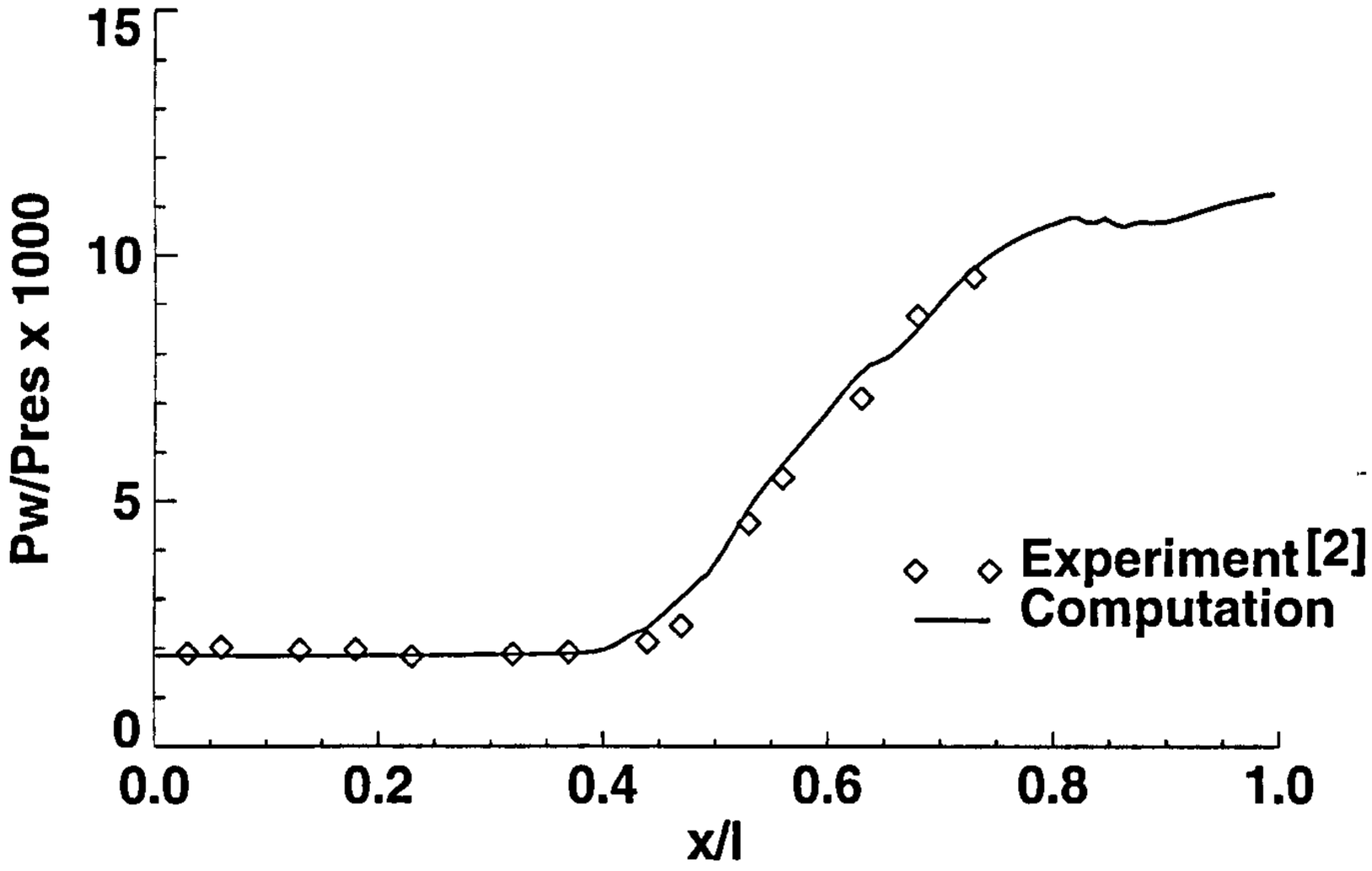

Figure 2.13. Experimental and Computational Surface Pressure Distributions (20° Flare)

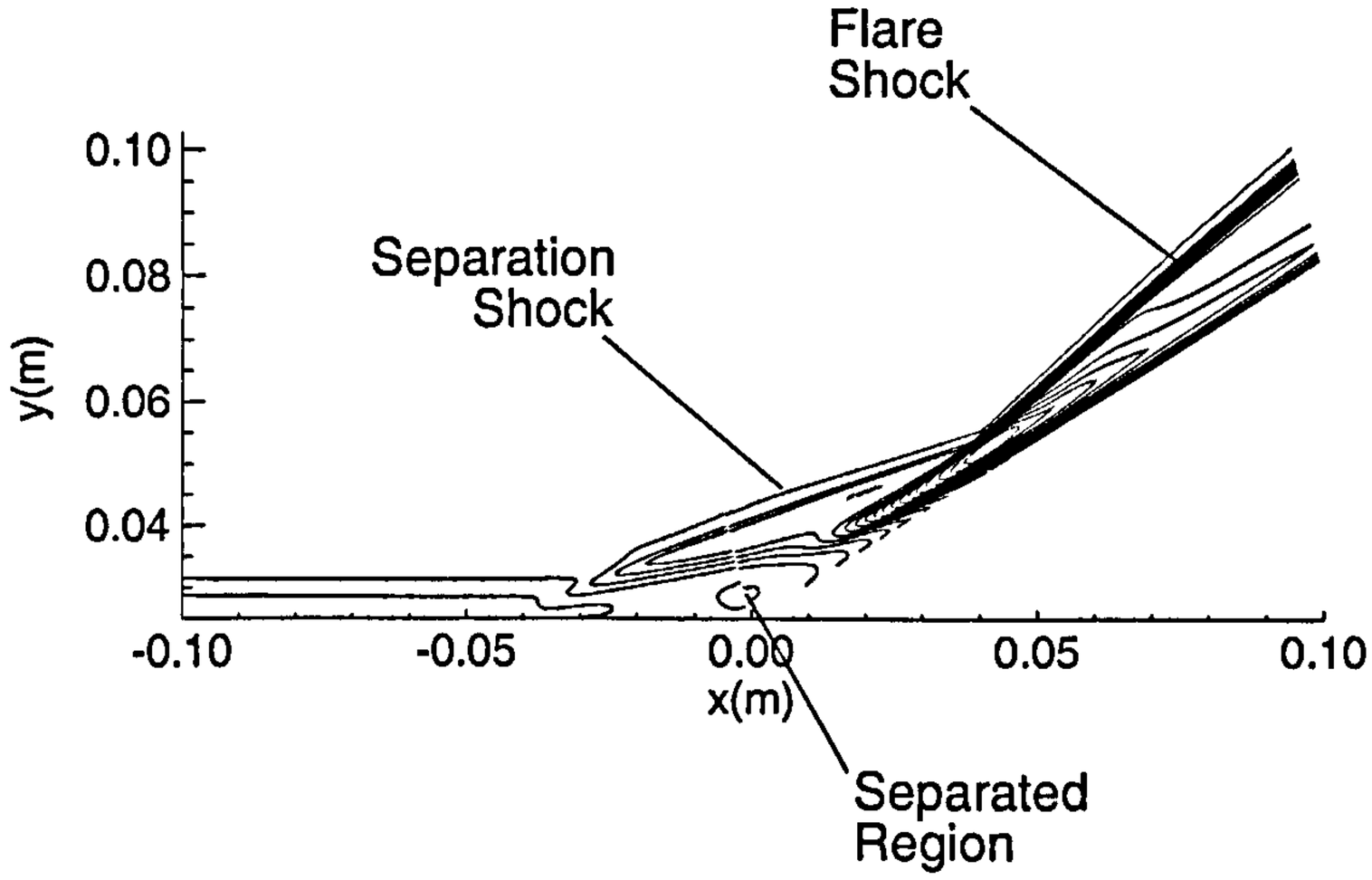

Figure 2.14. Schematic of Shock Separated Flow (30° Flare)

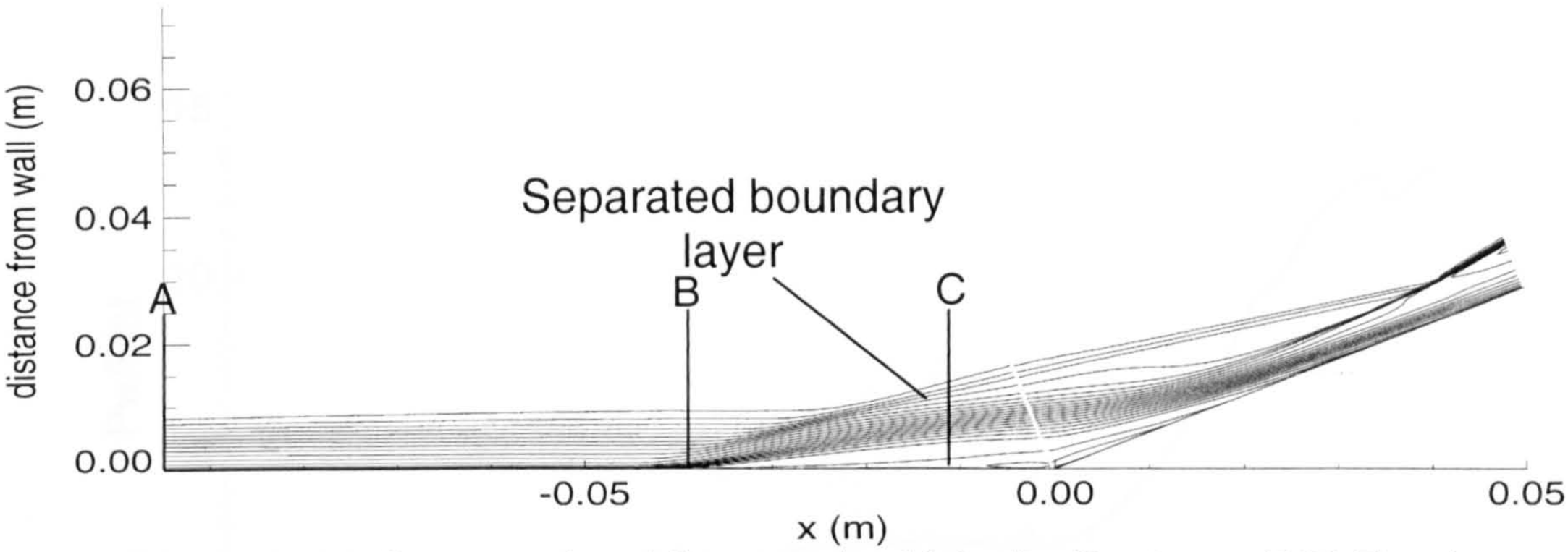

Figure 2.15. Computational Streamwise Velocity Contours (30° Flare)

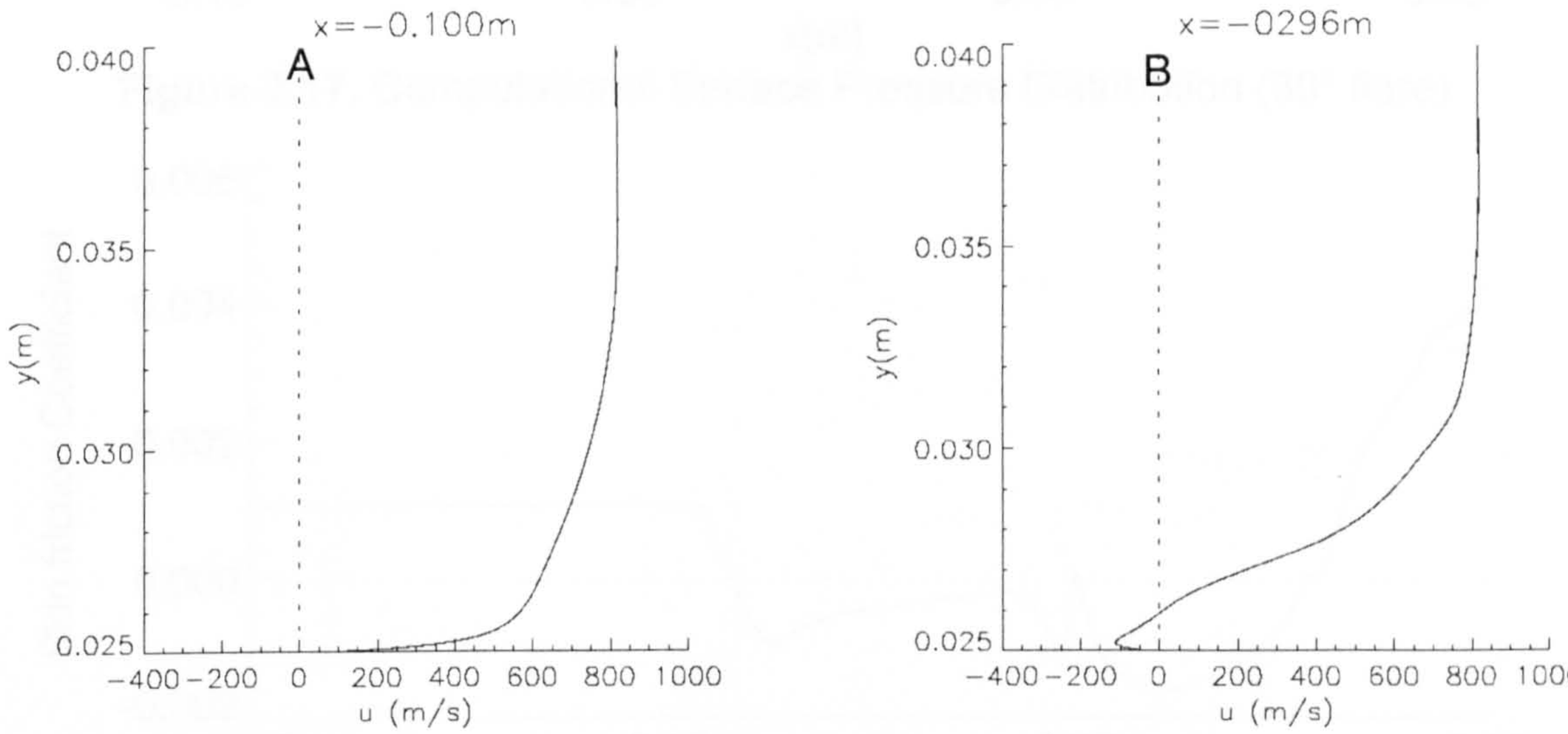

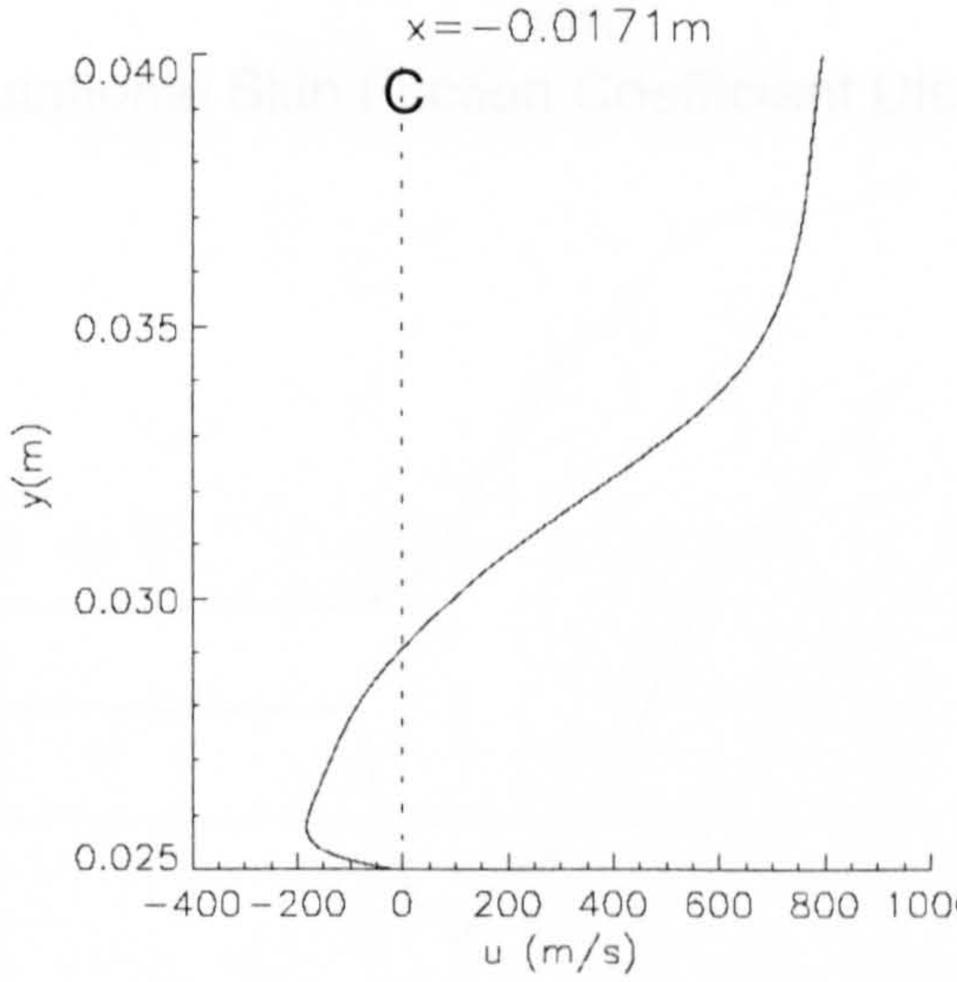

Figure 2.16. Computational Boundary Layer Profiles Showing Separation (30° Flare)

Figure 2.17. Computational Surface Pressure Distribution (30° flare)

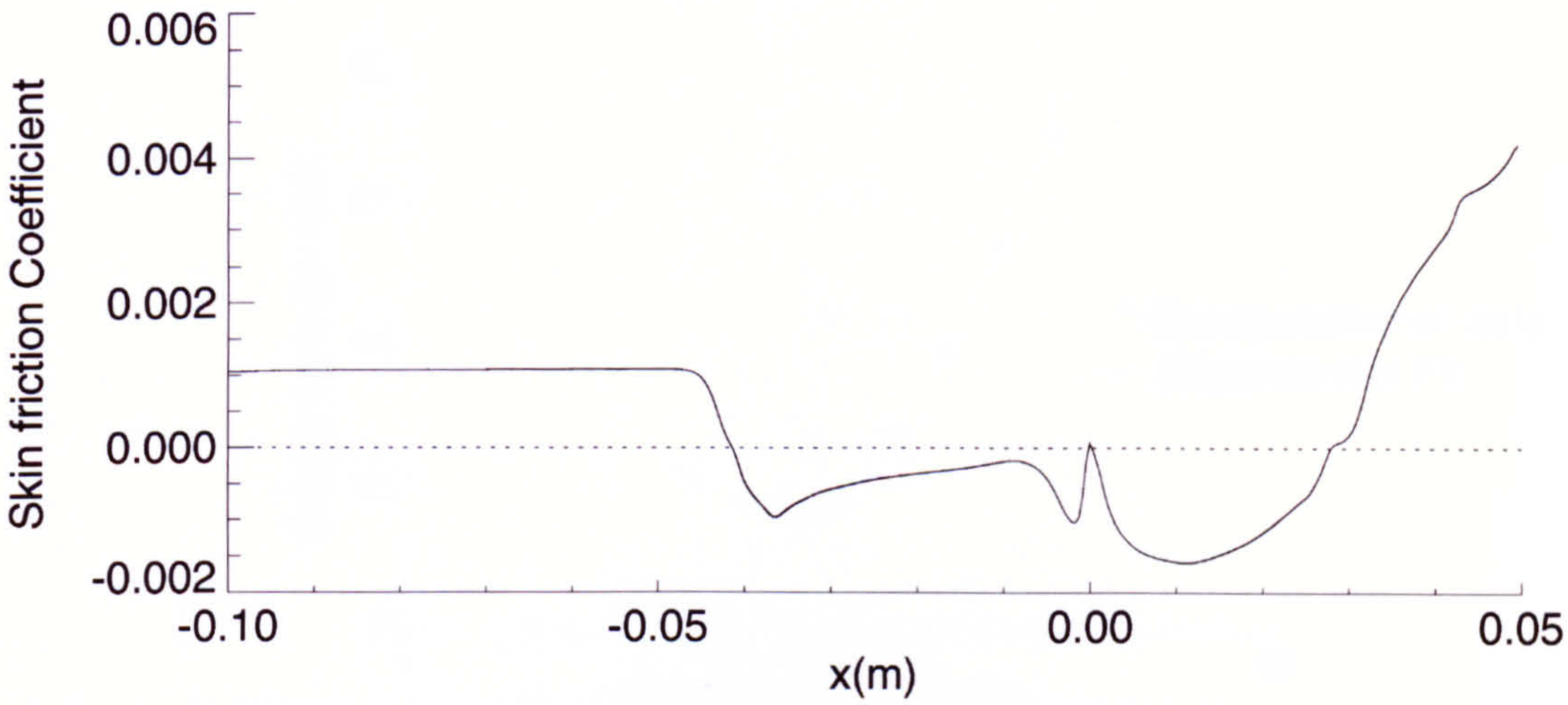

Figure 2.18. Computational Skin Friction Coefficient Distribution (30° flare)

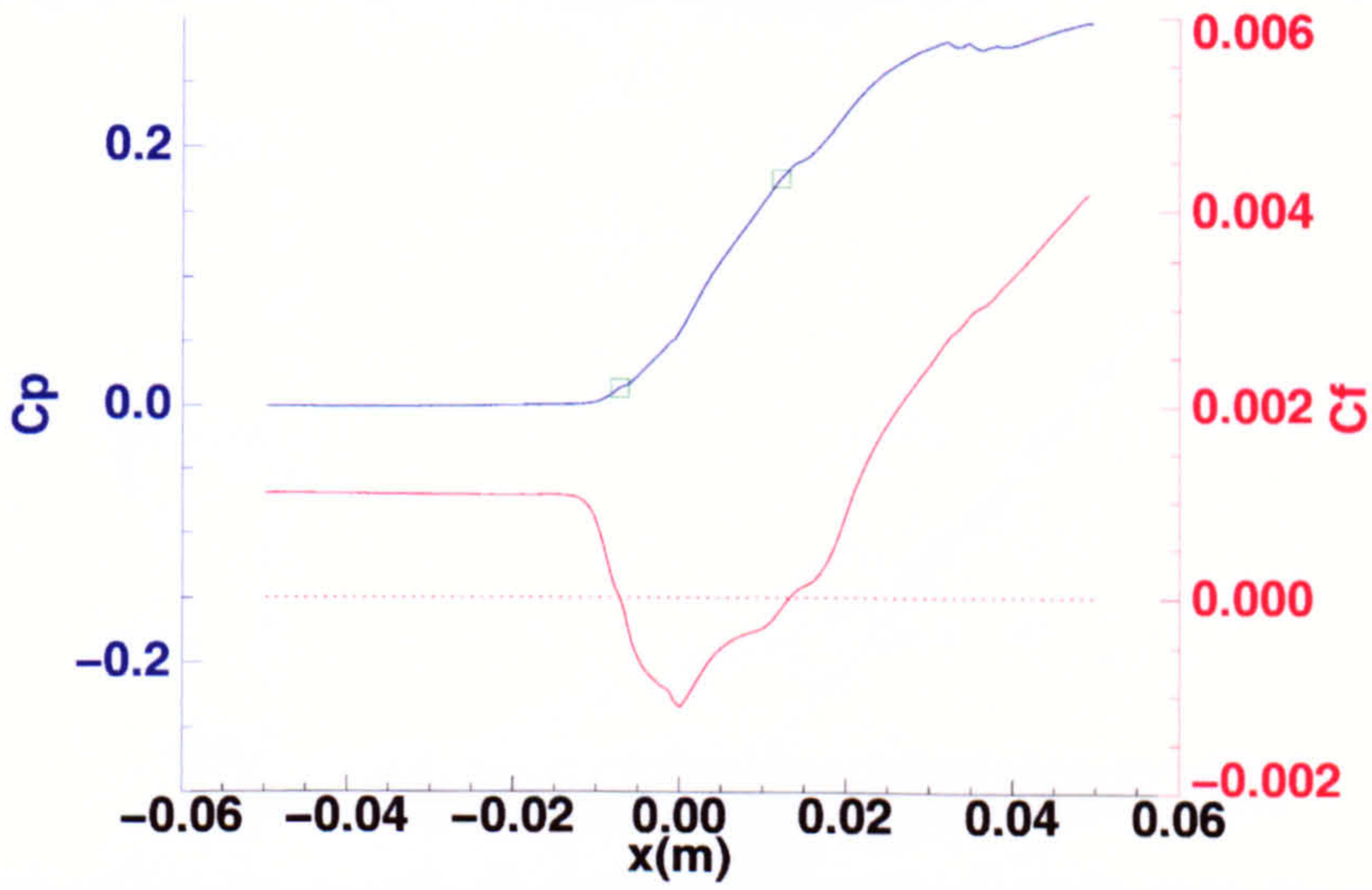

Figure 2.19. Computational Surface Pressure and Skin Friction Coefficients (20° Flare)

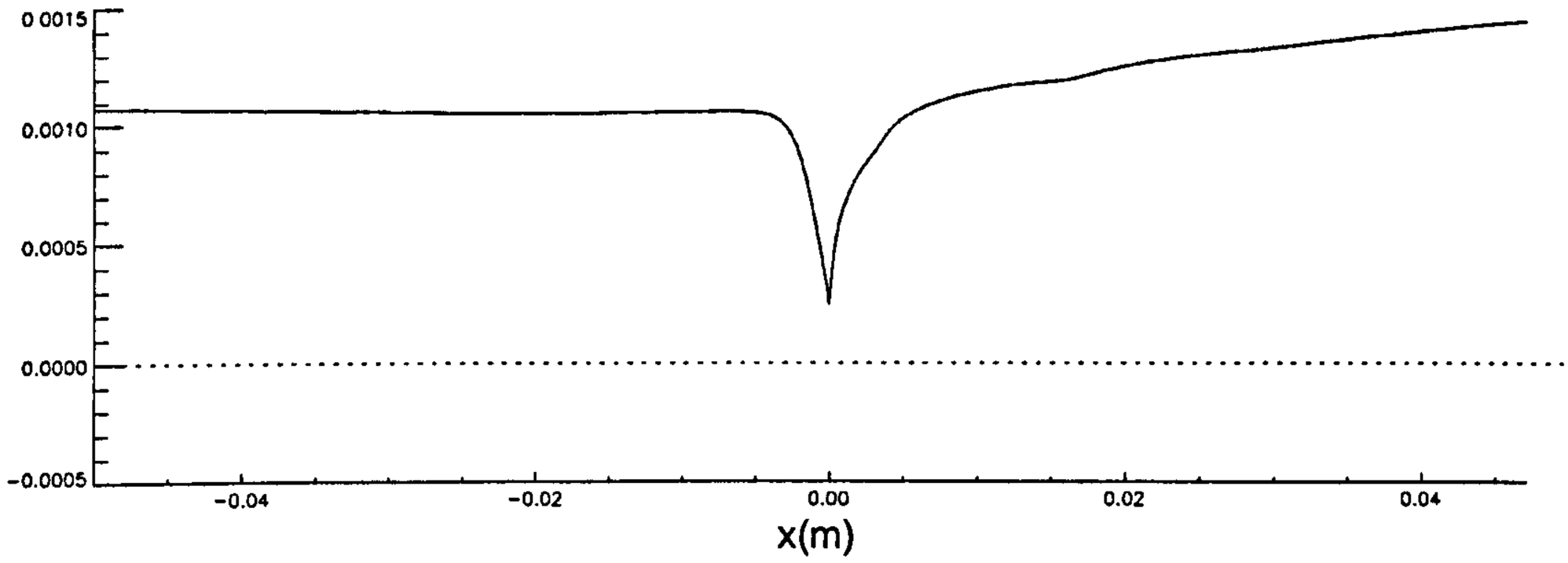

Figure 2.20. Computational Skin Friction Coefficient (5° flare)

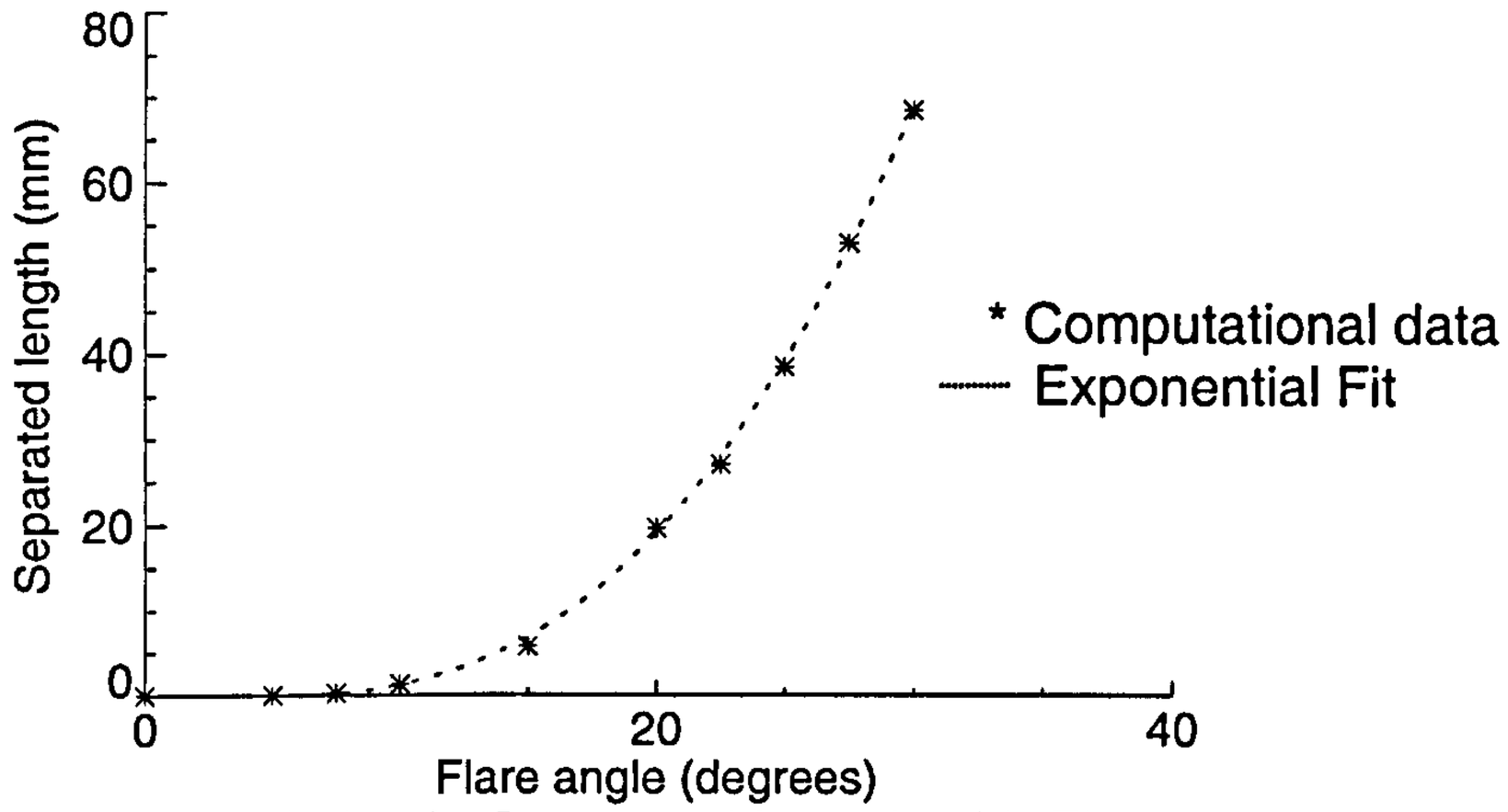

Figure 2.21. Variation in Separated Length with Flare Angle

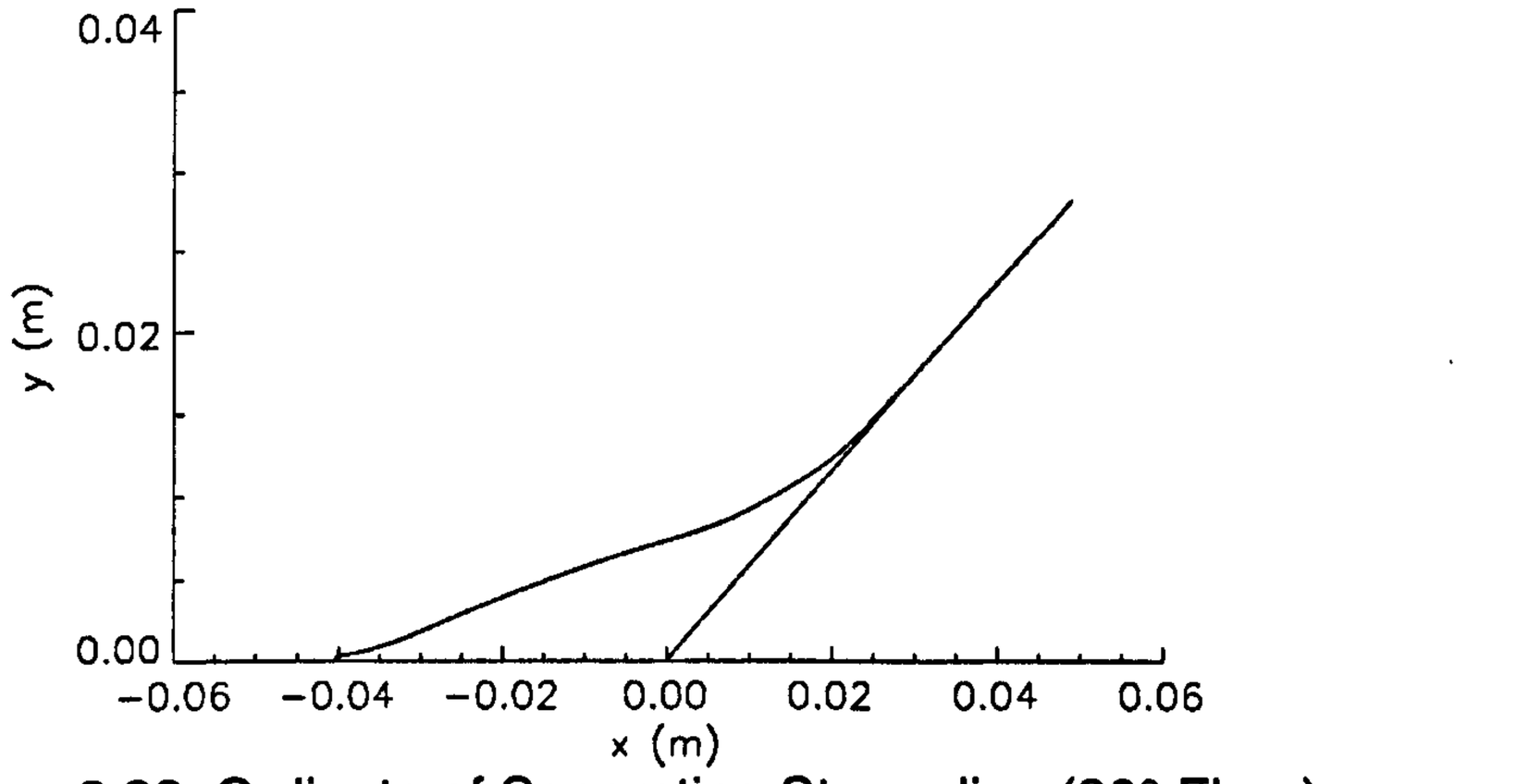

Figure 2.22. Ordinate of Separating Streamline (30° Flare)

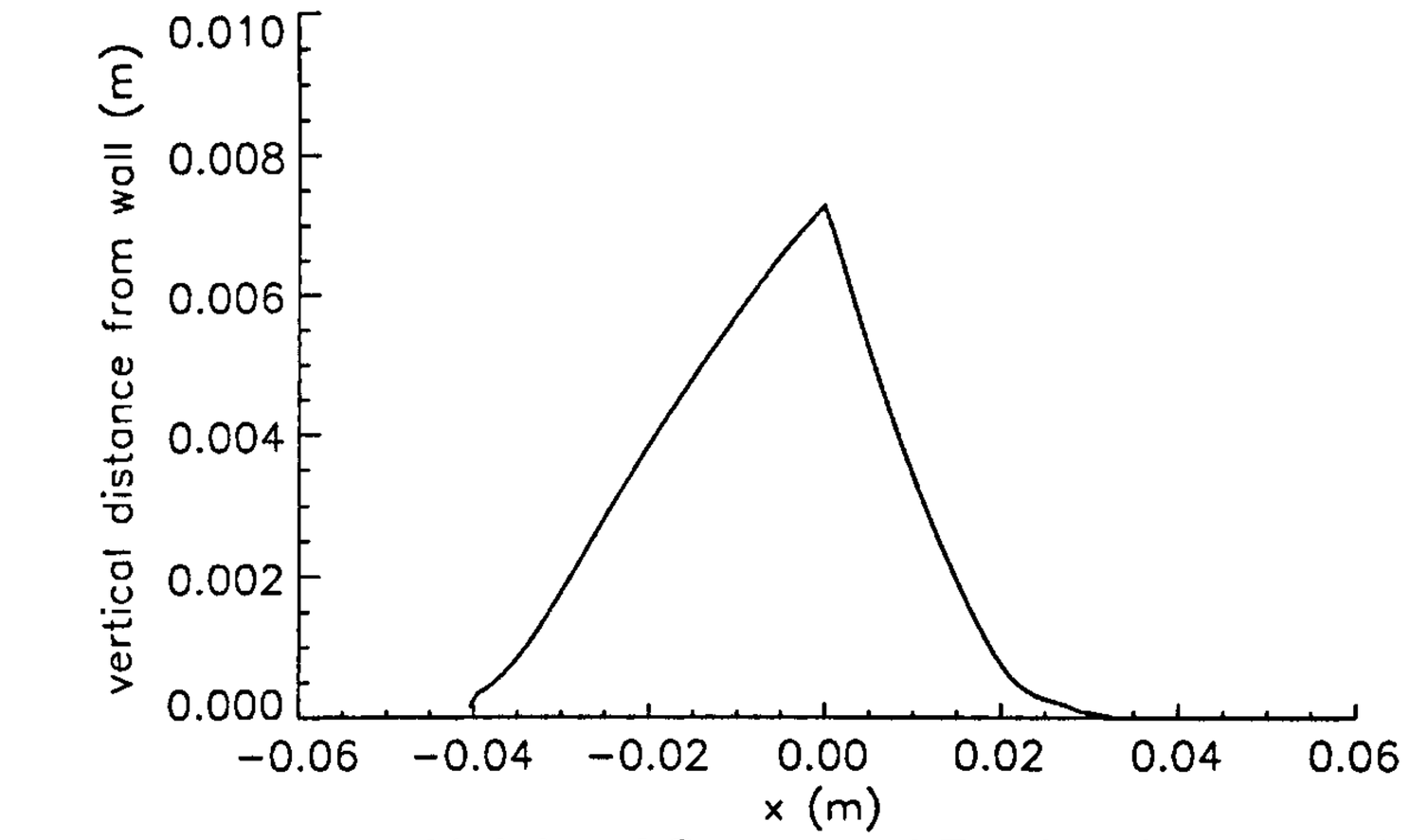

Figure 2.23. Height of Separated Region (30° Flare)

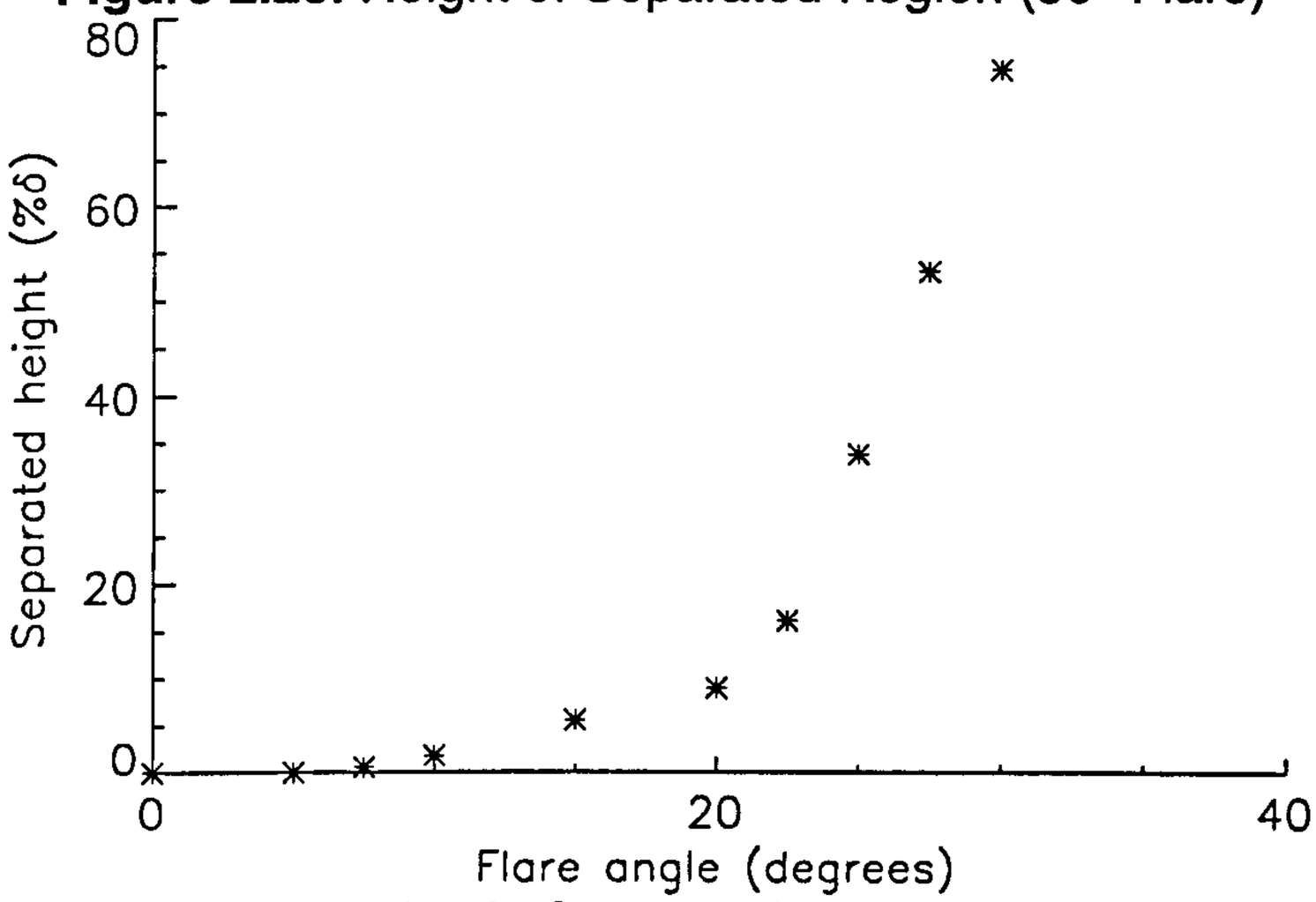

Figure 2.24 Variation in Separated Height with Flare Angle

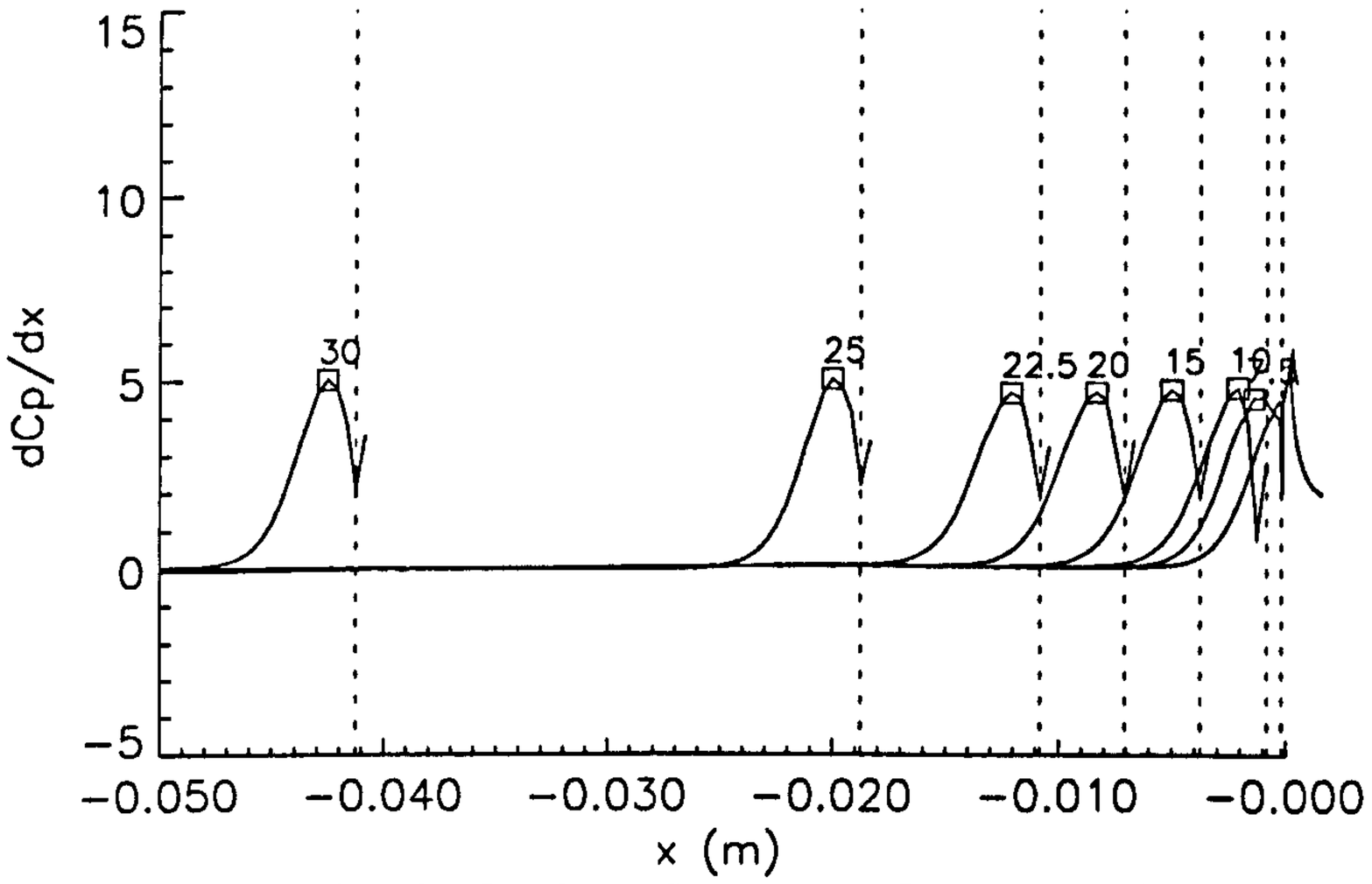

Figure 2.25. Variation in Surface Pressure Gradient with Flare Angle

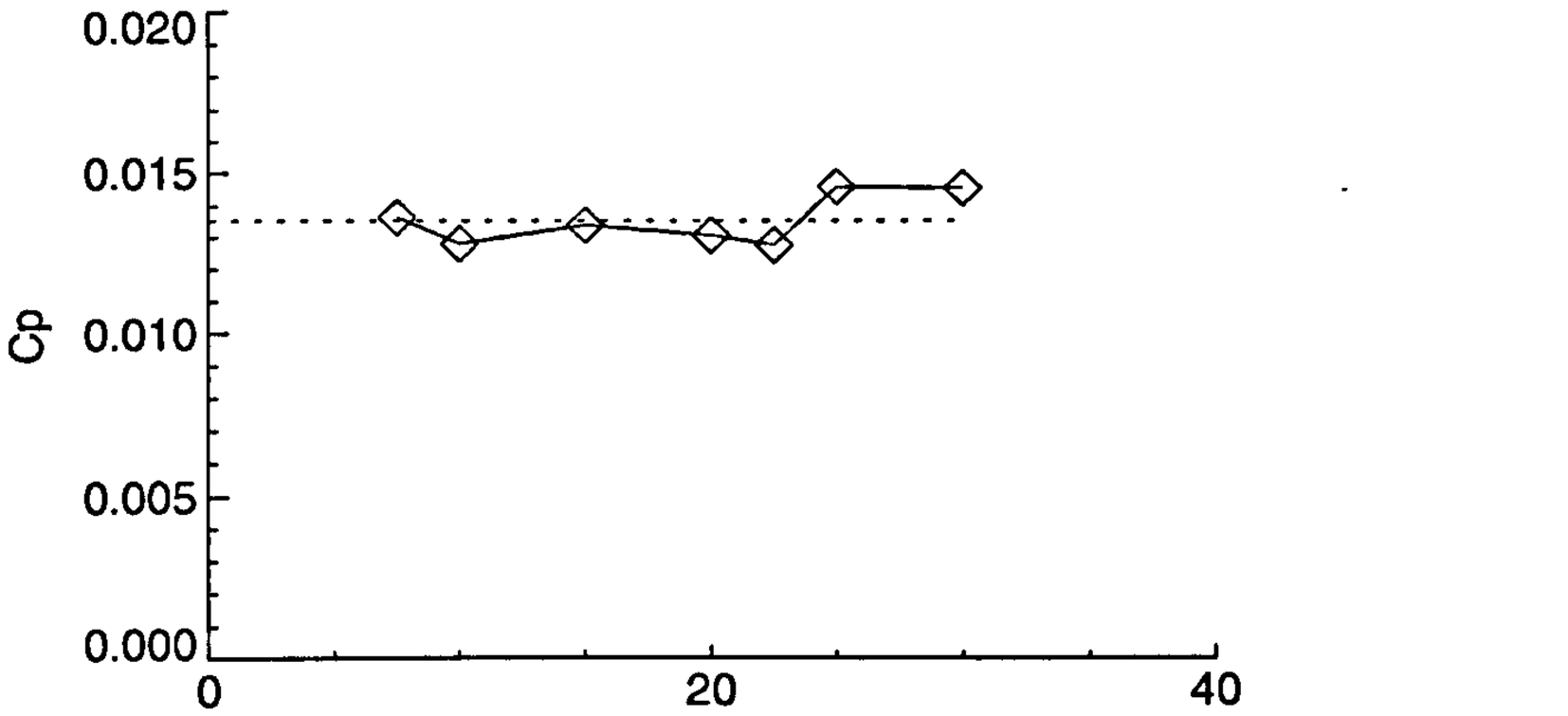

Figure 2.26. Variation in Surface Pressure Coefficient at Separation with Flare Angle

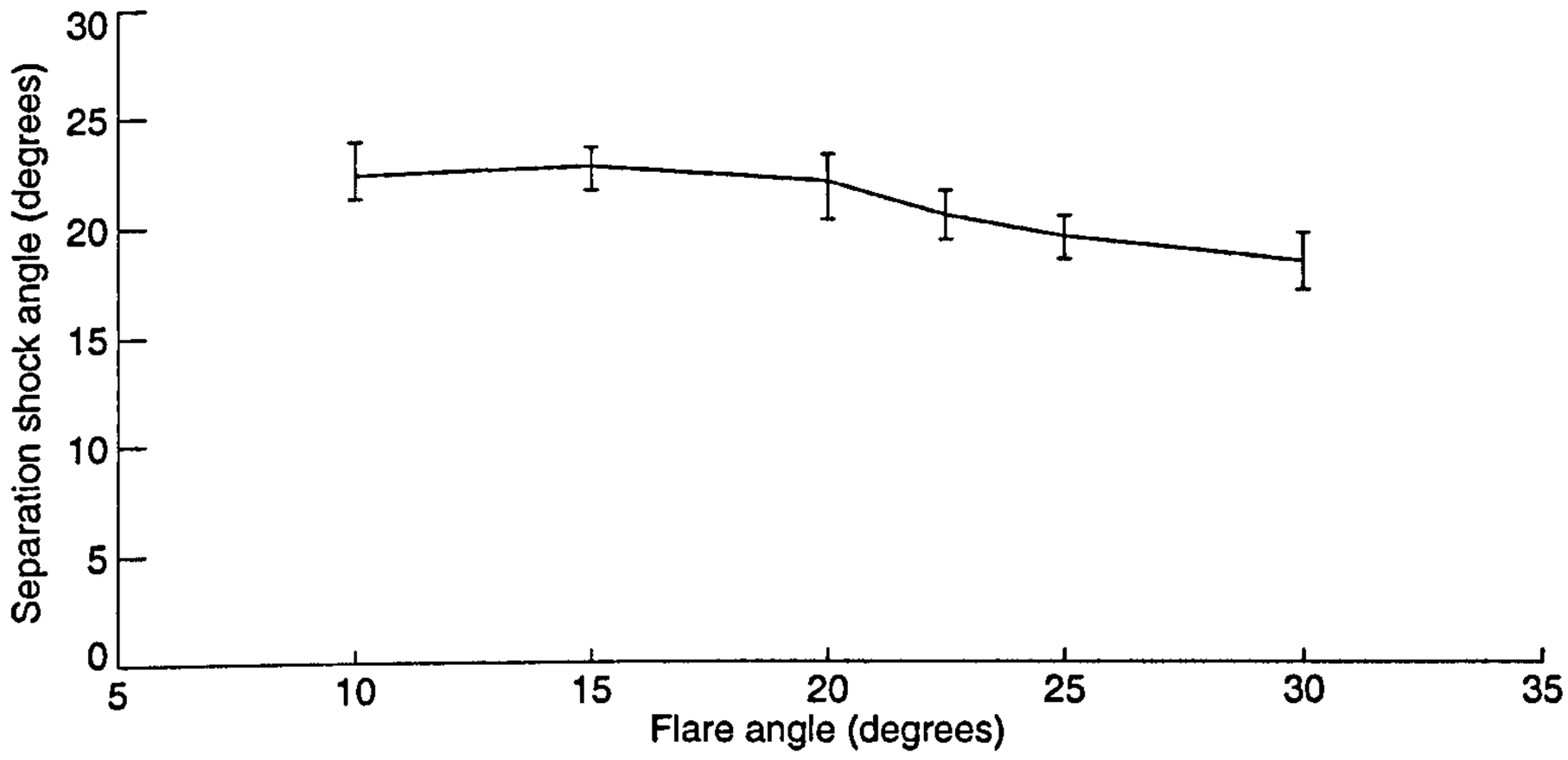

Figure 2.27. Variation in Separation Shock Angle with Flare Angle

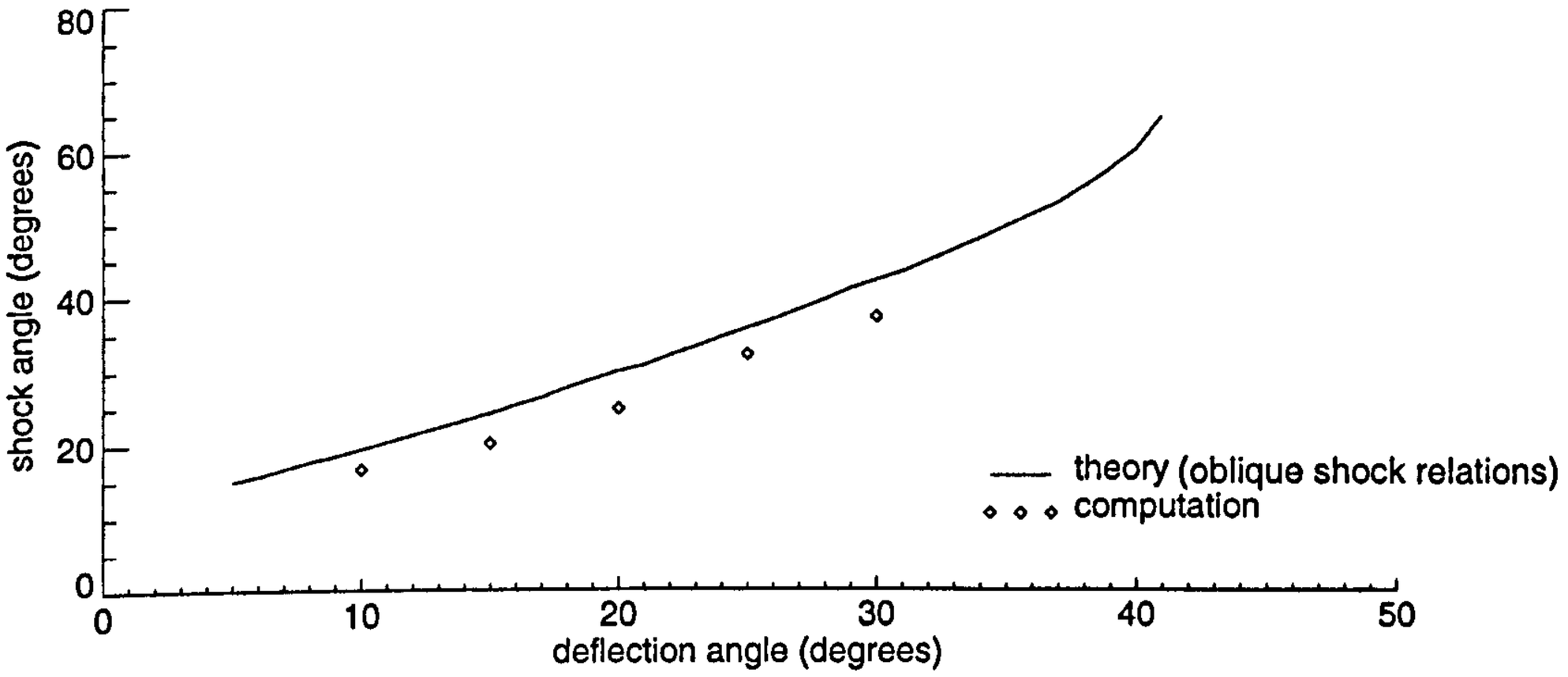

Figure 2.28. Variation in Separation Shock Angle with Flow Deflection Angle

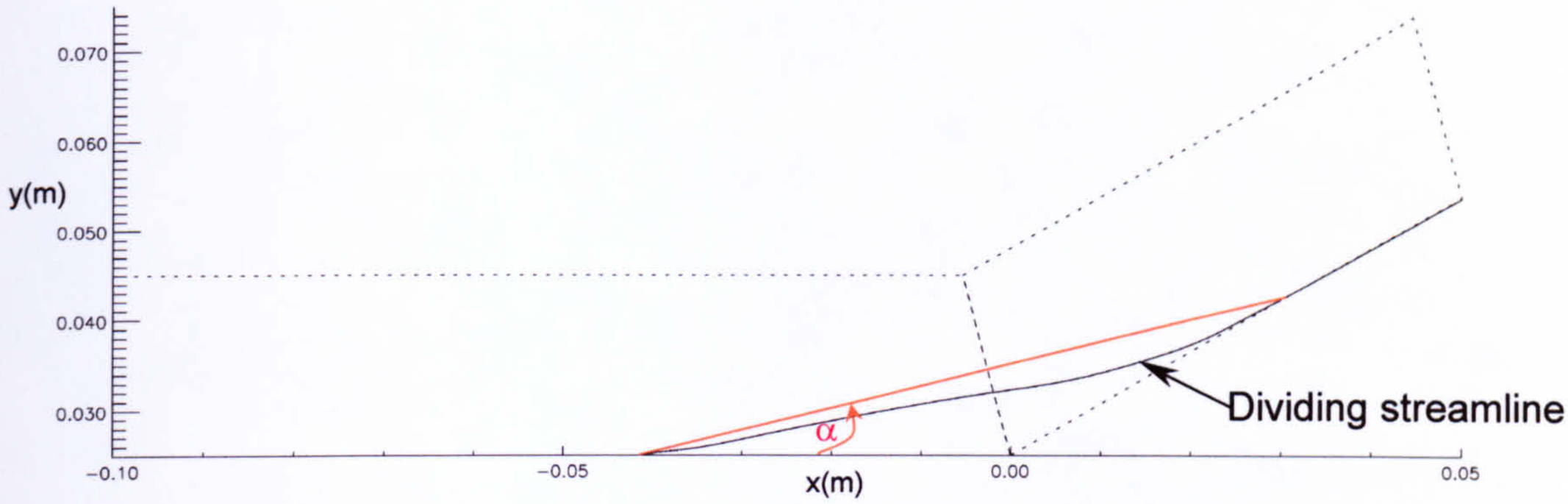

Figure 2.29. Streamline Circumscribing the Separated Region (30° Flare)

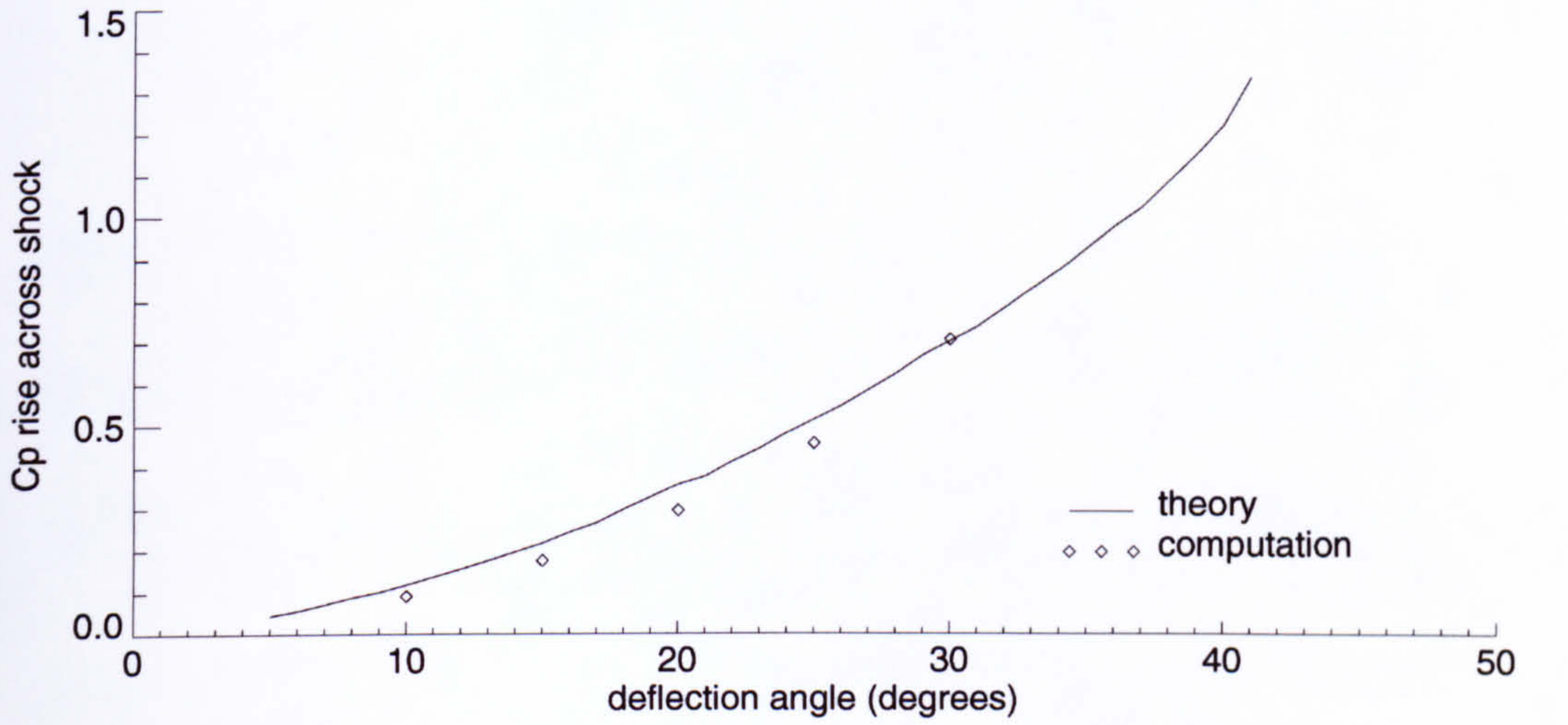

Figure 2.30. Variation in Pressure Rise Across Flare Shock with Flare Angle

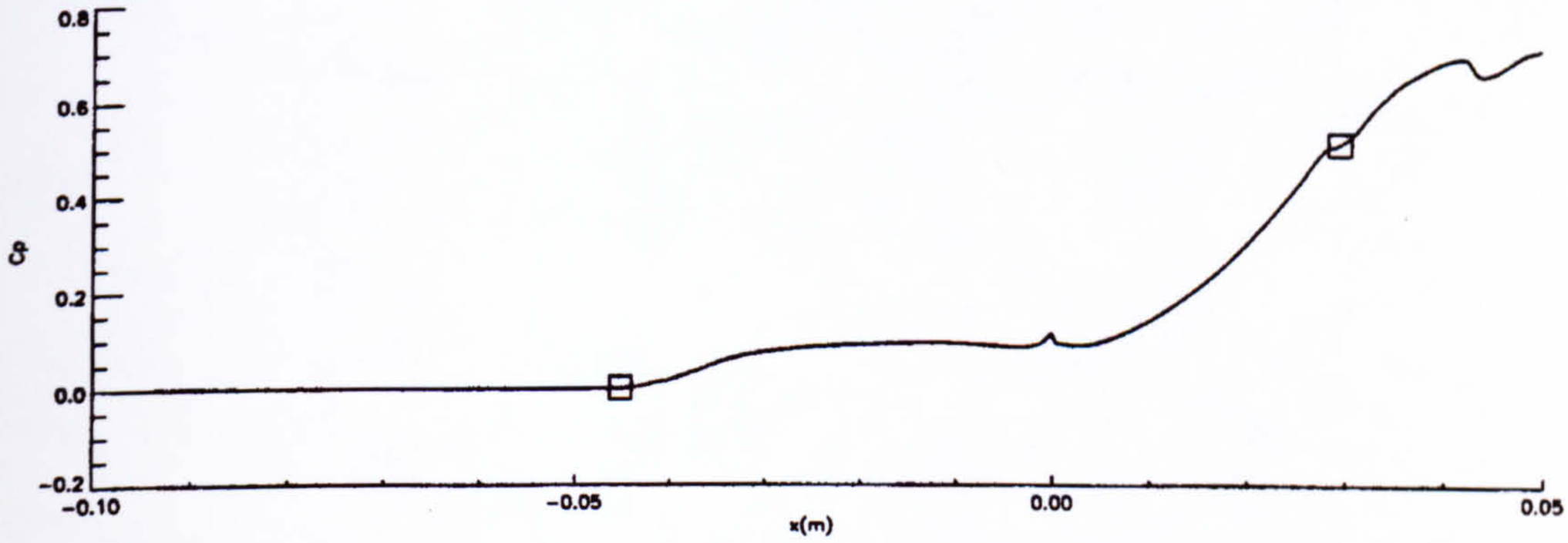

Figure 2.31. Surface Pressure Coefficient Distribution (30° Flare)

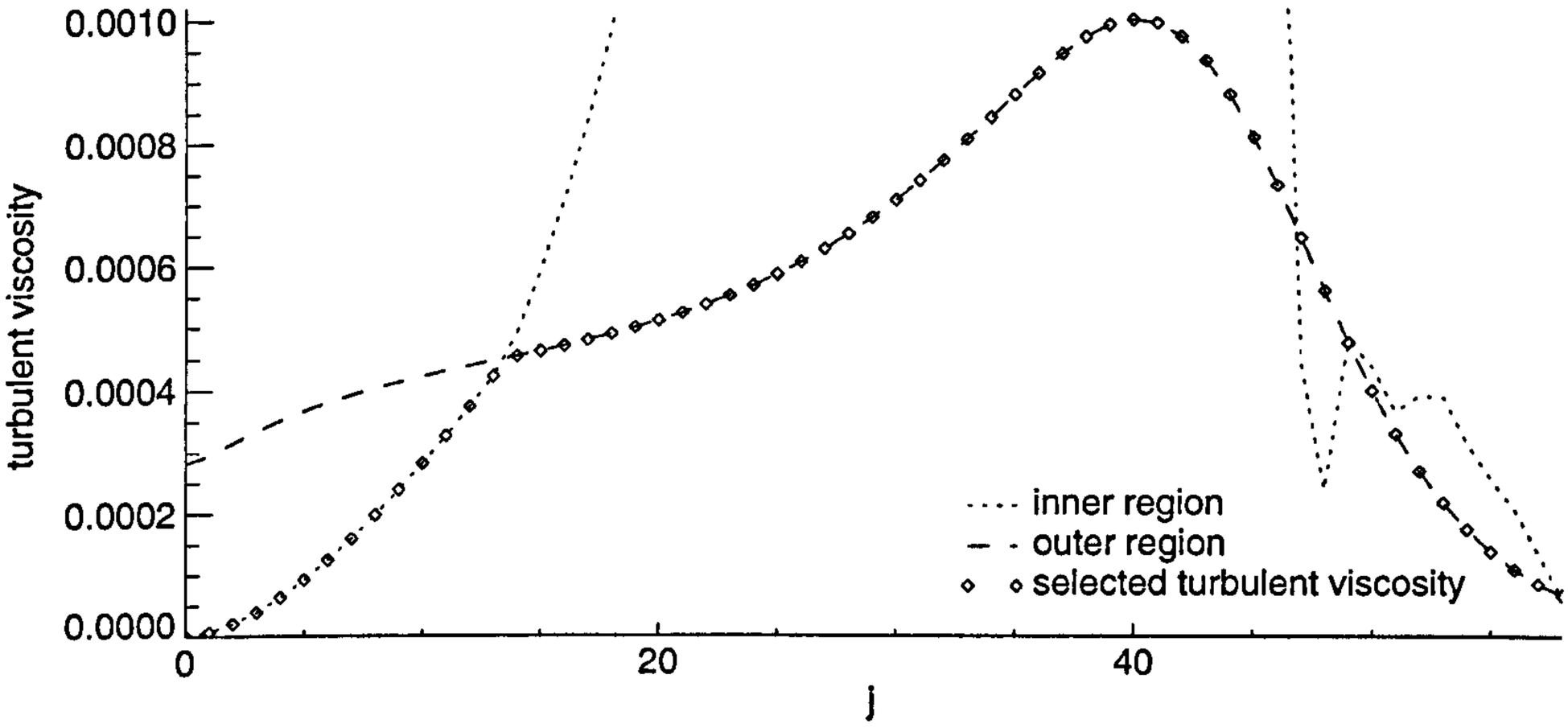

Figure 2.32. Variation in Turbulent Viscosity Through a Baldwin-Lomax Boundary Layer

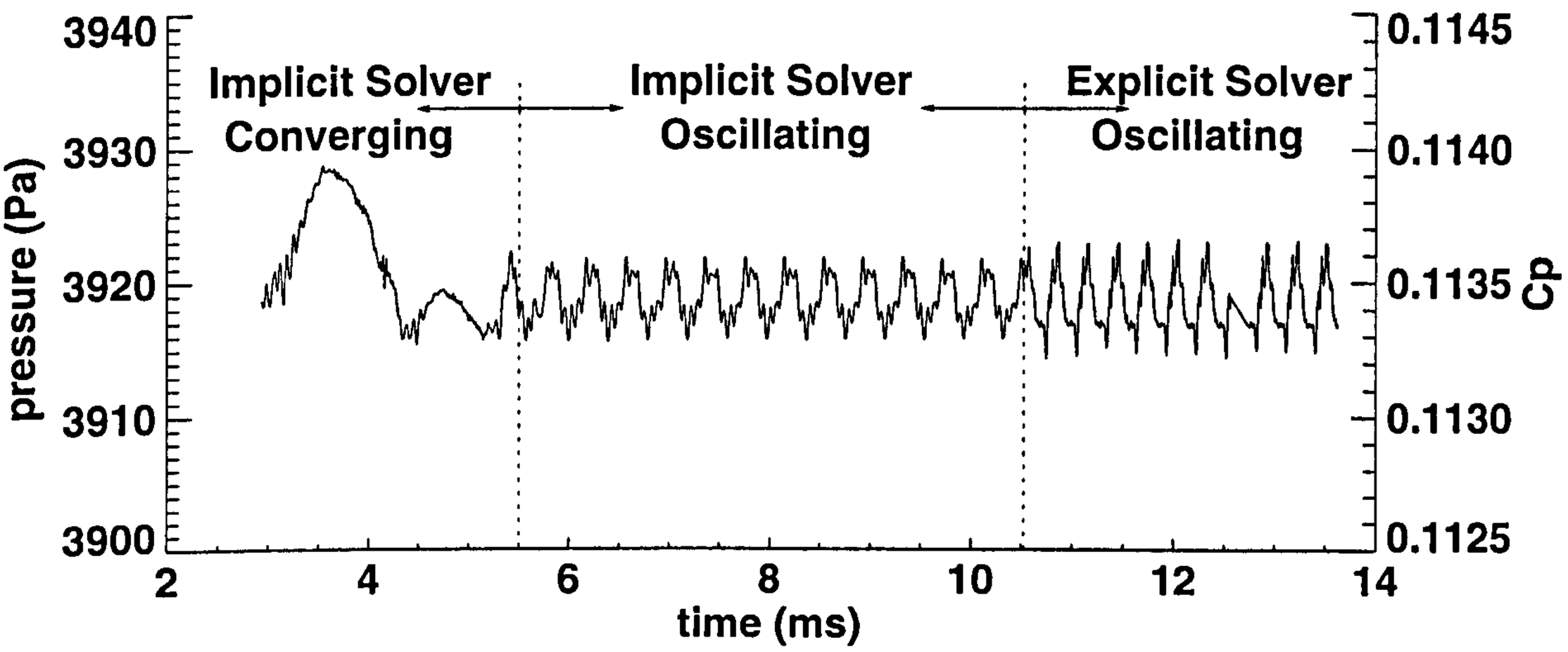

Figure 2.33. Fluctuations in Wall Pressure at the Cylinder Flare Junction (30° Flare) [58]

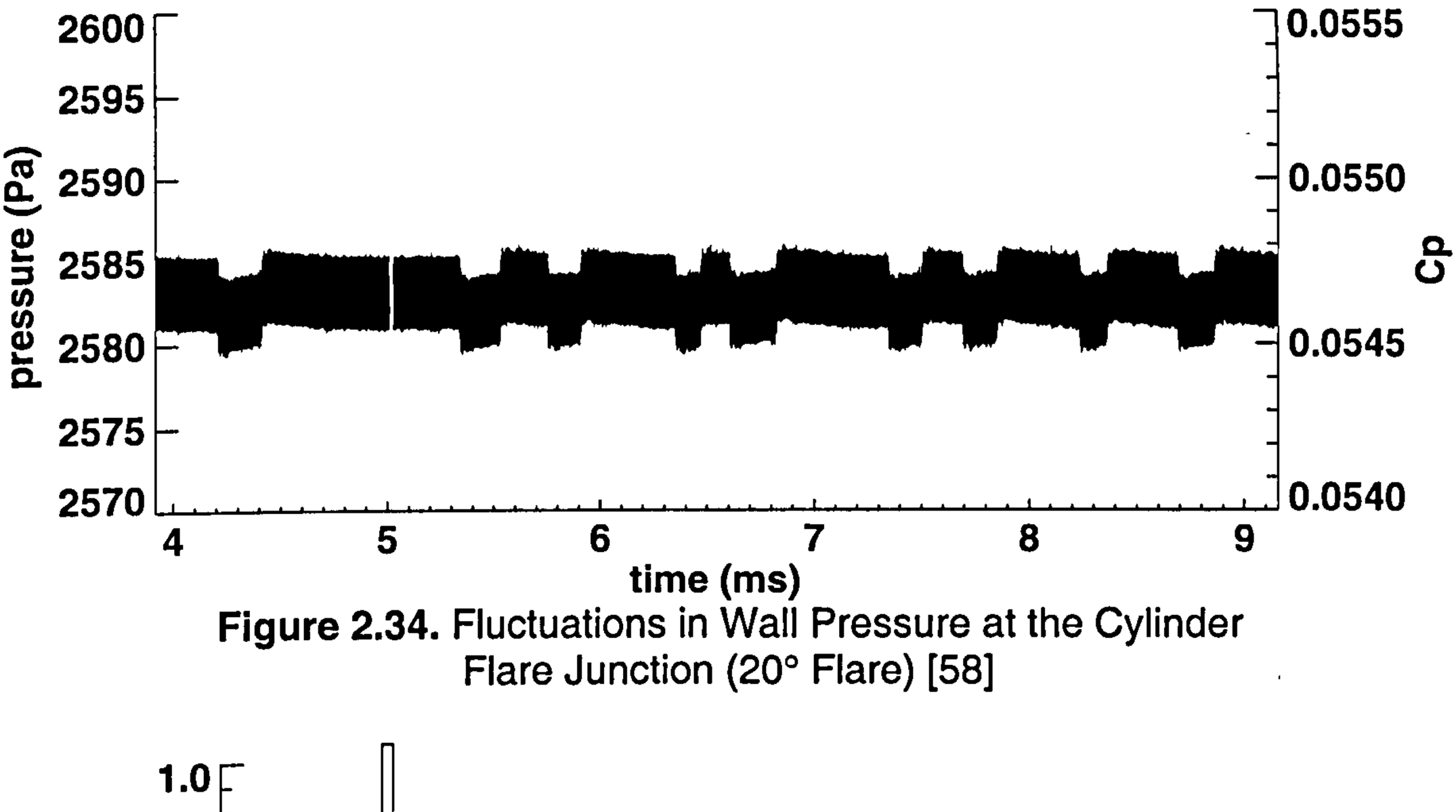

Figure 2.34. Fluctuations in Wall Pressure at the Cylinder Flare Junction (20° Flare) [58]

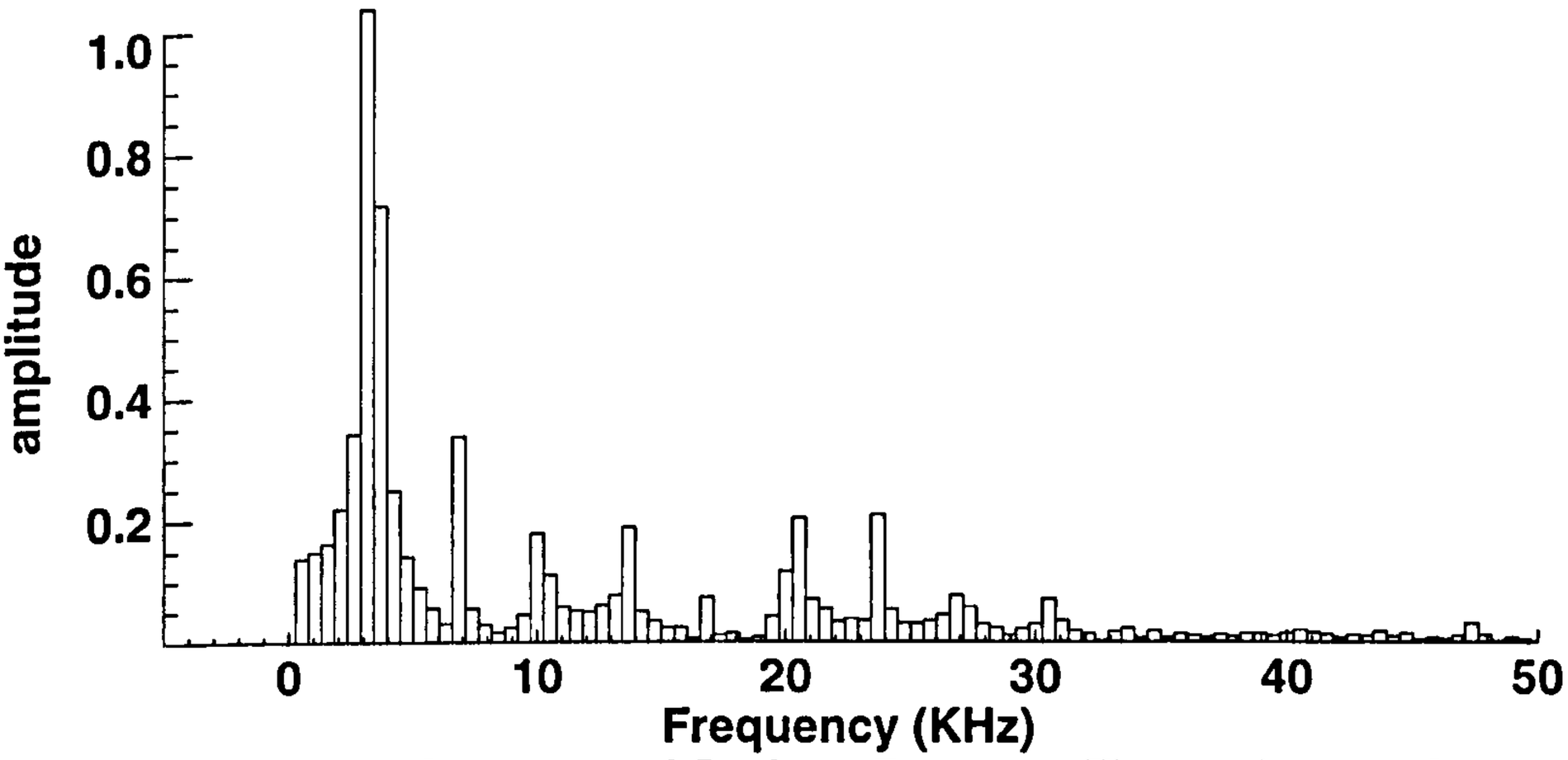

Figure 2.35. Fourier Spectrum of Surface Pressure Fluctuations at Cylinder-Flare Junction (30° Flare)

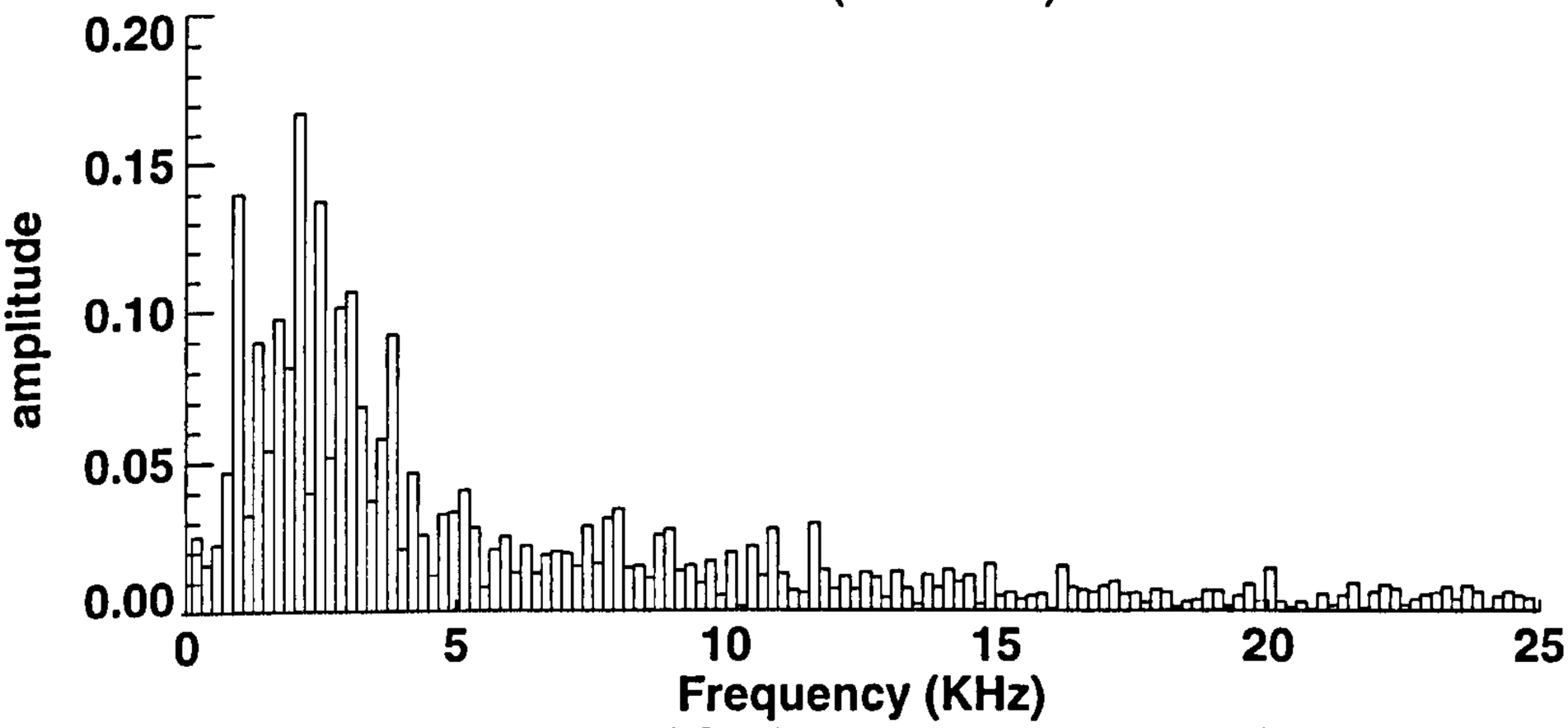

Figure 2.36. Fourier Spectrum of Surface Pressure Fluctuations at Cylinder-Flare Junction (20° Flare)

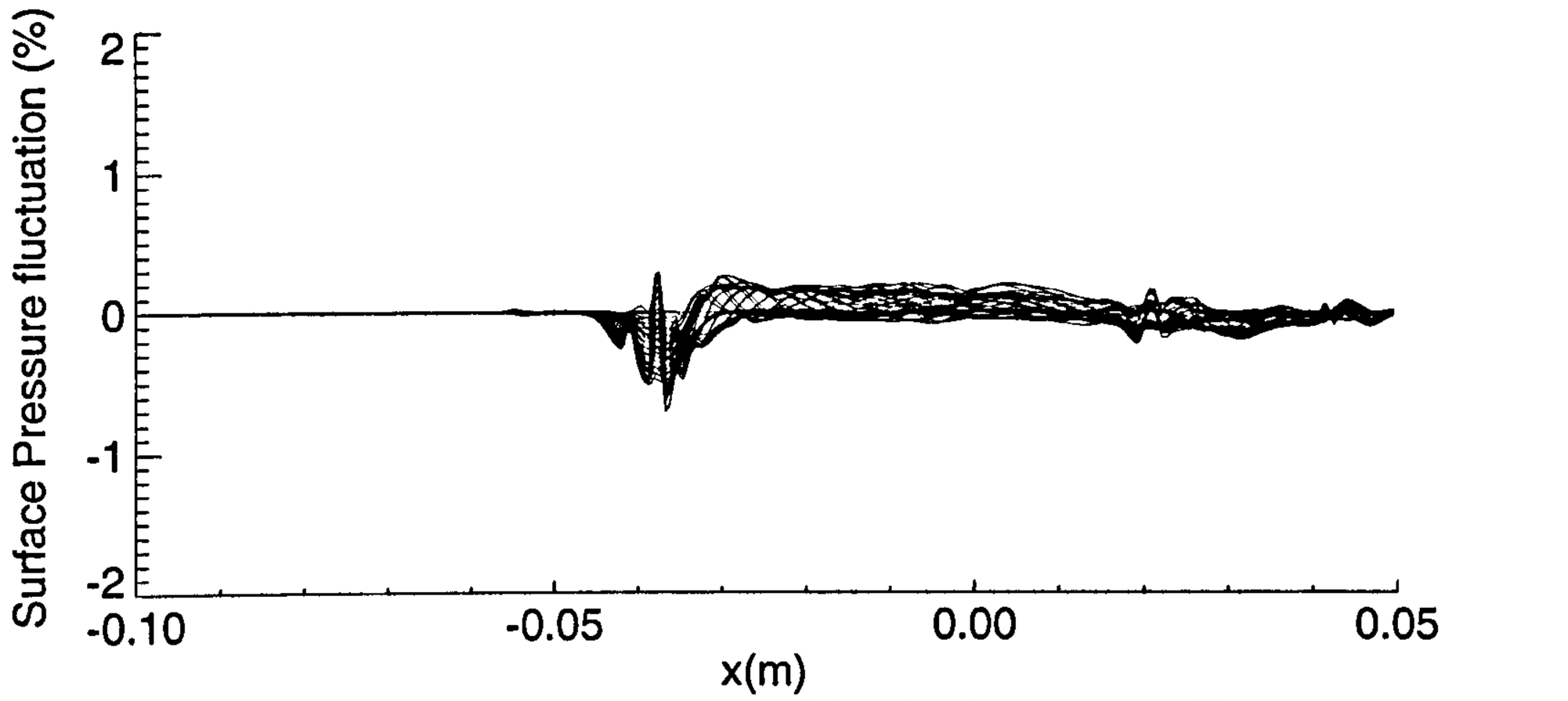

Figure 2.37. Surface Pressure Distributions – 30° Flare

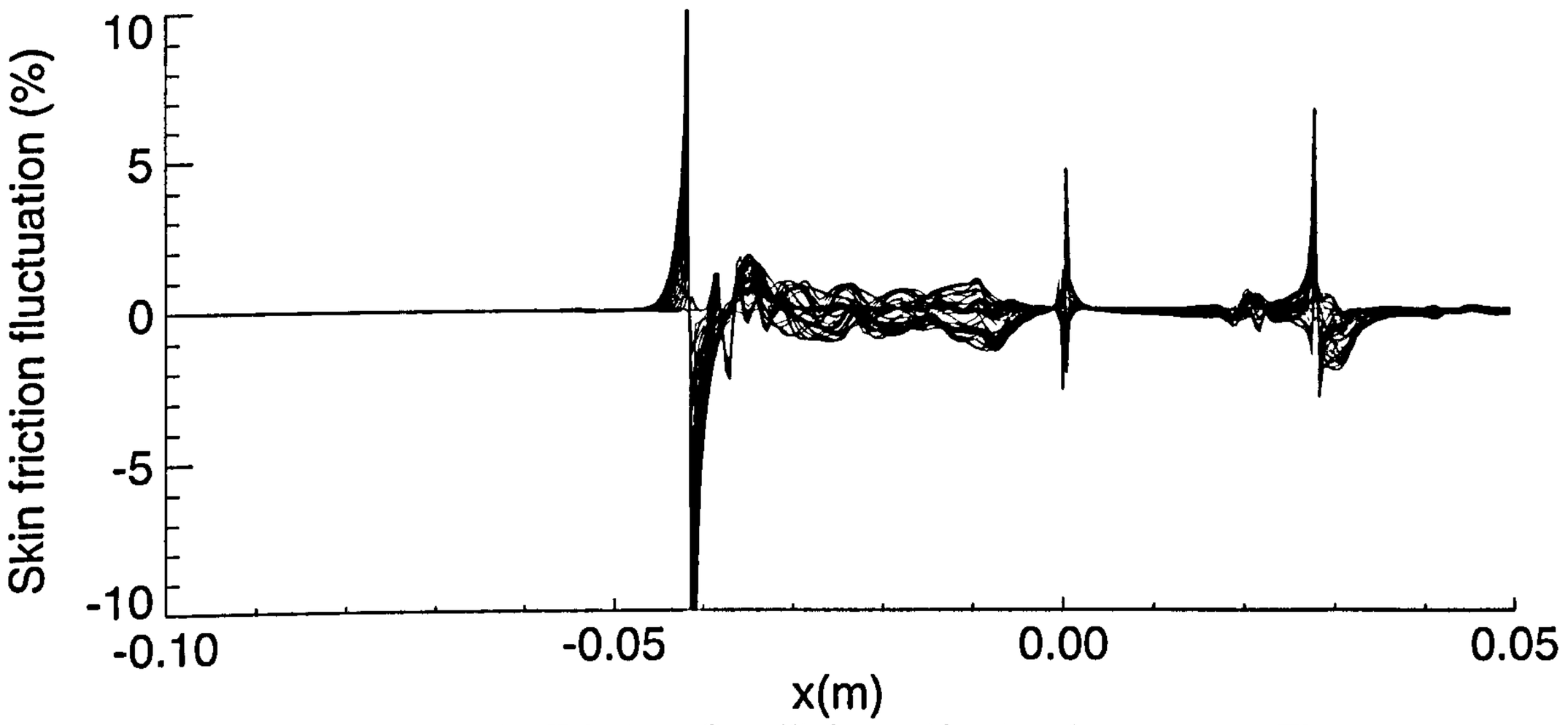

Figure 2.38. Skin Friction Coefficient Distributions – 30° Flare

3. Turbulent Flat Plate-Ramp Flows

Due to the large amount of available data (both experimental and computational) from Dolling and his co-workers on a 28° compression ramp flow at Mach 5, these form a useful basis for computational investigation and comparison. Despite the large amount of available experimental data, there is insufficient data to produce a complete boundary layer profile for computational analysis. Even had this been possible it may have proved difficult to match the experimental and computational boundary layers to produce transient free boundary layer insertion [60][61]. It was therefore necessary to grow a boundary layer over a flat plate to the required thickness (Figures 3.1 and 3.2 – schematic and flowfield respectively). In order to ensure sufficient upstream extent for the interaction, the location at which the boundary layer was of the correct thickness (15.1mm) was selected and a profile extracted back upstream. In this manner the boundary layer grows along the flat plate preceding the ramp and when the flow is three boundary layer thicknesses upstream of the hingeline, the boundary layer has the correct properties. This is illustrated in Figures 3.3 and 3.4, showing the experimental configuration, and the magnitude and orientations of the computational domains.

A summary of the flow conditions presented in references [14][15][16] are given in Table 3.1.

Using the flow conditions given in [14] as the preliminary data set, the parameters required for the computational simulations are:

$$T_\infty = \frac{U_\infty^2}{M_\infty^2 \gamma R} = \frac{775.0^2}{4.95^2 \times 1.4 \times 287} = 61.0^\circ K$$

$$e_\infty = C_V T_\infty = \frac{R}{\gamma - 1} T_\infty = \frac{287}{0.4} \times 61.0 = 43800 J$$

$$p_\infty = p_0 \left(1 + \frac{\gamma - 1}{2} M_\infty^2\right)^{\frac{\lambda}{1-\gamma}} = 2.28 \times 10^6 (1 + 0.2 \times 4.95^2)^{-3.5} = 4570 Nm^{-2}$$

$$\rho_\infty = \frac{p_\infty}{R T_\infty} = \frac{4570}{287 \times 61.0} = 0.261 kgm^{-3}$$

Viscosity computed using Sutherland's law:

$$\mu = \mu_{ref} \left(\frac{T_{ref} + C}{T + C}\right) \left(\frac{T}{T_{ref}}\right)^{\frac{3}{2}}$$

where C is Sutherland's constant (=110.0), μ_{ref}=1.79x10^{-5}kgm^{-1}s^{-1} , T_{ref}=288°K.

A planar turbulent boundary layer requires a significant length of flat plate to be modelled to achieve the required thickness of 15.1mm. Ignoring the

leading edge viscous interaction this length can be estimated:

For a turbulent *incompressible* boundary layer [161]:

$$\delta_{99} = \frac{0.37x}{\sqrt[5]{\mathrm{Re}_x}} = \frac{0.37x^{4/5}}{34.64}$$

$$\delta_{99} = 15.1\times10^{-3} m \Rightarrow x = 1.54m \qquad (102\delta)$$

3.1 Baldwin-Lomax Turbulence Model

Mesh convergence in terms of boundary layer profiles for the Baldwin-Lomax turbulence model is presented in Figure 3.5. The boundary layer profile selected as the inflow boundary condition is presented in Figures 3.6a-d.

By 'growing' a boundary layer along a flat plate with the Baldwin Lomax turbulence model and extracting boundary layer profiles at a location downstream of the leading edge (to give the required boundary layer thickness) the boundary layer parameters presented in Table 3.2 were obtained.

The skin friction coefficient measured experimentally and produced computationally is in reasonable agreement with the theoretical value at this location, which is $7.73\text{x}10^{-3}$ [160].

This profile was then used as the upstream boundary condition (Figure 3.4) so that larger values of y^+ (and hence fewer grid points) can be used for boundary layer computations than for the ramp flow computations. Thus using a pre-grown inflow eliminates the need for an excessively refined mesh when growing the incoming boundary layer.

A supersonic compressible turbulent boundary layer may be regarded as comprising four distinct regions[30]:

the laminar sub-layer ($y^+ \leq 5$),
the blending region ($5 < y^+ \leq 30$),
the log law region ($30 < y^+ \leq 1000$),
the outer region or defect layer ($y^+ > 1000$).

The inflow boundary layer in logarithmic boundary layer co-ordinates is shown in Figure 3.7 and it is seen that although the Baldwin Lomax model only models the effects of turbulence, it appears to successfully replicate the various layers within the turbulent boundary layer (cf. Figures 3.7 and 3.8 [30]). The four regions have been marked on Figure 3.7 and it is seen that the spatial extent over which the various layers are purported to exist correspond very closely to those produced with the Baldwin-Lomax turbulence model. Furthermore the values of κ and β are of the correct order; Coles and Hurst

[134] report for an incompressible turbulent boundary layer values for κ and β of 0.41 and 5.0 respectively. κ and β for the Baldwin-Lomax boundary layer presented in Figure 3.7 are 0.35 and 2.0 respectively. Whilst there appears to be a significant difference in β, in terms of the log-layer, this is not as poor an agreement as the numerical values suggest. The two dotted lines (marked as 'a' and 'b') in Figure 3.7 correspond to the log-layer plotted with Coles and Hurst's κ and β, and with the computationally obtained κ and β respectively.

Mesh convergence results for the time averaged flow over the 28° ramp are presented in Figure 3.9, and the selected mesh in Figure 3.10 (2 regions, each 100x240 cells, geometric stretching factor of 8 towards the wall and 4 towards the plate-flap junction). It was found that due to slight oscillations in the location of separation (possible due to the inherent unsteadiness in the flowfield) as shown in Figure 3.11, the residuals did not reduce significantly (Figure 3.12). It was ascertained that the fluctuations within the flowfield were minimal in absolute terms, but sufficient to exhibit oscillatory characteristics in the residuals.

Density and streamline plots (coloured by flow velocity) are presented in Figure 3.13 to show the various structures within the flow and that there appears to be sufficient upstream and downstream extent to accurately model the shock boundary layer interaction. These extents were subsequently verified as sufficient by extension and comparison.

It is seen from Figure 3.14 that the location of the time averaged computational pressure rise agrees with the location of the experimental time averaged pressure rise. As expected with the Baldwin Lomax turbulence model, the surface pressure rise under the separated region is over predicted[30], although downstream of reattachment the surface pressure recovers the theoretical inviscid pressure rise for a 28°, Mach 5 flow deflection.

Examining the skin friction coefficient to determine the precise location of separation and reattachment (Figure 3.15) reveals a total separated length of 77.6mm (5.1δ). For this configuration the experimentally reported unsteady separated region's length varied between 1.7δ and 3.6δ corresponding to 25.7mm and 54.4mm respectively. Since the location of separation for the time averaged experimental data agrees well with the location of the time averaged computation, reattachment must be predicted too far downstream. This is a known failing of the Baldwin-Lomax turbulence model[30]. It is seen that the flat plate skin friction coefficient (preceding the interaction) is constant and in reasonable agreement with the compressible theoretical value extracted from Figure 3.16[160]. This implies that the velocity gradient normal to the wall does not vary for a significant distance (approximately 150mm (9.9δ)) upstream of the interaction and hence the adverse pressure gradient (caused by the flow deflection) which results in momentum loss is not experienced by the flow for some distance from the inflow. This confirms the presence of sufficient upstream computational domain for the flow to be

adequately resolved (as shown previously by domain extension and comparison).

By extracting profiles through the boundary layer along the length of the computation domain (Figure 3.17), separation, the separation shock, reattachment and the ramp shock can all be identified.

Continuing the computation in an explicit time accurate manner produces oscillations of approximately 5.5kHz ($\bar{f} = 0.11$) (Figure 3.18), for a single computational pressure tap located at the hingeline. It is seen that self-sustained periodic oscillations are produced, and that the time averaged surface pressure is lower than the corresponding result from the time-averaged computation. This is to be expected since the pressure rise across a dynamically moving shock wave is known to be weaker than its static counterpart[104]. The amplitude of these oscillations is seen to be 5% of the RMS wall pressure at this location (55% of the static freestream pressure).

Normalising the surface pressure distribution fluctuations with respect to the freestream static pressure (Figure 3.19) shows oscillations with peak magnitude of approximately 55%. This compares favourably (in frequency) with the experimentally measured results (5kHz ($\bar{f} = 0.10$) and 48%[15]).

As in §2.3 neither motion of the separated region nor motion of the shock waves (as seen experimentally [14][15][16][17][21]) was observed. This is presumably why the is no evidence of unsteadiness at around 1kHz ($\bar{f} = 1.9\times10^{-2}$) (associated with the expansion and contraction of the separation bubble). The amplitude of the higher frequency components of the system (not associated with bubble expansion and contraction) around 5kHz ($\bar{f} = 9.7\times10^{-2}$) are likely to be over predicted. Since the shock wave is static, the pressure plateau is too high with associated over prediction of adverse pressure gradient and separation bubble. As the wall pressure plateau is over-predicted, a proportionate fluctuation in high frequency component, when normalised with respect to freestream static pressure, will appear larger than seen experimentally. The presence of high frequency oscillations without shock or separation bubble motion may by due to amplification of numerical noise in a similar manner to the suggested amplification of incoming boundary layer structures (Hypothesis I [23][24][65][100][102][132]). The lack of oscillations of lower frequency (1kHz ($\bar{f} = 1.9\times10^{-2}$)) associated with bubble expansion and contraction and shock motions may be due to the lack of an unsteady model in the turbulence model itself[30] (Hypothesis II[26][66][99] suggests that the unsteadiness in an inherent property of the separated region itself). The lack of low frequency oscillations, in the context of Hypothesis III [19][23][27] may be due to the lack of an incoming stimulus to invoke the prescribed response.

Examining the length of the separated region with time reveals that as for the variation in hinge-line pressure (RMS of the time accurate case was less than

the time-averaged results), the separated region has grown significantly in magnitude. The length of the separated region produced with the steady state computation was 77.6mm (5.1δ) , the mean separated length for the time-accurate case was 122.5mm (8.1δ) (Figure 3.20). The noise in separated length evident in Figure 3.20 is caused by the location of separation and reattachment (where the skin friction coefficient changes sign) with small fluctuations in the wall flow.

To verify that the steady state computation was fully converged, the computation was continued for further iterations (from the original converged solution). No change resulted.

It appears that the use of steady state, implicit, local time-stepping to produce a 'steady-state' solution for an inherently unsteady flowfield (despite the fact that the time accurate unsteadiness is small), produces erroneous results and the agreement between separation location for the steady state computations and experiment coincidental. This may, in part, be due to the use of local time stepping with the implicit solver – there is no true time step for each iteration and hence temporal effects will be unpredictably modelled.

It is noted that with the time accurate computations, the boundary layer is seen to separate further upstream than experimental boundary layer as expected with the Baldwin-Lomax turbulence model [30] (over prediction of the adverse pressure gradient will result in an overly large separated region).

Placement of twenty equally spaced computational pressure taps along the surface of the flat plate and the ramp and recording pressure fluctuations from t=3.6ms to 6.5ms shows the propagation of disturbances downstream through the boundary layer and recirculatory region (Figure 3.21). By tracing a disturbance in wall pressure from separation to the outflow, the propagation velocity is found to be 347.5m/s (45% U_∞) along the surface (0.195m in 0.5614ms (λ_2)). The frequency of the oscillations is seen to be approximately 5700Hz ($\bar{f} = 0.11$) ($5\lambda_1$=0.87ms). The fundamental frequency associated with the motion of structures through the separated region is approximately 3kHz ($\bar{f} = 5.8\times10^{-2}$) ($\lambda_3$=0.32ms).

McClure[19] reported the presence of turbulent signatures within the interaction region travelling at approximately 75%U_∞ (with spatial extent of 3.2δ-4.3δ and a temporal extent of 75-100μs). These signatures were also observed by Unalmis and Dolling[16] who report their magnitude to be 1-4 boundary layer thickness in extent, with a streamwise decay of 15-20 boundary layer thicknesses). The propagation velocity is then 581m/s, for which temporal extents of 75-100μs gives spatial extents of 43.6mm to 58.1mm (2.9δ-3.8δ). Since the frequency of the pressure fluctuations at the wall is in good agreement with those measured experimentally, and the propagation velocity is not, then it follows that the spatial and hence temporal extent of these structures is likely to be in error.

In order to try to ascertain the nature of the convected signatures, a series of density plots through the flowfield were stored (two hundred in total), plotted and used as a 'flick-book'. It transpired that, although not readily apparent, various regular structures were being created, amplified, convected and distorted. By sampling these images at selected regular intervals (Figure 3.22) and colouring the individual contours of the density plots on a per-structure basis, Figure 3.23 was produced. Such amplification of pressure signatures at or near separation, and through the free shear layer was reported by [15].

The maximum spatial extent of these structures is approximately 25mm (1.7δ). The structures are travelling at 347m/s i.e. 45%U_∞, (cf. 64%U_∞[10] or 75%U_∞[19]) giving a temporal extent of 72μs which compares favourably with reported temporal extents of 75μs-100μs [19].

As expected, since the frequency of oscillation is correct, the temporal extent of these signatures is similarly in good agreement with the experimental data. As the predicted propagation velocity is too small, the spatial extent of these structures is also too small. Gramann and Dolling [20] also report the presence of these structures up to twenty boundary layer thicknesses (302mm) upstream of the interaction – this is not apparent here (Figure 3.21). It may be possible to improve the quantitative accuracy of the Baldwin-Lomax predictions by applying modifications for strong adverse pressure gradients, e.g.[150][151]. Computations were repeated with the value of CFL halved, which, with the global time stepping, halves the timestep throughout the domain, and identical results produced, and hence temporal convergence was demonstrated.

3.2 Turbulent Flat Plate-Ramp Flow - K-ε Turbulence Model

Due to the differences observed between the Baldwin Lomax computation and the experimentally observed results, a second order turbulence model was employed to try to provide better resolution of the flowfield. It is known [30] that two equation models have the potential to provide more accurate predictions of the turbulent flows. There are many instances, however, where their performance can be erratic and/or unreliable. Whilst second order turbulence models have the ability to more accurately model the flow, there are several pre-conditions for the k-ε turbulence model which are not satisfied (i.e. the flow must be attached and there cannot be strong adverse pressure gradients). Nevertheless many researchers have applied such turbulence models to flows for which these pre-conditions are not satisfied, with varying degrees of success. As discussed in §1, there are no methods by which these turbulent flows can be predicted with all of the relevant restrictions and preconditions satisfied.

To verify the correct operation of the k-ε turbulence model in SPIKE, and to examine the efficacy of various two equation models for predicting the incoming turbulent boundary layer, EDDYBL[30] was used to generate a series of boundary layer profiles for comparison with the given experimental data. EDDYBL is a two dimensional and axisymmetric compressible boundary layer code used to compute boundary layer profiles and profile distributions. EDDYBL is a space marching code and hence produces solutions very rapidly (typically in under a second). This enables rapid assessment of mesh convergence and entire families of mesh independent boundary layer profiles can be produced with minimal computational expense. In this manner it was possible to employ various 2^{nd} order turbulence models to examine how well (or otherwise) they computed the boundary layer profiles obtained experimentally.

K-ε, k-ω, and multiscale turbulence models were evaluated and boundary layer profiles produced. The input and output parameters are summarised in Table 3.3 and presented in Figure 3.24.

By growing a flat plate k-ε boundary layer with SPIKE in the absence of a pressure gradient (with a Jones and Launder wall function) boundary layers with the following properties were produced:

It is seen that whilst δ and θ are adequately replicated, δ^*, H and skin friction coefficient are not. Selecting a profile on the basis of δ^* leads to a significant deviation in the other parameters. This problem is inherent in the technique of 'growing' boundary layers – which criterion does one use as basis of selecting a boundary layer profile.

It is seen from Figure 3.24 that the implementation of the k-ε turbulence model and wall function in SPIKE agree very well with that in EDDYBL and that the initial effects of the viscous interaction are not in evidence (EDDYBL does not include the effects of viscous interactions at the leading edge of the plate).

Limited boundary layer velocity profile data is available [16] and is reproduced in Figures 3.25 and 3.26. Extracting this data and comparing with the profiles produced by EDDYBL reveals marked variation in profile with wall function (Figure 3.27). It is seen that none of the four k-ε wall functions tested produce good agreement with the experimental data. The k-ω and multiscale models appear to follow the experimental data well (over the range of available experimental data : $100 \leq y^+ \leq 1500$).

When the original mesh used for the Baldwin Lomax computations was used for the k-ε computations, the pressure gradient was seen to extend as far as the inflow. The computational domain was consequently extended, upstream and the mesh convergence tests completed (Figure 3.28). Whilst mesh refinement is producing changes in wall pressure over the flap (although this is largely due to the change in wall cell size – this is a cell centred code), the adverse pressure gradient leading to separation for the three refined cases was found to be virtually identical.

Cursory examination of the pressure distribution (Figure 3.28) and the pressure and density fields (Figures 3.29 and 3.30 respectively) reveals that whilst the solution is correct in qualitative terms, in quantitative terms, agreement is very poor; separation is predicted 230mm (15.2δ) from the hingeline (cf. experimental measurement of 30mm (2.0δ)). Similar over prediction of separated length was seen by Dunagan et al [42] when applying a k-ε turbulence model to a shock boundary layer interaction.

There are many reasons why the k-ε turbulence model may have performed so poorly:

i. The Bousinesque eddy viscosity relationship is not valid for shock separated flows [30](although, if this is the source of the error, it is

interesting to note that the Baldwin Lomax model which also relies on this relationship does not appear to be as adversely affected).

ii. Wall functions are required despite the fact that the flow is separated and hence the applications of these functions is invalid within the separated region (although, it has been seen that the law of the wall used for cavity flow computations [60][61] with the k-ω turbulence model do not appear to suffer poor agreement with experiment).

iii. There could be problems with the specific wall function used (Jones and Launder). Wilcox[30] warns that many researchers have tried to change wall functions to try to provide more accurate predictions, whereas it is the underlying k-ε model that is at fault, not the wall functions. For this reason no other wall functions were tested here.

iv. The k-ε turbulence model is known to perform poorly for flows with significant adverse pressure gradients[152]. Wilcox [153]showed that relative to the problems of adverse pressure gradient, the effects of wall functions are minor.

It is noted that additional complexity in a turbulence model does not necessarily imply improved prediction of the flow as suggested by Wilcox[30].

Reference	93-3134 [14]	93-4335 [15]	94-2363 [16]
$T_{o,\infty}$	359°K	356°K	355°K
$P_{0,\infty}$	$2.28x10^6Nm^{-2}$	$2.34x10^6Nm^{-2}$	$2.24x10^6Nm^{-2}$
M_∞	4.95	4.92	4.95
U_∞	$775ms^{-1}$	$770ms^{-1}$	$768ms^{-1}$
Re_∞	$49.9x10^6m^{-1}$	$66.8x10^6m^{-1}$	$48.0x10^6m^{-1}$
δ_0	$15.1x10^{-3}m$	$19.3x10^{-3}m$	$15.0x10^{-3}m$
δ^*	$6.7x10^{-3}m$	$9.0x10^{-3}m$	$6.6x10^{-3}m$
θ	$0.661x10^{-3}m$	$0.75x10^{-3}m$	$0.647x10^{-3}m$
Π	0.78	0.44	0.78
H	10.20	12.0	10.20
Re_θ	$3.16x10^4$	$5.01x10^4$	$2.97x10^4$
Cf	$7.74x10^{-4}$	$7.6x10^{-4}$	$7.74x10^{-4}$

Table 3.1. Flow Parameters for Mach 5, 28° Ramp Flow

Parameter	Required [14]	Computed profile (at x=1.750m)
δ	15.1mm	15.1mm
δ^*	6.7mm	7.3mm
θ	0.661mm	0.645mm
H	10.20	11.32
Re_θ	$3.16x10^4$	$3.21x10^4$
Cf	$7.74x10^{-4}$	$7.51x10^{-4}$

Table 3.2. Computation and Experimental Boundary Layer Parameters

Model	*k-ε-ch*	*k-ε-flb*	*k-ε-jl*	*k-ε-ls*	*k-ε-ys*	*kω+*	*kω-*	*ms +*	*ms -*	*Reqd.*
Cf_{IN}	7.74E-4	7.74E-4	7.74E-4	7.74E-4	7.74E-4	7.74E-4	7.74E-4	7.74E-4	7.74E-4	N/A
δ_{IN}	1mm	1mm	1mm	1mm	1mm	1mm	1mm	1mm	1mm	N/A
H_{IN}	10.2	10.2	10.2	10.2	10.2	10.2	10.2	10.2	10.2	N/A
$Re_{\theta IN}$	2000	2000	2000	2000	2000	150	150	150	150	N/A
S	1.505m	1.410m	0.850m	0.850m	1.165m	1.400m	1.350m	1.485m	1.400m	N/A
#x (n)	225	208	243	217	209	249	299	246	291	N/A
#y	70	37	75	50	50	150	150	150	150	N/A
Ratio	1.10	1.11	1.10	1.10	1.10	1.10	1.10	1.10	1.10	N/A
δ	17.65mm	17.24mm	17.15mm	17.12mm	17.99mm	16.43mm	16.26mm	16.37mm	16.38mm	15.1mm
δ^*	7.28mm	7.40mm	8.54mm	8.77mm	8.06mm	7.70mm	7.70mm	7.85mm	7.81mm	6.7mm
Re_θ	3.19E4	3.35E4	3.60E4	3.80E4	3.53E4	3.36E4	3.35E4	3.50E4	3.46E4	3.16E4
H	11.4	11.1	11.9	11.6	11.4	11.5	11.5	11.2	11.3	10.2
Cf	7.10E-4	8.88E-4	1.45E-3	1.55E-3	1.00E-3	8.15E-4	8.27E-4	7.97E-4	8.20E-4	7.74E-4

Table 3.3. Comparison of Experimental with Various Computational Boundary Layer Profiles

Parameter	Required	Computed profile (at x=1.750m)
δ	15.1mm	15.1mm
δ^*	6.7mm	8.6mm
θ	0.661mm	0.669mm
H	10.20	12.84
Re_θ	$3.16x10^4$	$3.31x10^4$
Cf	$7.74x10^{-4}$	$1.45x10^{-3}$

Table 3.4. Comparison of Experimental with SPIKE Boundary Layer Profiles

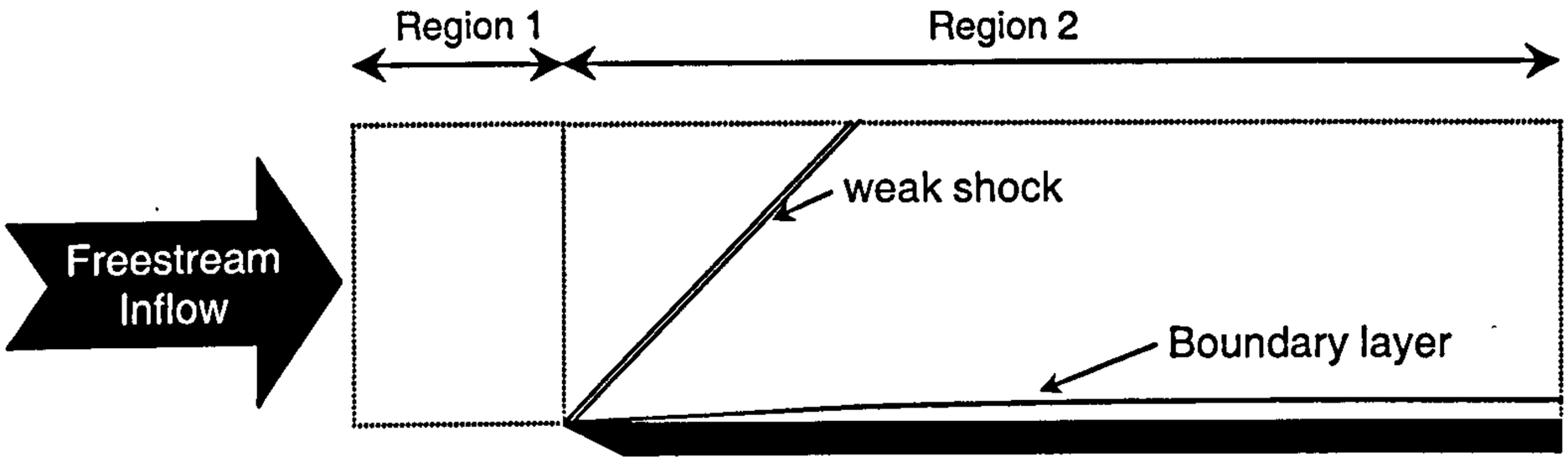

Figure 3.1. Schematic of Boundary Layer Development Over a Flat Plate

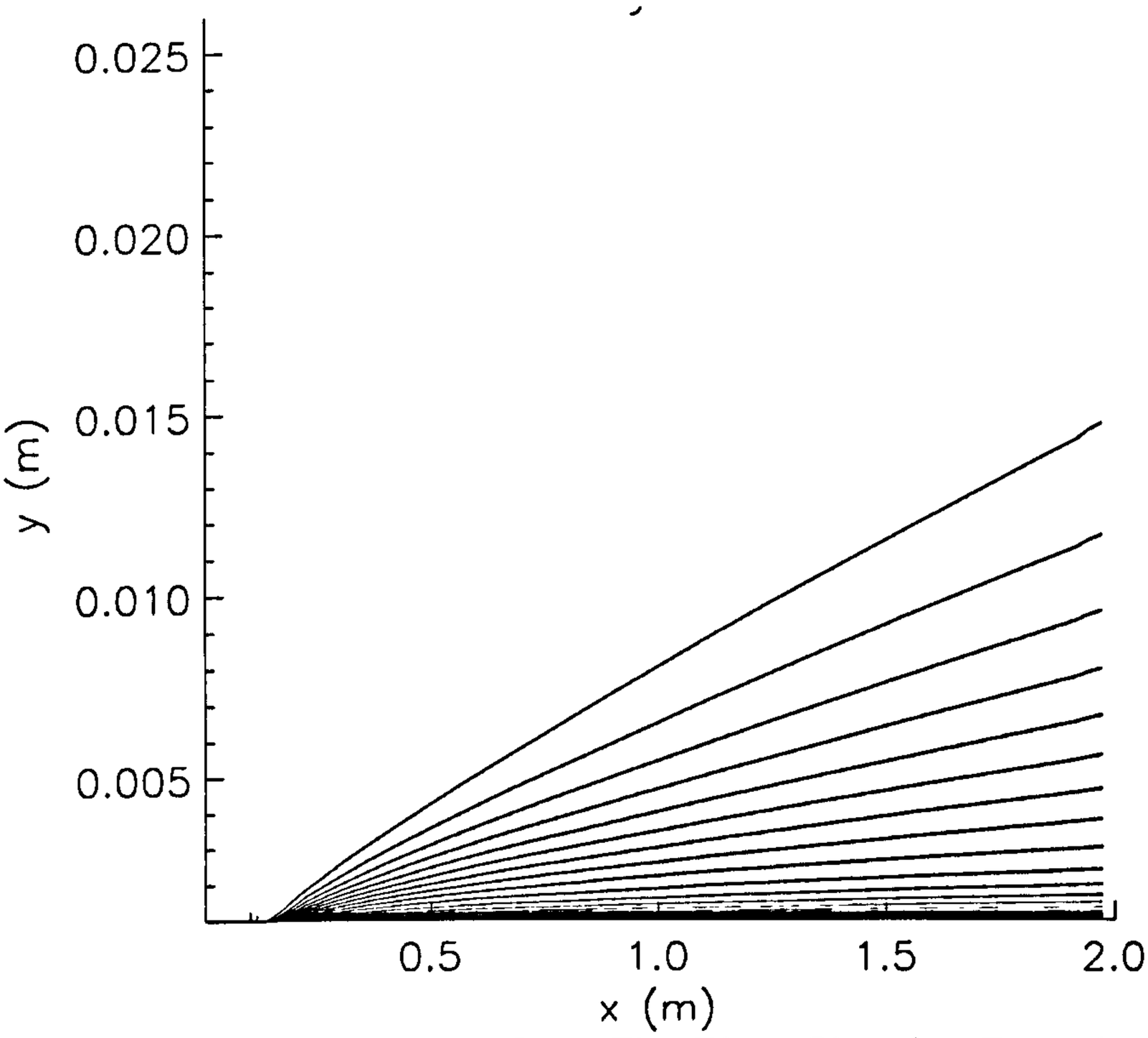

Figure 3.2. U Velocity Contours Over Flat Plate Showing Boundary Layer Development

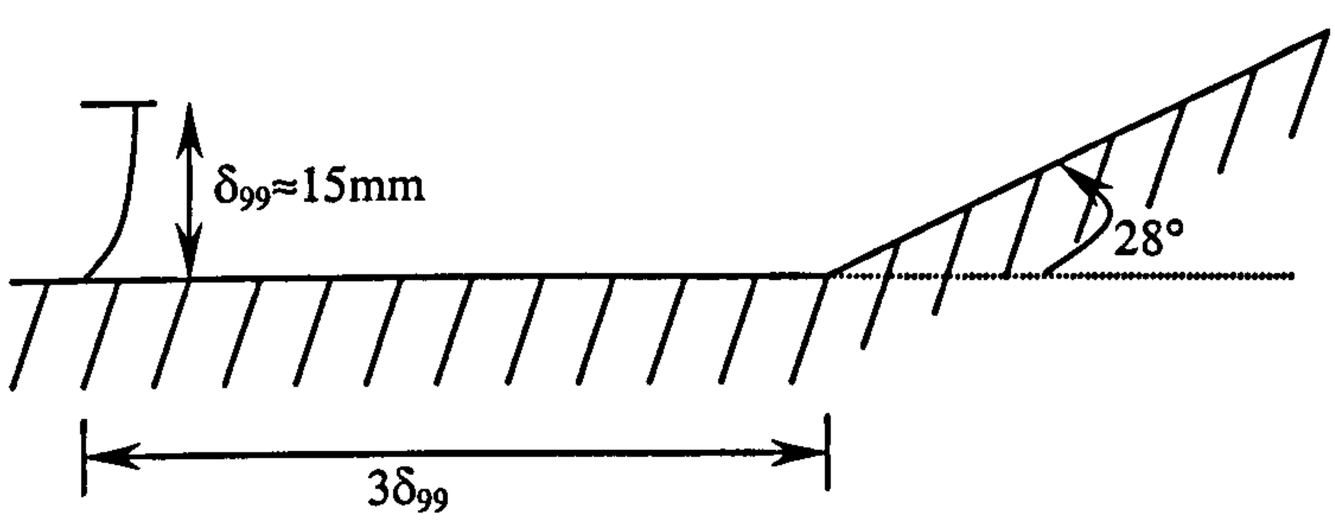

Figure 3.3. Schematic of Dolling Ramp Flows

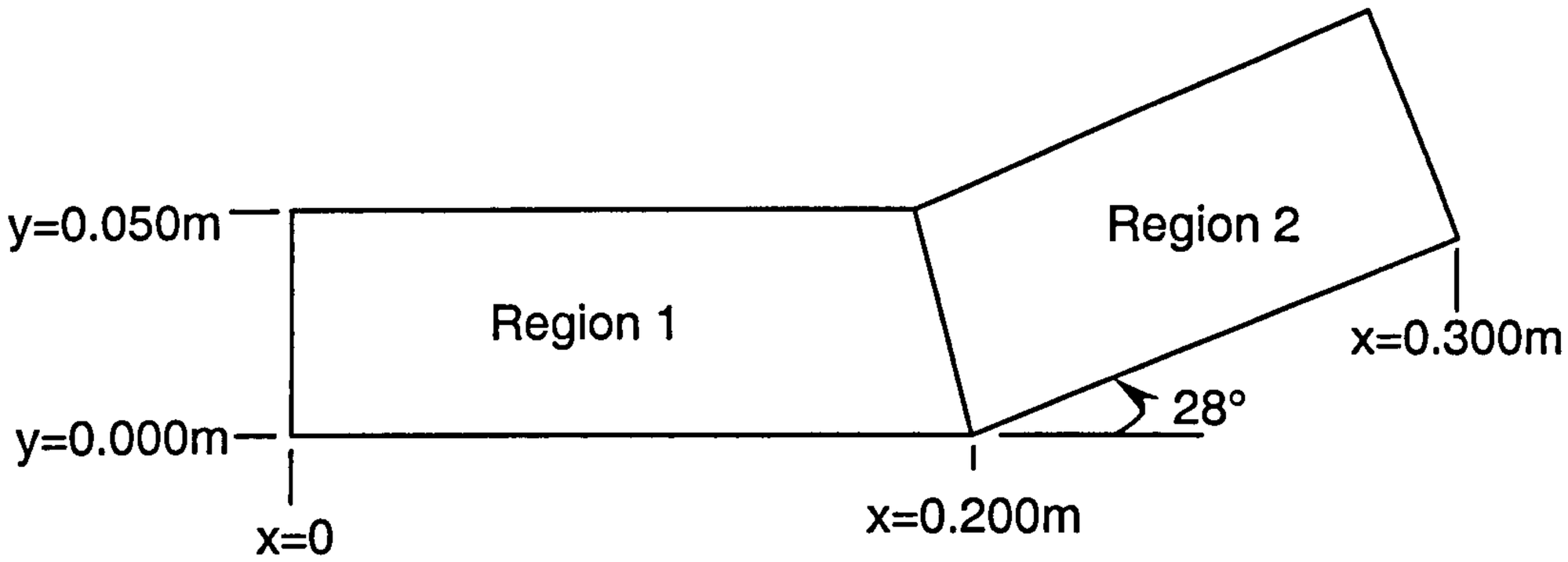

Figure 3.4. Schematic of Computational Domain

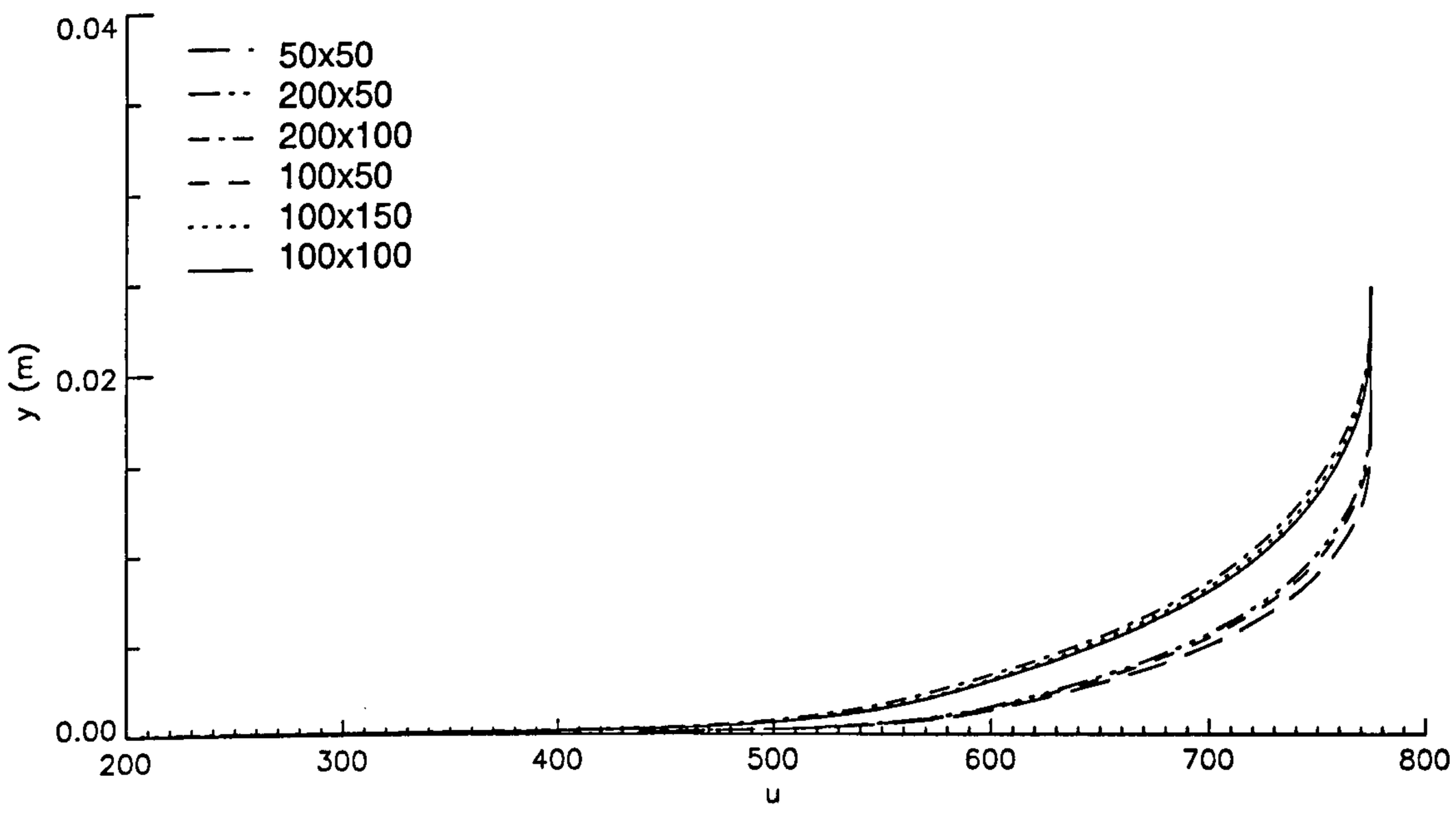

Figure 3.5. Mesh Convergence Plot – Boundary Layer Profiles Computed With Baldwin Lomax Turbulence Model

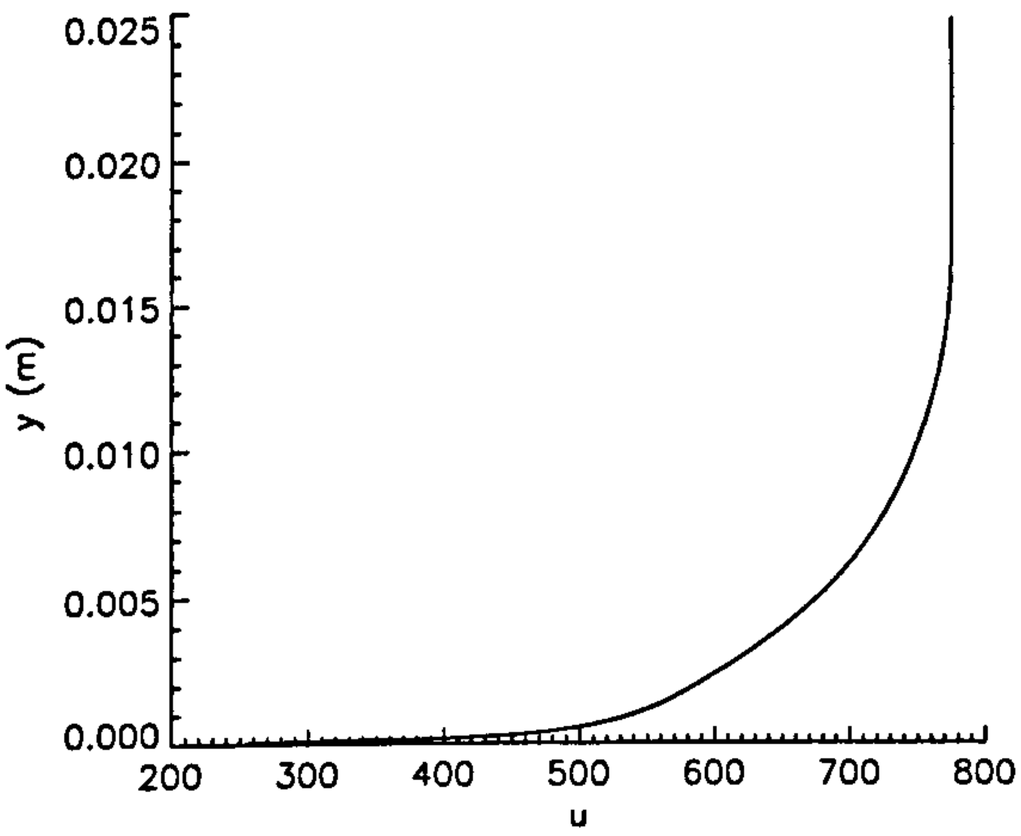

Figure 3.6a. U Velocity

Figure 3.6b. Density

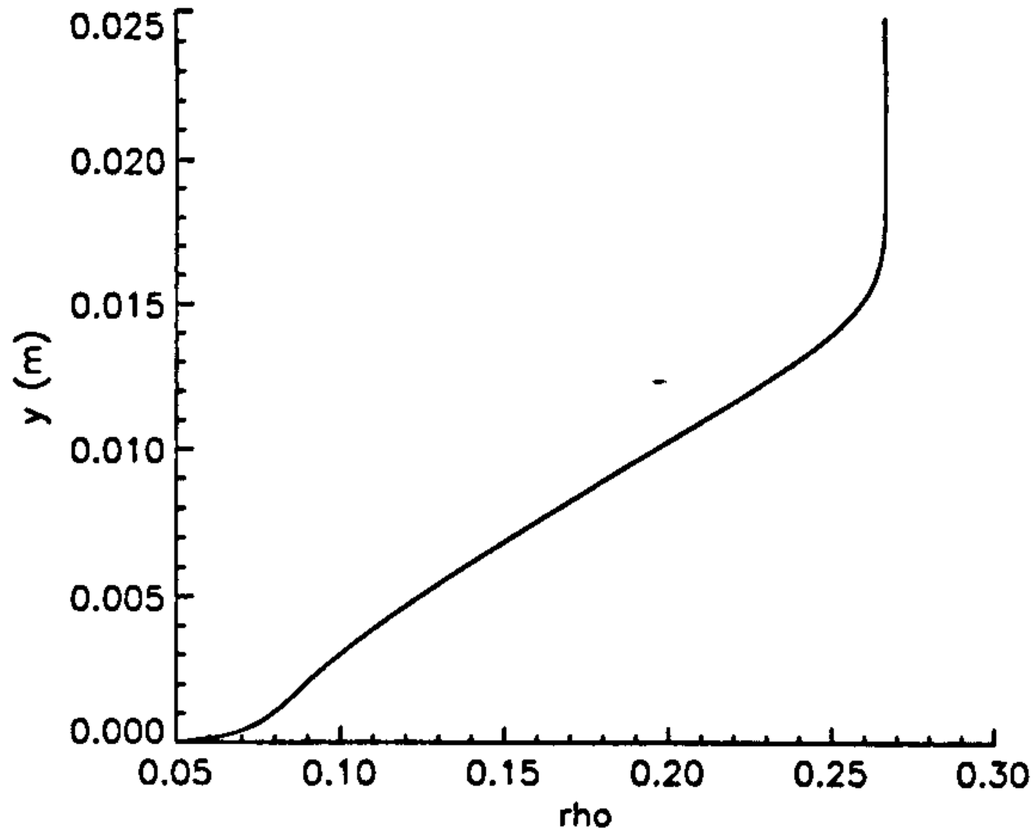

Figure 3.6c. V Velocity

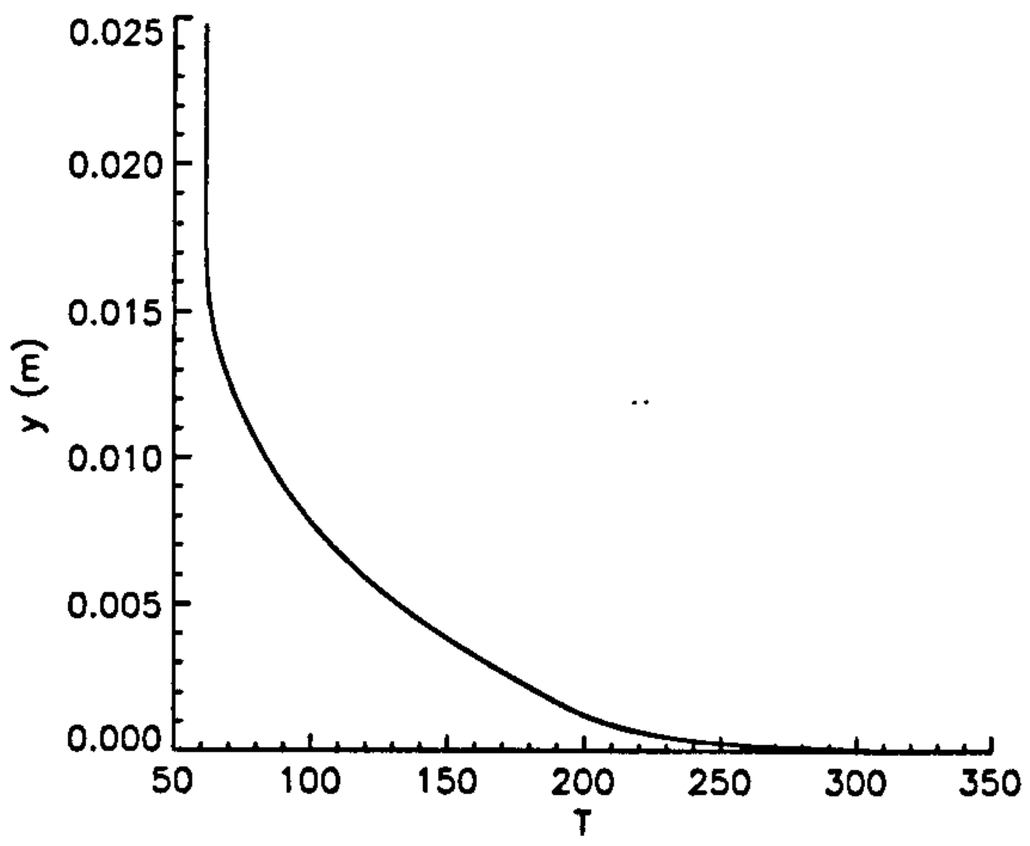

Figure 3.6d. Temperature

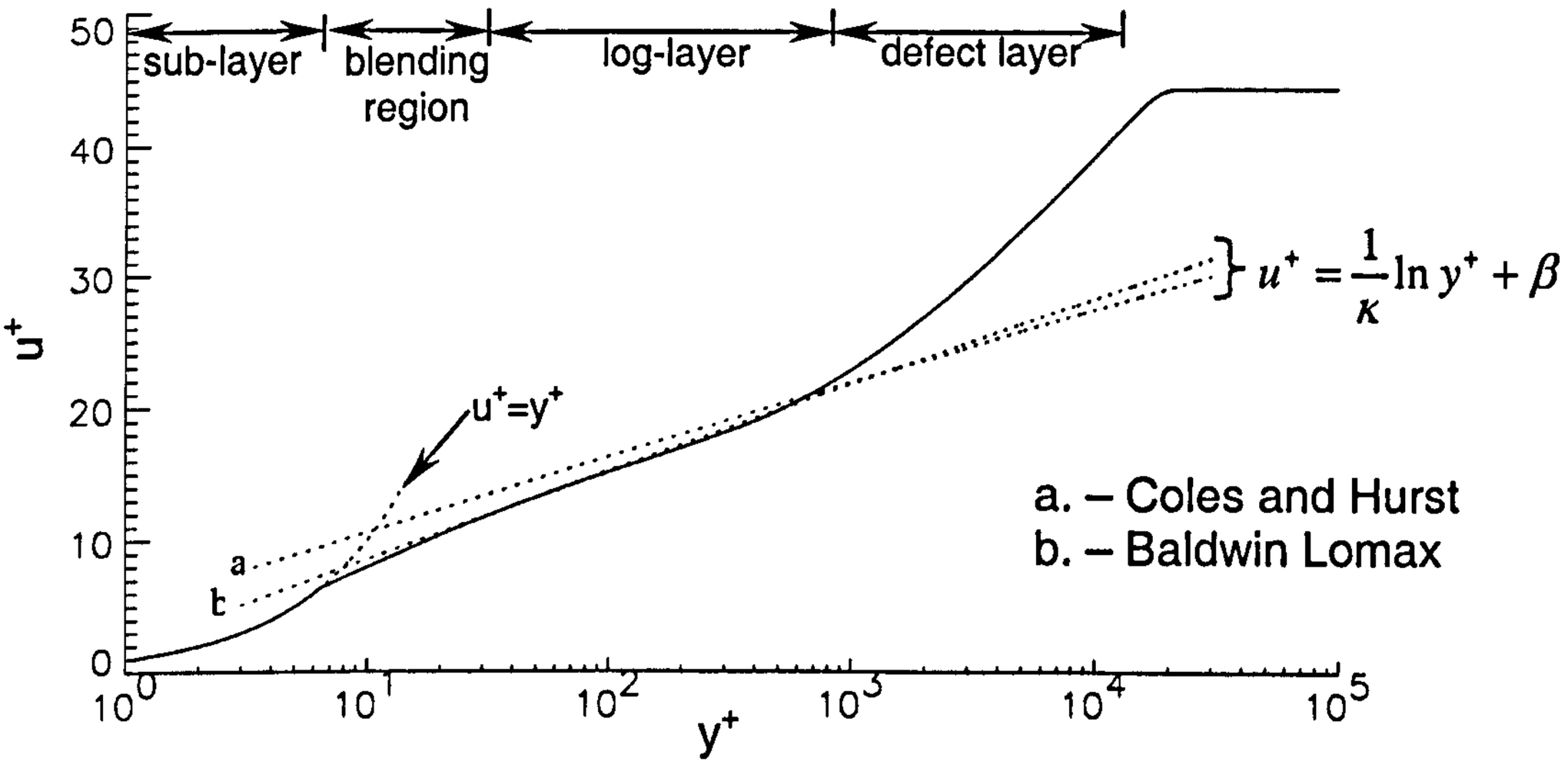

Figure 3.7. Baldwin-Lomax Boundary Layer Structure

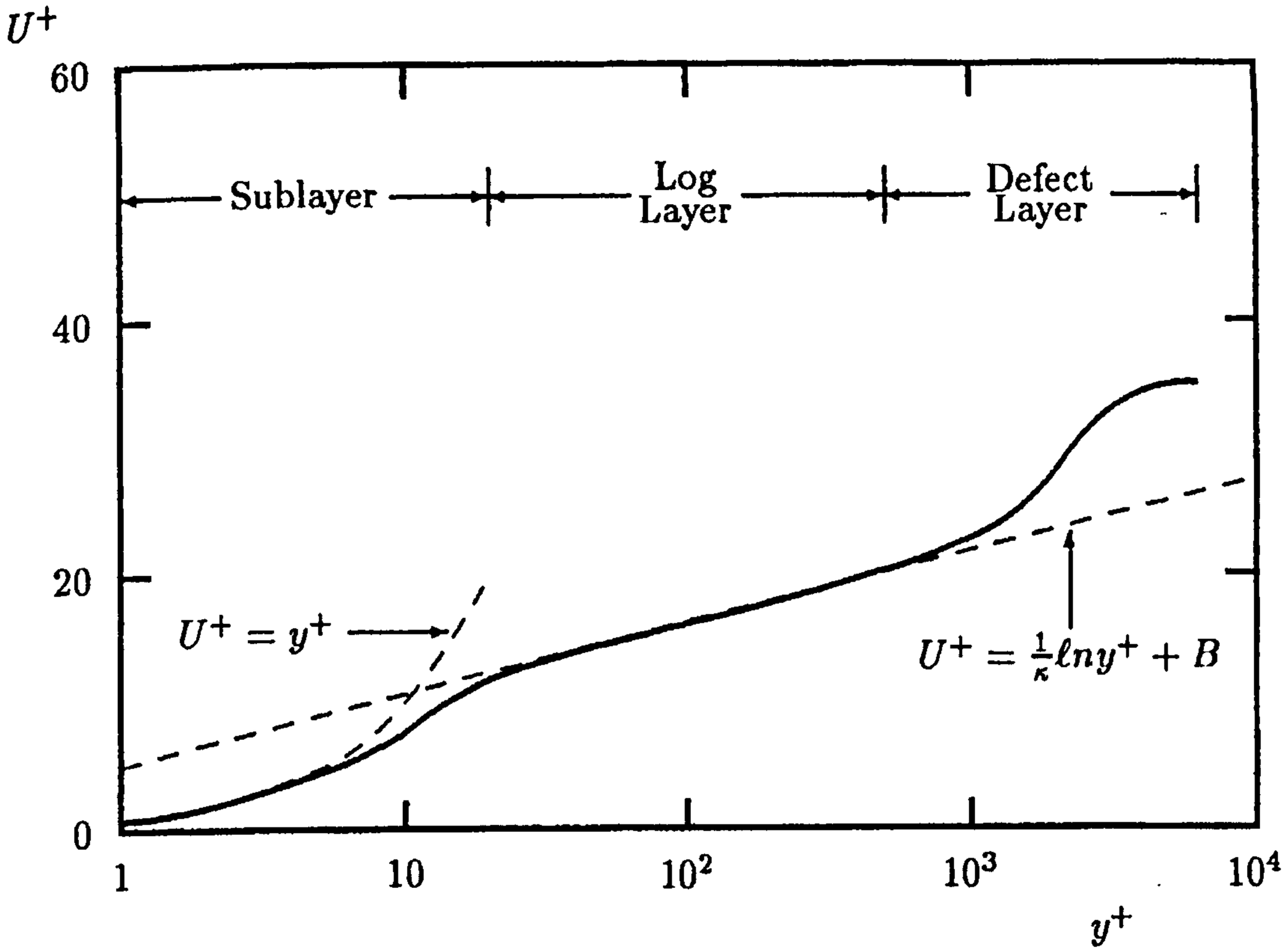

Figure 3.8. Velocity Profile Through a Typical Turbulent Boundary Layer [30]

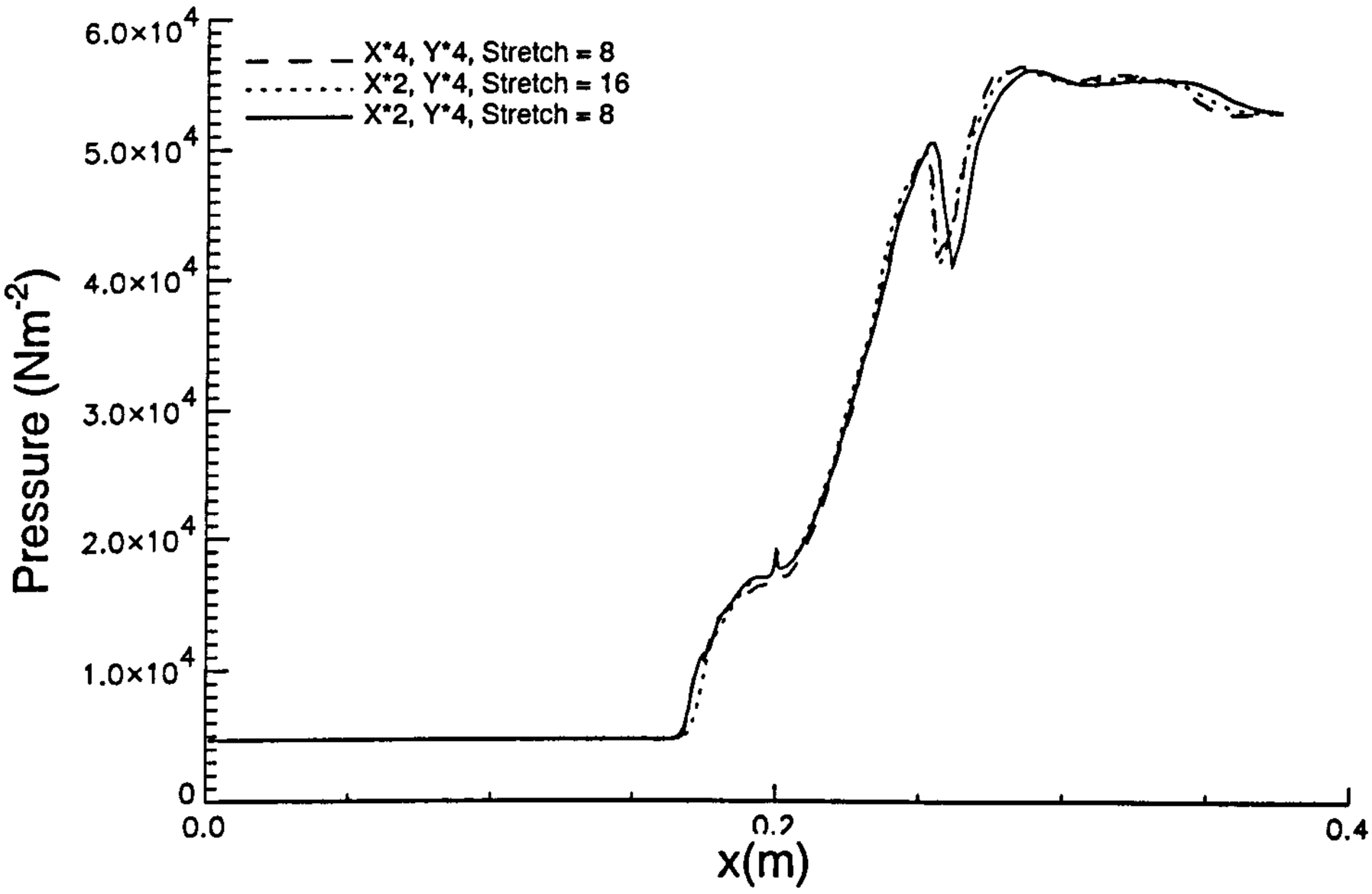

Figure 3.9. Mesh Convergence Plot – Surface Pressure – Mach 5 28° Ramp Flow

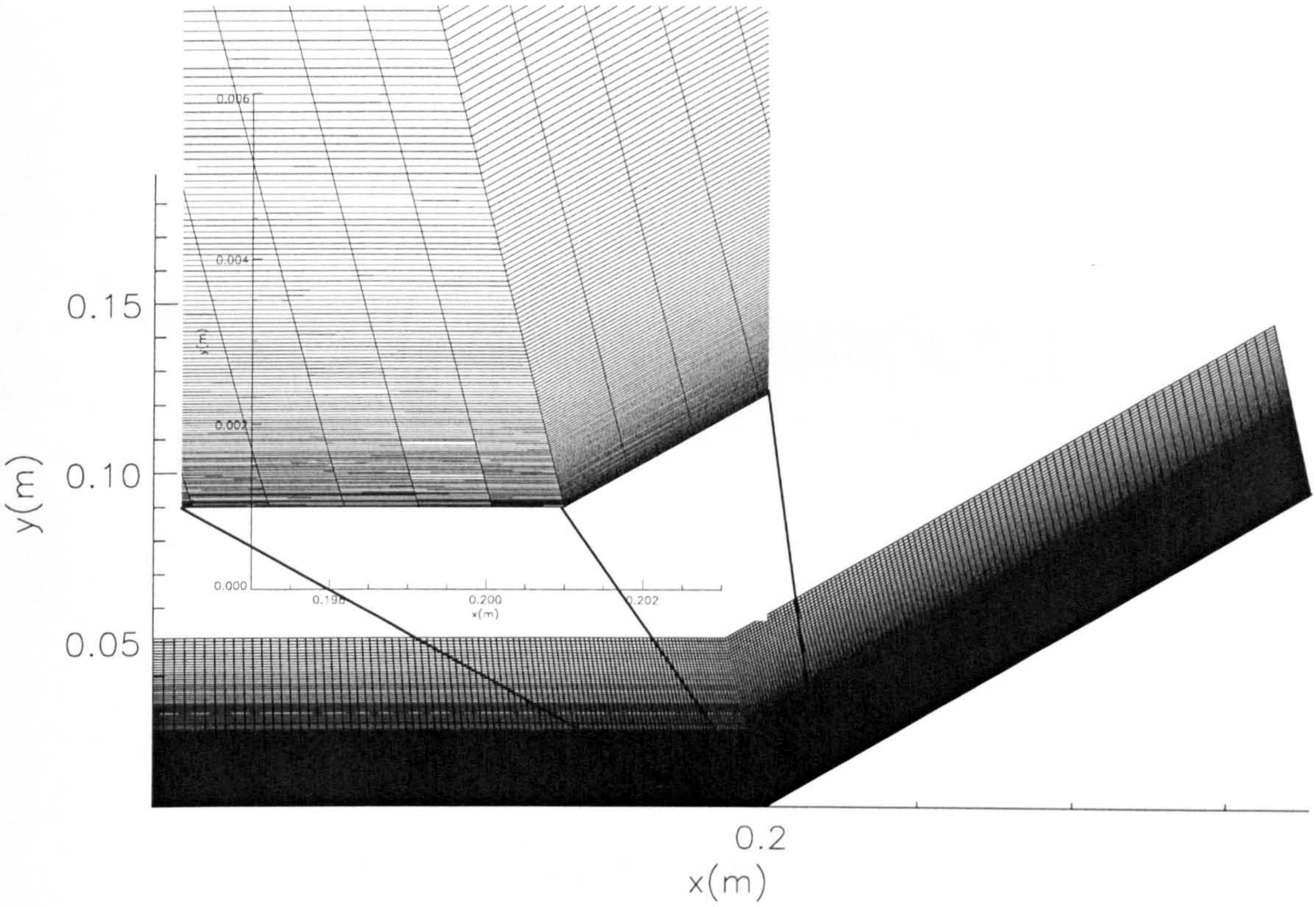

Figure 3.10. Computational Mesh

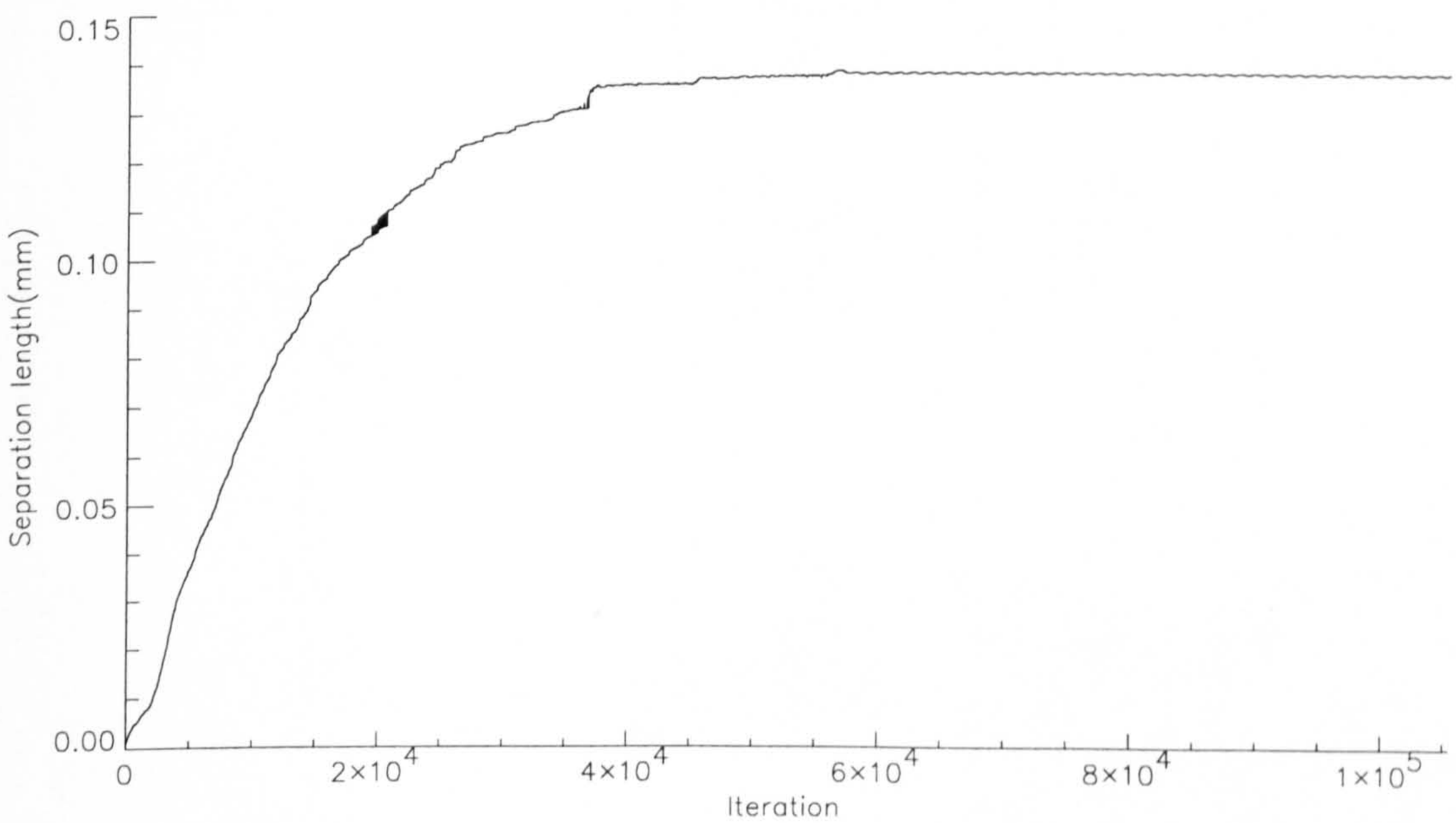

Figure 3.11. Separation Length Variation With Iteration

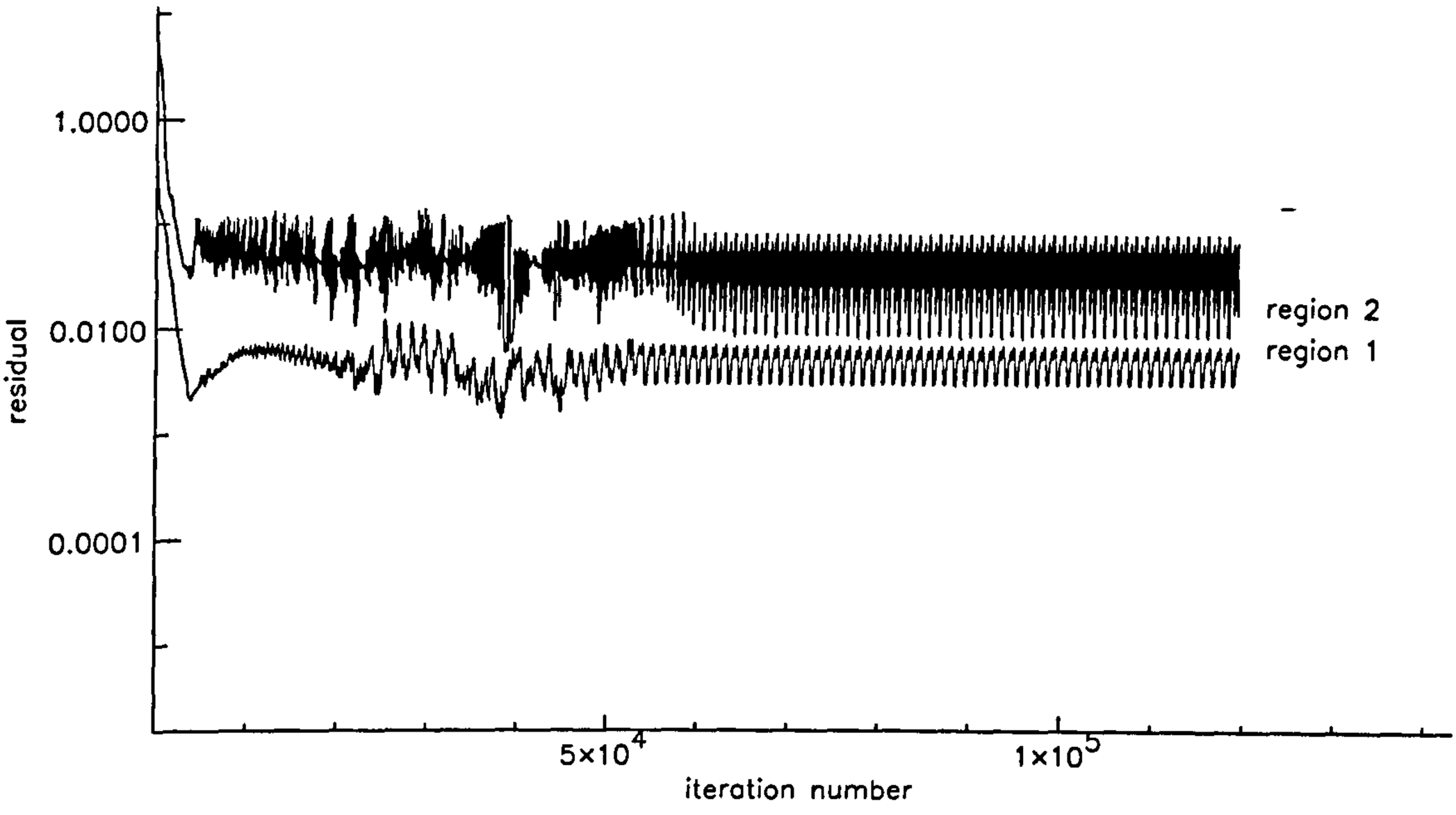

Figure 3.12. Residual Plot - Mach 5, 28° Ramp

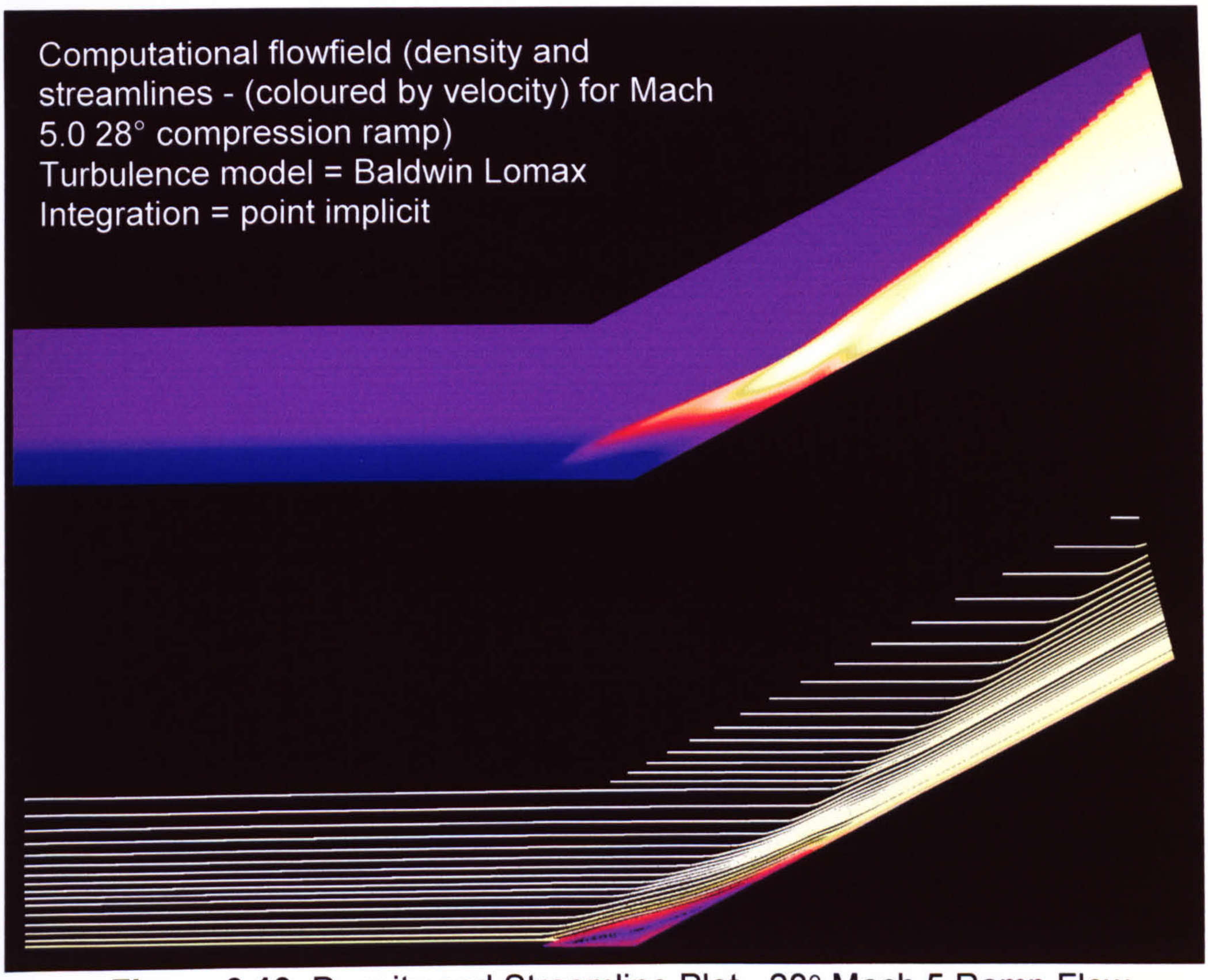

Figure 3.13. Density and Streamline Plot - 28° Mach 5 Ramp Flow

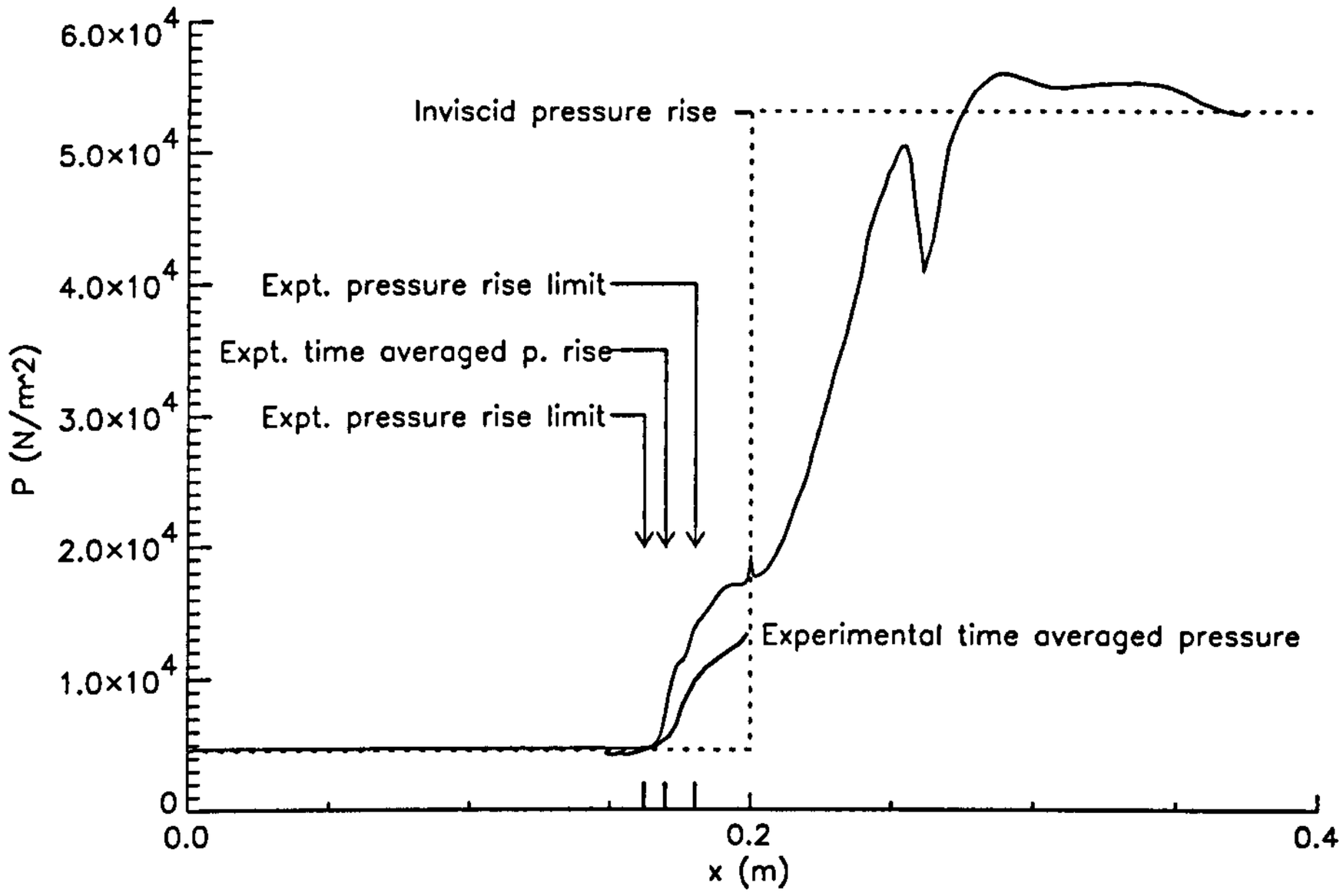

Figure 3.14. Experimental and Computational Surface Pressure Distributions

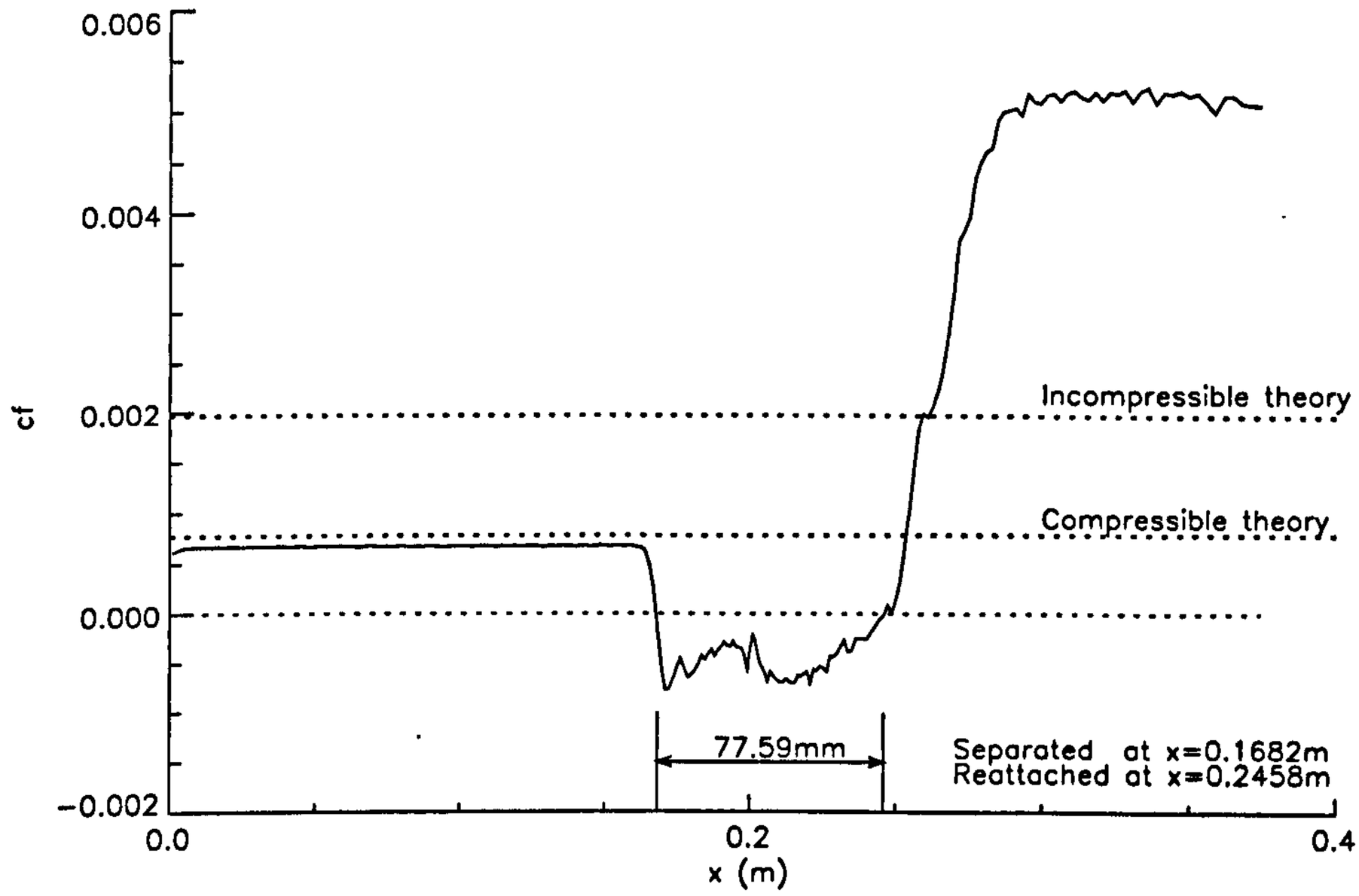

Figure 3.15. Computational Skin Friction Coefficient Distribution [58].

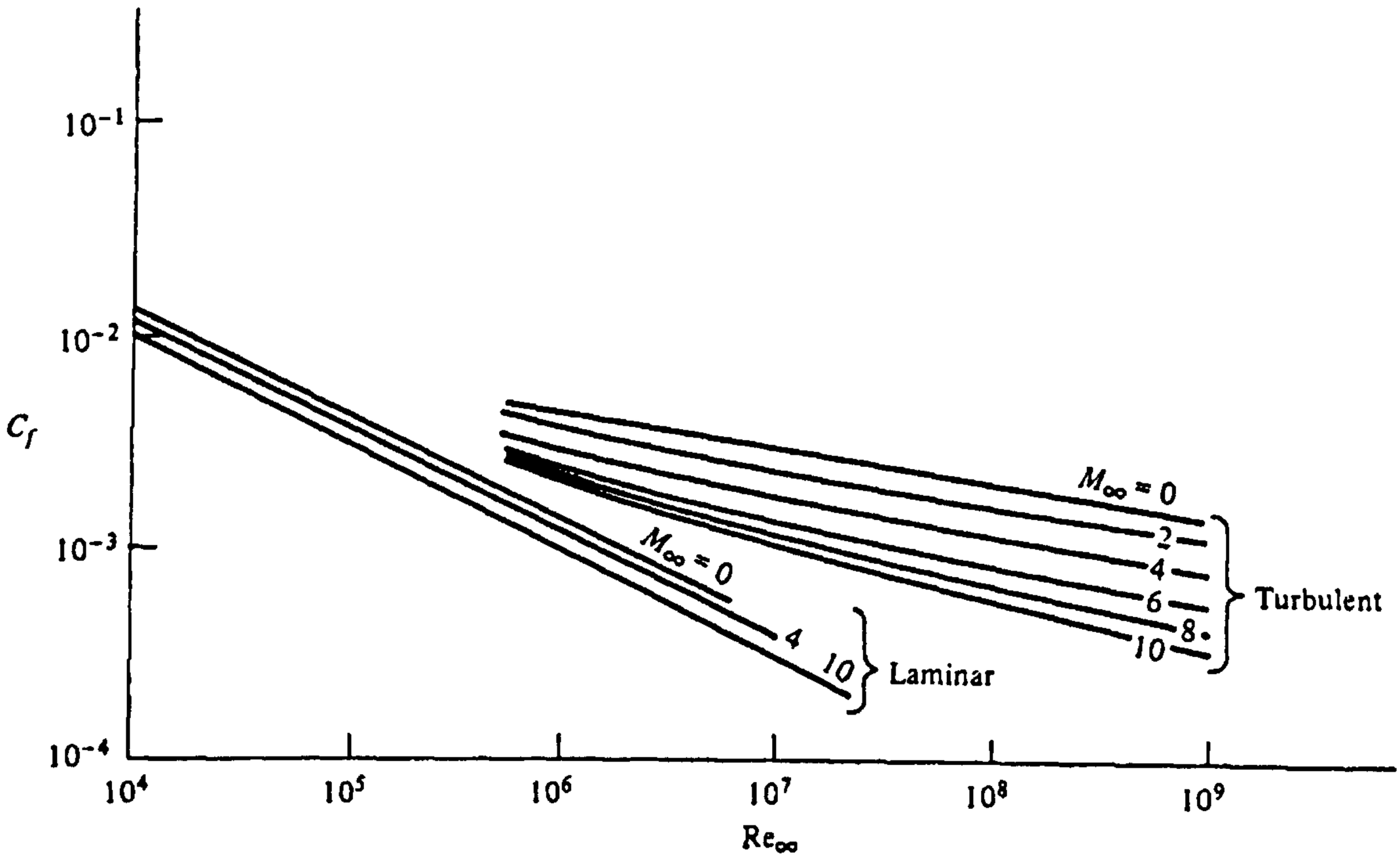

Figure 3.16. Flat Plate Skin Friction Coefficient Variation with Reynolds Number [160]

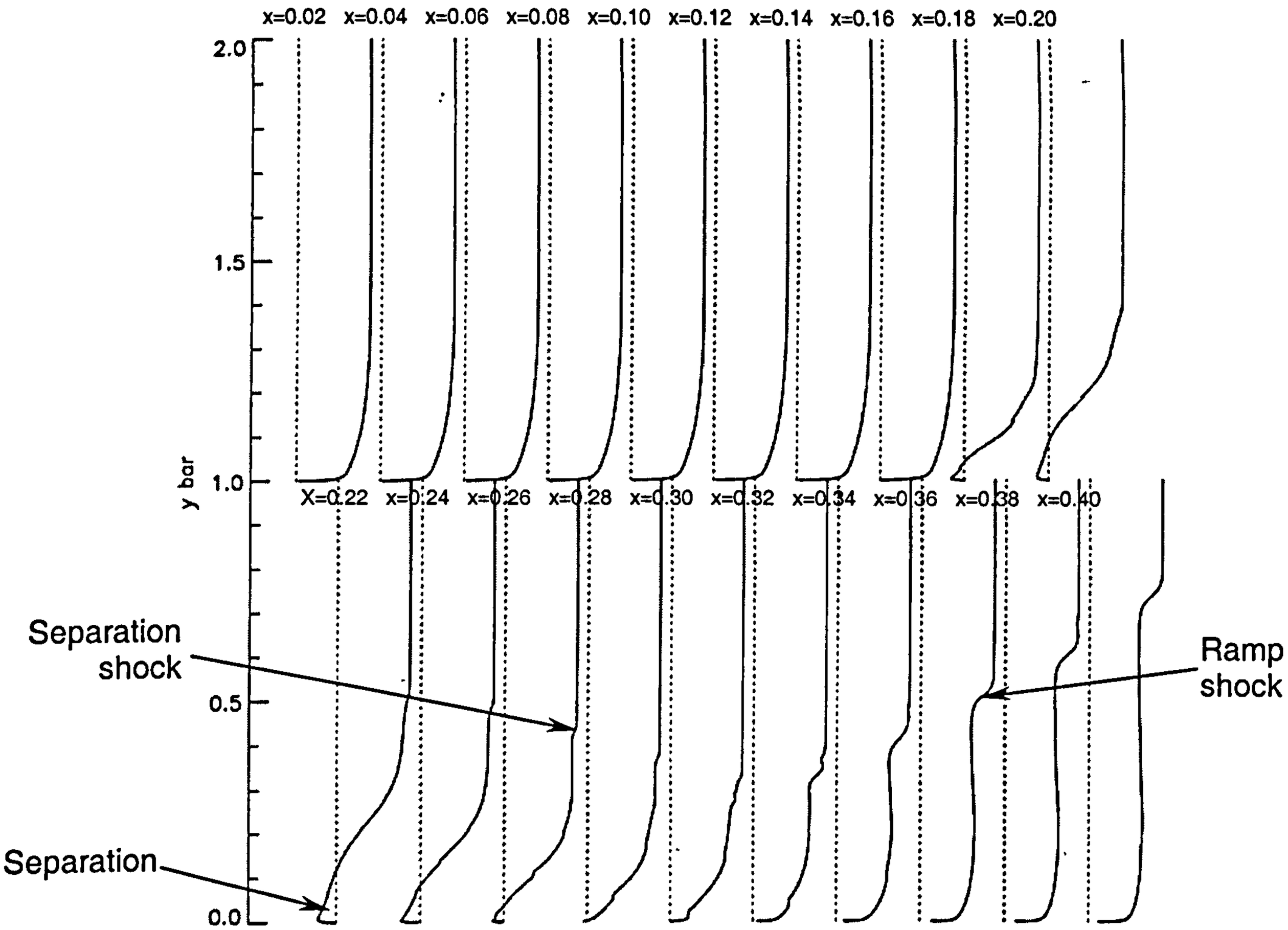

Figure 3.17. Velocity Profiles Through the Shock Boundary Layer Interaction

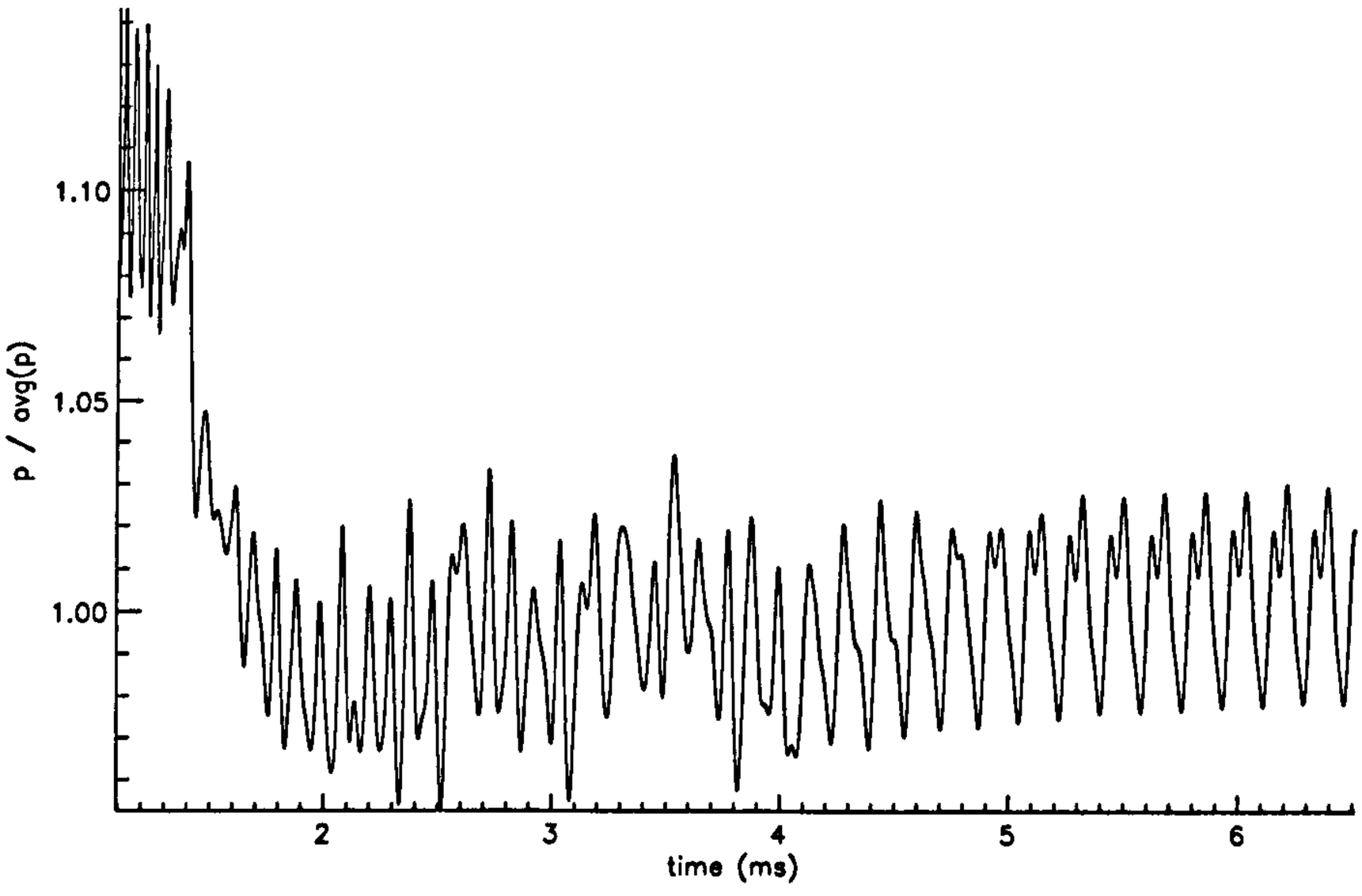

Figure 3.18. Surface Pressure Fluctuations at the Hingeline

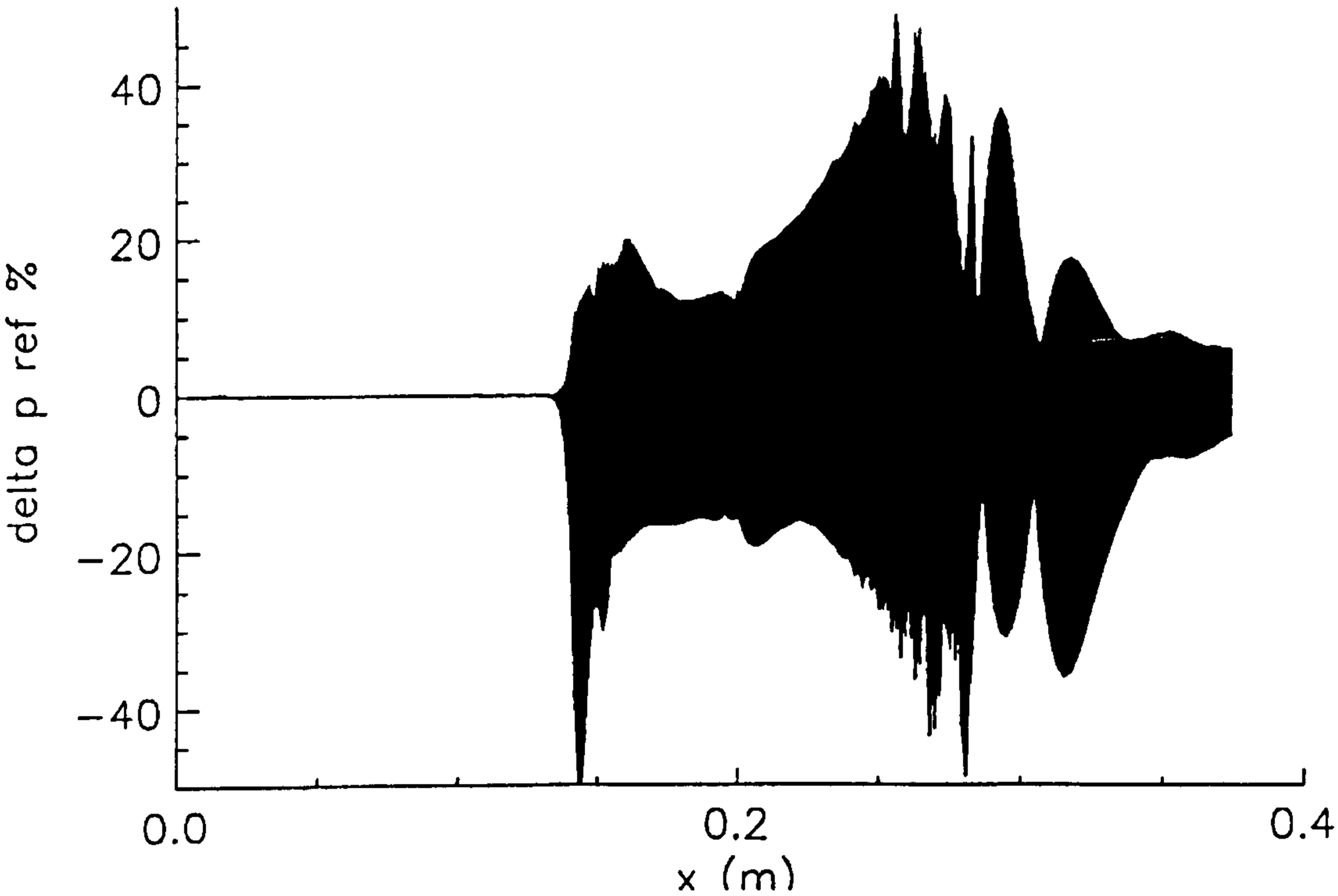

Figure 3.19. Surface Pressure Distribution Fluctuations

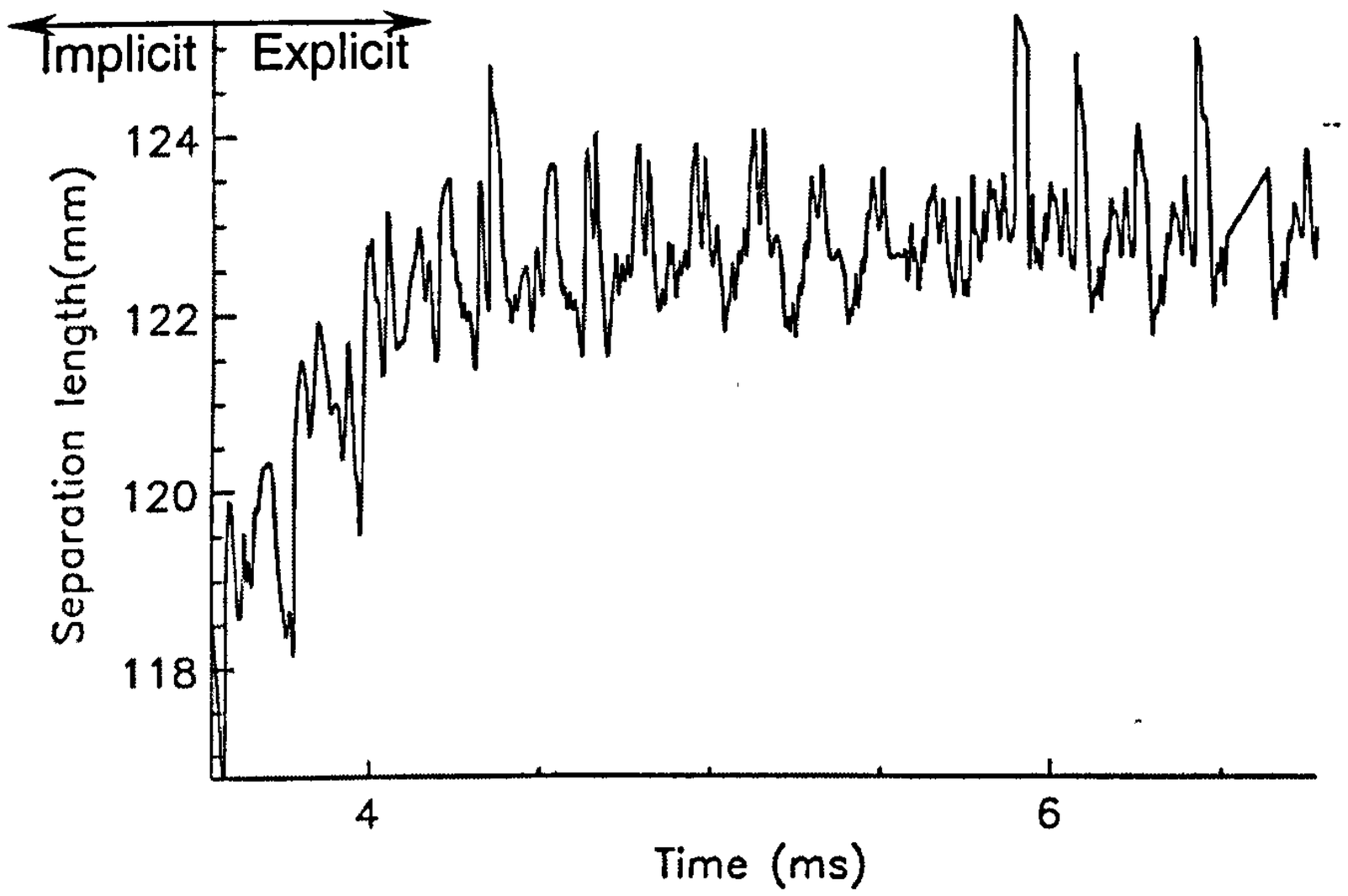

Figure 3.20. Variation in Separated Length With Time

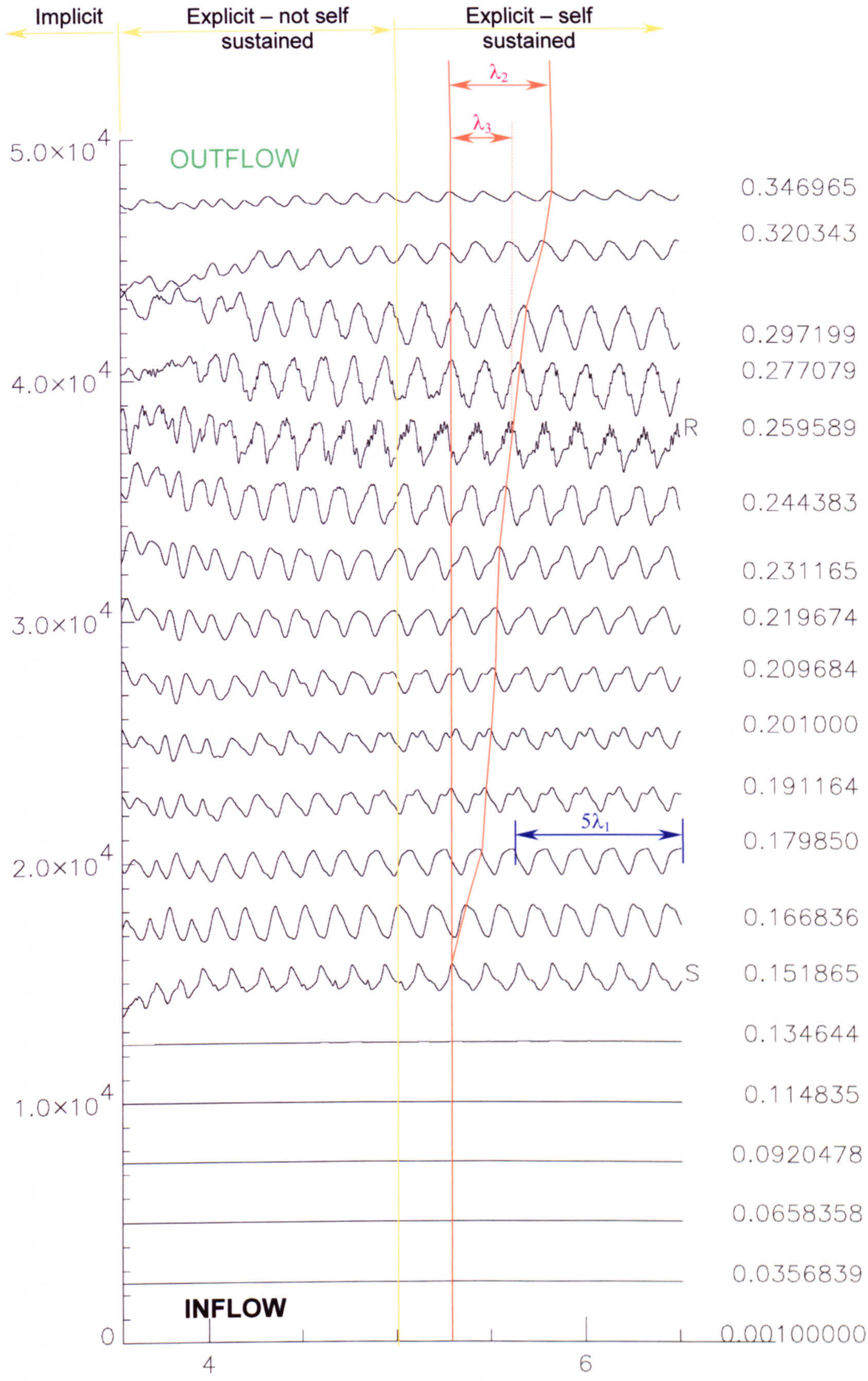

Figure 3.21. Surface Pressure Histories Along The Flat Plate and Flap

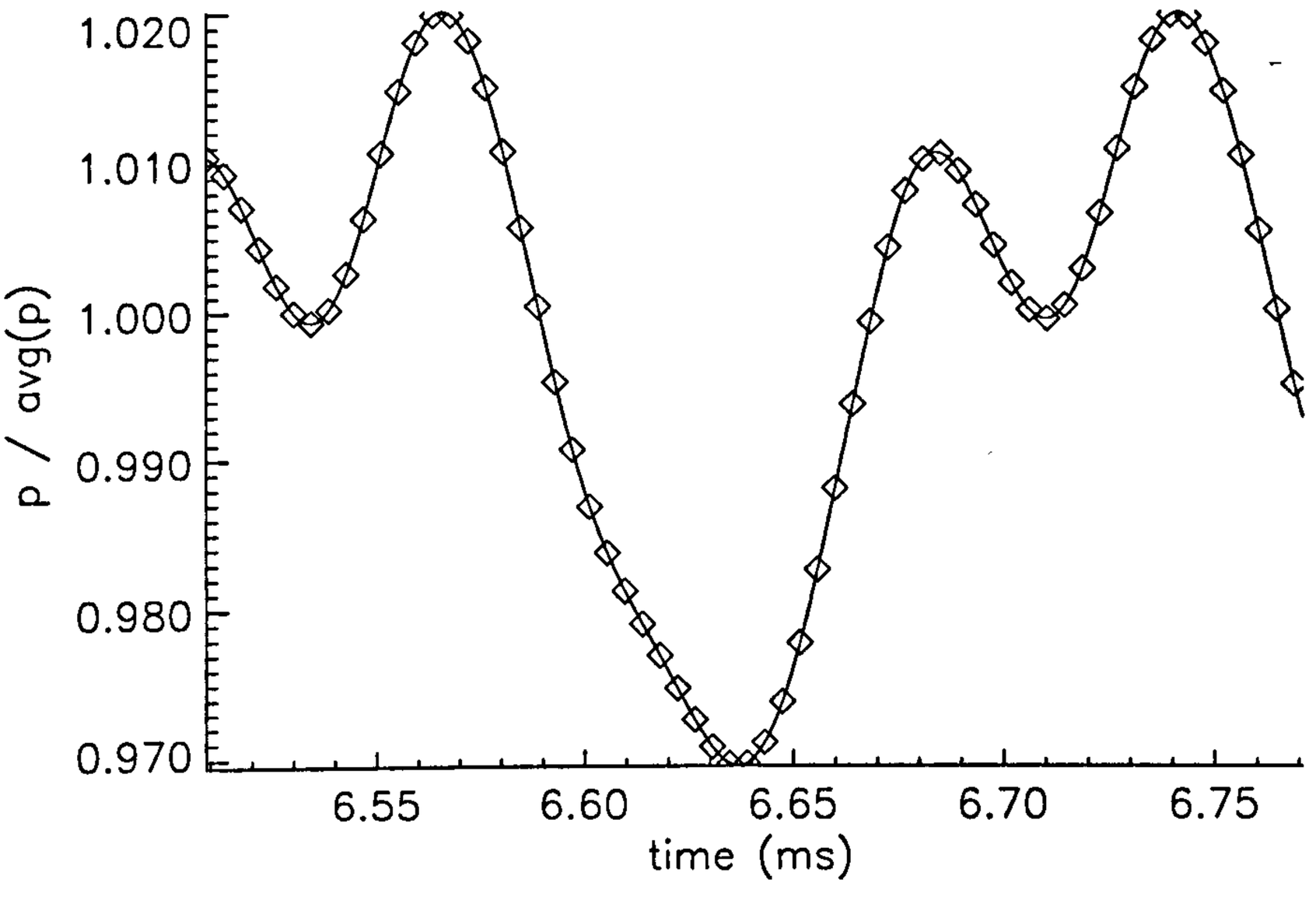

Figure 3.22. Computational Flowfield Sampling Times

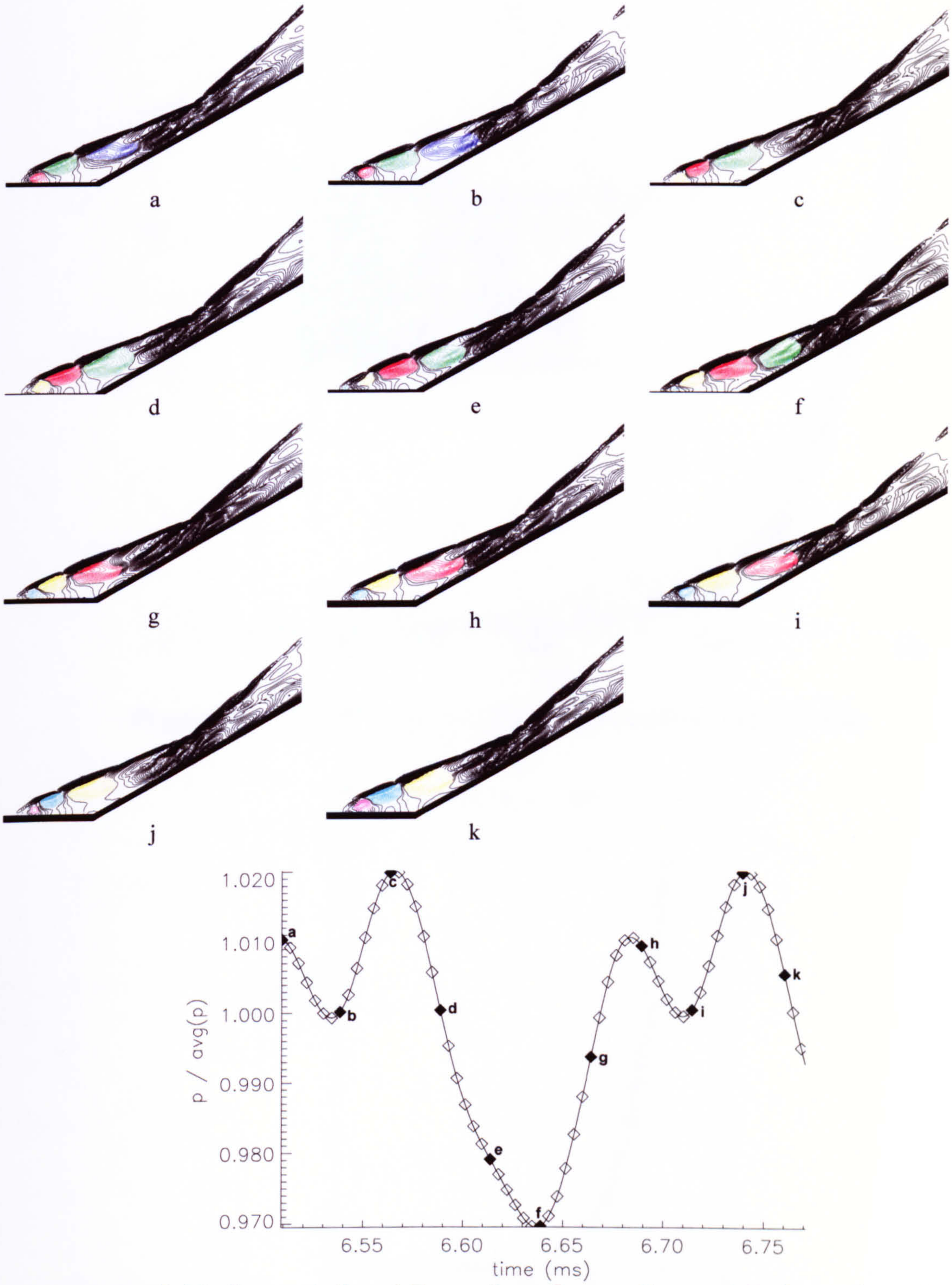

Figure 3.23. Computational Formation, Convection and Deformation of Flow Structures (Density Contours)

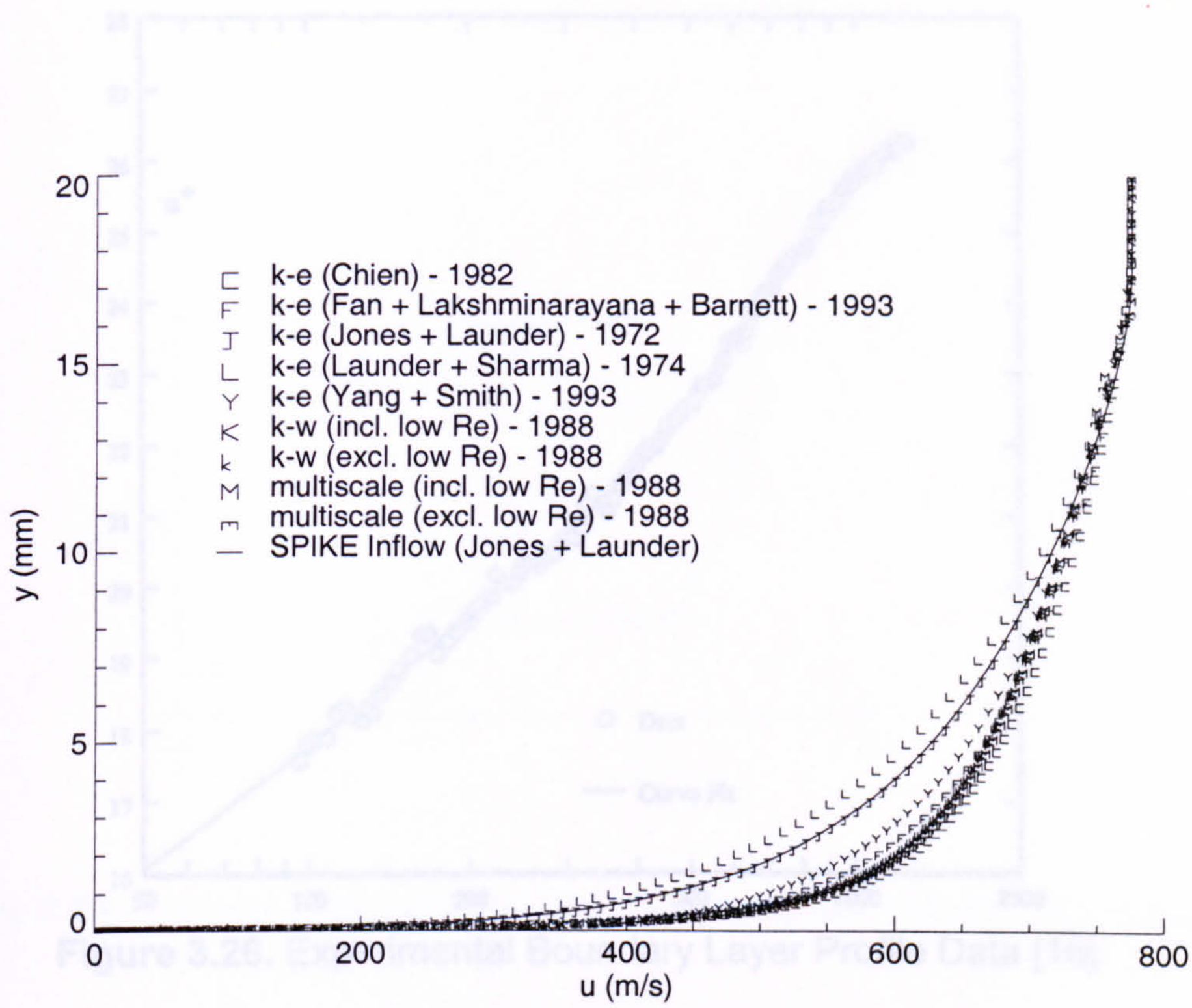

Figure 3.24. k-ε, k-ω and Multiscale Boundary Layer Profiles

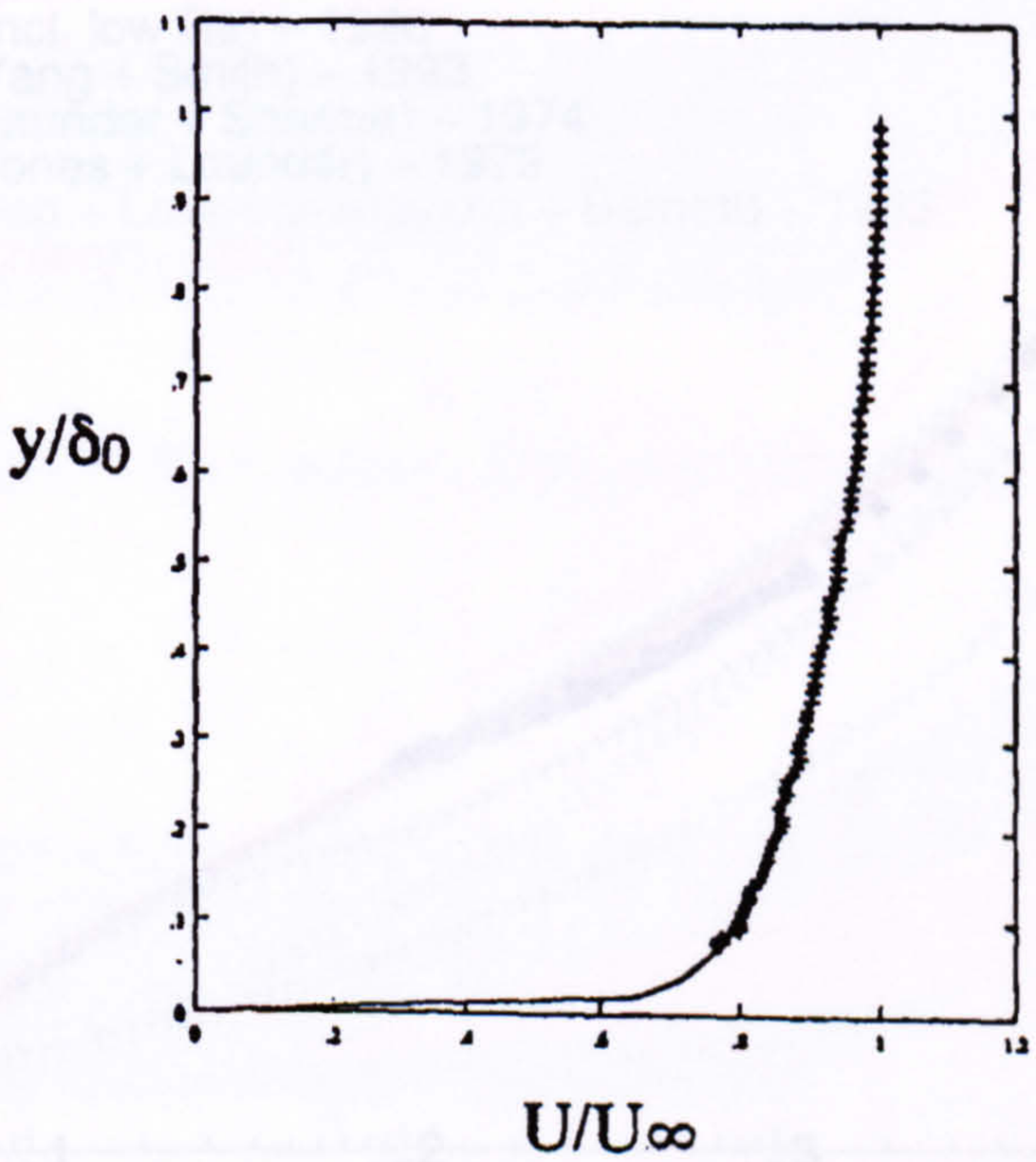

Figure 3.25. Experimental Boundary Layer Profile Data [16]

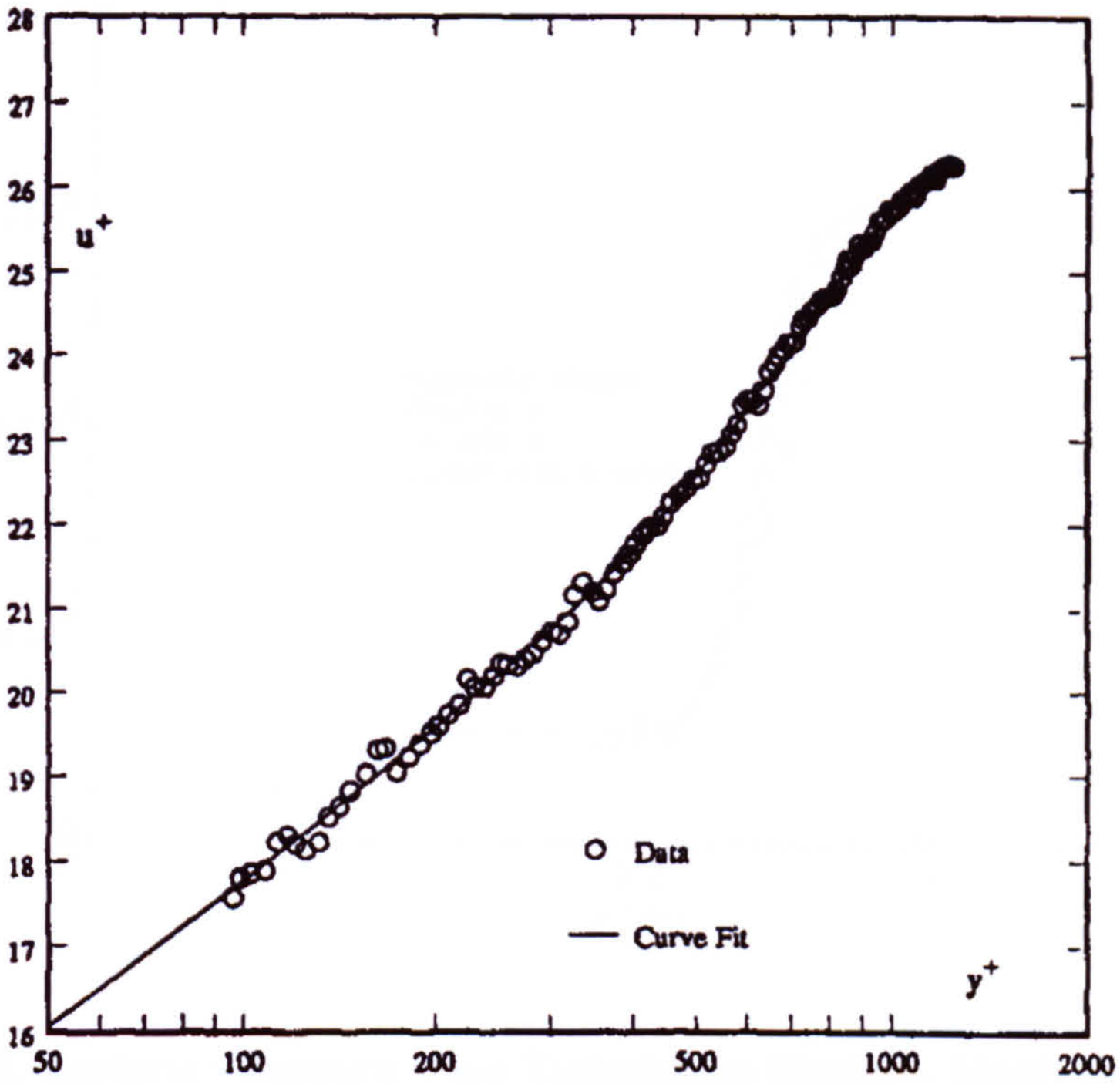

Figure 3.26. Experimental Boundary Layer Profile Data [16]

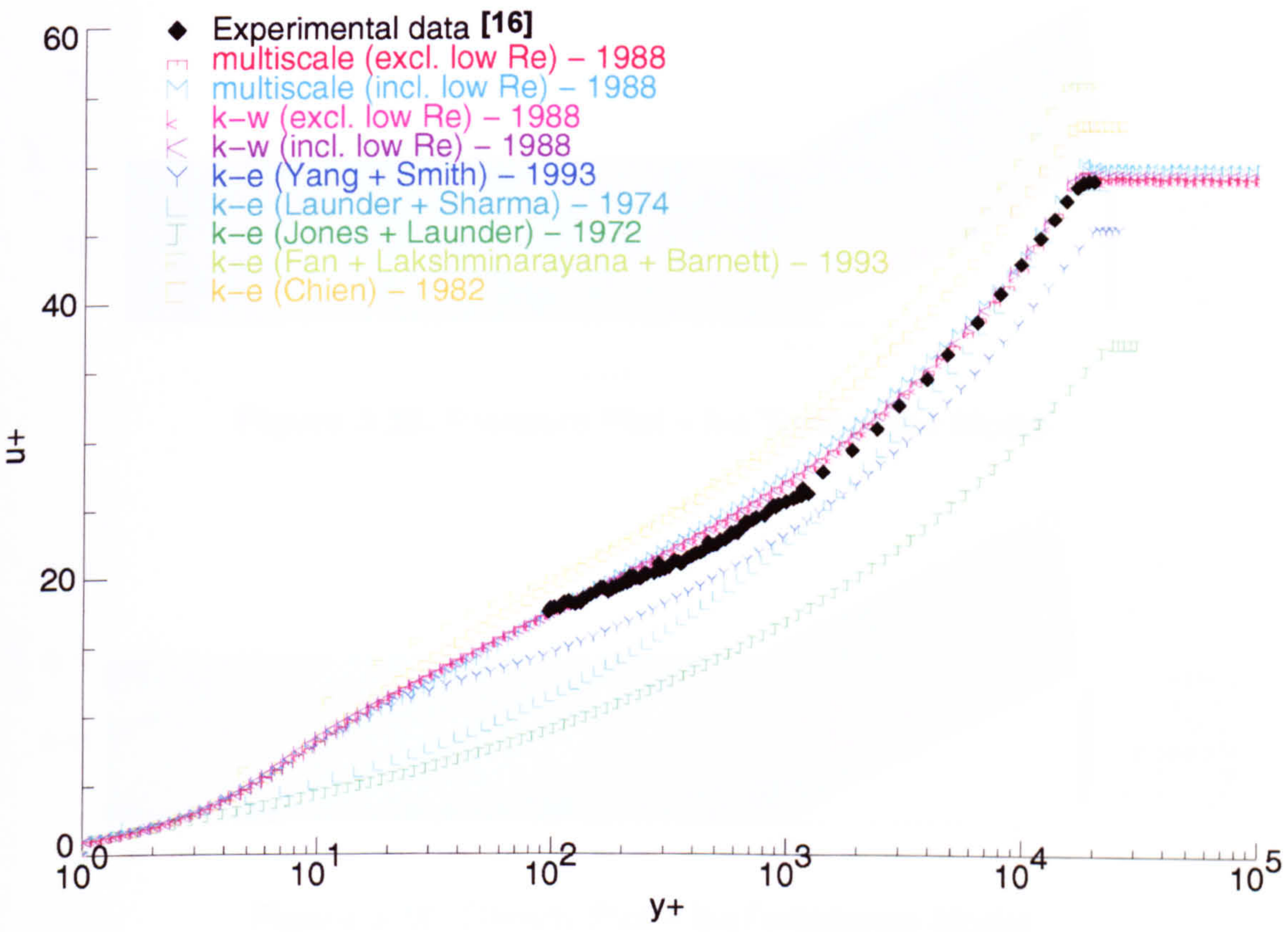

Figure 3.27. Experimental, k-ε, k-ω and Multiscale Boundary Layer Profiles

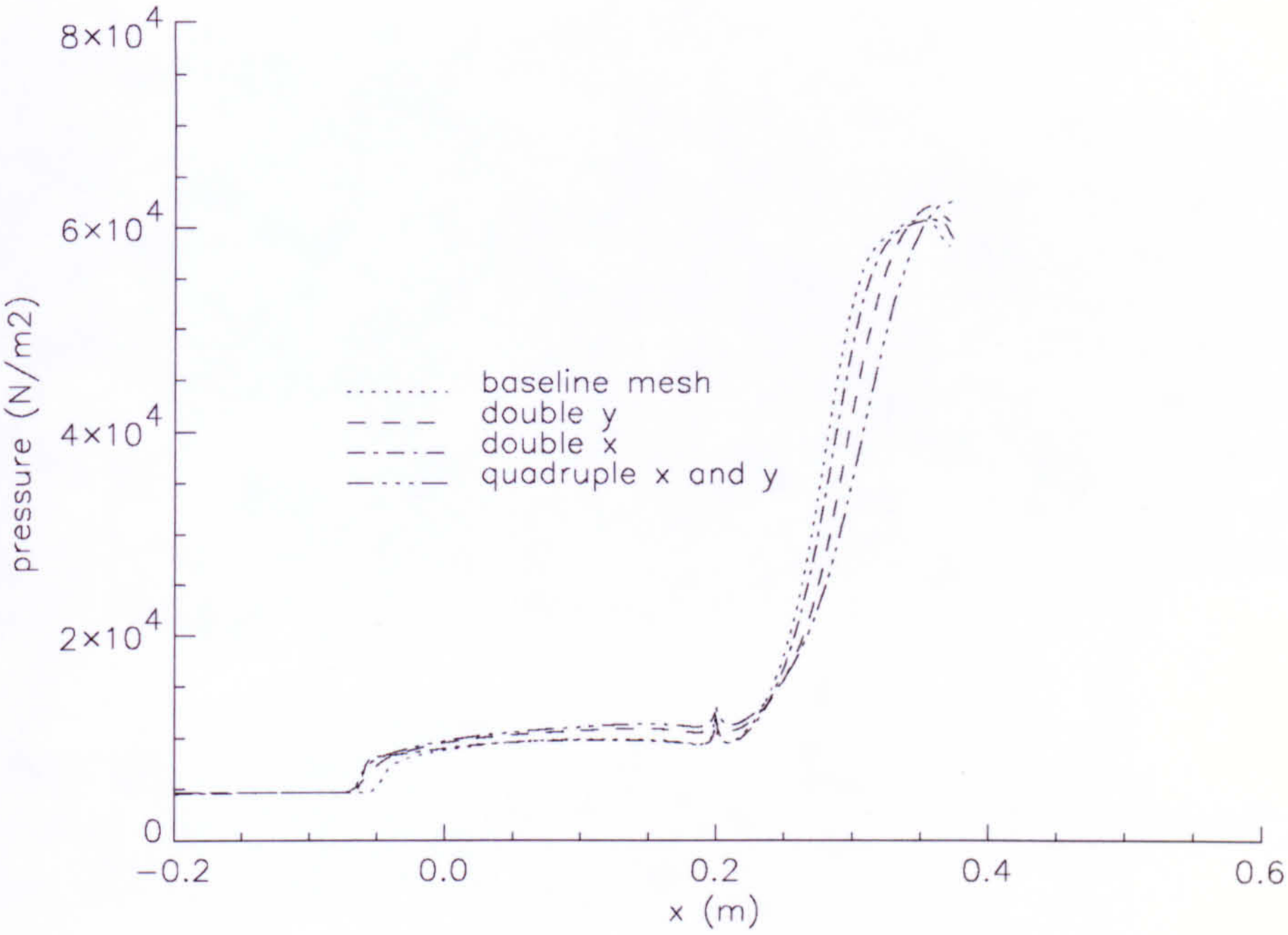

Figure 3.28. Surface Pressure – k-ε Turbulence Model – Mesh Convergence

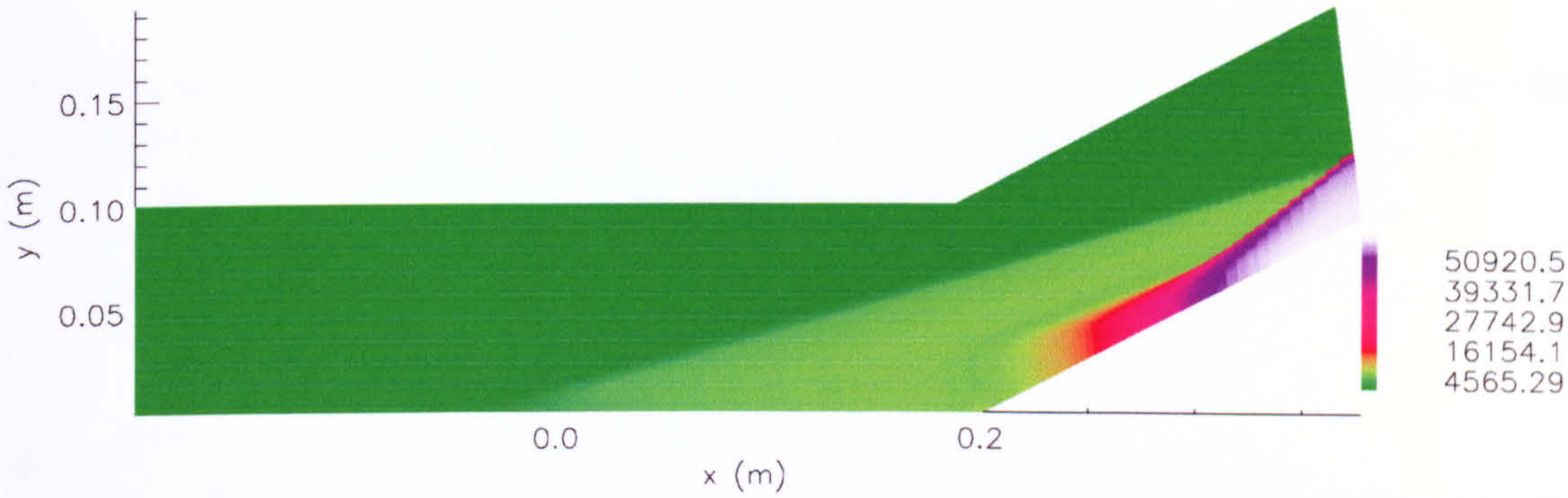

Figure 3.29. Pressure Plot – k-ε Turbulence Model

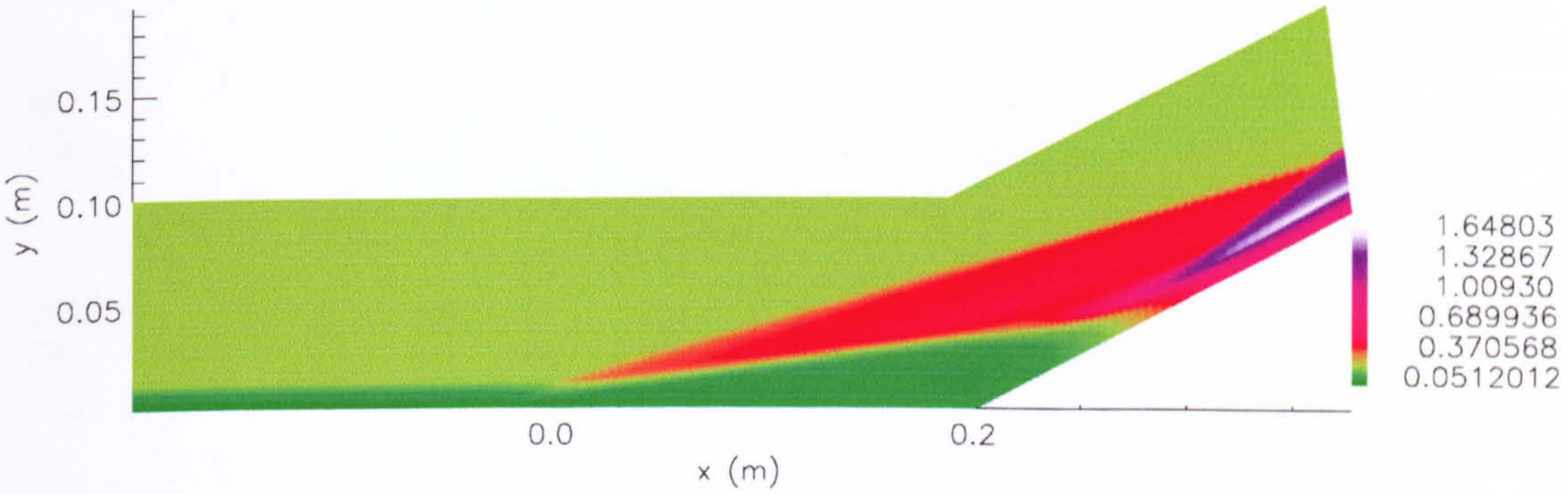

Figure 3.30. Density Plot – k-εTurbulence Model

4. Dynamically Deployed Flap Flows

Kuehn [6][7] discovered that for slowly varying ramp angles there was no evidence of hysteresis, and moreover, the instantaneous flowfield for a specific dynamic ramp angle was identical to its steady state counterpart. This only holds for relatively slowly moving ramps i.e. where the flowfield is quasi-steady. It has been shown that for 'rapidly' moving flaps this is not necessarily the case[117]. Smith [67] showed that for very rapidly deployed flaps the flow is no longer quasi-steady and that additional unsteady shock boundary layer interactions must be occurring. Smith [67] used flow conditions and ramp angles that for the steady state cases produced no unsteady phenomena.

4.1 Problem Description

A schematic of the configuration used by Smith [67] is presented in Figure 4.1. The flow conditions were:

$M_\infty=6.85$
$Re_\infty=2.45\times10^6 m^{-1}$
$P_0=551600 Nm^{-2}$
$T_\infty=58.74°K$

For these flow conditions, incipient separation would be expected for flow deflection angles of 5° for a purely laminar flow (Figure 4.2)[142].

$\mathrm{Re}_L \approx 4\times10^5$, so from Figure 4.2,

$$\frac{\beta_{incip}}{\sqrt{M_\infty}} \approx 2 \Rightarrow \beta_{incip} \approx 2\sqrt{6.85} \approx 5^o .$$

4.2 DRAMR

Both static and dynamic computations were undertaken with DRAMR[70]. DRAMR is an adaptive mesh refinement code developed for optimal computational efficiency, generality and feature resolution. DRAMR may be run in either finite volume or operator split modes (both were examined here and it appears that operator split gives identical results to finite volume), however finite volume computations were undertaken throughout lest operator split should prove inapplicable to these flows, boundary conditions and/or turbulence model implementation. A Roe based Reimann solver was used with a Harten entropy fix. Adaptive mesh refinement (AMR) [68][69] is particularly effective for the resolution of moving shock waves e.g. blast problems, intermediate and exterior ballistics, etc. For this class of problem, conventional meshing techniques either involve massive computational overheads (due to excessive resolution) or produce poor quality results (due to lack of refinement of the shock wave). DRAMR offers a framework within which a range of algorithms can be applied to a wide range of problems on

the basis of their specific merits for specific problems. DRAMR employs the AMR algorithm to solve systems of discretised partial differential equations with appropriate boundary conditions. The conventional version of DRAMR integrates these equations over body fitted structured meshes comprising quadrilateral cells. Adaption is performed using localised patches to create a grid hierarchy providing enhanced spatial accuracy when and where required (as determined by user determined criteria) (illustrated in Figure 4.3). DRAMR currently solves the Navier-Stokes and Euler equations either two dimensionally or axisymmetrically employing AMR to produce solutions with significantly increased spatial resolution with minimal increase in computational cost.

Throughout DRAMR the following non-dimensionalisation is employed to provide enhanced numerical accuracy[69]

$$\bar{x} = \frac{x}{L}, \bar{y} = \frac{y}{L}, \bar{u} = \frac{u}{u_\infty}, \bar{v} = \frac{v}{u_\infty}, \bar{\rho} = \frac{\rho}{\rho_\infty}, \bar{E}_t = \frac{E_t}{\rho_\infty u_\infty^2}, \bar{p} = \frac{p}{\rho_\infty u_\infty^2}$$

Where L is the reference length used in the definition of Reynolds number i.e. by setting L=1m the normalised lengths are physical lengths and the Reynolds number is the unit Reynolds number.

4.3 Adaptive Body Capture

This sections details an approach which exploits the automatic grid formation associated with AMR to capture arbitrary bodies and facilitate their motion. Due to the complexities of assessing mesh convergence within an adaptive meshing environment, for the majority of the cases presented here, automatic mesh refinement on the basis of flowfield parameters was disabled. The complexities of ensuring mesh sufficiency in an adaptive environment are discussed in §4.4.

4.3.1 Background.

Numerical solutions of the Navier-Stokes equations are widely used to predict viscous flows around arbitrary geometries. It has only recently become possible to compute dynamic flowfields around moving/shape changing configurations (e.g. bodies undergoing ablation, sabot separation, etc.). For the efficient computation of such flowfields two significant problems need surmounting. The first relates to the body motion itself, which requires body fitted grids to be re-meshed as the body moves, which is often prohibitively expensive. The second difficulty relates to the production of an optimally refined three-dimensional grid although various techniques are available to minimise the overheads incumbent in over-refinement.

In the interests of solution accuracy and the ability to more accurately compute turbulent flows, only structured (or locally structured) quadrilateral techniques were considered (and only those with potential for extension into three-space).

With DRAMR, Navier-Stokes computations are typically obtained with body

fitted grids [70][62][71] whereby the mesh is 'wrapped' around the body, with baseline mesh refinement based on a-priori knowledge of the flowfield (for example, the presence of shear layers) (an example of a body fitted grid is given in Figure 4.4).

In contrast a cartesian mesh is one in which the bodies are merely overlaid on an underlying grid and the boundary conditions modified to account for non-quadrilateral/hexahedral cells at the body surface (an example is given in Figure 4.5) [72][73][74][75][76]

There are merits and problems with each of these approaches, and are given in Table 4.1.

Graphical representation of the extension of these schemes for moving bodies is given in Figures 4.6 and 4.7. Both of these schemes present difficulties when extended to accommodate moving bodies:

Body fitted grids:	Remeshing at every iteration is computationally expensive, Unless the envelope of motion is small user intervention will be required to prevent highly stretched and/or skewed or corrupt meshes being produced.
Cartesian grids:	Remeshing is computationally inexpensive, The scheme needs to cater for cell creation and destruction as the body moves over the underlying grid.

Thus whilst body fitted grids are suitable for stationary body flows, their applicability to moving body flows is somewhat limited.

To circumvent some of these difficulties the concept of the Chimera grid emerged whereby two or more grids are overset: a rotating/translating body fitted grid for the near-body flow and a stationary underlying cartesian grid [77][78][79][80]. While this avoids many of the problems associated with body fitted grids (whilst retaining their obvious merits), other difficulties arise. These include difficulties with shape change for example, ablation and flap deployment, for which the body fitted grid will require remeshing as the surface deforms (as with body fitted grid motions), and for multibody interactions for example, sabot discard and stores release, where the overset grids are likely to impinge on one another (e.g. for a four petal sabot, six grids are used in the same physical space – one for each petal, one for the projectile and one for the background grid). The Chimera grid algorithms require free cells around each separate body, which presents difficulties for a multiple body configuration such as that illustrated in Figure 4.5 (none of the bodies can be in contact and hence small gaps must be artificially introduced between each of the sabot petals and the projectile).

In the interests of maintaining complete generality, the approach adopted here is to employ an underlying grid, with the body imposed as a set of local boundary conditions. To accurately capture the flow physics and arbitrary body geometries, hierarchical grid adaption of the form employed by DRAMR is adopted.

4.3.2 Capturing an Arbitrary Surface Geometry.

For the scheme to be truly arbitrary no assumptions can made regarding the geometry of the body to be meshed. For the code to be efficient, unnecessarily small cells are to be avoided. This suggests the use of a coarse underlying grid in conjunction with extensive adaption, to capture the body geometry to within a specified accuracy. Achieving this within the existing DRAMR framework is simplified since the mechanisms for refinement are already in place. By flagging the appropriate cells for refinement, one may refine around the surface of an arbitrary body (or bodies), and hence the grid will describe the body surface. To determine where the surface of the body is, and hence which cells to refine, each cell must be assessed to determine whether it is completely within or completely without the body. Cells which are neither must necessarily straddle the body surface and are therefore marked for refinement.

Determining whether a point is inside or outside of a body is an important issue in terms of computational overhead, as discussed in the following section.

4.3.2.1 Interior, Exterior or Boundary analysis.

Various algorithms and techniques exist, which may be used to assess whether a point is within or without an arbitrary closed curve (in two dimensions these have traditionally been developed for 'flood fill' or scan-line conversion algorithms). Three of the most likely candidates were considered:

i The "parity rule" examines the number of lines crossed when drawing a line from the point of interest to a 'far distant point'. If the number of intersections with bodylines is odd, then the point is interior, if the number is even then the point is exterior. Points on the boundary obviously require special consideration. In the context of this technique, 'a far distant point' can be a convenient geometric point outside of the computational domain. Great care must be taken not to intersect body vertices – for example, by using multiple far distant points.

ii The "non-exterior rule" examines every possible pair of points in the domain. A line is drawn between every pair of points in the domain and if no intersections with any body line segments occur then both points are external.

iii The "non-exterior winding rule" uses an imaginary marker placed at the point of interest, attached to an imaginary length of string. The free end of the string is used to trace a complete circuit of the body and if the string has not wound around the marker then the point is external (this is illustrated schematically in Figure 4.8).

Of the three algorithms described above (iii) is the most applicable to the class of problem examined here and shows the greatest scope for optimisation.

Coding the non-exterior winding rule requires a deal of care when considering its application to a body comprised of a finite number of vertices and straight-line segments, instead of an analytical surface. The first consideration is the maximum possible angular increment or decrement that can occur when travelling between two consecutive body points (in the context of the angular step induced by the non-general solution to the inverse trigonometric functions).

If the maximum increment or decrement to the winding angle is given by $\Delta\alpha_{MAX}$, then this corresponds to a point very close to a bodyline segment whose vertices are very far away (illustrated in Figure 4.9). It is apparent from Figure 4.9 that unless the point of interest is on the line segment (excluded by precondition) then for three points within a finitely large domain, the maximum angular increment is always less than π. Due to the harmonic nature of trigonometric functions, general solutions to a trigonometric inverse contain multiples of 2π. It can therefore be concluded that for an arbitrary increment or decrement in winding angle, a magnitude of π or greater must stem from the general solution, with the true angular increment or decrement equal to 2π minus the apparent increment/decrement. In this way, with care, a winding register can be kept to record the number of entire revolutions of the winding angle, and hence the change in winding angle produced by an entire traversal of the body surface may be quantified in quadrant terms rather than angular terms, thus avoiding computationally expensive trigonometric inversions.

The winding algorithm is coded thus:

The body surface must be closed, with vertices in $\underline{bx}$ and $\underline{by}$.

Firstly a bounding box is checked:

$$\left\{\min(\underline{bx}) \geq \underline{x}_p \geq \max(\underline{bx})\right\}, \left\{\min(\underline{by}) \geq \underline{y}_p \geq \max(\underline{by})\right\} \Rightarrow \textit{exterior}$$

Check whether or not the point is on the boundary subject to a small limit (ε):

$$\overline{\underline{dx}} = \overline{\underline{bx}} - x_p$$
$$\overline{\underline{dy}} = \overline{\underline{by}} - y_p$$
$$\overline{\underline{d^2}} = \overline{\underline{dx}}.\overline{\underline{dx}} + \overline{\underline{dy}}.\overline{\underline{dy}}$$
$$\min(\overline{\underline{d^2}}) \le \varepsilon \Rightarrow boundary$$

As discussed above, care must be taken with maximum angular increments in the context of winding. To this end, a new function *stan* was created as a specific tangent function with guaranteed domain and codomain. The winding algorithm is then: (with ϕ=number of laps, Φ=lap angle (=$2\phi\pi$), and α=current angle)

$$\phi = \Phi = 0, \alpha = \alpha' = s\tan^{-1}\left(\overline{\underline{y}}_p - \overline{\underline{by}}, \overline{\underline{x}}_p - \overline{\underline{bx}}_1\right)$$

for I=1,#$\overline{\underline{bx}}$

$$\overline{vx} = \overline{\underline{x}}_p - \overline{\underline{bx}}_i$$
$$\overline{vy} = \overline{\underline{y}}_p - \overline{\underline{by}}_i$$
$$\alpha = \Phi + s\tan^{-1}(\overline{vy}, \overline{vx})$$

Do not use ≥ for reasons of maximum increment

$$|\alpha - \alpha'| > \pi \Rightarrow \begin{cases} \alpha' > \alpha \Rightarrow \phi \to \phi + 1 \\ \alpha' < \alpha \Rightarrow \phi \to \phi - 1 \\ \Phi = 2\pi\phi \\ \alpha = \Phi + s\tan^{-1}(\overline{vy}, \overline{vx}) \end{cases}$$

$$\alpha' = \alpha$$

endfor

$$\Delta\alpha = |\alpha_0 - \alpha|$$

$\Delta\alpha > \pi \Rightarrow INSIDE$ Ideally, 0 and 2π are the only two possible values, but

$\Delta\alpha \le \pi \Rightarrow OUTSIDE$

using π as the threshold allows for significant numerical errors.

To ensure optimal accuracy the arctangents are in the required quadrant ($0 \le \text{stan}^{-1}(\Delta y, \Delta x) \le 2\pi$, $\forall\Delta y \forall\Delta x$), stan is defined as follows:

$$
\begin{aligned}
&function \quad s\tan(\Delta y, \Delta x)\\
&N = \Delta y\\
&D = \Delta x\\
&\left.\begin{aligned}
|N| < \varepsilon &\rightarrow \begin{cases} \Delta y = 0 \\ N = 0 \end{cases}\\
|D| < \varepsilon &\rightarrow \begin{cases} \Delta x = 0 \\ D = 0 \end{cases}
\end{aligned}\right\} \text{Force trips for problematically small numerators and/or denominators}\\
&\Delta x \Delta y = 0 \Rightarrow \left\{\begin{aligned}
\Delta x > 0 &\Rightarrow ANS = 0; RETURN\\
\Delta x < 0 &\Rightarrow ANS = \pi; RETURN\\
\Delta y > 0 &\Rightarrow ANS = \pi/2; RETURN\\
\Delta y < 0 &\Rightarrow ANS = 3\pi/2; RETURN
\end{aligned}\right\} \text{Trips for problematically small numerators and/or denominators}\\
&ANS = \pi/4\\
&\left.\begin{aligned}
N < D &\Rightarrow ANS = \tan^{-1}(N/D)\\
D < N &\Rightarrow ANS = \frac{\pi}{2} - \tan^{-1}(D/N)
\end{aligned}\right\} \text{Always divide by larger number for numerical accuracy}\\
&\left.\begin{aligned}
\Delta x > 0, \Delta y > 0 &\Rightarrow RETURN\\
\Delta x > 0, \Delta y < 0 &\Rightarrow ANS = 2\pi - ANS; RETURN\\
\Delta x < 0, \Delta y > 0 &\Rightarrow ANS = \pi - ANS; RETURN\\
\Delta x < 0, \Delta y < 0 &\Rightarrow ANS = \pi + ANS; RETURN
\end{aligned}\right\} \text{Place result in the correct quadrant}
\end{aligned}
$$

Adaption to recover the body surface is then simply:

$$
\begin{aligned}
&\underline{c} = INDEXgij(GRD, I + \underline{IV}_i, J + \underline{JV}_i), where \quad \underline{IV} = [0,1,1,0], \underline{JV} = [0,0,1,1]\\
&\underline{\overline{xc}} = \underline{\overline{x}}(\underline{c}), \quad \underline{\overline{yc}} = \underline{\overline{y}}(\underline{c})\\
&\underline{f}_c = wind(\underline{\overline{xc}}, \underline{\overline{yc}})\\
&v = and(\underline{f})\\
&v = INSIDE \Rightarrow refine(IJ) = 0\\
&v \neq INSIDE \;\&\&\; v \neq OUTSIDE \Rightarrow refine(IJ) = 1
\end{aligned}
$$

In this manner, straddling cells are automatically refined, interior cells are disabled from being refined (to conserve computational resources), and elsewhere adaption can occur of spatial gradients.

A few simple rules can be contrived which will decrease the computational overhead required to ascertain the status of every point. For example, if a bounding box is placed around the body then points exterior to the bounding box can be flagged as exterior to the body without recourse to the non-exterior winding rule.

The non-exterior winding rule can be greatly optimised by avoiding the

trigonometric inversions by examining the sign of Δx and Δy (where $(\Delta x,\Delta y)$ represents the vector from the point of interest to an arbitrary body vertex) and determining which quadrant the vector is in. Assessing winding on a quadrant basis is far less expensive than on an angular basis, although care must be taken with inter-quadrant boundaries.

When each vertex in the grid has been examined, each cell can be assigned a state (either inside, outside or boundary). There are sixteen types of valid cell as enumerated in Table 4.2 and illustrated in Figure 4.10 (boundaries excepted):

Care must be taken to avoid producing 'illegal' cells, for example cells G and J in Figure 4.10 and cells similar in nature to that illustrated in Figure 4.11.

Flagging all of the straddling cells for refinement, refining and repeating the entire process, allows for successive grid levels to be created, and thus the geometry to be captured to an arbitrary precision (this process is illustrated in Figure 4.12). Figure 4.12 shows an instance of the application of this technique in meshing a turbine compressor blade. There is potential for further optimisations through the nature of the hierarchical refinements, for example cells with exterior parents are necessarily exterior. Meshing bodies with 'sharp corners' will produce instances of an 'illegal' cell (as per Figure 4.11), however with successive levels of refinement this problem becomes less and less significant due to the minimisation of the blunting (blunting is inevitable with any cell centred scheme). The criteria used for adaption are given in Table 4.3.

Thus with this technique, the surface of a body can be captured to specified accuracy merely by altering the number of levels of adaption and the nature of the adaption performed at each grid level. Physical adaption at each grid level can be adjusted, and either globally enabled or inhibited by adjusting the spatial gradient flagging tolerances.

4.3.3 Static Computations.

4.3.3.1 Boundary Conditions

Traditional cartesian cutting algorithms apply no slip/no flow boundary conditions at the body surface where the cells are cut. Such cell cutting produces non-quadrilateral cells which require special consideration by the flow solver. Cell splitting can be used as a means of ensuring that all cells are quadrilateral (Figure 4.13) although this will lead to the production of either an unstructured quadrilateral mesh or an excessive number of sub-grids. Grids created in this manner are likely to be unsatisfactory both in terms of quality and computational efficiency. A related problem with cartesian cutting is the 'small-cell' problem [81] in which very small cells are produced which limit the global timestep and hence impair convergence, particularly for time accurate

computations requiring global time steps. Cell merging is commonly used to avoid small cells and the presence of non-quadrilateral cells by the production of larger quadrilateral cells (Figure 4.14). This, however, produces locally unstructured grids and is therefore not a viable technique for use within the structured DRAMR environment.

To overcome all of these problems a more fundamental approach is adopted. Since local grid adaption is relied upon to accurately recover the surface of the body to within an arbitrary precision, it is possible to refine, such that the cell centres are arbitrarily close to the body surface and hence cell deformation is unnecessary. By assuming that the cell centres are sufficiently near the body surface to be virtually on the surface, the boundary conditions are greatly simplified. It is worth noting that conventional body fitted grids used in conjunction with cell centred schemes will not accurately model the surface of the geometry (since the cell vertices are used to describe the geometry and the cell centres to describe the flow physics). I.e. the geometric accuracy of body fitted cell centred schemes is determined by the dimensions of the wall cells. A similar effect is evident here, whereby the accuracy of the modelled body surface is dictated by the size of the 'wall' cells.

4.3.3.2 Viscous no-slip condition

The simplest boundary condition for testing the code is that of a viscous no-slip condition (the inviscid boundary condition has to take account of local body slope). This boundary condition is enforced using:

$$\begin{bmatrix} \overline{\rho}' \\ \overline{\rho u}' \\ \overline{\rho v}' \\ \overline{E_t}' \end{bmatrix} = \begin{bmatrix} \overline{\rho} \\ \overline{\rho u} \\ \overline{\rho v} \\ \overline{E_t} \end{bmatrix} + \begin{bmatrix} 0 \\ -\overline{\rho u} \\ -\overline{\rho v} \\ -\frac{1}{2}\overline{\rho}(\overline{u}^2 + \overline{v}^2) \end{bmatrix}$$

} No slip – flow velocity at the surface is zero.
} Remove kinetic energy from total energy (due to momentum loss).

giving conservation of mass (both locally and globally), the required momentum deficit at body surface and the corresponding correction to the energy equation.

By application of this boundary condition, viscous solutions for arbitrary bodies in arbitrary flows can be produced (e.g. Figure 4.15). The flowfield in Figure 4.15 was produced by Mach 4.95 flow over a NACA 65-009 aerofoil (chord length=0.0762m (3"), Reynolds number based on chord length = 49.9×10^6). The underlying baseline mesh is a uniform grid of 100x100 cells of dimension 3.81mm x 3.81mm. Adaption using flowfield spatial gradients has been disabled and the refinement for body capture comprises two levels of 4x4 refinement giving a geometric body resolution of ±0.1mm (0.15% chord length).

4.3.3.3 Inviscid boundary condition

The inviscid boundary condition needs to account for local body slope in order to only remove the flow momentum normal to the wall. There are two ways in which the local body slope can be accurately resolved:

i Examine each of the four faces of the cell in question and flag according to whether or not the face is cut (one interior cell/boundary vertex and one exterior/boundary vertex). If there are exactly two cut faces then loop around the body computing the intersections of each of the cut faces with each body segment using:

$$\begin{pmatrix}\varepsilon_1\\ \eta_1\end{pmatrix}+\alpha\begin{pmatrix}\varepsilon_2-\varepsilon_1\\ \eta_2-\eta_1\end{pmatrix}=\begin{pmatrix}x_1\\ y_1\end{pmatrix}+\beta\begin{pmatrix}x_2-x_1\\ y_2-y_1\end{pmatrix}$$

$$\Rightarrow \alpha=\frac{(\eta_1-y_1)(x_2-x_1)-(\varepsilon_1-x_1)(y_2-y_1)}{(\varepsilon_2-\varepsilon_1)(y_2-y_1)-(\eta_2-\eta_1)(x_2-x_1)}$$

By examining the interpolant/extrapolant α, between pairs of body points (ε_1,η_1), (ε_2,η_2) the body vertex pair intersecting the cut face are easily identified ($0\leq\alpha\leq1$). Thus by identifying exactly where along each cut face the intersects occur the local surface gradient can be computed.

ii Looping around the body and finding the two closest consecutive body vertices to a chosen point directly yields the local surface gradient.

These two techniques are similar in nature and both have advantages and disadvantages. Approach (i) is thorough and accurate, especially for multiple complex geometries (although at a greater computational expense). Approach (ii) is rapid, although with inadequate refinement can prove slightly inaccurate (when the refined cell centres are not close enought to the body surface) and can experience difficulties with bodies which are thin relative to the mesh dimensions (the thin body problem is discussed is §4.3.6.9)..

Assuming that the local surface vector is known ($\underline{t}$) then the inviscid boundary condition is defined thus:

The momentum parallel to the surface (which is to remain after application of the boundary condition) is given by:

$$\hat{\underline{t}}\bullet\underline{\overline{U}}=\begin{bmatrix}\hat{\underline{t}}_x\\ \hat{\underline{t}}_y\end{bmatrix}\bullet\begin{bmatrix}\overline{u}\\ \overline{v}\end{bmatrix}=\overline{u}\hat{\underline{t}}_x+\overline{v}\hat{\underline{t}}_y=\left\{\overline{u}\underline{t}_x+\overline{v}\underline{t}_y\right\}\left|\underline{t}\right|^{-1}$$

This remaining momentum will be in the direction prescribed by the body surface vector ($\underline{t}$), and hence the boundary condition becomes:

$$\begin{bmatrix} \overline{\rho}' \\ \overline{\rho u}' \\ \overline{\rho v}' \\ \overline{E_t}' \end{bmatrix} = \begin{bmatrix} \overline{\rho} \\ \overline{\rho}\left(\bar{u}\underline{t}_x + \bar{v}\underline{t}_y\right)\underline{t}_x \frac{1}{|\underline{t}|^2} \\ \overline{\rho}\left(\bar{u}\underline{t}_x + \bar{v}\underline{t}_y\right)\underline{t}_y \frac{1}{|\underline{t}|^2} \\ \overline{E_t} - \frac{1}{2}\overline{\rho}\left(\sqrt{\bar{u}^2 + \bar{v}^2} - \sqrt{\bar{u}'^2 + \bar{v}'^2}\right) \end{bmatrix}$$

The energy equation in the above boundary condition corrects for the loss of normal momentum by removing all of the pre-boundary condition kinetic energy, and then supplementing the total energy with the kinetic energy post-application of the momentum equation boundary conditions.

This boundary condition ensures no flow through the body surface and, modifies the energy equation to account for the normal momentum deficit. Due to the arbitrary nature of these extensions, no distinction is made between the flow inside the body and the flow outside the body, and hence to ensure that the local surface vector is in the correct 'right-handed' direction a simple post boundary condition check is made:

$$\bar{u}'^2 + \bar{v}'^2 \geq \bar{u}^2 + \bar{v}^2 \Rightarrow \underline{t}' = -\underline{t}$$

Thus, if the total velocity after application of the boundary condition is greater than pre-application, the surface vector was pointing the 'wrong way' and the boundary condition is re-applied with the reversed surface vector. Illustrations of the flowfield pre- and post-application of the boundary conditions prior to the first iteration are given in Figures 4.16, 4.17 and 4.18. Arrow lengths in these velocity vector plots are scaled according to both grid level and velocity. It is seen from Figure 4.18 that the boundary conditions are applied consistently at the 'sharp' trailing edge. Iterating to convergence produces the flowfield given in Figure 4.19. Conditions for this computation are identical to those used for the viscous computation shown in Figure 4.15.

4.3.4 Rate of Convergence

Since AMR creates significantly refined meshes where required and coarse meshes elsewhere (and the lack of cut cells and hence the avoidance of the small cell problem) convergence is rapid.
The series of figures 4.20a-4.20l show the evolution of the flowfield with time. In iterative terms, the solution progressed as follows:

Frame	a	b	c	d	e	f	g	h	i	j	k	l
T bar	0.20	0.40	0.60	0.80	1.00	1.20	1.40	1.60	1.80	2.00	2.50	3.00
#	21	42	63	84	105	126	147	168	189	210	261	312
cpu(mins)	7	15	25	35	46	57	69	83	92	105	147	189

The CPU times given above were for computing the flowfield on a SUN SPARC 2000, which is a relatively slow machine. Despite this, a full Navier Stokes solution was produced in around three hours, although convergence may have been reached after approximately two. It is seen that the

computational cost per iteration increases and then stabilises – this is as the mesh develops with the developing flowfield.

4.3.5 Validation

There is very little experimental data for supersonic prismatic bodies since the majority of data for prismatic bodies is for wing sections, which for supersonic applications tend to be swept and hence are not suitable for validation of the two-dimensional code. Surface pressure coefficient distributions were found for a NACA 65-009 aerofoil at low supersonic Mach numbers at various angles of attack [82]. Consequently the validation data presented here are for supersonic flow over an aerofoil section, representing the only available data. Comparison between experiment and computation at Mach 1.62, 4° angle of attack are presented for the windward and leeward surfaces in Figures 4.21 and 4.22 respectively. There is no experimental dynamic supersonic data for validation purposes, and hence a quasi-steady configuration was examined.

4.3.6 Dynamic computations

For dynamic computations two additional complexities arise: firstly the grid structure changes with time, and secondly, modifications to the boundary conditions are necessary to account for body motion and local surface velocity.

4.3.6.1 Dynamic meshing

During computations involving moving body surfaces, cells within the computational domain will change state (for example, interior to exterior) as the body moves, and hence a stratagem was formulated to handle newly created/destroyed cells in a locally and globally conservative manner. An array of mirror cells was created whereby cells straddling the body surface are assigned a mirror cell, corresponding to the nearest totally external cell on the same grid level. The mirror cell stencil comprises sixteen vertices (a three by three cell stencil centred on the cell of interest). By assessing the state of each of these cells and selecting the closest to the cell of interest, the mirror cell array is populated. Straddling cells requiring mirrors are illustrated in Figure 4.23, and their mirror cells in Figure 4.24 (the grid lines are coloured according to grid level).

Mirror cell calculation is performed thus:

Considering a 3x3 cell stencil:

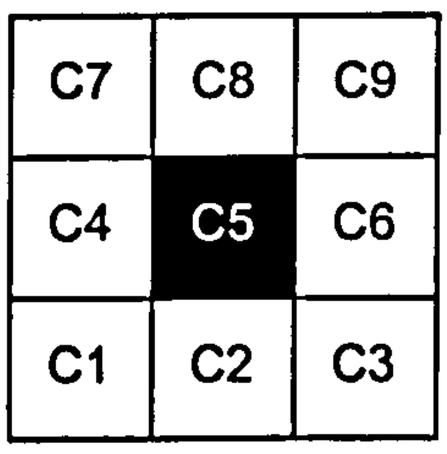

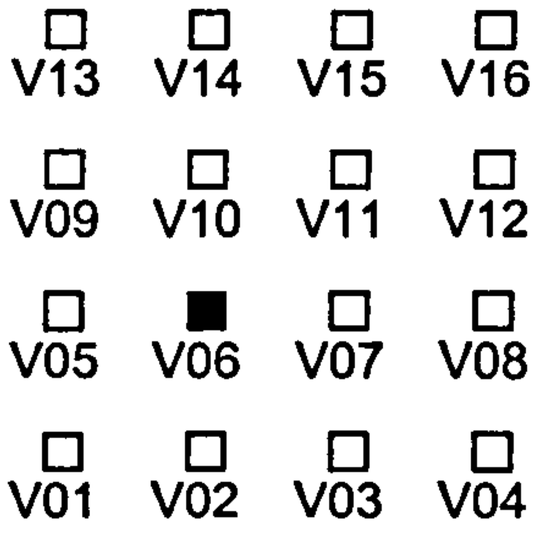

Giving vertex offsets:

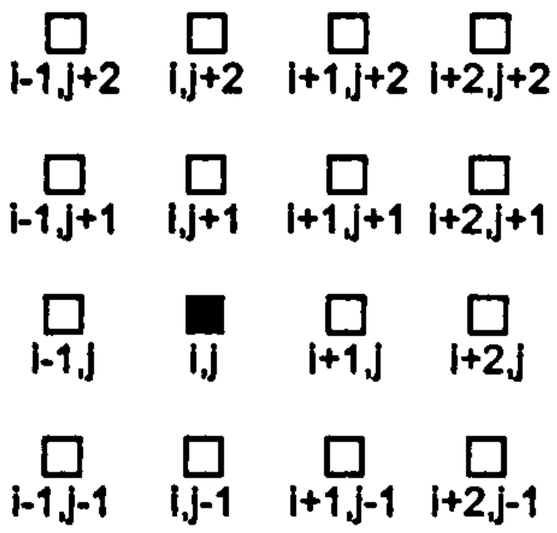

and offset arrays IO and JO:

$$\underline{IO} = [-1,0,1,2,-1,0,1,2,-1,0,1,2-1,0,1,2]$$
$$\underline{JO} = [-1,-1,-1,-1,0,0,0,0,1,1,1,1,2,2,2,2]$$

Applying the winding algorithm to the 3x3 cell stencil:

$$\underline{F} = wind\left(\underline{\overline{X}}(IJ + \underline{IO} \times Ibmp + \underline{JO} \times Jbmp), \underline{\overline{Y}}(IJ + \underline{IO} \times Ibmp + \underline{JO} \times Jbmp)\right)$$

Then the verdict for each cell can be computed using the cell vertex matrix M:

$$M = \begin{bmatrix} 1 & 2 & 3 & 5 & 6 & 7 & 9 & 10 & 11 \\ 2 & 3 & 4 & 6 & 7 & 8 & 10 & 11 & 12 \\ 5 & 6 & 7 & 9 & 10 & 11 & 13 & 14 & 15 \\ 6 & 7 & 8 & 10 & 11 & 12 & 14 & 15 & 16 \end{bmatrix}$$

$$\underline{V} = AND\left\{\underline{F}_{M_{i,1}}, \underline{F}_{M_{i,2}}, \underline{F}_{M_{i,3}}, \underline{F}_{M_{i,4}}\right\}$$

Throughout, the following values are defined:
INSIDE=1
OUTSIDE=2
BOUNDARY=4
UNDEFINED=8
In this manner bitwise operators can be used to assess a cell's status.

Mirror cells are computed by finding the nearest fully interior or exterior cell (for interior mirror and exterior mirror respectively):

$$\begin{bmatrix} \underline{\overline{X}_c} \\ \underline{\overline{Y}_c} \end{bmatrix} = \tfrac{1}{4} \sum_{q=1}^{4} \begin{bmatrix} \underline{\overline{X}}(IJ + Ibmp \times \underline{IO}_{M_{c,q}} + Jbmp \times \underline{JO}_{M_{c,q}}) \\ \underline{\overline{Y}}(IJ + Ibmp \times \underline{IO}_{M_{c,q}} + Jbmp \times \underline{JO}_{M_{c,q}}) \end{bmatrix}$$

$$\underline{d}_c = \left| \left\{ \underline{\overline{X}}_{c,5} - \underline{\overline{X}}_{c,i} \right\}^2 + \left\{ \underline{\overline{Y}}_{c,5} - \underline{\overline{Y}}_{c,i} \right\}^2 \right| \quad c = 1 \ldots 9$$

For an exterior mirror:

$$\underline{M_E} = c : \underline{V}_{c,q} = OUTSIDE, q = 1 \ldots 9$$
$$and \quad \underline{d}_{c,q} = \min\left(\underline{d}_{c,r}\right), r = 1 \ldots 9$$

and similarly for the interior mirror array.

With a given angular velocity and timestep two angular body rotations are assessed at each iteration. Cell states are computed for each of the angular states and compared, to locate which cells have changed state due to the

body motion (a simple schematic of cell destruction is given in Figure 4.25). If a cell is destroyed, then the corresponding mirror cell is augmented with the destroyed cell's conserved fluxes (i.e. the fluid is pushed into the mirror cell). If a cell is created then the corresponding mirror cell donates half of its conserved fluxes to the newly created cell. Whilst this appears to be a somewhat contrived stratagem it is analogous to the commonly employed technique of cell merging and splitting which is routinely exploited in cartesian cutting algorithms (to avoid the small cell problem). Furthermore, since all transfers occur at the same grid level, and the underlying grids used here are uniform, no modifications are required to accommodate variations in cell area (or unit volume) as both the donor and recipient must be of the same dimensions.

For this technique to function correctly it is important that as cells change from internal to external (or vice versa) they pass through the straddling state (otherwise valid mirror cell data will not be available). By insisting that all cells pass through the straddling state, the body line segments cannot move faster than half the minimum cell dimension at each iteration. For long bodies with high angular velocities, rapidly translating bodies or excessive refinement (producing very small cells) could necessitate a reduction in CFL number. A reduction in CFL number would produce a reduced timestep and hence a reduced body surface motion at each iteration. This restriction could be avoided, but has been retained for simplicity and since this situation did not arise when computing any of the flows presented here. If the body surface were to be allowed to move across more than one cell per iteration then the body surface trajectory will need to be computed in cell traversal terms and a computationally expensive cell hunting flux transfer algorithm would need to be devised. By restricting the body surface motion in this manner, the boundary conditions can be imposed with a 3x3-cell stencil. A trap was set in the code to verify that at each iteration no cells have changed from fully interior to fully exterior or vice versa. Should this occur, the time step is halved and the secondary angular position recomputed. In this manner the code can take account of rapidly moving surfaces or parts of surfaces.

4.3.6.2 Non-stationary boundary conditions

The static boundary conditions were modified to reflect the change in the momentum equations and energy equation due to the local surface velocity resulting from the body motion. For an arbitrary body motion as illustrated in Figure 4.26, the magnitude of the velocity of the point (x_2,y_2) is equal to $\omega\lambda$, where:

$$\lambda = \frac{(x_2 - x_1)\cos\alpha + (y_2 - y_1)\sin\alpha}{\cos\alpha + \sin\alpha}$$

Hence with the magnitude of the velocity and the argument of the velocity from the local normal body surface vector, the additional terms in the momentum equations can be computed (with appropriate adjustments to the energy equation).

The moving body boundary conditions are thus:

If u_m and v_m are the u and v velocities of a moving point on the surface of the body, then the viscous (no slip) boundary condition becomes:

$$\begin{bmatrix} \overline{\rho}' \\ \overline{\rho u}' \\ \overline{\rho v}' \\ \overline{E_t}' \end{bmatrix} = \begin{bmatrix} \overline{\rho} \\ \overline{\rho u} \\ \overline{\rho v} \\ \overline{E_t} \end{bmatrix} + \begin{bmatrix} 0 \\ -\overline{\rho u} + \overline{\rho u_m} \\ -\overline{\rho v} + \overline{\rho v_m} \\ -\frac{1}{2}\overline{\rho}(\overline{u}^2 + \overline{v}^2) + \frac{1}{2}\overline{\rho}(\overline{u_m}^2 + \overline{v_m}^2) \end{bmatrix}$$

This boundary condition is identical to the static viscous no-slip boundary condition, with the exception that the non-dimensional flow velocity at the surface after application of the boundary condition is equal to the non-dimensional velocity of the surface. The energy equation is corrected as before to account for the loss or gain in momentum.

The inviscid boundary condition becomes:

$$\begin{bmatrix} \overline{\rho}' \\ \overline{\rho u}' \\ \overline{\rho v}' \\ \overline{E_t}' \end{bmatrix} = \begin{bmatrix} \overline{\rho} \\ \overline{\rho}\left(\overline{u}\underline{t}_x + \overline{v}\underline{t}_y\right)\underline{t}_x \frac{1}{|\underline{t}|^2} + \overline{\rho u_m} \\ \overline{\rho}\left(\overline{u}\underline{t}_x + \overline{v}\underline{t}_y\right)\underline{t}_y \frac{1}{|\underline{t}|^2} + \overline{\rho v_m} \\ \overline{E_t} - \frac{1}{2}\overline{\rho}\left(\overline{u}^2 + \overline{v}^2\right) + \frac{1}{2}\overline{\rho'}\left(\overline{u}'^2 + \overline{v}'^2\right) \end{bmatrix}$$

This boundary condition is identical to the static inviscid boundary condition, with the exception that the non-dimensional flow velocity at the surface after application of the boundary condition is equal to the sum of the velocity in the body surface geometric direction and the velocity of the body surface itself. The energy equation is corrected as before.

4.3.6.3 Internal flowfield reconstruction

Since there is a flowfield within the body itself and it is not possible to provide explicitly defined ghost cells, it is important that the flowfield immediately adjacent to the body surface on the inside of the body is correctly imposed. To effect this the pressure distribution within the body is set to mirror the pressure distribution immediately outside of the body. This is accomplished in an analogous manner to the mirror cell techniques used for body motion, except that for the internal flowfield reconstruction the nearest totally *internal* cells are selected. This, in conjunction with the boundary conditions specified earlier, ensure zero flow through the surface or zero velocity at the surface (inviscid or viscous respectively) and a zero temperature and pressure gradient across the wall. Should there be a requirement to impose an isothermal boundary condition rather than the innate adiabatic boundary condition it would be trivial to modify the total enthalpy term to impose such a condition.

4.3.6.4 Forced body motion

To evaluate the cell creation and destruction algorithms, a fixed angular velocity was imposed on an aerofoil and the body allowed to turn. Density and streamwise velocity plots are given in Figures 4.27and 4.28. The flowfields in Figure 4.27 and 4.28 are for a Mach 1.62 flow over a NACA 65-009 aerofoil (chord length=0.0762m (3"), Reynolds number based on chord length = 1.07×10^6). The underlying baseline mesh is a uniform grid of 100x100 cells 3.81mm x 3.81mm. Adaption using flowfield spatial gradients has been disabled and the refinement for body capture comprises two levels of 4x4 refinement, giving a geometric accuracy of ±0.1mm.

4.3.6.5 Computation of Forces and moments

To compute the forces and moments acting on the body surface, pressure distributions are extracted from the solution. For static body fitted methodologies this is trivial, however for an arbitrary moving body this is more complex. By examining every grid cell and selecting the cells, which are neither completely interior nor completely exterior, all of the cells straddling the wall are found and for each of these cells the *two* nearest body vertices are located and stored. For each of these body line segments, all of the wall cells which share the two vertices of the line segment as their nearest two body vertices are assumed to contain fluid exerting pressure on the body segment. By summing all of the individual pressure contributions for each line segment and dividing by the number of contributors, an average surface pressure distribution for the body segment is produced (Figure 4.29). It is seen in Figure 4.29 that lower surface trailing edge is not fully captured – this is due to the 'thin-body' problem described in §4.3.6.9. Multiplying each of the pressure segments by its perpendicular distance from the centre of rotation (moment arm) the pitching moment distribution is computed (Figure 4.30). Plotting the moment distribution against position along the aerofoil illustrates the magnitude of the moment contributions and the sign change at the centre of rotation (Figure 4.31). Plotting the absolute magnitude of the pitching moment distribution shows the difference between the upper and lower surfaces and hence the overall driving moment for the ensuing motion (Figure 4.32).

4.3.6.6 Equations of motion in polar form:

Newton's second law in polar form can be expressed as:

$$\omega' = \omega + \alpha \Delta t$$

$$\tau = I\alpha$$

Where ω is the initial angular velocity, ω' is the angular velocity after a time increment Δt under the action of an angular acceleration α. The angular acceleration is related to the overall moment (τ) about the centre of rotation and the moment of inertia (I) about the same point.

4.3.6.7 Physical Parameters

The centre of gravity, total mass and moment of inertia for our arbitrary planar bodies was computed by direct numerical integration (Figure 4.33). For the wing section selected here the centre of rotation was fixed at 20% chord from the leading edge and made of solid aluminium (ρ=2700kgm^{-3}). The mass for a 1m length of aerofoil section is 967g, with centre of gravity 32mm from the leading edge and the moment of inertia about 20% chord from the leading edge is 5.82x10^{-4}kgm^2.

4.3.6.8 Computation of Freely Rotating Aerofoil

A constrained aerofoil motion was simulated by fixing the axis of rotation of the test case presented in §4.3.3.2 at 20% chord from the leading edge, obtaining a converged solution (for the aerofoil at an initial pitch of 4°) and then allowing the aerofoil to move under the action of its own forces and moments. The ensuing motion is given in Figure 4.34 as a plot of incidence vs. time. The wavelength of the oscillation is ≈98Hz and the damping is ≈20% per cycle. A slowly moving body will interact with a flowfield in a quasi-steady state, i.e. the solution at any instant will correspond to the static solution with body in the same static orientation. A dynamically moving body with associated flow interaction will approximate a sequence of static solutions if the body's reduced angular frequency ($\omega c/2u$) is of order less than one[117] (for inviscid flows). If the body's reduced angular frequency is of order one or greater, then this may no longer be the case. For this test case (which is dominated by the inviscid flow), $\omega c/2u \approx 0.04$ and hence the solution is likely to be quasi-steady and hence quasi-steady validation techniques may be used. Having established that the solution was quasi-steady, and that the body motion may be predicted analytically by undertaking a one-degree of freedom trajectory simulation using forces and moments obtained from static experimental data. By examining the surface pressure coefficient distributions presented in [82], re-dimensionalising the pressures and integrating, the forces and moments acting on a section of the wing were produced. The re-dimensionalised computational pitching motion is presented for comparison with the experimental data in Figure 4.34. It is seen that the results are in reasonably good agreement and that the computational results differ qualitatively from the experimental results by the inclusion of pitch damping. The angular position with respect to time appears to be in reasonable agreement with the experimental data. Angular velocity is given in Figure 4.35. The angular acceleration (Figure 4.36) is somewhat 'noisy'. Due to the number of timesteps required to perform an oscillation of the wing section and the moment of inertia of the wing, this high frequency 'noise' does not affect the angular position with respect to time. It was computed [138] that on the basis of the surface pressure distributions given in [82] that the oscillatory frequency is approximately 100Hz, and the damping approximately 18% per

cycle. This appears to agree well with the computed data and quasi-steady simulation.

4.3.6.9 The 'thin-body' problem

With these algorithms, globally or locally 'thin' bodies can cause difficulties with the reconstruction of the surface pressure. The thin body illustrated in Figure 4.37 manifests these problems. In this example selecting the two nearest body vertices to p_i will yield the points p_{n+1} and p_{n+5}. When the surface pressure is reconstructed, this pressure contribution will be considered as invalid since its two nearest body vertices are not consecutive. Evidently this problem can arise wherever there are two or more non-consecutive body vertices who are less distant than the two consecutive body vertices. To avoid this problem one can subdivide each body segment into n smaller segments (solely for the purposes of body surface pressure recovery). For any possible configuration it is possible to find an integer n into which each segment can be subdivided to provide a consecutive pair of body vertices as nearest neighbours. To avoid errors at locations where the body is 'thin' the number of contributors to each body segment can be examined and where this is equal to zero the surface refined and the process repeated. This will ensure that a pressure is correctly resolved for each and every body segment. This can be automated by subdividing a line segment and updating the body surface array. The only complexity is how to interpolate to generate the additional body surface points required. The preferred options are linear interpolation, splined interpolation and analytical description.

There is no reason why the body shape should not be modified whilst the code is running to provide a shape change mechanism (for example, for ablation and moveable control surfaces). Body shape change is as 'trivial' as moving the body and proved necessary for the computation of Smith's[67] rapidly deployed flap presented in §4.5.

4.4 Static Transitional Ramp Flows

A series of static and dynamic experiments were performed by Smith [67] at Southampton University using a Mach 6.85 isentropic light piston compression tube wind tunnel. The flow conditions (and inferred conditions for the computations) were:

$Re_\infty=2.45x10^6m^{-1}$
$P_0=551600Nm^{-2}$
$T_\infty=58.74K$
$P_\infty=153.0Nm^{-2}$
$\rho_\infty=0.008764kgm^{-3}$
$u_\infty=1070.0ms^{-1}$
$\mu_\infty=3.8275x10^{-6}kgm^{-1}s^{-1}$

The gas used throughout these experiments was nitrogen (γ=1.4). Two predictions were made of the value of molecular viscosity (μ) at these low temperatures and pressures. Using Sutherland's law with reference values of $\mu_{ref}=1.66x10^{-5}kgm^{-1}s^{-1}$ and $T_{ref}=273°K$ [134], the freestream static molecular viscosity is found to be $\mu_\infty=4.07x10^{-6}kgm^{-1}s^{-1}$. Due to possible inaccuracies with Sutherland's law at such low temperatures, extrapolation of low temperature, low pressure molecular viscosities [136] gives a reference value of $\mu_\infty=4.12x10^{-6}kgm^{-1}s^{-1}$. These values agree reasonably with the molecular viscosity calculated by Smith[67] (inferred from values of Reynolds number, freestream density and velocity given in [67]) of $\mu_\infty=3.83x10^{-6}kgm^{-1}s^{-1}$ (a variation of ≈7.5%).

The test geometry comprised a flat plate (155mm in length) with a flap attached at the trailing edge (51mm in length) as illustrated in Figure 4.1. Experimental data [67] are available in the form of schlieren images and heat transfer measurements for various static and dynamic configurations. The flowfield over the flat plate is entirely laminar, whilst as the flap angle is increased, the flow undergoes transition in the free shear layer, ultimately leading to turbulent reattachment[137]. It was shown that in all cases the static flap flows exhibited no unsteadiness.

Since the flow is (dependent on location and flap angle) laminar, transitional and turbulent, a mesh was required for which mesh convergence was established for all of these flow regimes. It is known that laminar shock boundary layer interactions are steady[10] and that relatively small shock turbulent boundary layer interactions are also likely to be steady[6][7]. For the configurations examined by Smith, all of the fixed flap shock boundary layer interactions were steady[67].

Due to the relative merits of the Baldwin-Lomax turbulence model over the k-ε model seen in §3.1 and §3.2, the Baldwin-Lomax model was used for these

computations. An advantage of the zero equation turbulence models is that they postprocess existing flowfields to infer a turbulent viscosity and hence no special considerations are necessary to account for moving body surfaces. As the computations presented here are a pre-cursor to the dynamically moving cases it was desirable to employ the same turbulence model for both (to facilitate direct examination of the dynamic effects via comparison between the moving and static cases). Devising accurate boundary conditions for the production and dissipation of turbulent kinetic energy at the surface of a moving body for a two equation turbulence model is likely to prove difficult.

Initial computations were undertaken with the SPIKE code, whilst simultaneously verifying an implementation of a non-dimensional Baldwin-Lomax turbulence model (Appendix B) within the hierarchical meshing code DRAMR. Implementation of an efficient Baldwin-Lomax turbulence model within DRAMR was complicated by the lack of global grid structure (due to refinement) and due to the non-dimensionalisation. DRAMR was required for computationally affordable enhanced spatial accuracy and to use the extensions devised for arbitrary body deformation/motion (presented in §4.3.6.1), which are required for the subsequent rapidly deployed flap computations. Mesh refinement on the basis of flowfield spatial gradients was disabled throughout, to avoid the added complexities of ensuring sufficient spatial resolution for both static and dynamic cases.

Assessing grid convergence in a non-adaptive environment is relatively straightforward since, for any mesh independent computation the grid should, by definition, have no effect on the solution. In order to ensure that the equations are modelling the flow to the best of their ability, it is important that mesh convergence studies are undertaken to verify that the resolution of the grid is not affecting the characteristics of the solution. With non-adaptive codes one simply increases the grid resolution in each dimension until the iteratively converged solution is no longer affected (or the dynamic characteristics in the case of unsteady flows). It is then concluded that mesh resolution is sufficient and hence the correct solution for the equations and boundary conditions is deemed to have been obtained.

With adaptive grids this process is more complex. A cursory examination of the problem suggests that the problem is not too onerous for meshing techniques which flags cells for refinement with physical spatial gradient(s) exceeding n% of the maximum physical spatial gradient within the grid level (as employed within DRAMR). A route to establishing convergence may be:

i. Set the flagging tolerance (gradients greater that the flagging tolerance multiplied by the maximum gradient are refined) to 0.0 (or negative) to enforce adaption everywhere within the grid level.
ii. Iterate to a converged solution (or regular oscillations for unsteady flows).
iii. Progressively increase the flagging tolerance until the solution is affected.

iv. Revert to the previous flagging tolerance and double the resolution of the adapted patch (in the dimension being assessed).
v. If the solution is affected then the solution must still be sensitive to mesh resolution ∴ repeat from step i.

It is necessary to repeat from step i, since the global maximum spatial gradient (based on adjacent cells) may have been affected, and hence different cells may be flagged as requiring refinement.

Matters become progressively more complex as successive grid levels are added to the mesh hierarchy, for example using a Roe based Reimann solver, shock waves are resolved over three adjacent grid cells. Adding another level of adaption will refine the shock over three grid cells in the refined grid. This will be extrapolated to the coarser grid causing an increase in the maximum computed spatial gradient. This, in turn, can lead to a reduction in refinement due to the increase in global maximum computational spatial gradient, and hence could conceivably lead to the cells causing the original increase in global spatial computational gradient at the lower grid level no longer being flagged. This could produce oscillatory adaption, which in turn is likely to lead to convergence anomalies or lack of convergence (real or perceived).

To reliably and accurately perform mesh convergence analysis within an adaptive meshing environment the steps i-iv above are valid only for one level of adaption. Whenever a modification to the mesh is made at grid level N, steps i-v must be repeated for each and every grid level thereunder (starting from 0 and ending at N-1). Only then may the two solutions be compared to assess mesh dependence.

Due to the potential complexity of undertaking spatial refinement using adaption on the basis of flowfield spatial gradients, simultaneously with ensuring sufficient refinement to recover the body surface and capture the boundary layer, spatial gradient adaption was disabled. This resulted in a significant increase in computational cost, as a sufficiently fine baseline mesh had to be used throughout, even where such refinement was unnecessary. Fortunately the cost of undertaking these computations, whilst high, was not prohibitive and the luxury of over-refinement could be borne.

Smith[67], in his preliminary discussion of steady state results purports the flow to be laminar across the range of flap angles (0°-40°) (for the $Re_\infty=2.45\times10^6 m^{-1}$ flows). In subsequent discussions Smith[67] acknowledges that even for experiments at this Reynolds number the flow is not laminar for all flap angles. For a plate of length 0.206m (flap angle = zero), the flow is likely to be laminar throughout the flowfield (Re=504,700 over the length of the plate, and typically $Re_{cr}\approx500{,}000$). As the flap angle is increased the flow will undergo transition and hence a turbulence model will be required that can adequately predict the flow for all of the flap angles that were examined experimentally.

To ensure that implicit local time stepping was not adversely affecting the results (as seen in §3), several computational test cases were continued using an explicit time-accurate solver and the results were found to be identical. This is attributed to the fact that these flows are inherently steady, whereas the flows examined in §3 were inherently unsteady.

Preliminary laminar and fully turbulent (Baldwin-Lomax) computations were performed to establish mesh convergence. It was discovered that meshes which were sufficient for the Baldwin Lomax computations were also sufficient for the laminar computations (since the turbulence is imposed as a scalar of the laminar molecular viscosity, this is not surprising). Hence mesh convergence was concentrated on fully turbulent flows. A typical mesh convergence plot (for a 25° flap) is presented in Figure 4.38 and it was discovered that modelling the wake flow was unnecessary (for larger flap angles the flow may not reattach on the flap and disturbances downstream of the flap trailing edge may have an influence of the behaviour of the separated region). It was established that with the exception of the last two or three grid points on the flap, the wake flow is unimportant for these computations. Experimental results are presented in Figure 4.39, and reconstructed in Figure 4.40 together with the results of these preliminary computations, highlighting the fact that the experimental results lie between the fully laminar and the fully turbulent computations. Separation of the flow is only evident above 5° computationally (laminar) and 6° experimentally[67] which compares well with the prediction of the onset of separation presented in §4.1 of 5°. A typical flowfield, including underbody and wake flows is presented in Figures 4.41, 4.42, and 4.43 (for a fully turbulent 25° flap flow). As with the flare cases presented earlier, it is seen that for small flap angles, separation does not occur, as also observed by[154][155][156][157].

Due to the concerns surrounding accurate location of the position of separation through pressure and/or optical techniques, the methods by which separated length was being determined were examined. It is known that estimating the location of separation by visual means (e.g. schlieren) is fraught with error, especially for thick boundary layers and/or high Mach numbers (due to the reduced angle of the separation shock to the freestream). Whilst the boundary layer produced here is relatively thin, errors can still be relatively large. Figure 4.44 shows a computational flowfield shaded according to absolute density gradient. It is seen that if one assumes that separation occurs where the projected separation shock would reach the wall, an appreciable error would result (in this case an error of 18.2mm or 24%).

It is noted that since all of these flows are inherently stable, the separation shock would not have exhibited either streamwise motion or spanwise ripple. Spanwise ripple can cause further difficulties in obtaining separation shock positions for two-dimensional unsteady flows via optical techniques due to the 'smearing' effect of the observed shock waves.

It has been seen computationally that locating separation with oil flow

visualisation may also prove difficult due to the low shear stress at the wall. Figures 4.45 and 4.46 show velocity profiles at separation and reattachment, and it is seen that whilst there is an appreciable contra-streamwise shear at reattachment, the magnitude of the shear near separation is small. Since it is the shear stress at the wall at separation and reattachment that moves the oil towards these locations, resolution of the location of separation position could be difficult and/or inaccurate. However, flow visualisation has been successfully employed in spite of severe constraints, for example oil flow visualisation using hypersonic gun tunnels.

Smith [67] obtained separation locations by projecting normal to the wall at the furthest upstream occurrence of the separation shock ("separation location has been taken as the intersection of the separation shock with the visible edge of the boundary layer"[137]). It is seen from Figure 4.44, that this should yield reasonably accurate results.

Various techniques were examined to try to replicate the static data of Smith whilst still employing the simple zero equation model of Baldwin and Lomax. Since the experimental data falls between the fully laminar and fully turbulent and the flowfield is recognised as being transitional [67][137] various techniques were examined to modify the spatial extent over which the flow was being modelled as turbulent. This, in no way, is intended to emulate the complex process of flow transition, and is simply to provide reasonable agreement between static computational and experimental data for the purposes of examining the performance of adaptive body recovery for dynamically varying separated flows. The numerical transition fixes examined included:

- Instantaneous transition at the hingeline (Figure 4.47a),
- Instantaneous transition at separation (Figure 4.47b),
- Laminar at separation[6], fully turbulent at reattachment – fixed (Figure 4.47c)*,
- Laminar at separation[6], fully turbulent at reattachment – floating (Figure 4.47d)*,
- Laminar at separation[6], becoming turbulent over ΔRe_∞=125,000 (Figure 4.47e)*,
- Laminar at separation[6], becoming turbulent over ΔRe_∞=250,000 (Figure 4.47e)*,
- Laminar at separation[6], becoming turbulent over ΔRe_∞=500,000

---

[6] Separation in the hierarchical environment is trivially defined as:

$$\bar{x}_{sep} = \min\left\{\max(\underline{\bar{x}}), \underline{\bar{x}}(q)\right\} \forall q : \left\{\bar{u}(q) \le 0, \frac{\bar{t} L_{ref}}{U_\infty} - t_{start} \ge 0, \bar{y}(q) \ge \bar{y}_{plate}\right\}$$

Hence, if the computational physical time is before that at which the flap is set to start moving, then the location of separation is artificially forced to the furthest downstream extent available, and hence the flow is laminar throughout. This is explained further in §4.5.

(Figure 4.47e)*.

* Whilst instantaneous transition is readily achieved (setting μ_t=0.0 upstream of transition), transition of the flow over a finite distance requires implementation of a 'degree' of turbulence at each location. To cast this in computational terms and to enforce laminar and turbulent flows where required, an under relaxation factor χ is used to scale the turbulent viscosity μ_t. This is similar in nature to the method suggested by Dhawan and Narasimha[158]. In preference to using an arbitrarily contrived profile for transition, an experimental profile was imposed. Figure 4.48 presents a variation in Stanton number with Reynold's number for laminar, turbulent and transitional flow over an elliptic cone[139]. Sampling this data and fitting the results with a polynomial produces a variation in χ with Re_x (Figure 4.49) which was included in the Baldwin Lomax turbulence model. The polynomial fit is illustrated in Figure 4.49 and is given by:

Defining $\bar{x} = \frac{Re_x - 417000}{795000}$ (i.e. $0 \le \bar{x} \le 1$ over the transition region),

$$\chi = 0.01469 + 0.08472\bar{x} + 2.3151\bar{x}^2 - 1.4226\bar{x}^3$$

In this manner if a fixed (or floating) point is chosen to be the location at which the transition process is to occur, then a solution can be produced with laminar, transitional and fully turbulent flows as required.

The results obtained using the various techniques are presented in Figure 4.50.

An example transitional flowfield generated using adaptive body surface recovery (ΔRe_∞=250,000 with a 15° flap angle) is presented in Figure 4.51 and is seen not to depart significantly from that which might be expected for either a fully laminar or fully turbulent flow.

With this model, for small flap angles the flow is entirely laminar, yet for larger flap angles the shock boundary layer interaction is transitional or fully turbulent. Experimental and computational variation in separation position with flap angle is given in Figure 4.52, and reasonable agreement is seen for angles up to ≈25° with the ΔRe_∞=250,000 model. It has been suggested [137] that with all experimental data presented in [67] there will be 3D effects caused by lateral spillage, or by shock boundary layer interaction induced effects on the side plates, and that the largest flap angle flows are likely to be the worst affected. This may, in part, account for some of the variation between experiment and computation, evident in Figure 4.52.

4.5 Dynamically Deployed Flap

Kuehn [6][7] discovered that for slowly varying angle supersonic ramp flows there was no evidence of hysteresis and moreover the instantaneous flowfield for a specific ramp angle was identical to its steady state counterpart. This only holds for relatively slowly moving ramps i.e. where the flowfield is quasi-steady[117]. Smith [67] showed that for rapidly deployed flaps (peak angular velocity 52.4 radians per second, with a flap deployed from 0° to 40° over 20ms) the flow is unsteady (no longer quasi-steady). The reduced angular frequency, however, is $\frac{52.4\times 0.051}{2\times 1070}=1.2\times 10^{-3}$ which is clearly of order less than one. It is believed that that this flow is unsteady (in spite of having a reduced angular frequency of order less than one) because the flow is dominated by a large viscous separated region and that assessing unsteadiness on the basis of reduced angular frequency assumes the flow to be inviscid, which is clearly not the case.

Smith[67] concluded that the lag in unsteady separation growth was principally due to acoustic and mass entrainment phenomena. Quantifying likely acoustic propagation delays within a computed separated region was effected by examining all computational locations within the separated region in terms of local speed and local flow velocity. For the 30° flap deployment (for example), the local sound speed within the separation bubble was found to be $0.42U_\infty \le c \le 0.47U_\infty$, with an average local sound speed of $0.44U_\infty$. Including the local contra-streamwise velocity at each location within the separated region produced propagation velocities of $0.42U_\infty \le c+(-u) \le 0.62U_\infty$ with an average $c+(-u)$ of 0.55 U_∞ (-u is used since u is measured in the streamwise direction and is negative for the reversed flow). It is seen that the contra-streamwise velocity is of the same order of magnitude as the freestream velocity and hence quasi-stability should not be assumed.

Using the technique of adaptive body recovery, the flow over rapidly deployed flaps (for which experimental data are available [67]) were computed. Preliminary computations were undertaken to ensure that sufficient baseline mesh resolution had been achieved and that the solutions to the static cases with the under-relaxed Baldwin-Lomax turbulence model were producing the same results for the body captured cases as those previously produced with the body fitted grid computations. Due to the lack of viscous stretching in the body captured case, the baseline mesh has to be particularly fine. This could be avoided by applying refinement near to the body surface on an anisotropic variable basis. Once these validations had been satisfactorily completed (an example of which is given in Figure 4.53) dynamic computations were undertaken. An initial flat plate flow (flap deployment angle = zero) was generated for use as the starting condition for computation of the ensuing motion.

The positional history and velocity histories for the flap deployment are given in Figures 4.54 and 4.55[67], and tabulated in Appendix H. To provide smoothly varying flap motion for the computations, these data were fitted with cubic splines, the results of which are presented in Figures 4.56 and 4.57 and used for the ensuing computations. To ensure consistency, the angular positional history was derived by integration of the angular velocity history.

Determination of cells undergoing creation or destruction is performed by examining two body positions at each iteration and analysing cells whose positional status (inside, outside, or boundary) has changed. To ensure the greatest accuracy for these computations, the following temporal body placement scheme was employed.

i. Set the initial body angle according to the profile in Figure 4.57 (based on the physical time elapsed from the start of the body motion),
ii. Set the initial angular body rate according to Figure 4.56,
iii. Compute the time step (subject to the CFL condition),
iv. Set the angular increment according to (ii) and (iii),
v. Set the final angular position according to (i) and (iv).

In this manner the flap prescribes exactly the same motion as the experiment. Minute errors are in evidence between the predicted angular position and angular rate at the end of an iteration, and the new values computed at the beginning of the next (due to the size of the time step and the magnitude of the angular acceleration these are small). Positional errors are typically of the order of 10^{-6}%. Since the positional errors are due to extrapolation using linearised angular velocities, the errors in angular velocity must be similarly small.

These computations are coded as:

$$\begin{bmatrix}\alpha\\ \dot{\alpha}\end{bmatrix}^{n}=\begin{bmatrix}\Omega\\ \dot{\Omega}\end{bmatrix}_{i}+\left\{\frac{t-\psi_i}{\psi_{i+1}-\psi_i}\right\}\begin{bmatrix}\Omega_{i+1}-\Omega_i\\ \dot{\Omega}_{i+1}-\dot{\Omega}_i\end{bmatrix},\quad \textit{where,}\quad \prod_{i=j}^{j+1}(t-\psi_i)\le 0,\ \text{and } 0\le j\le \text{number}$$

of $t,\Omega,\dot{\Omega}$, triples. Where the $t,\Omega,\dot{\Omega}$, triples are the discretised data points taken from Figures 4.56 and 4.57[67] .Then,

$$\tilde{\alpha}^{(n+1)}=\alpha^{(n)}+\Delta t\dot{\alpha}^{(n)}$$

$$t=\frac{\bar{t}L_{ref}}{U_\infty}-t_{start},\qquad \Delta t=\frac{\bar{t}^{(n+1)}-\bar{t}^{(n)}}{U_\infty}L_{ref}$$

$$\text{Relative error}=\begin{bmatrix}(\tilde{\alpha}^{(n+1)}-\alpha^{(n+1)})(\alpha^{(n+1)})^{-1}\\ (\tilde{\dot{\alpha}}^{(n+1)}-\dot{\alpha}^{(n+1)})(\dot{\alpha}^{(n+1)})^{-1}\end{bmatrix}$$

To produce iteratively converged flat plate solutions (laminar) prior to the flap's subsequent motion, a physical time is computed: $t_{phys}=LU_\infty(\bar{t}-\bar{t}_{start})$ where $\bar{t}_{start}$ is selected as the non-dimensional time at which the flat plate flow is known to be converged (based on previous mesh dependence tests). Due

to the temporal term in the location of separation, prior to $\bar{t}_{start}$ being attained laminar flow is enforced throughout. In this manner the computation progresses to a converged steady laminar flat plate flow, and then the flap is automatically released and the transitional turbulence model engaged. This avoids problems associated with the formation of tiny localised separated regions forming during the numerics of the computation starting.

Inserting a pair of initial values $(\alpha = 0, \dot{\alpha} = 0)$ immediately before the body motion commences, ensures that before the flap is deployed, the flap is locked in place and the dynamic boundary conditions are forced to their static counterparts.

Initial computations used a hinged flat plate-flap configuration (as per the experimental configuration), but due to the low densities and pressures in the flow, the code experienced numerical difficulties with the dynamically strengthening expansion on the underside of the flap. It was shown previously that the wake flow need not be modelled in order to accurately predict the flow over the flap, and hence these difficulties were circumvented by utilising the innate ability of the code to model flows over arbitrarily deforming geometries. Body rotation was replaced by iterative reconstruction of the body surface so that at every iteration the entire surface of the flat plate and the flap was recreated, with the underside of the flat plate extended to create a flat plate-wedge configuration (seen in Figure 4.65 and 4.66) (the computational overhead for this was insignificant). Figure 4.65 shows the computational flowfield (density) with increasing flap angle. Figure 4.66 presents the computational mesh for the flap at 30° showing the automatic mesh refinement at the body surface used to impose the required boundary conditions.

Experimental data of Smith[67] for the variation in separation length (measured from the hingeline) with dynamic and static flap angle is presented in Figure 4.58, and the lag in separated length in Figure 4.59.

Since the static experimental and computational transitional separated lengths differ, to assess lag, the difference between the computational static and computational dynamic results are presented.

To demonstrate temporal convergence the computations were repeated with the value of CFL halved, which, with the global time stepping, halves the timestep throughout the domain. Identical results were produced for the variation in separation and reattachment positions with time.

The recorded angular position is presented in Figure 4.60 and it is seen that the computational ramp angle exactly follows the prescribed experimental motion. When the flap attains maximum deployment, it is locked in place and the angular velocity and accelerations are set to zero.

The location of separation with time is presented in Figure 4.61, and with flap

angle in 4.62.

Figure 4.63 presents the dynamic lag in length terms (normalised with respect to flap length) for both the experiment and the computation. It is seen that although the onset of dynamic lag is well-predicted (≈20°), the magnitude of the lag in length terms is not. This was expected, and is attributed to the over-prediction in separation length by the turbulence model at higher incidences for the steady computations (Figure 4.50).

Presenting the dynamic lag in angular terms (as per Smith[67]), whereby the angular lag is defined to be the difference between the dynamic flap angle and the steady flap angle required to produce the same position of separation, overcomes this difficulty. This is illustrated in Figure 4.64 and it is seen that agreement between the experimental and computational angular lag is good.

The peak angular lag appears to be approximately ≈5°, which compares favourably with the experimentally reported lag of 6°.

Sample instantaneous density plots as the flap is dynamically deployed are presented in Figure 4.65. The colour range for all of the plots in Figure 4.65 are identical ($0 \leq \overline{\rho} \leq 10$).

Issue	Body fitted grid	Cartesian grid
Refinement to accurately resolve boundary layers, etc.	Straightforward – stretching towards the body surface allows for the required point placement within regions of high viscous shear, etc.	Difficult – enhanced near wall resolution can only be achieved by widespread refinement of the underlying grid with excessive increase in computational cost or via variable anisotropic refinement with AMR.
Near wall orthogonality (for accurate turbulence modelling).	Can be enforced for convex surfaces, and optimised for concave surfaces.	Difficult, if not impossible (dependent on configuration).
Cost of producing a new mesh.	High, requiring significant user intervention.	Very low, requiring little or no user intervention.
Requirement for multiple domain solvers.	Often required for all but the simplest geometries.	Not required.
Cell skew.	Can be difficult to achieve an acceptable level of skew.	Non-existent apart from with the non-quadrilateral/hexahedral cells at the body surface.
Other comments:	None.	For truly cartesian grids resolution of fluxes perpendicular to the cell edges can be removed (except at the wall) for a reduction in computational overhead. Small cells (due to cutting) can drastically impair convergence and cell merging techniques are often required.

Table 4.1. A Comparison of Body Fitted and Cartesian Gridding Schemes

Configuration	Vertex 1	Vertex 2	Vertex 3	Vertex 4
A	Exterior	Exterior	Exterior	Exterior
B	Exterior	Exterior	Exterior	Interior
C	Exterior	Exterior	Interior	Exterior
D	Exterior	Exterior	Interior	Interior
E	Exterior	Interior	Exterior	Exterior
F	Exterior	Interior	Exterior	Interior
G	Exterior	Interior	Interior	Exterior
H	Exterior	Interior	Interior	Interior
I	Interior	Exterior	Exterior	Exterior
J	Interior	Exterior	Exterior	Interior
K	Interior	Exterior	Interior	Exterior
L	Interior	Exterior	Interior	Interior
M	Interior	Interior	Exterior	Exterior
N	Interior	Interior	Exterior	Interior
O	Interior	Interior	Interior	Exterior
P	Interior	Interior	Interior	Interior

Table 4.2. 16 Cell Types Possible With Quad-Vertex Winding

No. Interior	No. Exterior	Action	Reason
0	4	None	Cell is completely exterior.
1	3	Adapt	Cell is straddling the body.
2	2	Adapt	Cell is straddling the body.
3	1	None.	Adjacent cell will have a single interior vertex.
4	0	Inhibit adaption	Prevent adaption on physical grounds – complete inside body.

Table 4.3. Refinement Criteria Used For Body Capture.

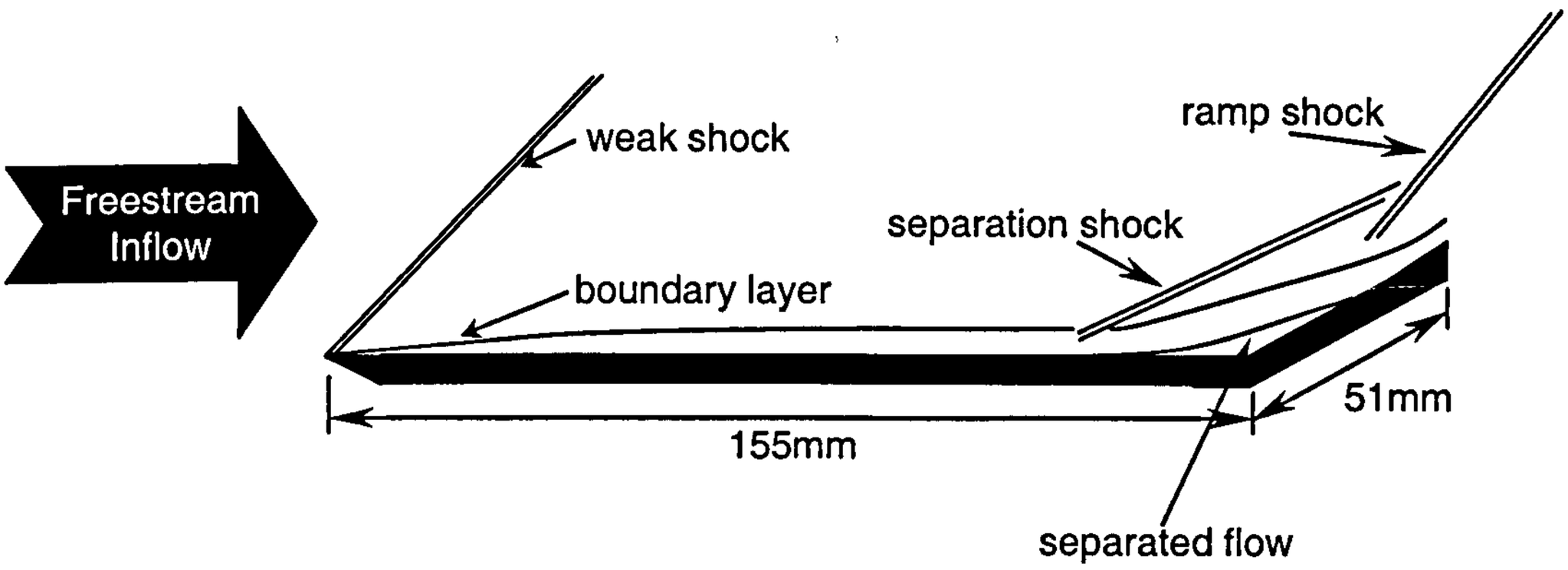

Figure 4.1. Schematic of Smith [ref] Experimental Configuration [67]

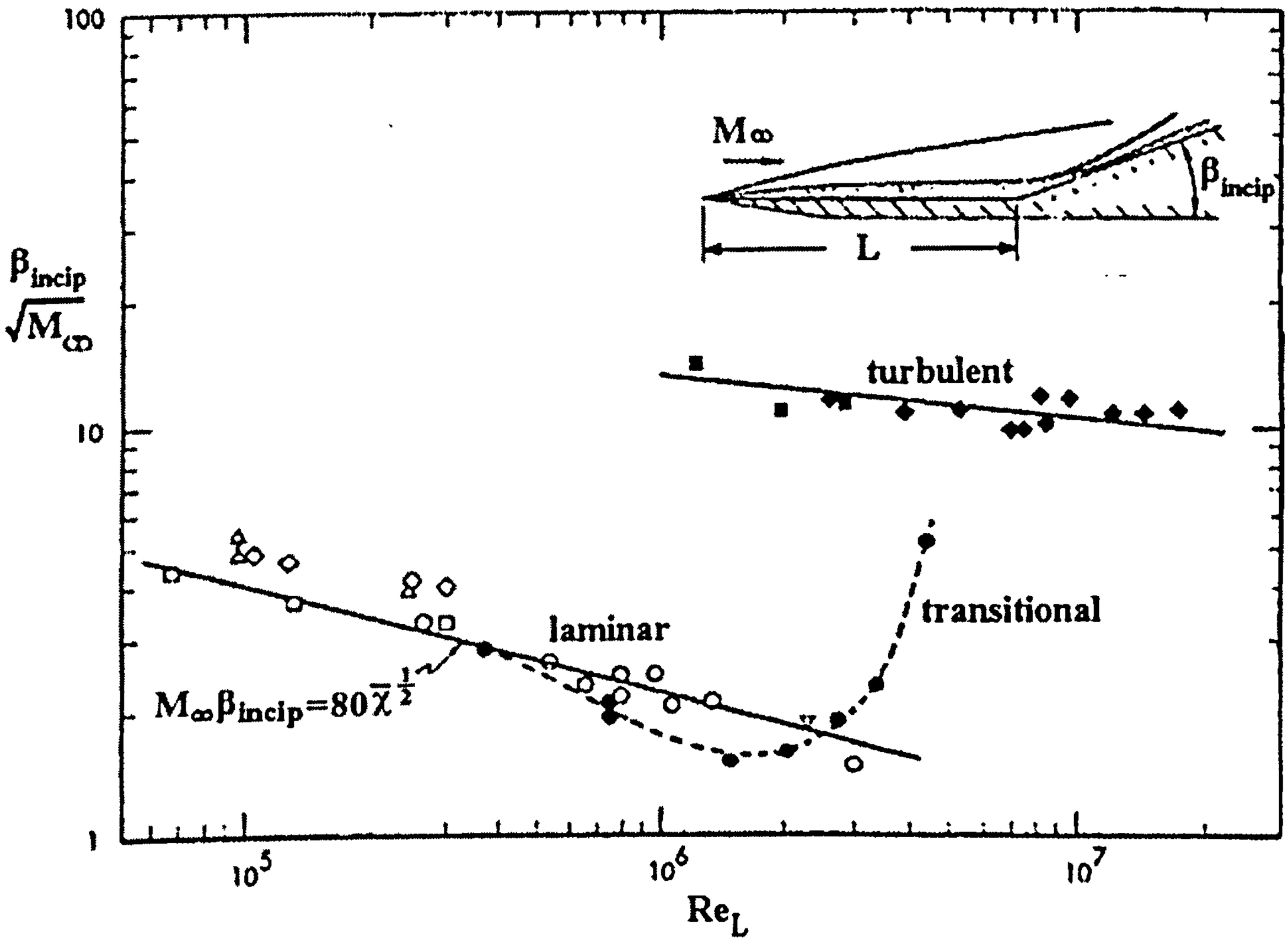

Figure 4.2. Incipient Separation Angles for Laminar, Transitional and Turbulent Flows [142]

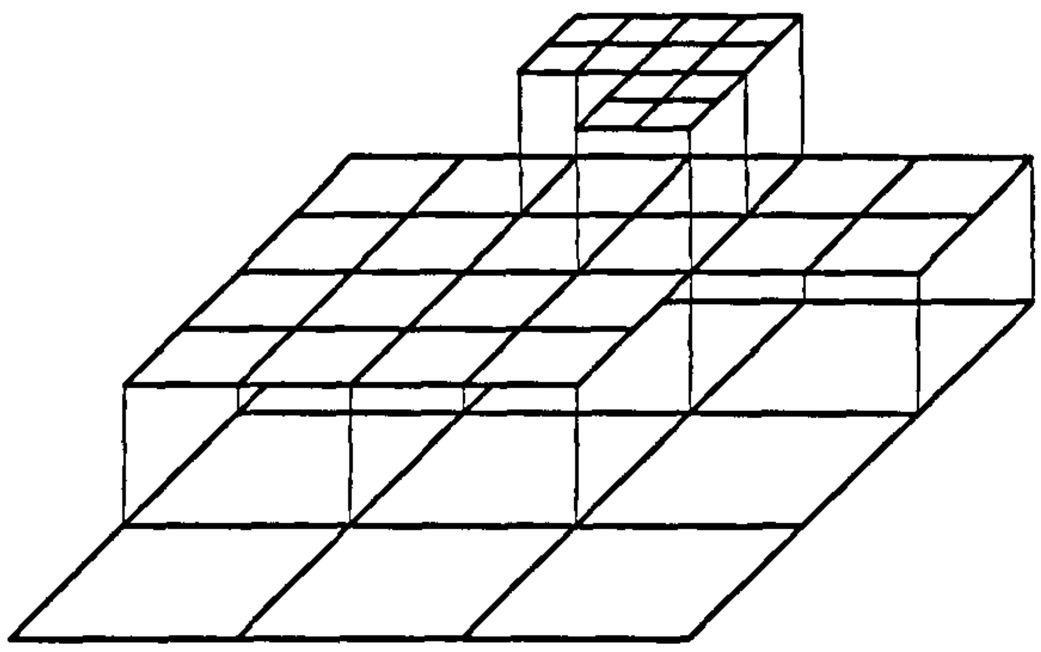

Figure 4.3. Hierarchical Mesh Refinement

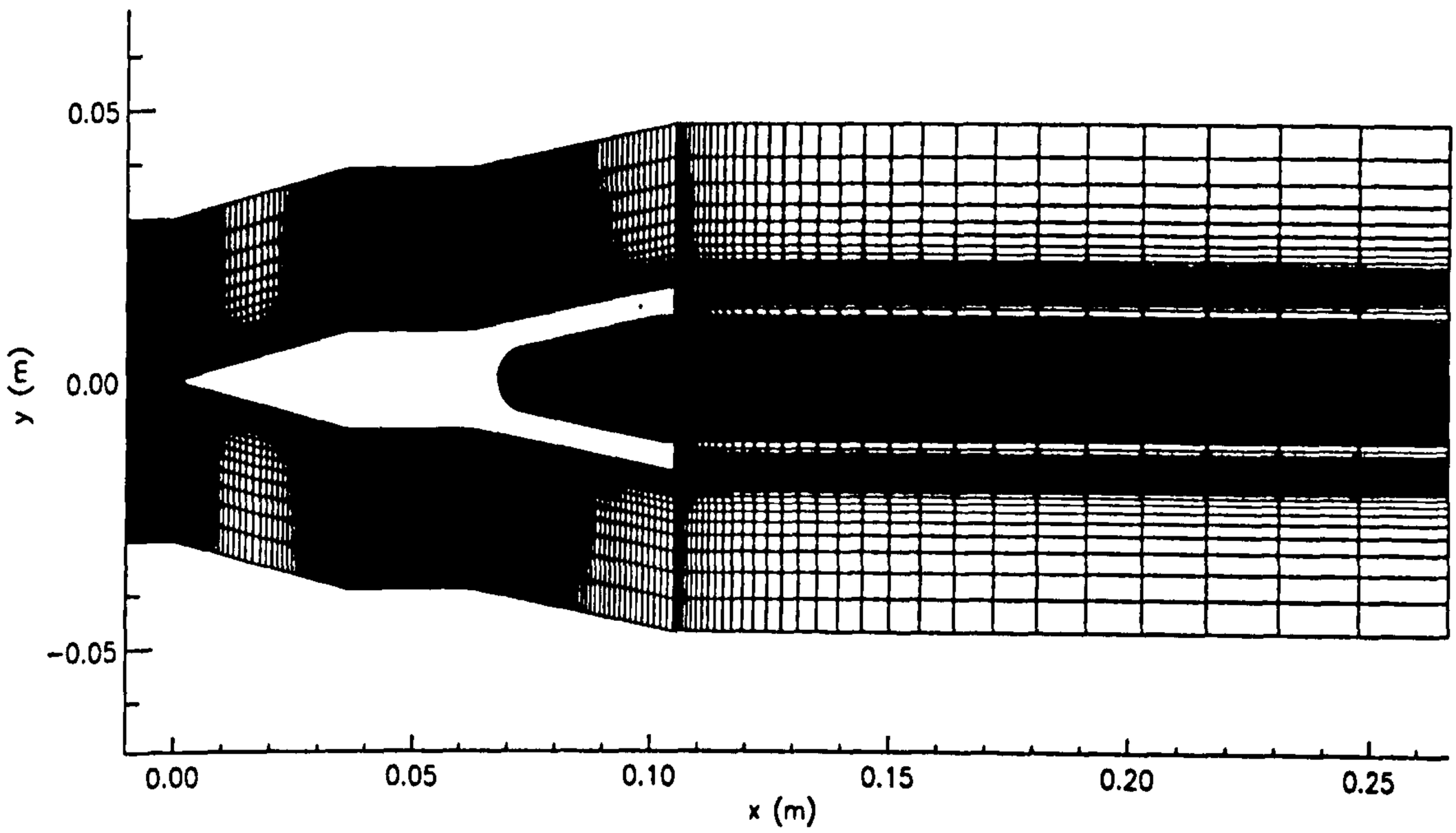

Figure 4.4. CAN4 Axisymmetric Body Fitted Mesh

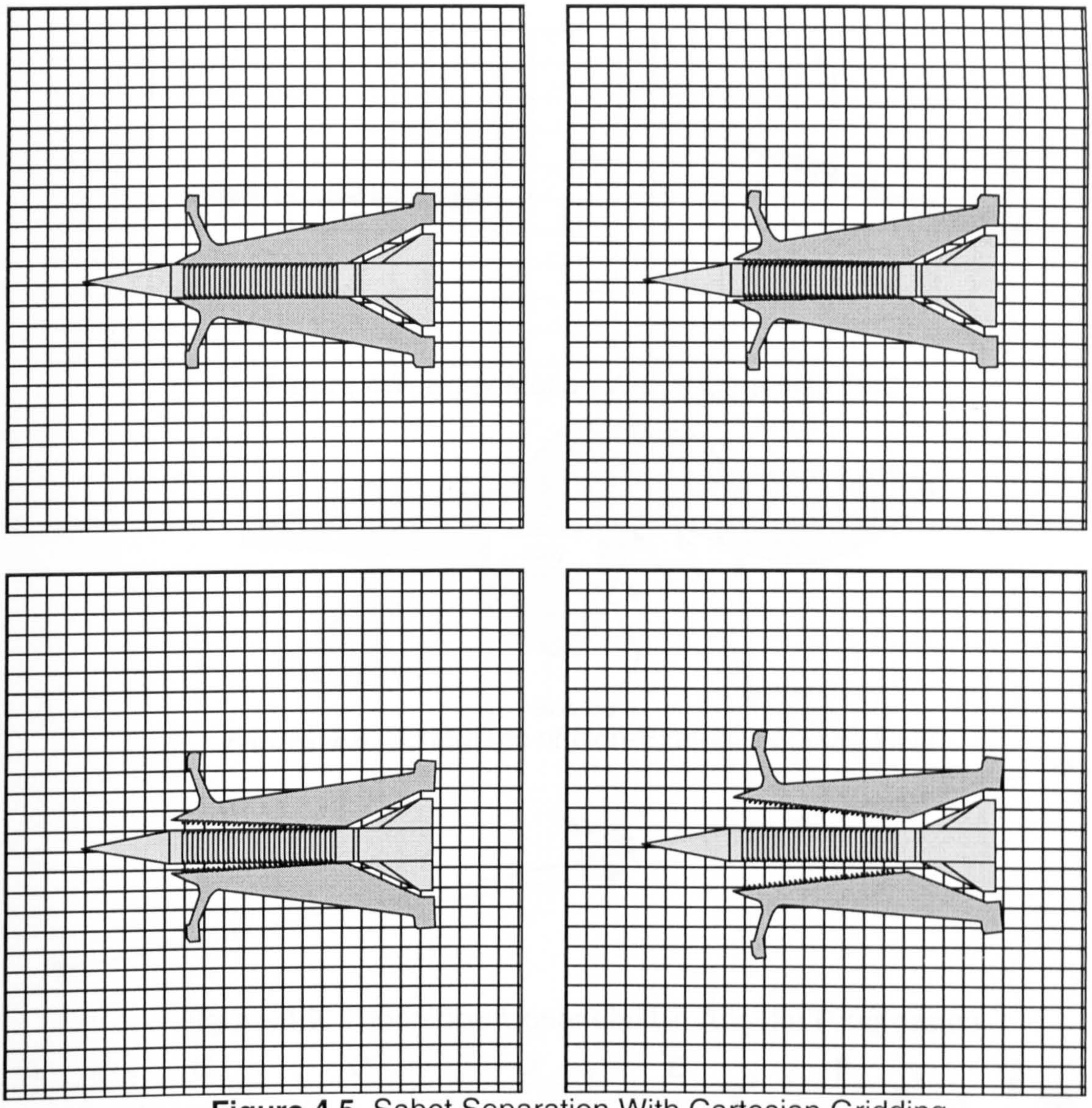

Figure 4.5. Sabot Separation With Cartesian Gridding

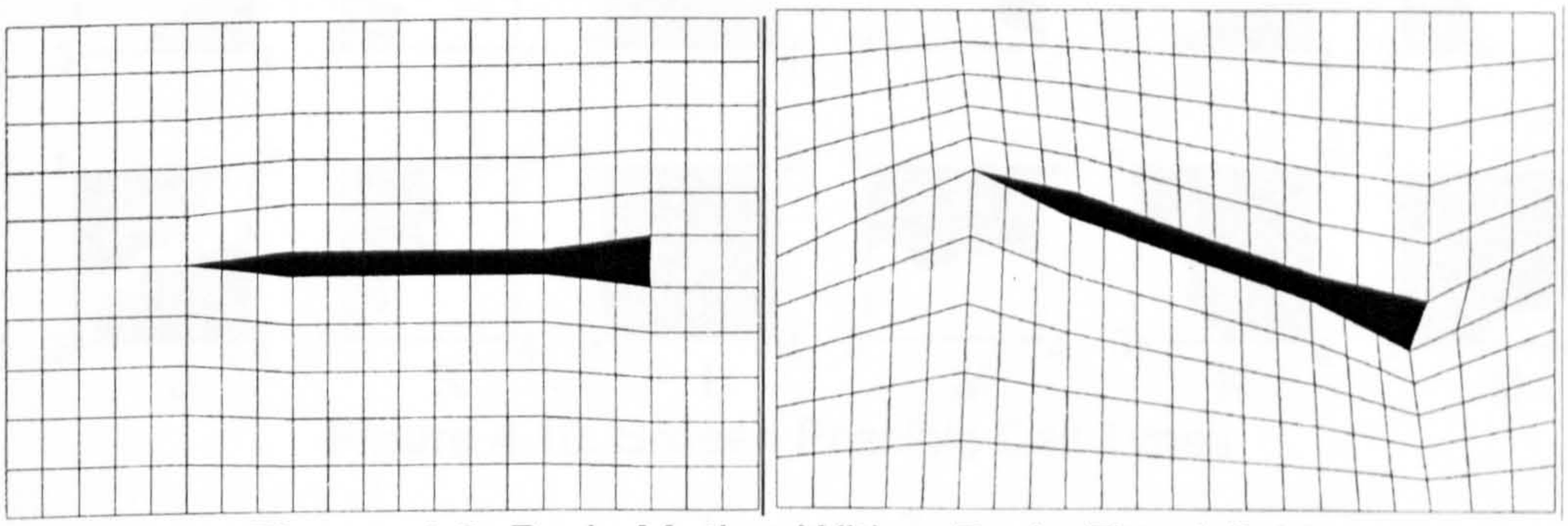

Figure 4.6. Body Motion With a Body Fitted Grid

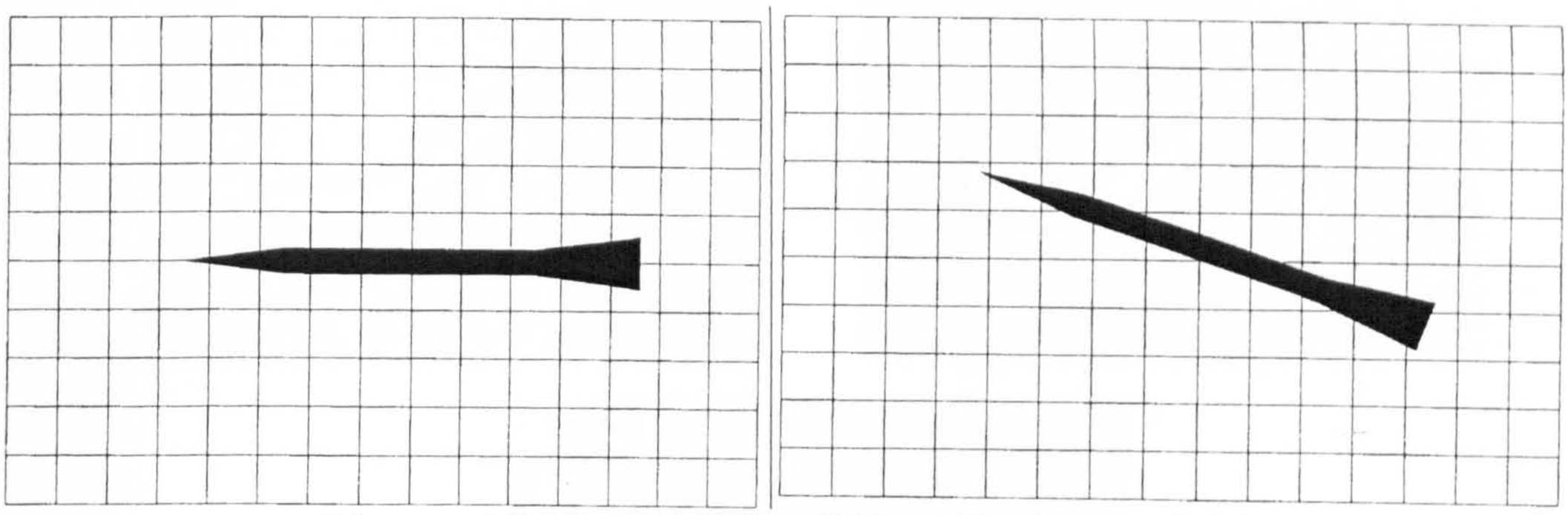

Figure 4.7. Body Motion With a Cartesian Grid

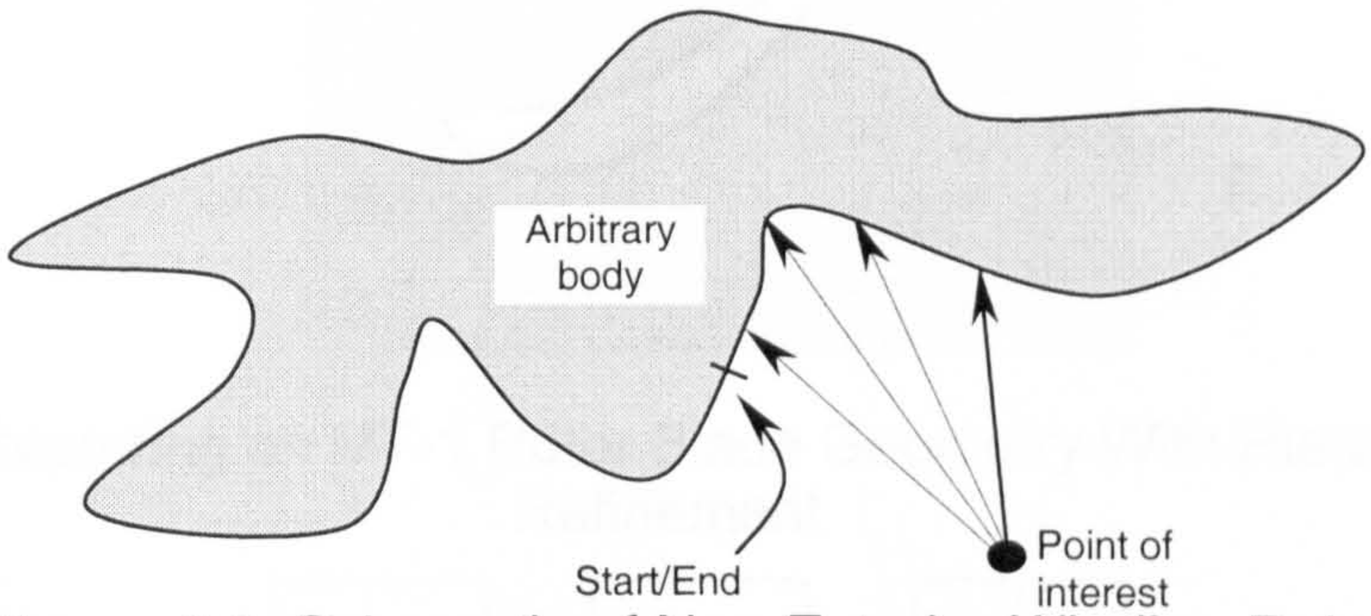

Figure 4.8. Schematic of Non-Exterior Winding Rule

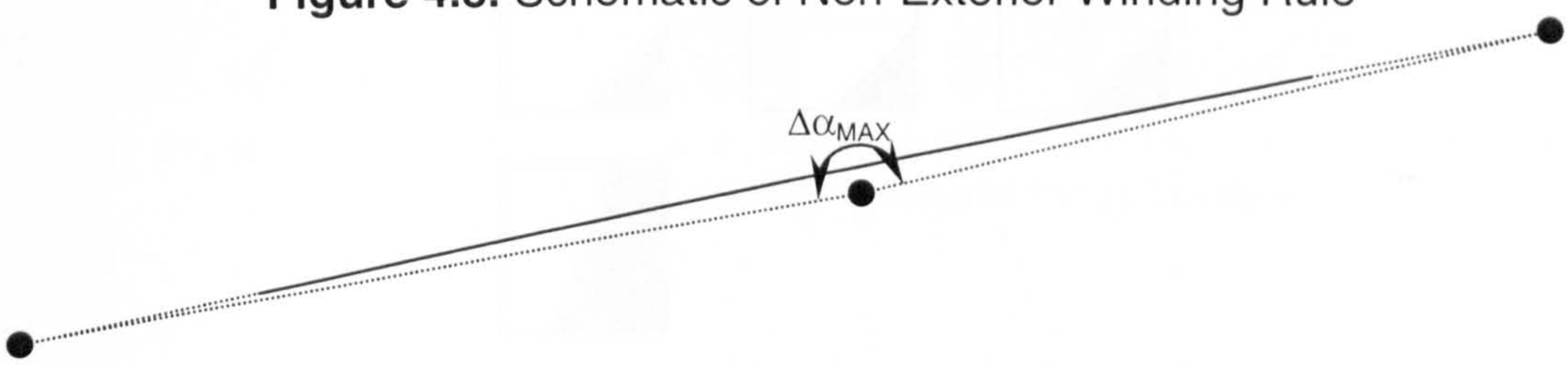

Figure 4.9. Theoretical Upper Limit in Angular Progression

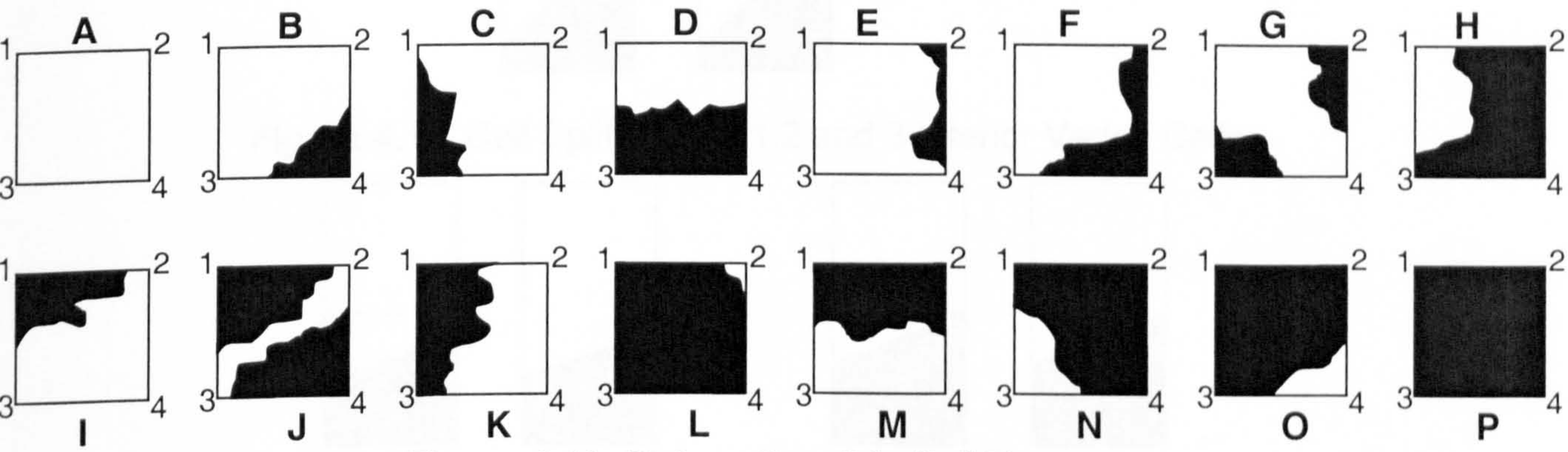

Figure 4.10. Sixteen Possible Cell Types

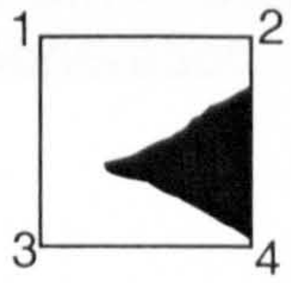

Figure 4.11. 'Illegal' Cell

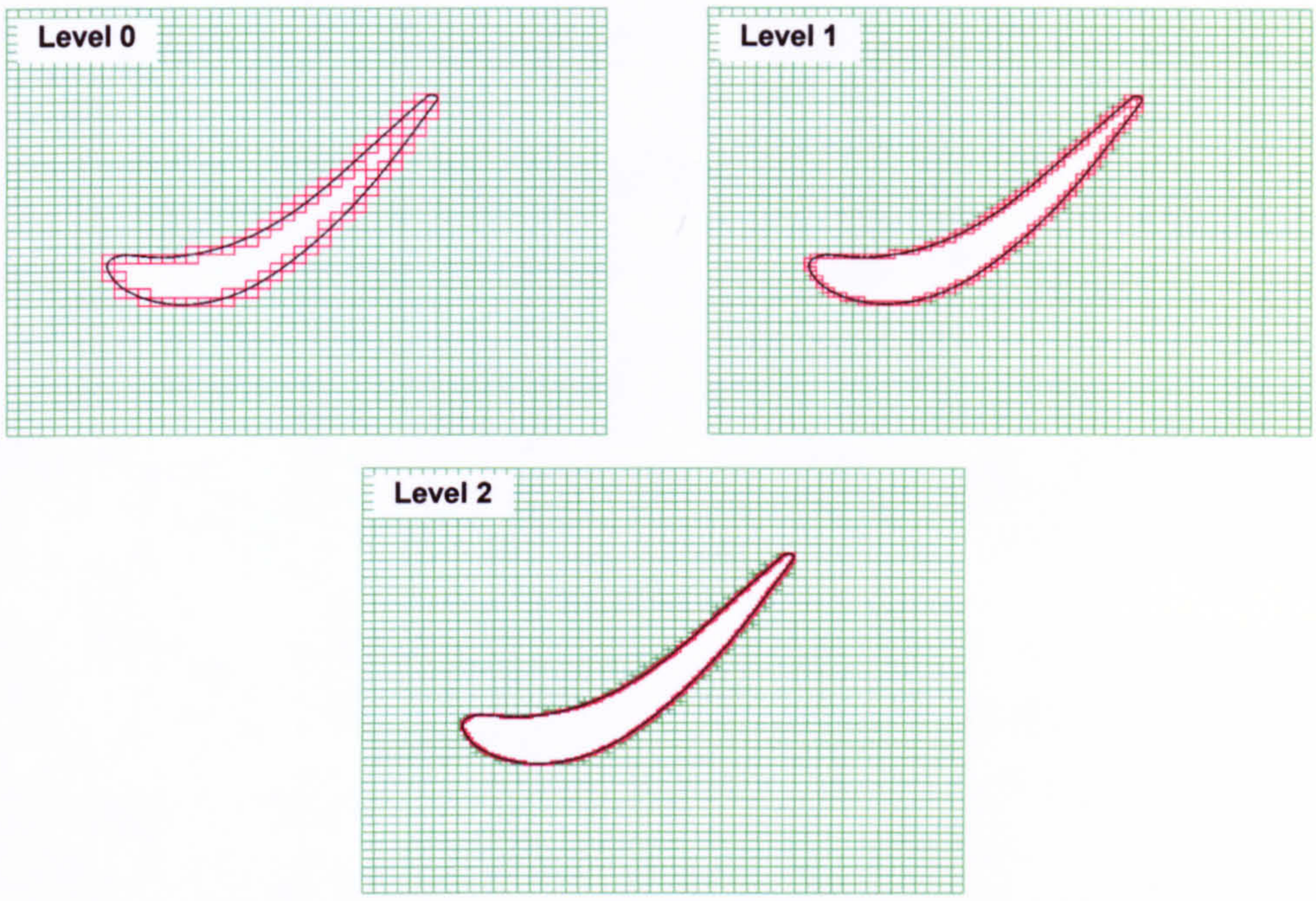

Figure 4.12. Capturing an MT-1 Rotor Blade Geometry With Hierarchical Mesh Refinement

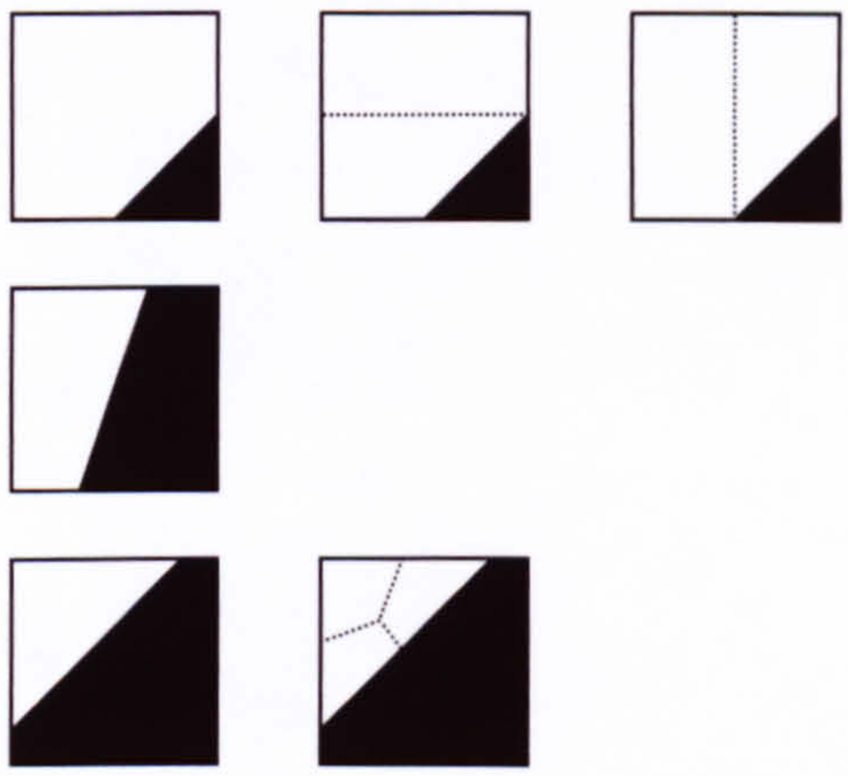

Figure 4.13. Cell Splitting For 1,2 and 3 Interior Vertex Cells

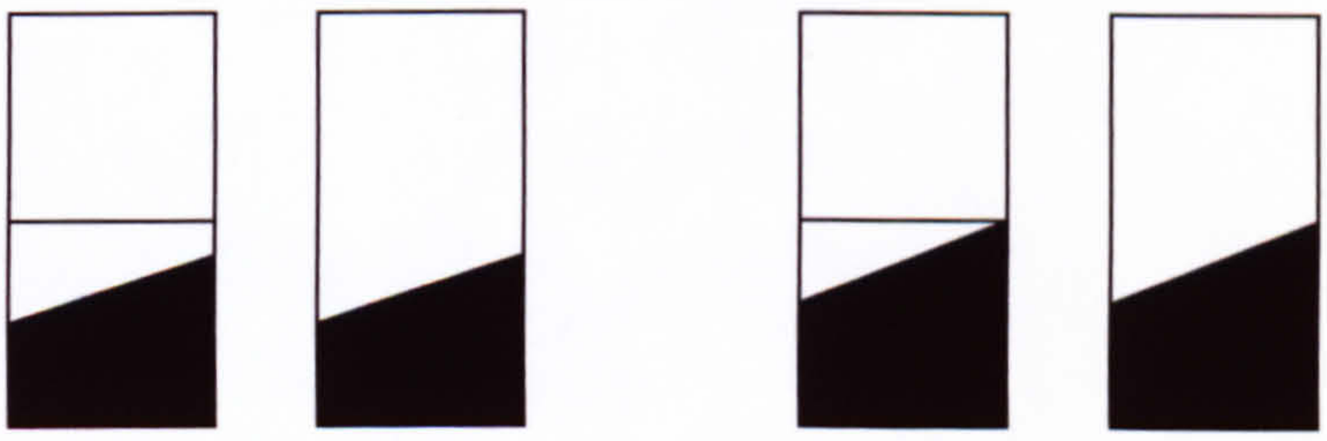

Figure 4.14. Cell Merging to Avoid Small Cells and Ensure Quadrilateral Cell Generation

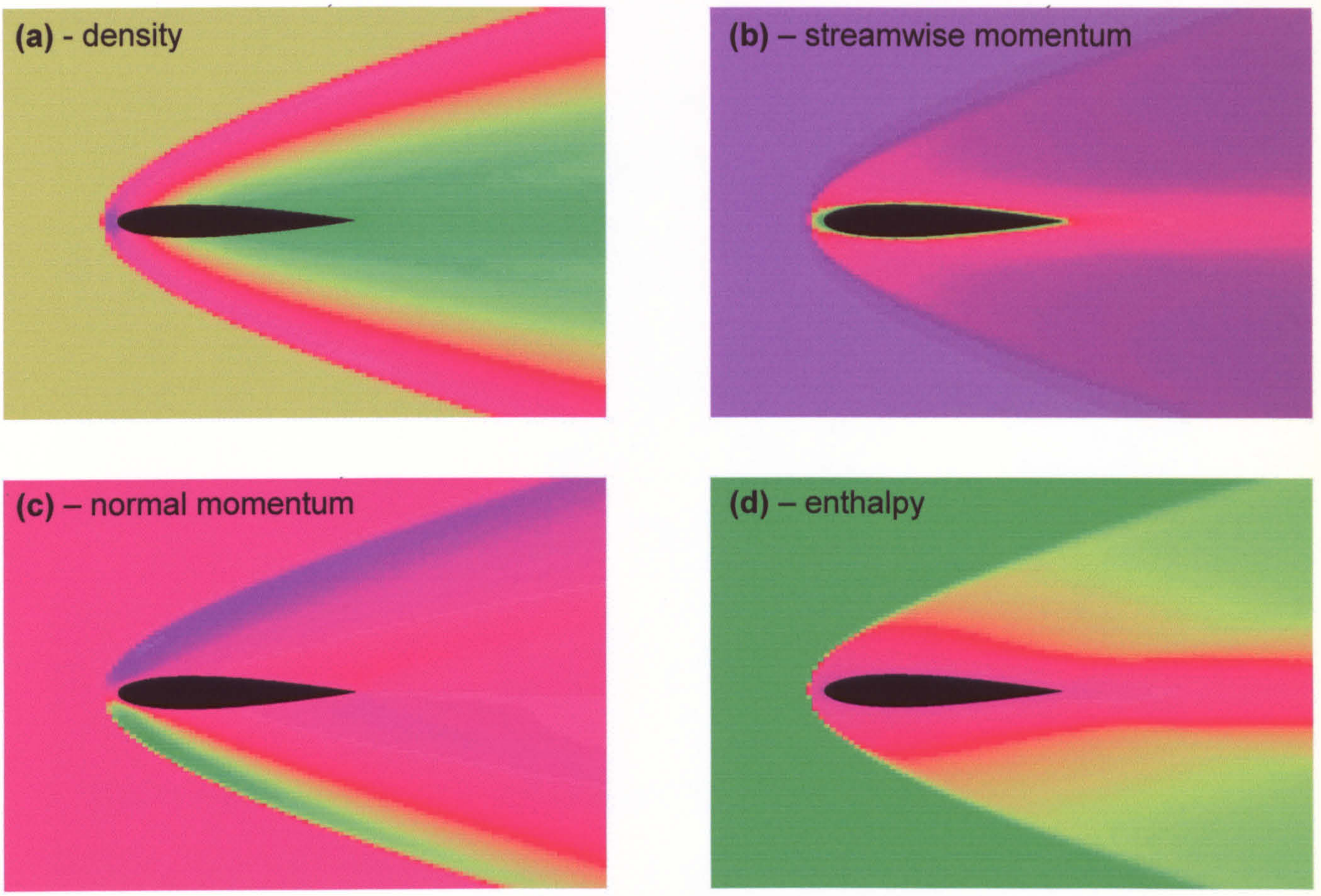

Figure 4.15. Computational Viscous Mach 5 Flow Over NACA 65-009 Aerofoil Employing Adaptive Body Recovery

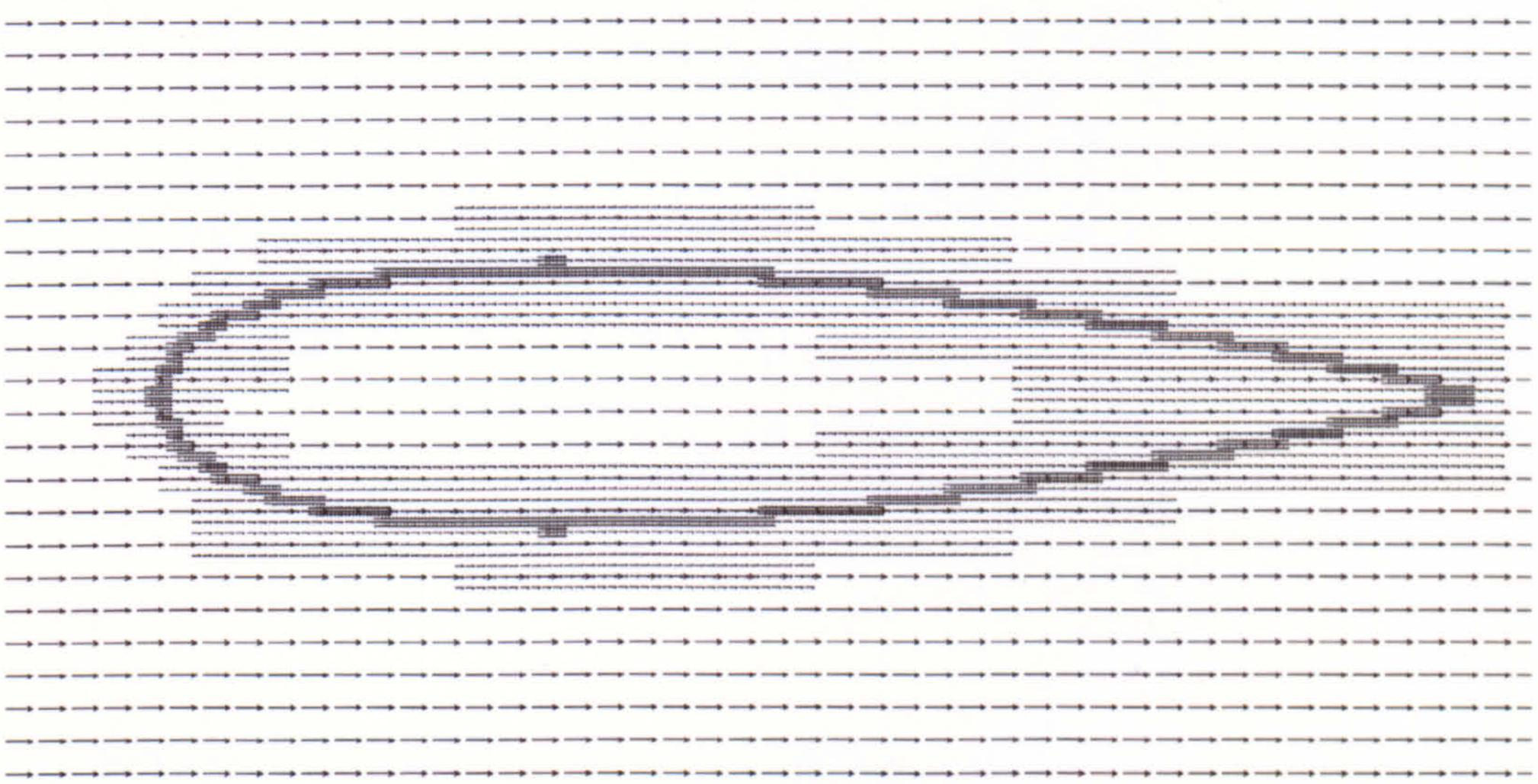

Figure 4.16. Flowfield Prior to First Iteration – Viscous Flow

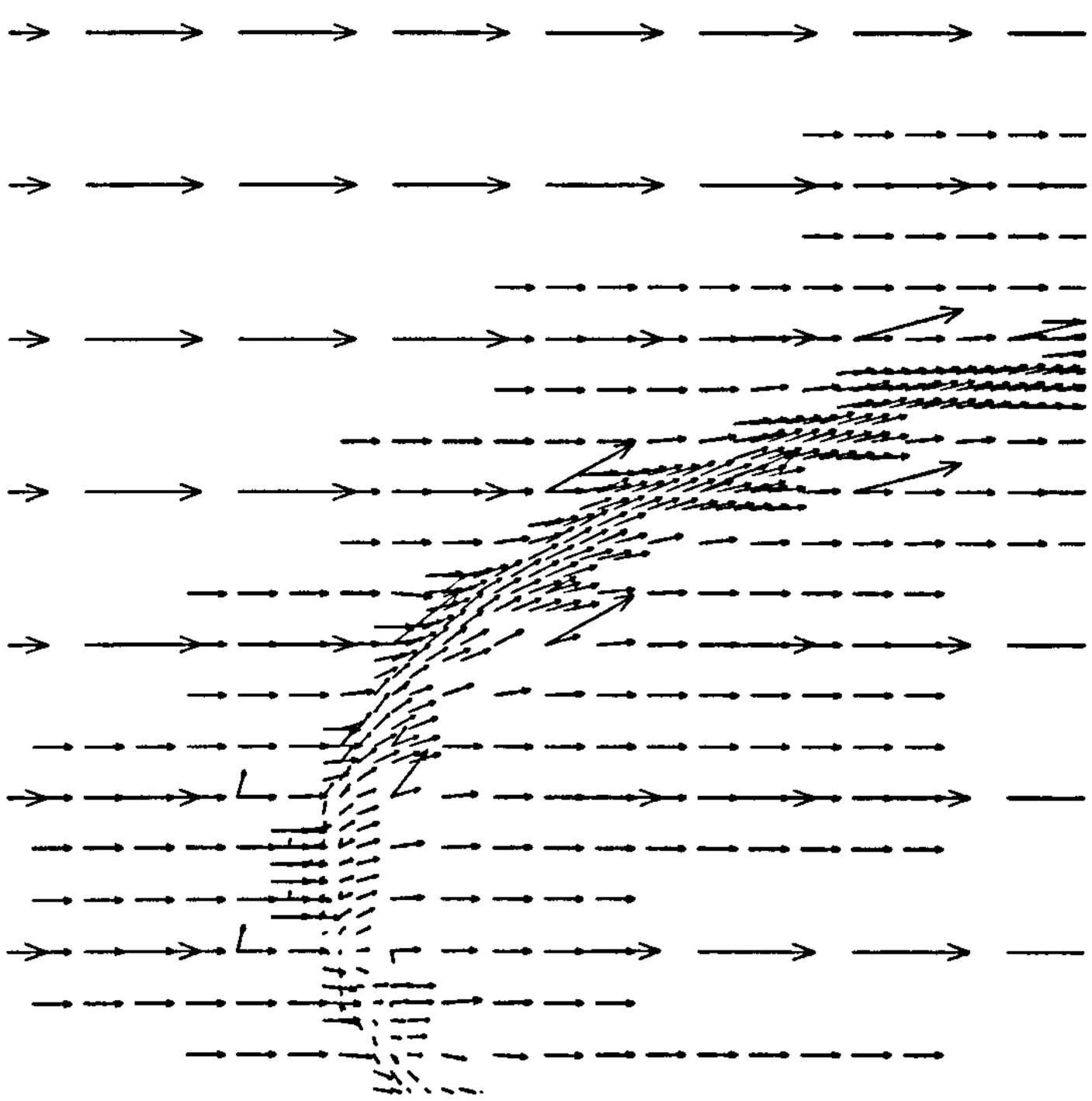

Figure 4.17. Flowfield Prior to First Iteration – Inviscid Flow – Leading Edge.

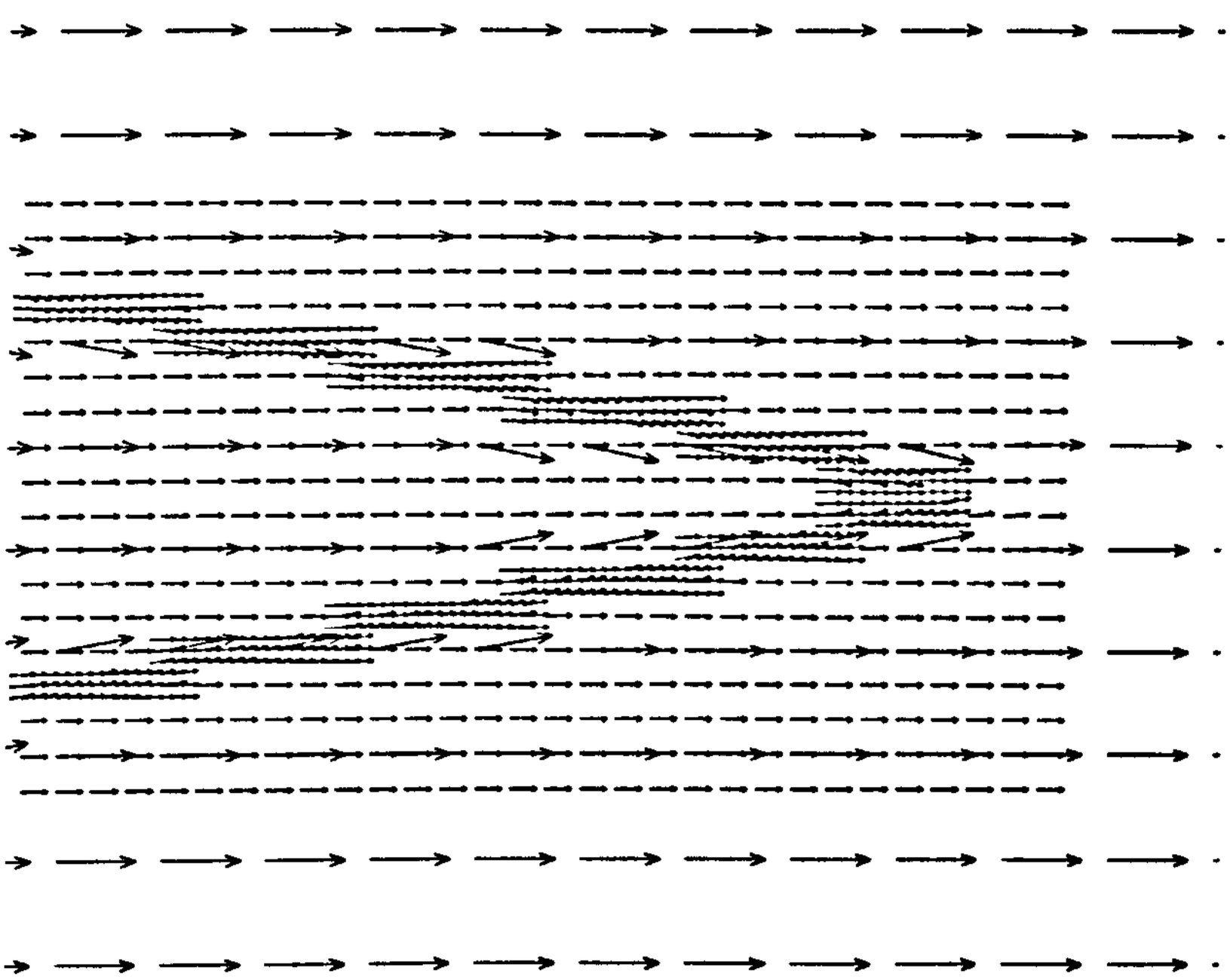

Figure 4.18. Flowfield Prior to First Iteration – Inviscid Flow – Trailing Edge.

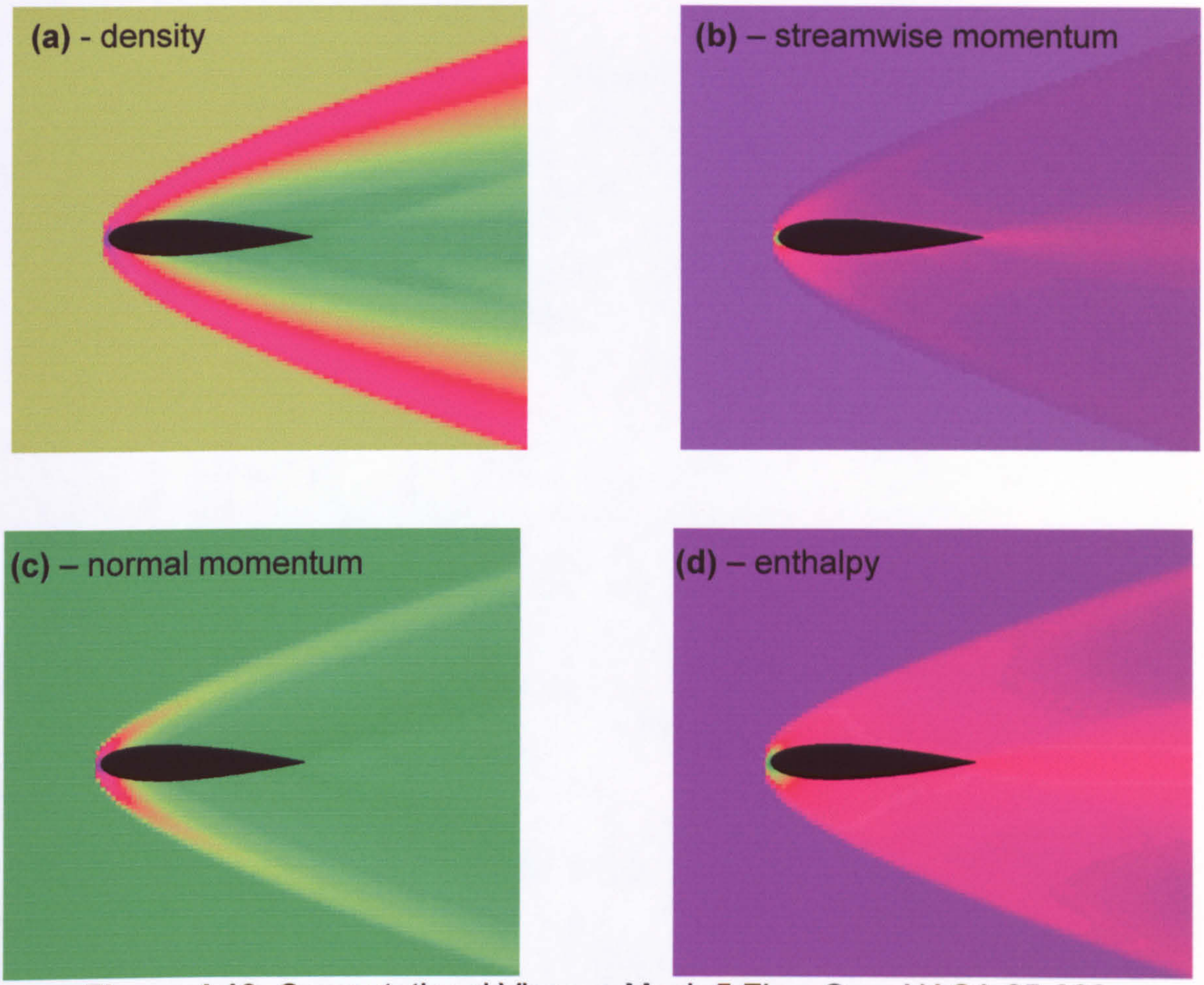

Figure 4.19. Computational Viscous Mach 5 Flow Over NACA 65-009 Aerofoil Employing Adaptive Body Recovery

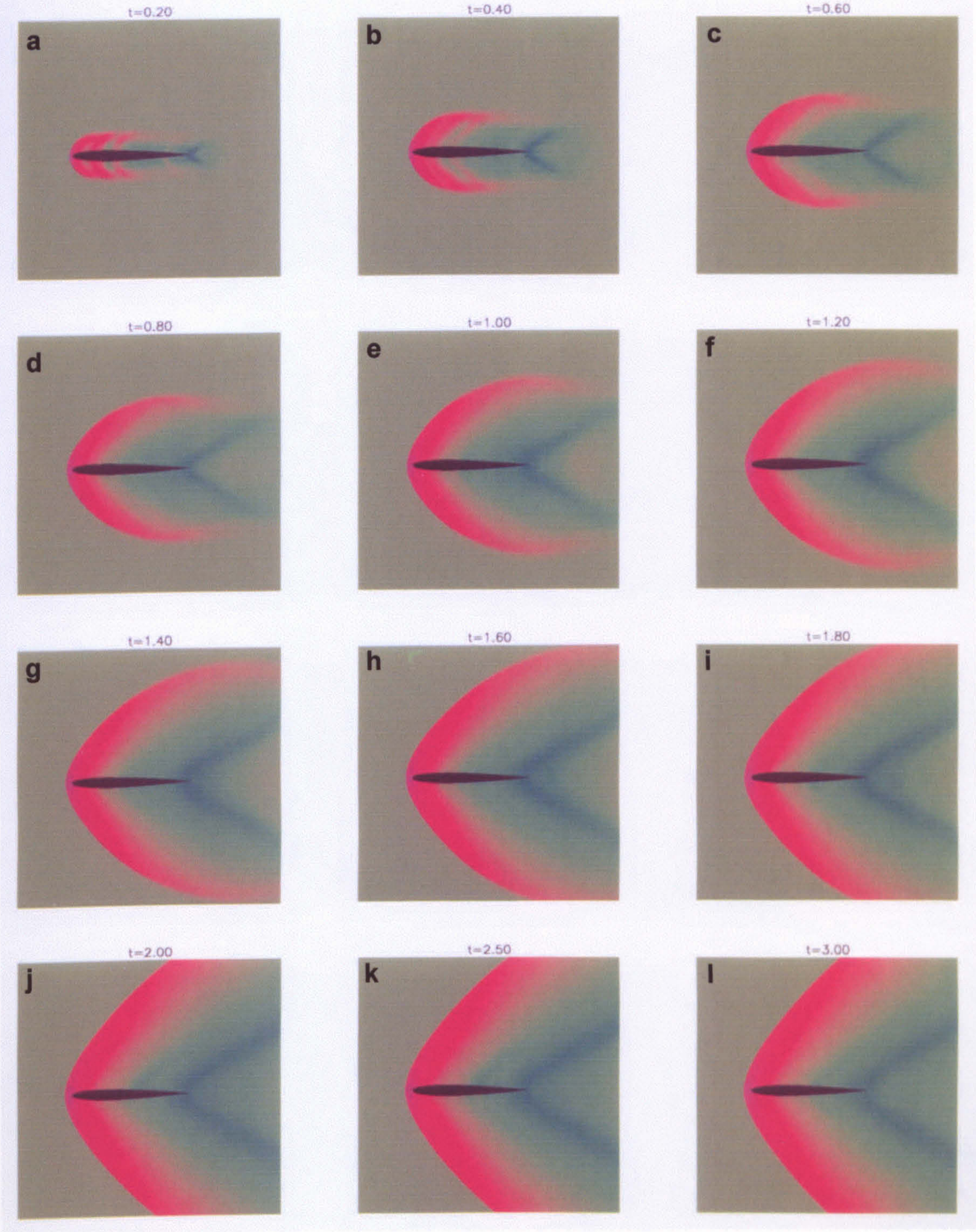

Figure 4.20. Convergence of an Inviscid NACA65-009 Aerofoil Flow

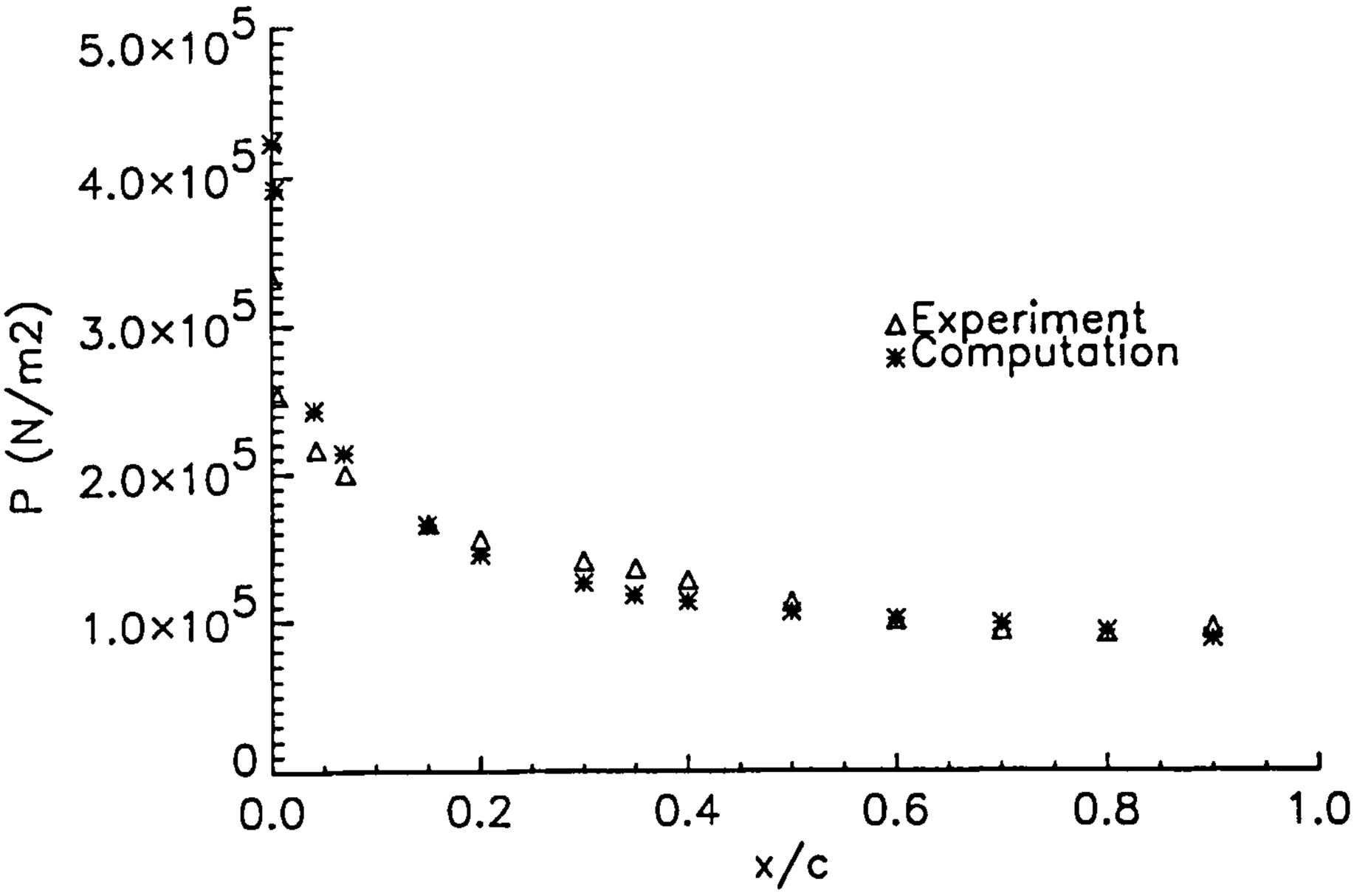

Figure 4.21. Windward Surface Pressure Distribution

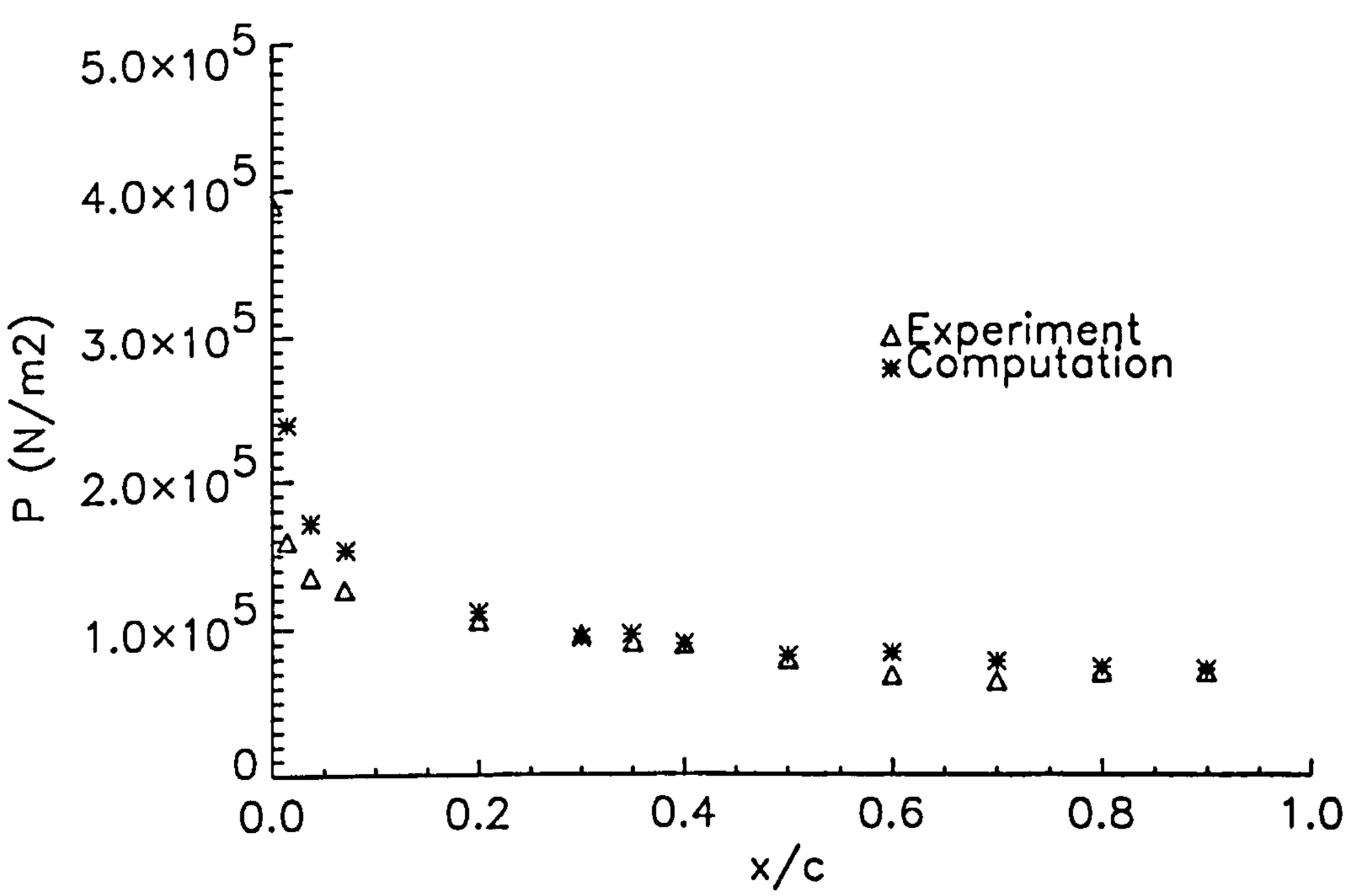

Figure 4.22. Leeward Surface Pressure Distribution

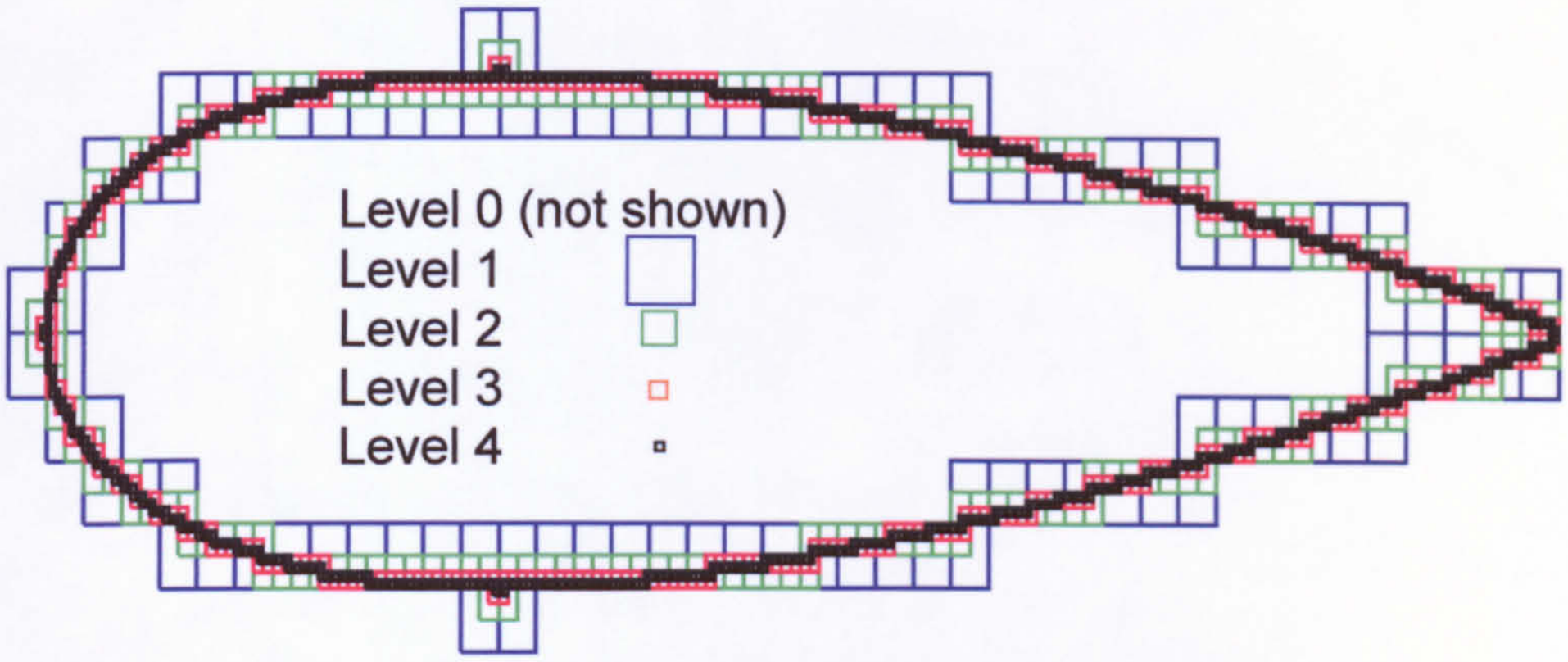

Figure 4.23. Body Surface Grid Hierarchy

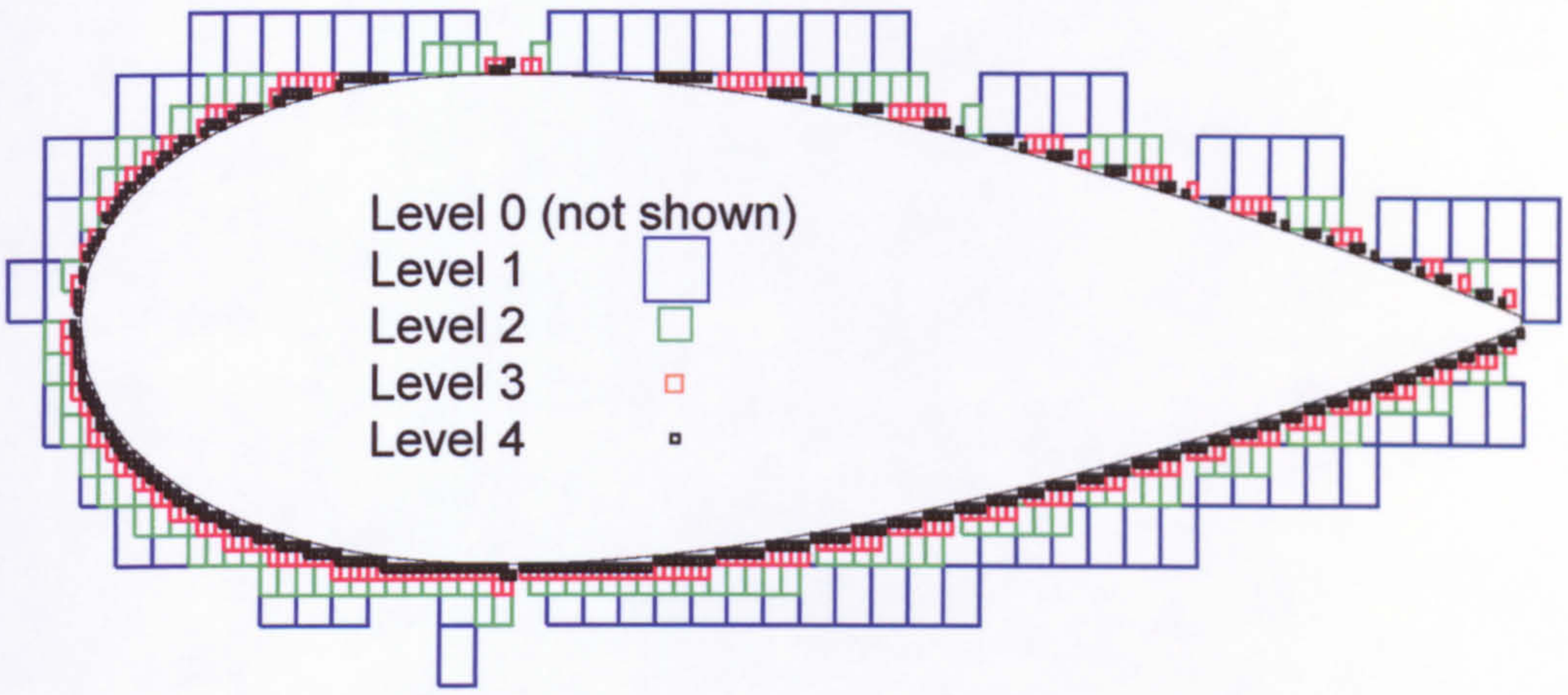

Figure 4.24. Mirror Cell Grid Hierarchy

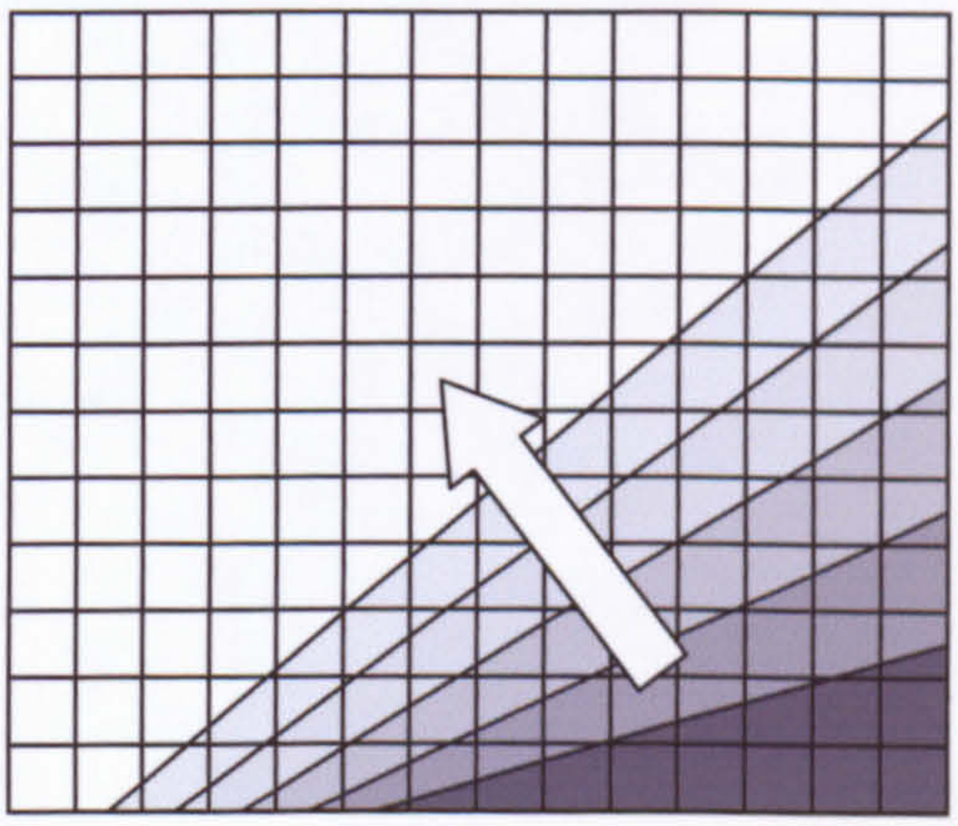

Figure 4.25. Cell Destruction Due To Surface Motion

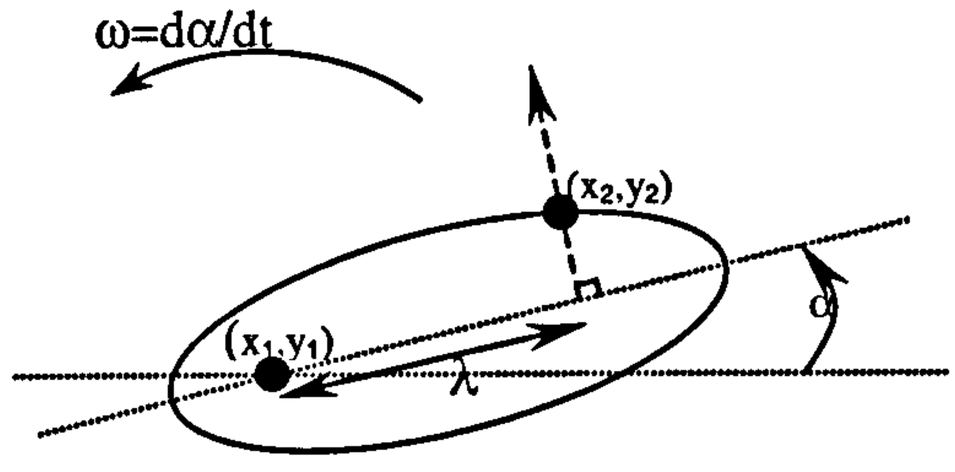

Figure 4.26. Angular Body Motion

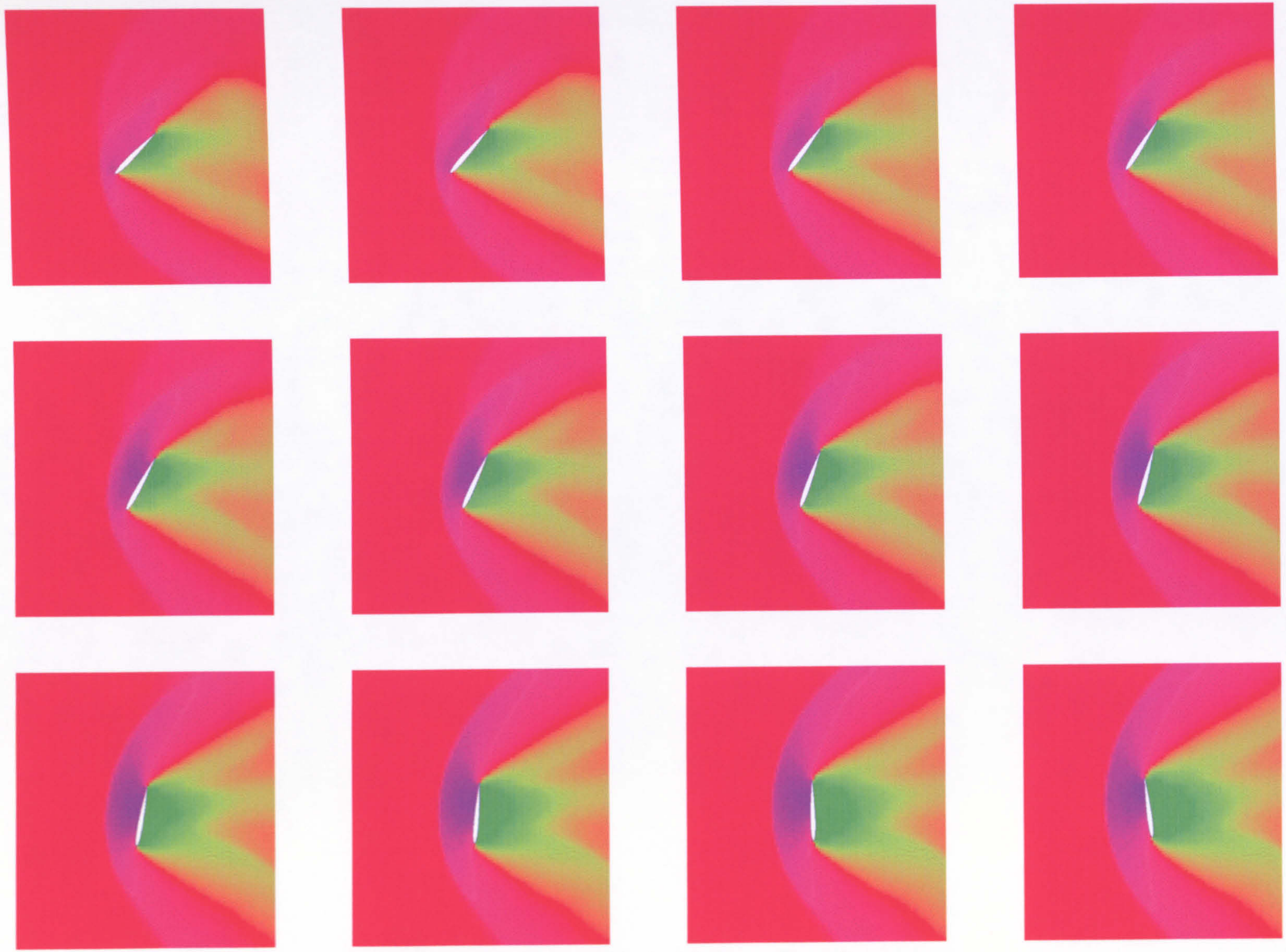

Figure 4.27. Forced Body Motion - Density

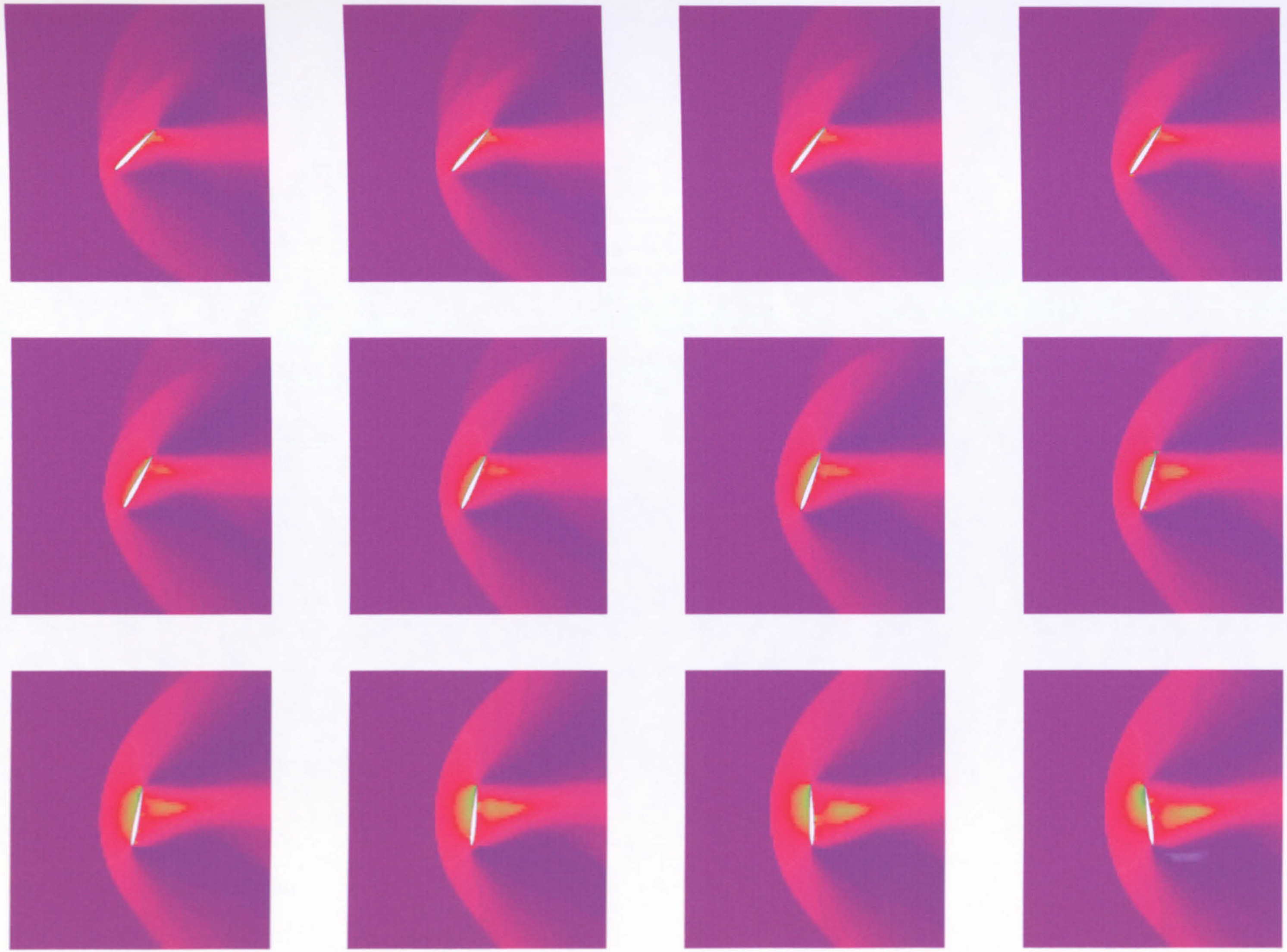

Figure 4.28. Forced Body Motion – Streamwise Velocity

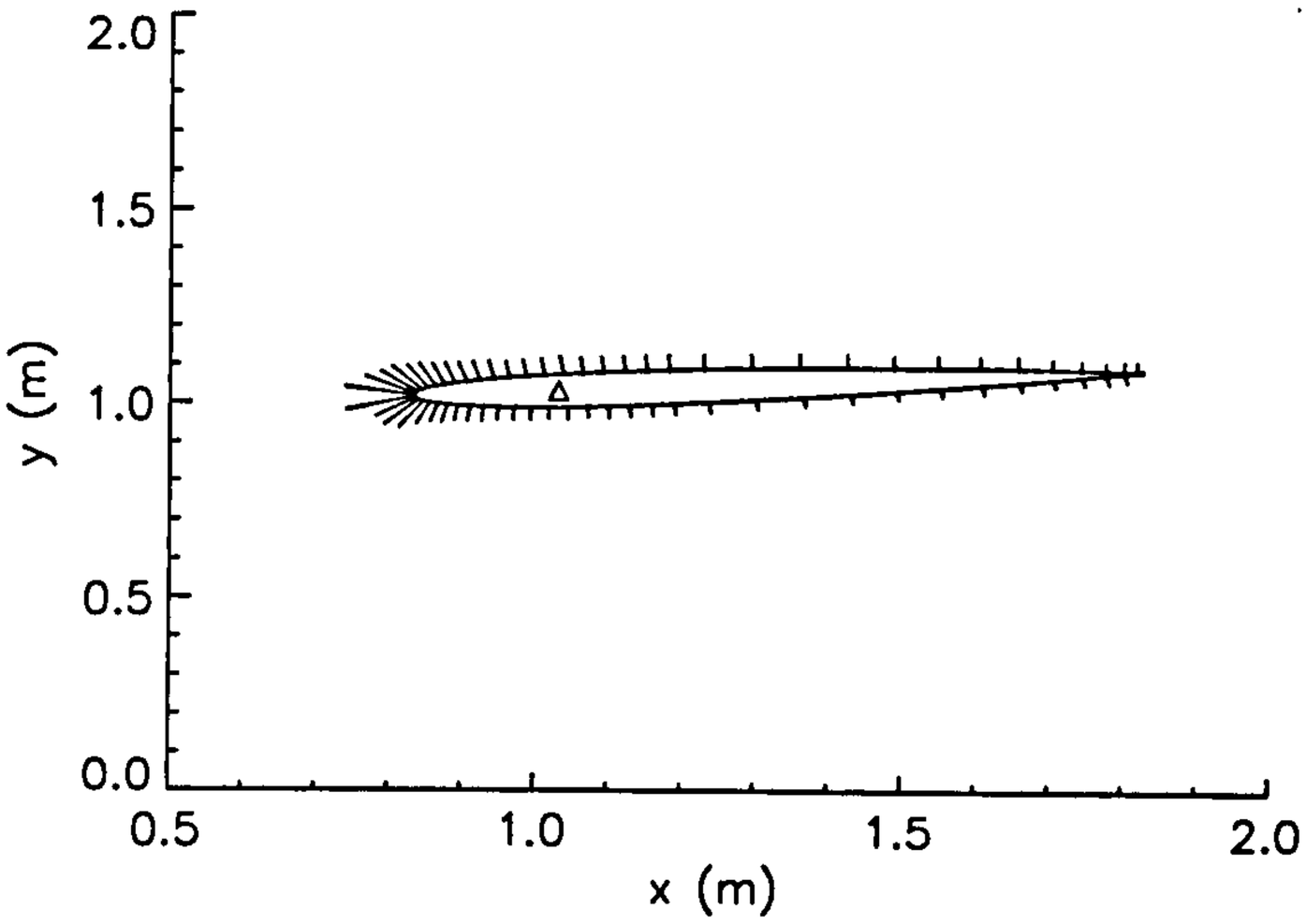

Figure 4.29. Surface Pressure

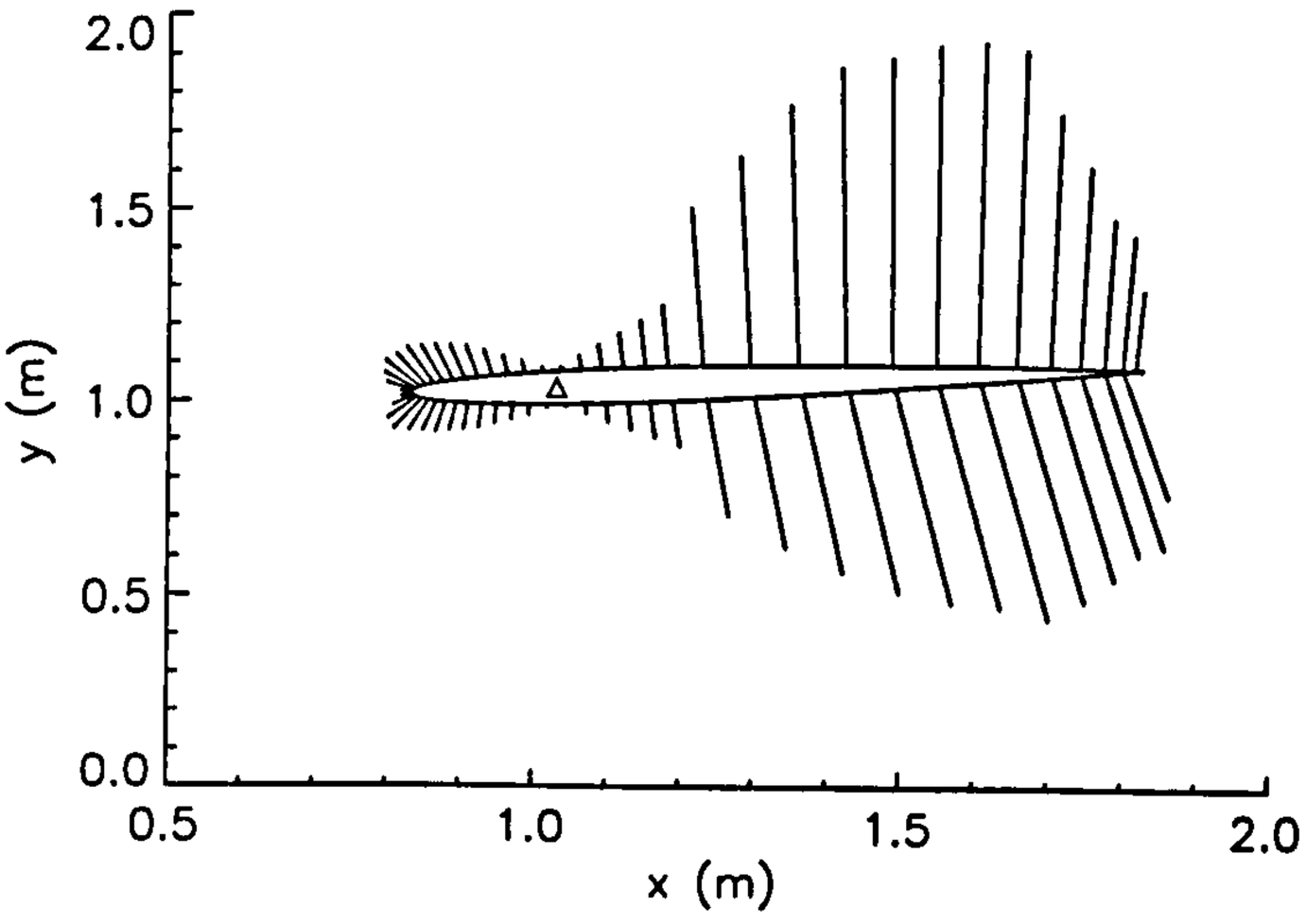

Figure 4.30. Moment Distribution

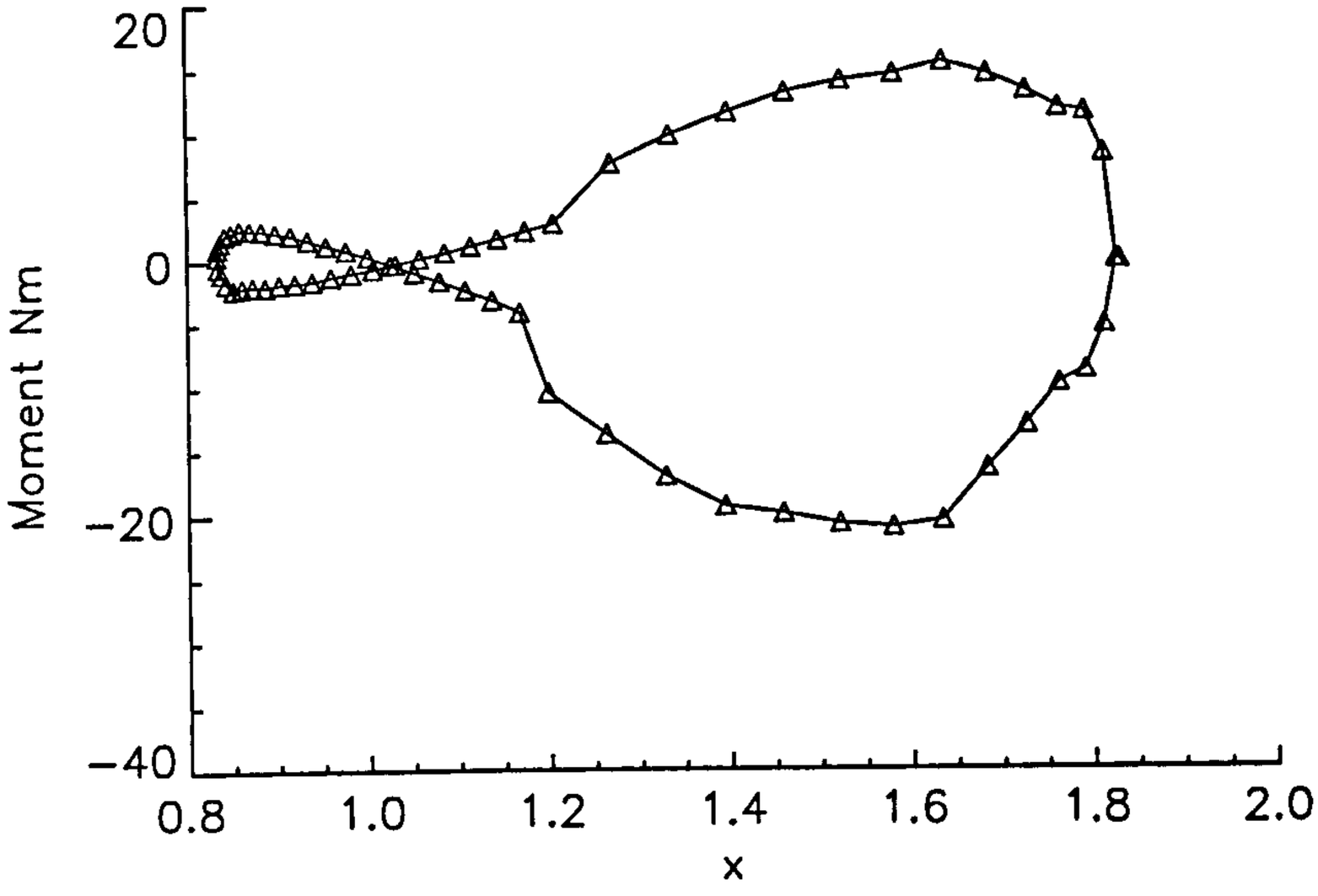

Figure 4.31. Moment Contributions

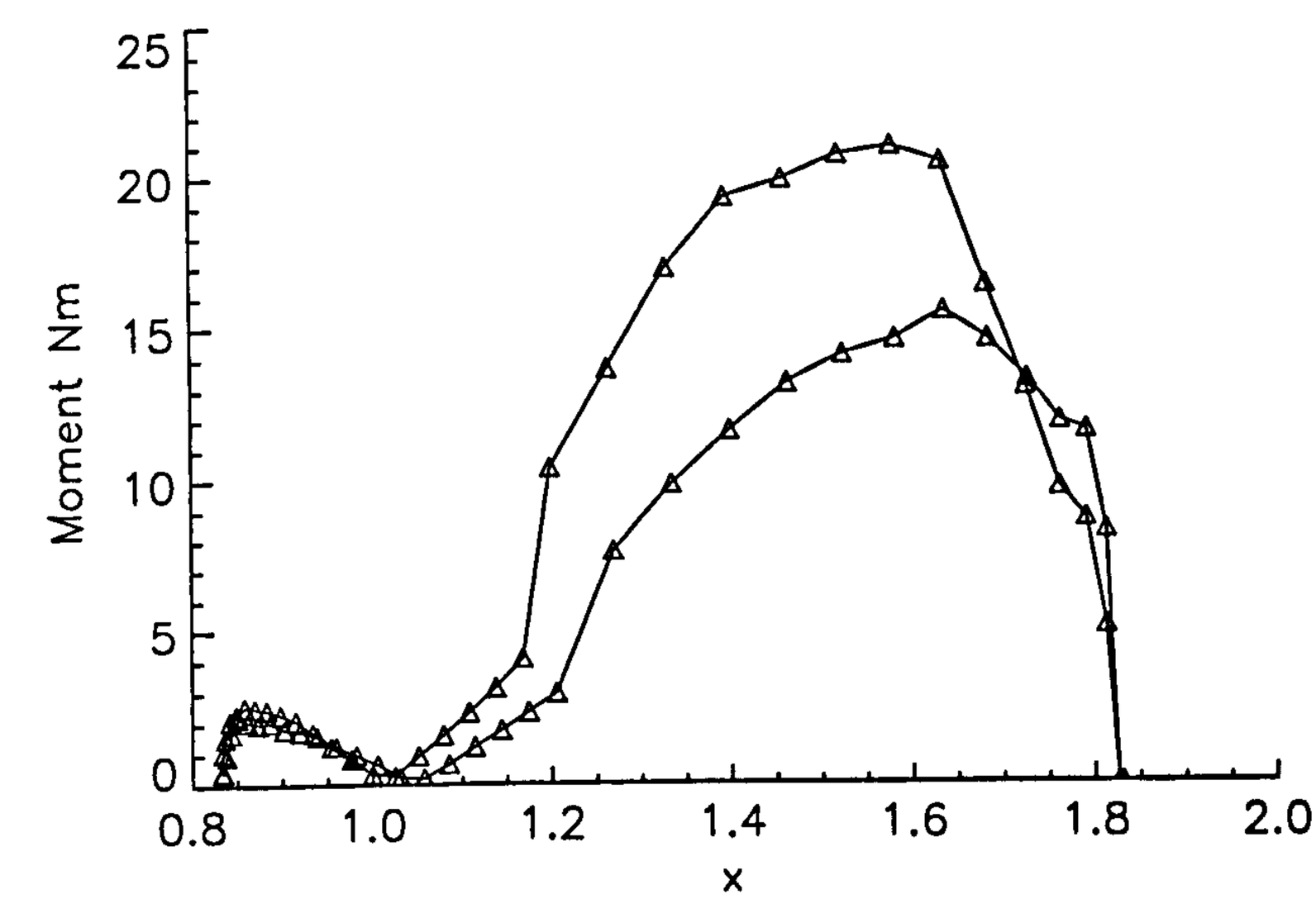

Figure 4.32. Absolute Moment Contributions

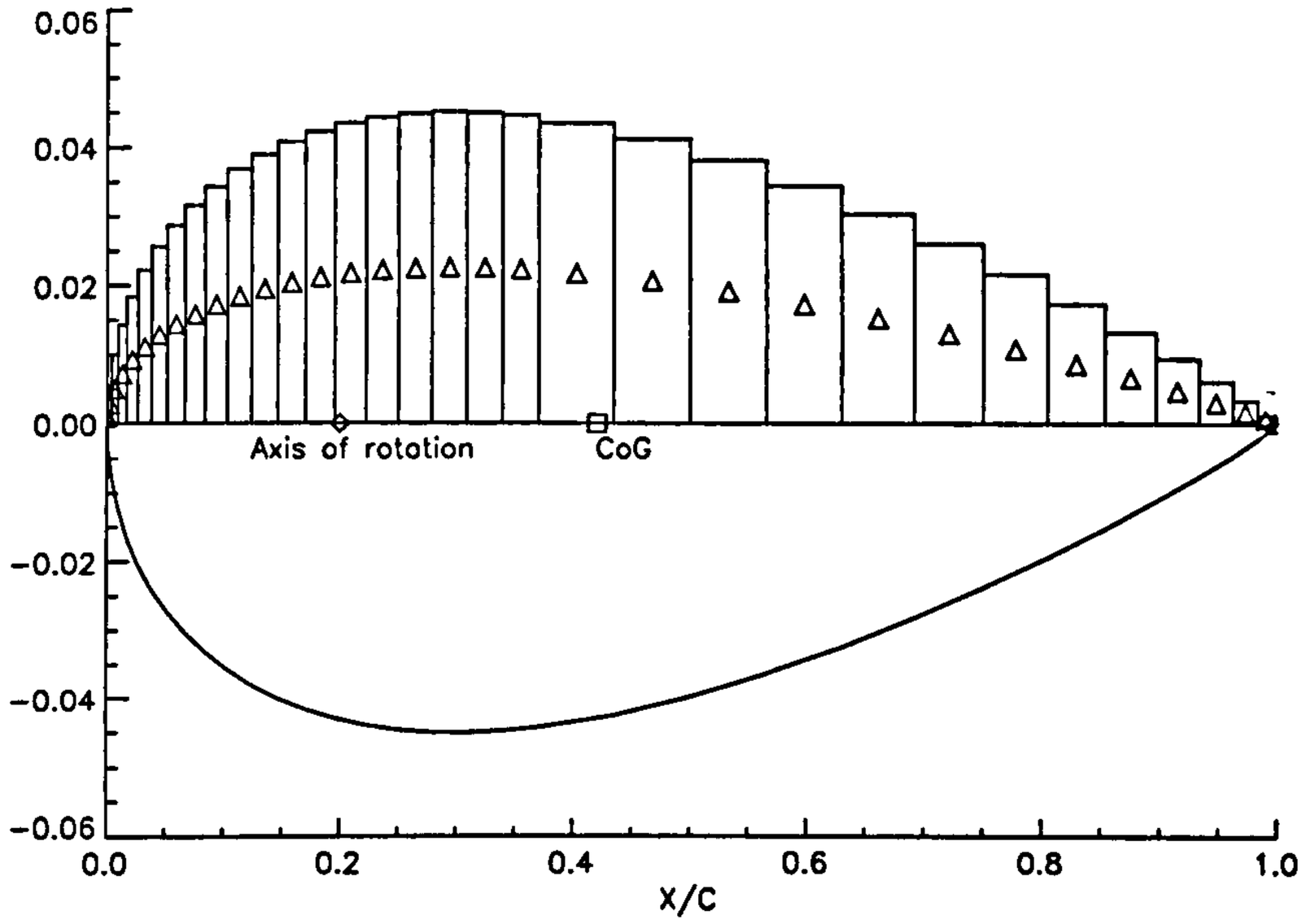

Figure 4.33. Numerical Integration of Body Surface

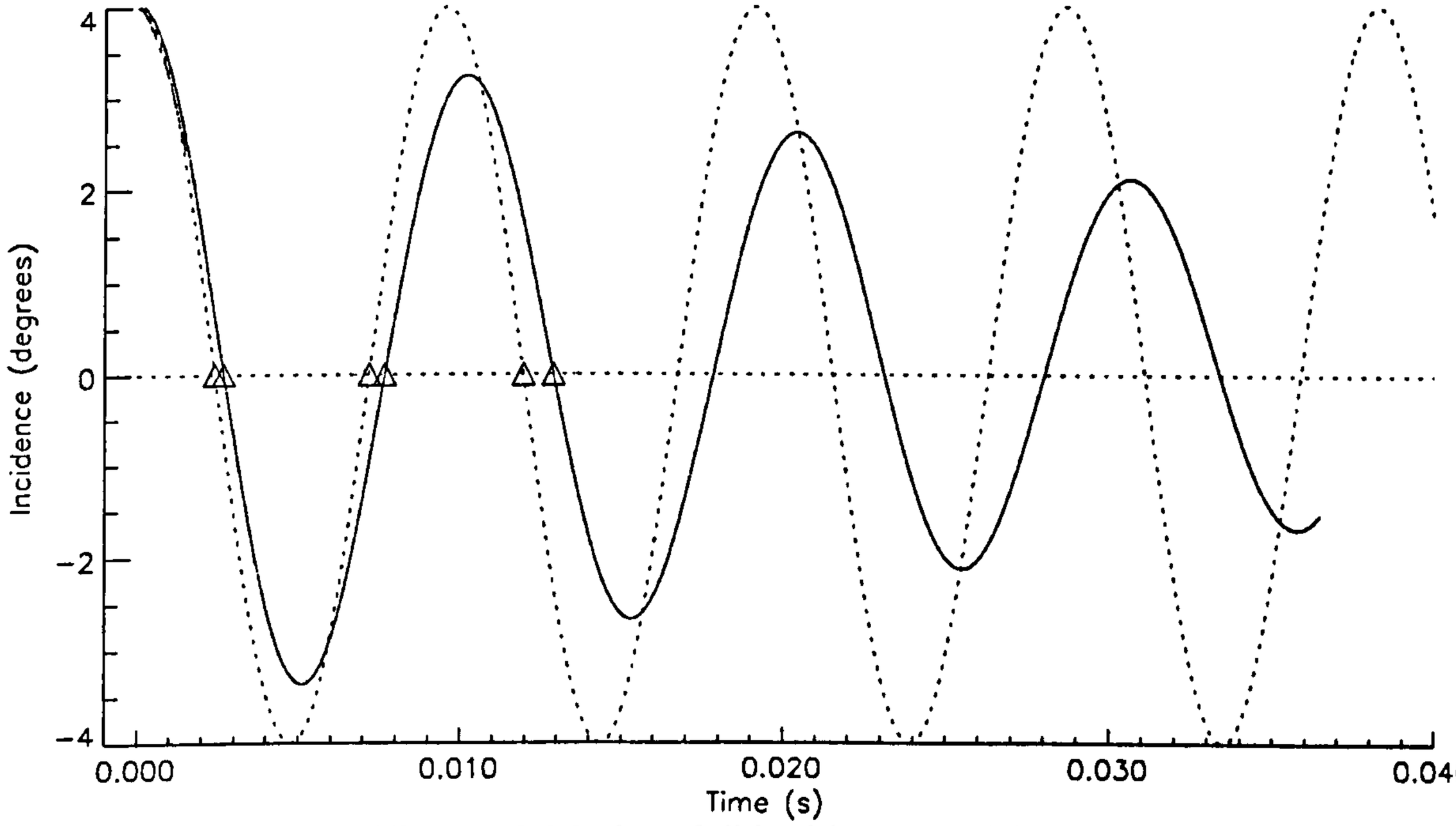

Figure 4.34. Aerofoil Incidence vs Time

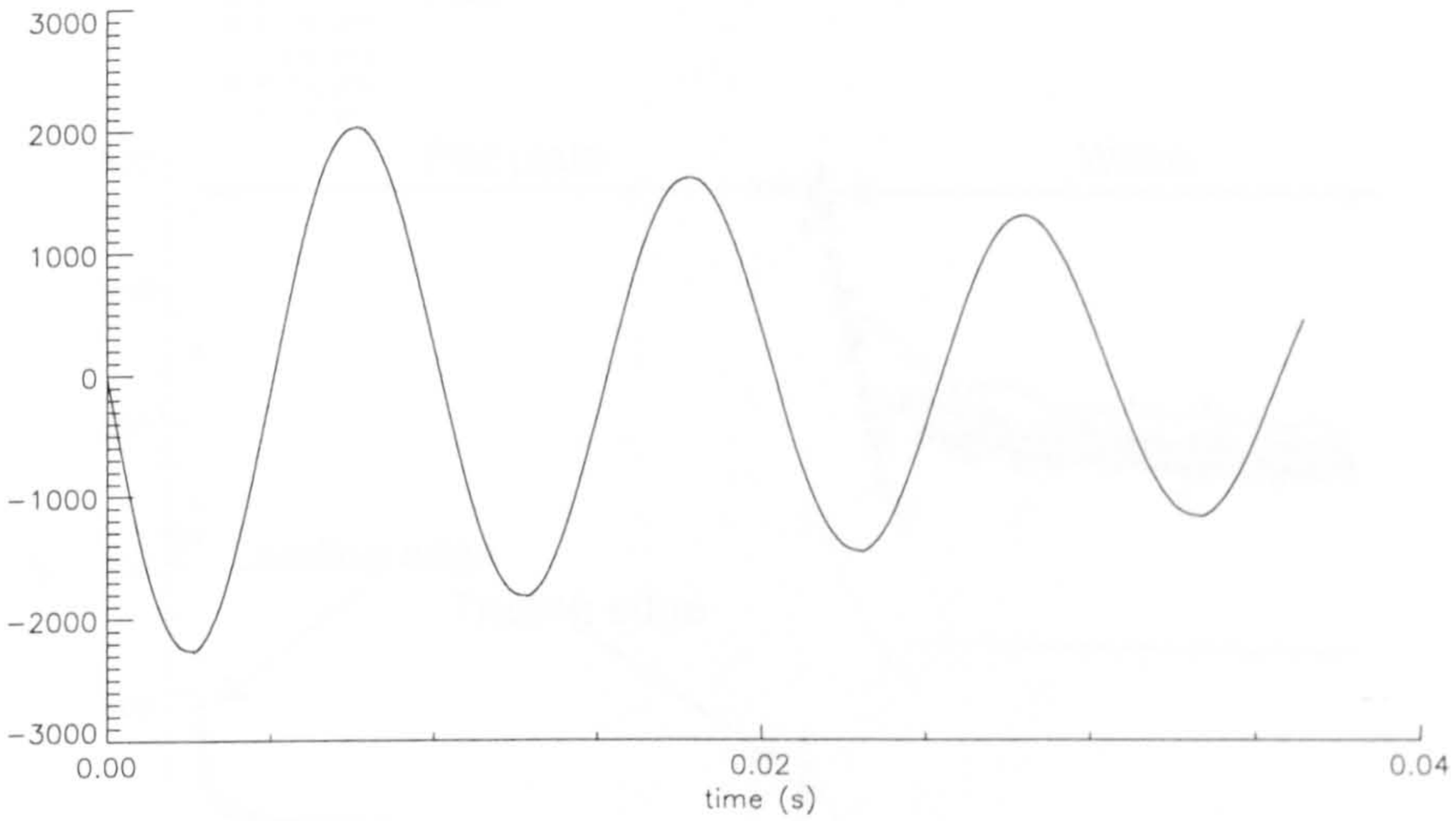

Figure 4.35. Aerofoil Angular Velocity vs Time

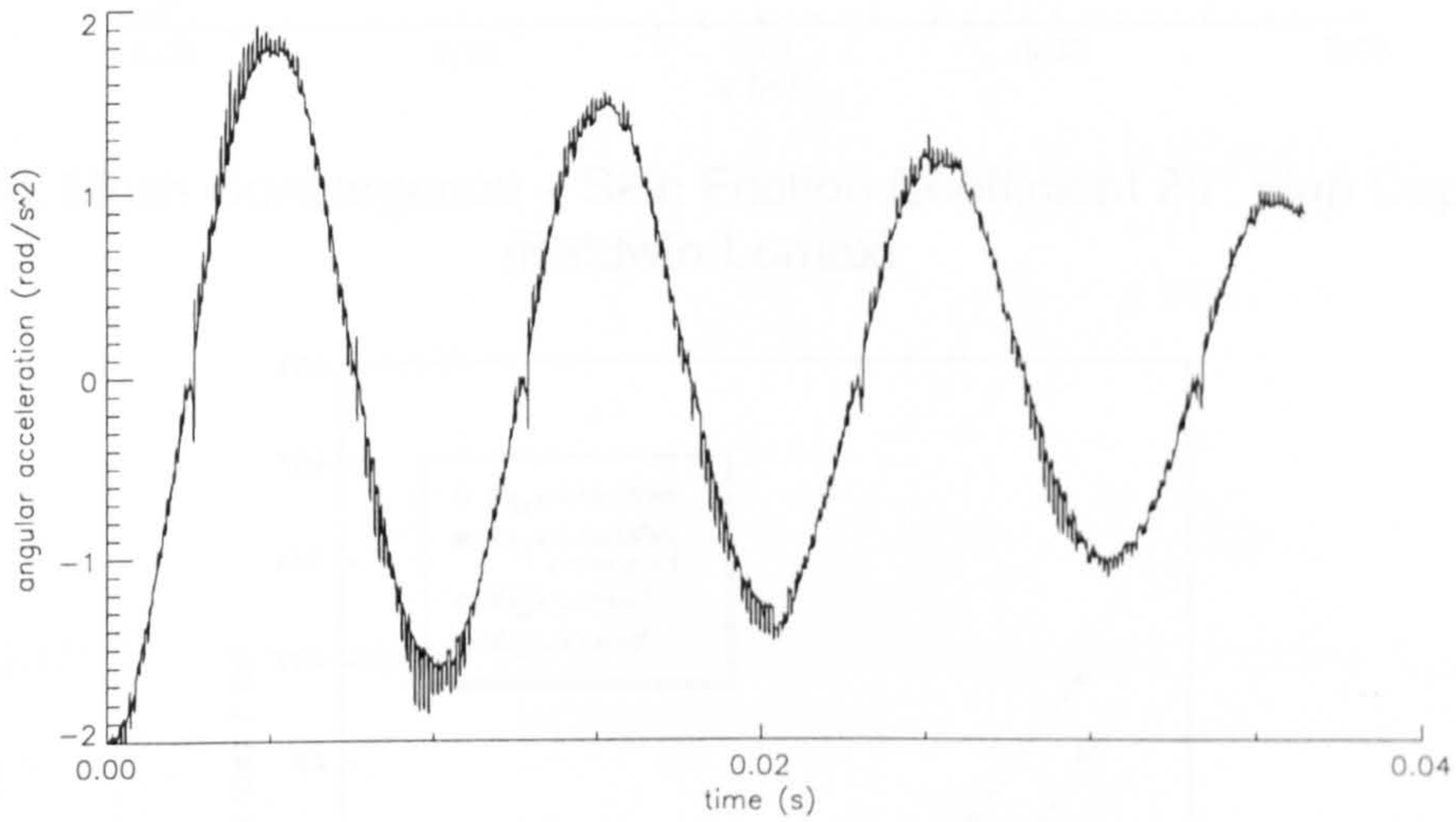

Figure 4.36. Aerofoil Angular Acceleration vs Time

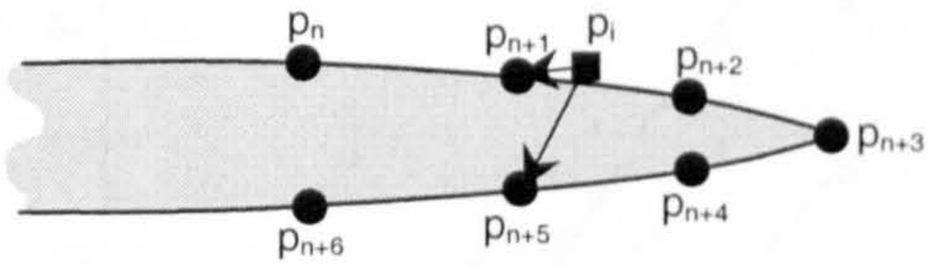

Figure 4.37. The 'Thin-Body' Problem

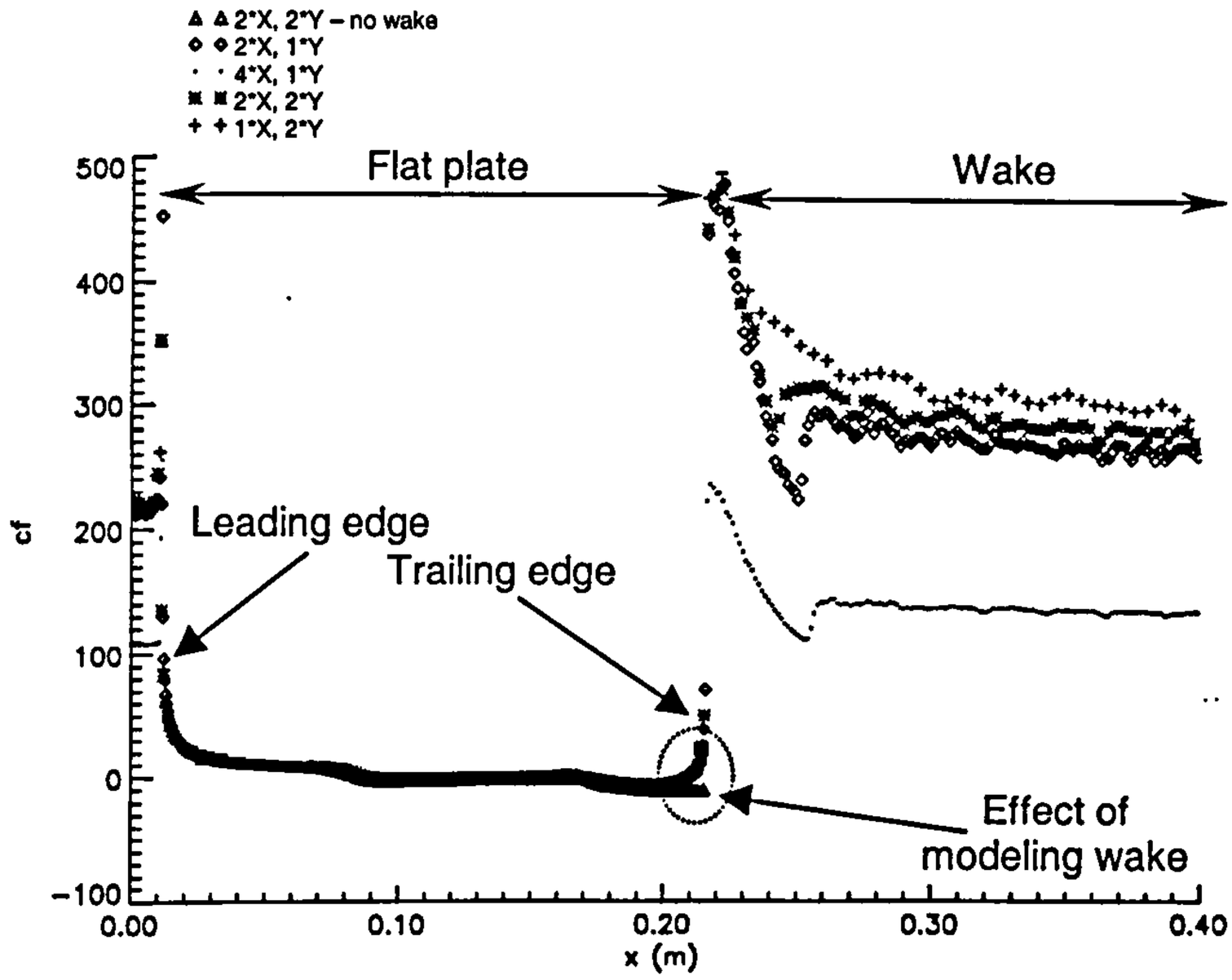

Figure 4.38. Mesh Convergence – Skin Friction Coefficient 20° Flap Deployment (Baldwin-Lomax)

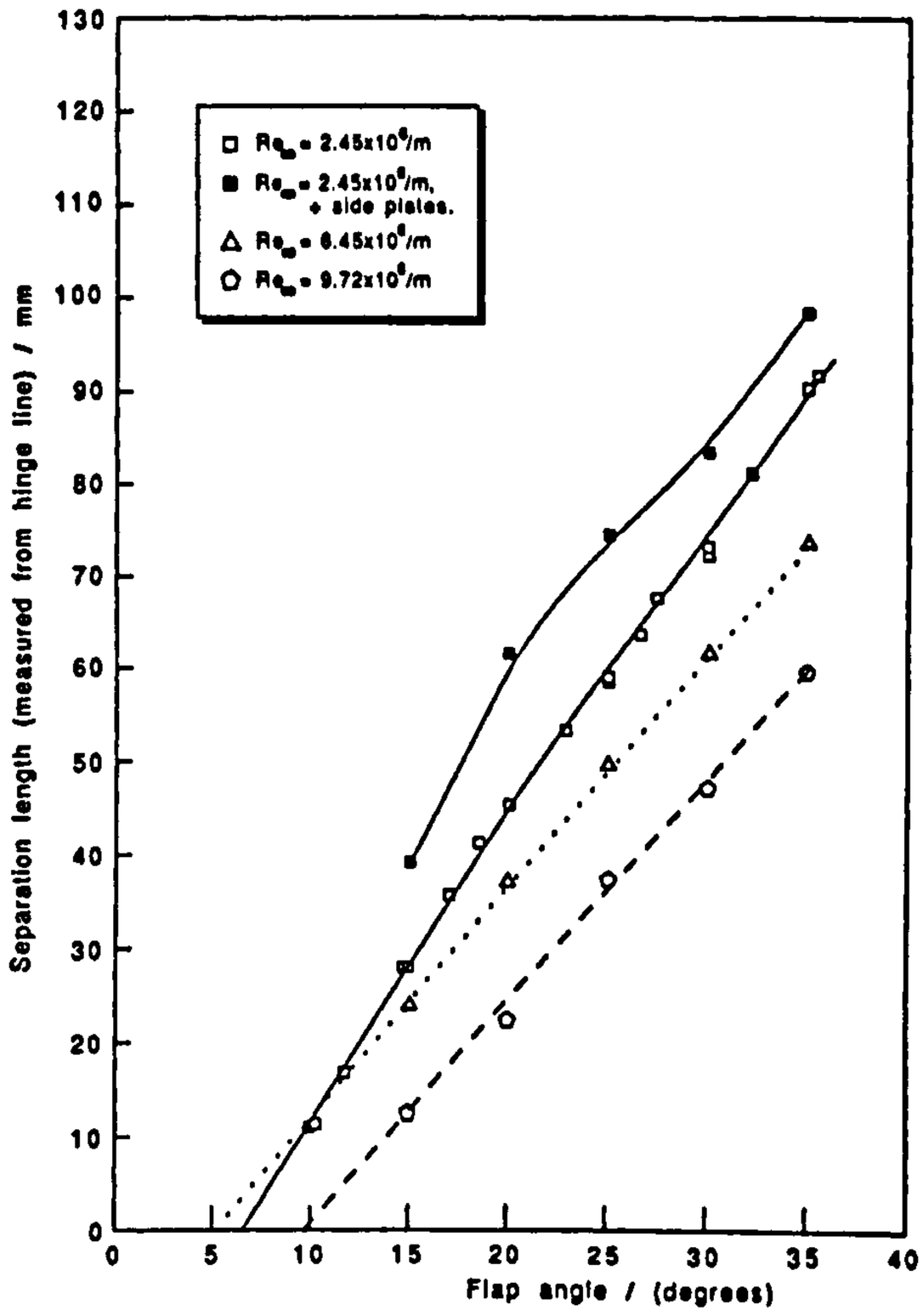

Figure 4.39. Experimental Separation Position With Flap Angle

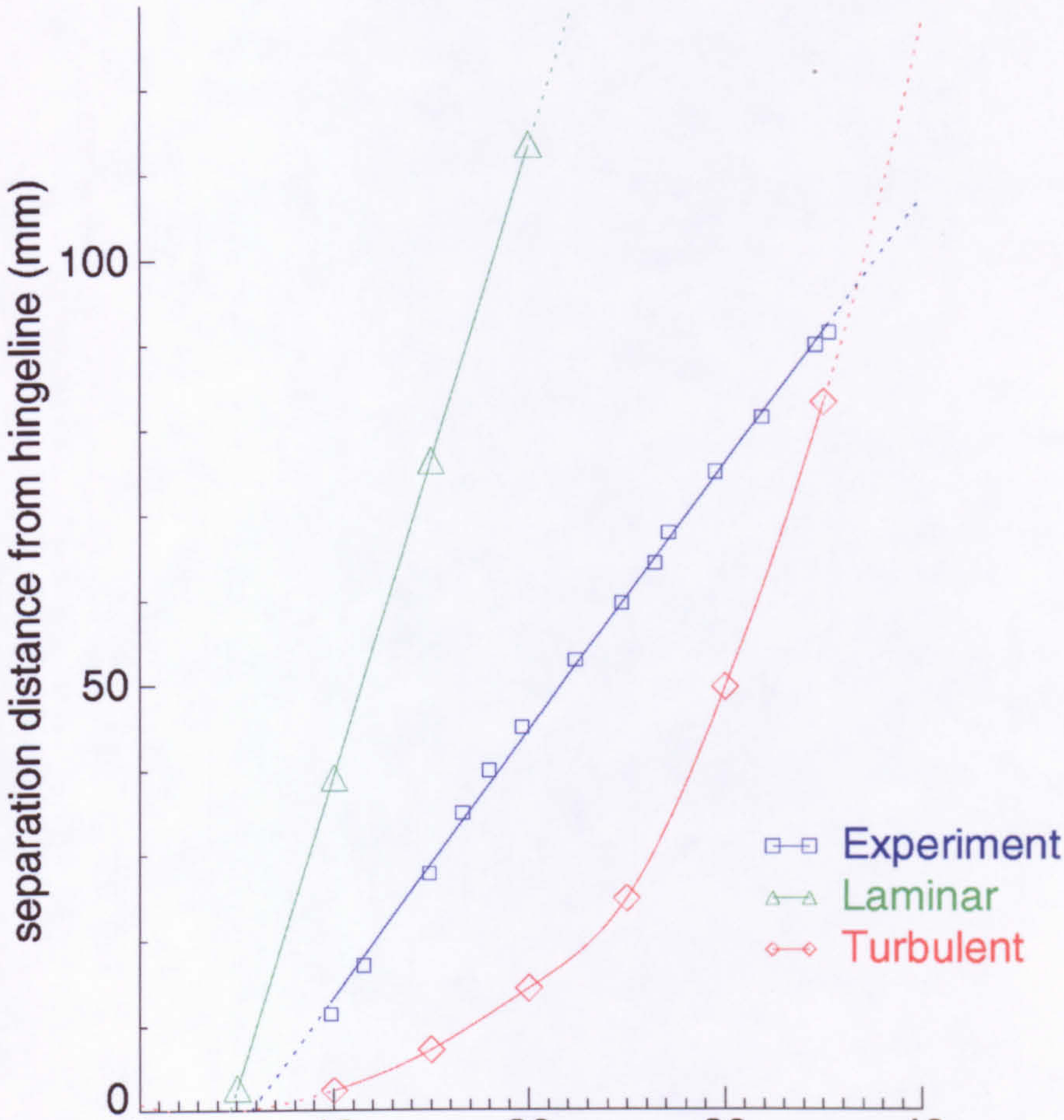

Figure 4.40. Experimental and Computational Separation Location Variation With Flap Angle

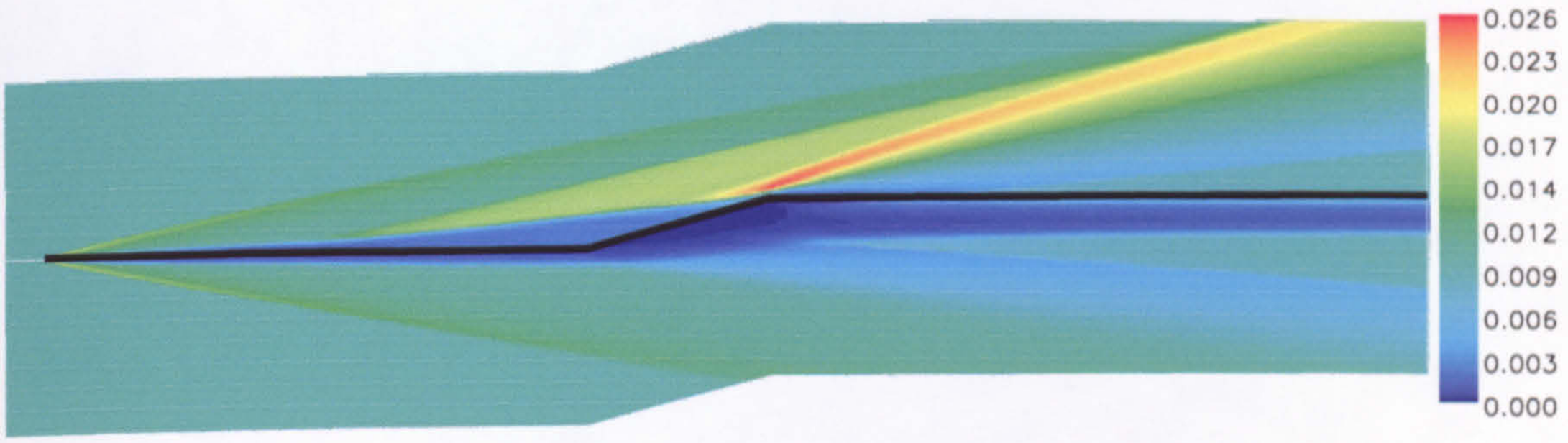

Figure 4.41 Density Plot - 25° Ramp Flow

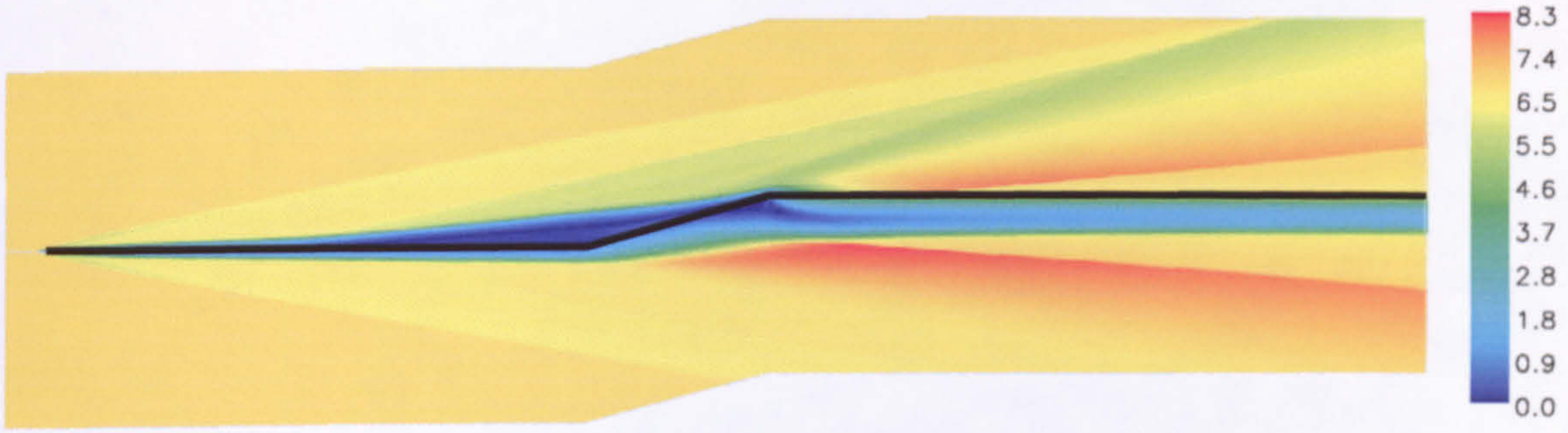

Figure 4.42 Mach Number Plot - 25° Ramp Flow

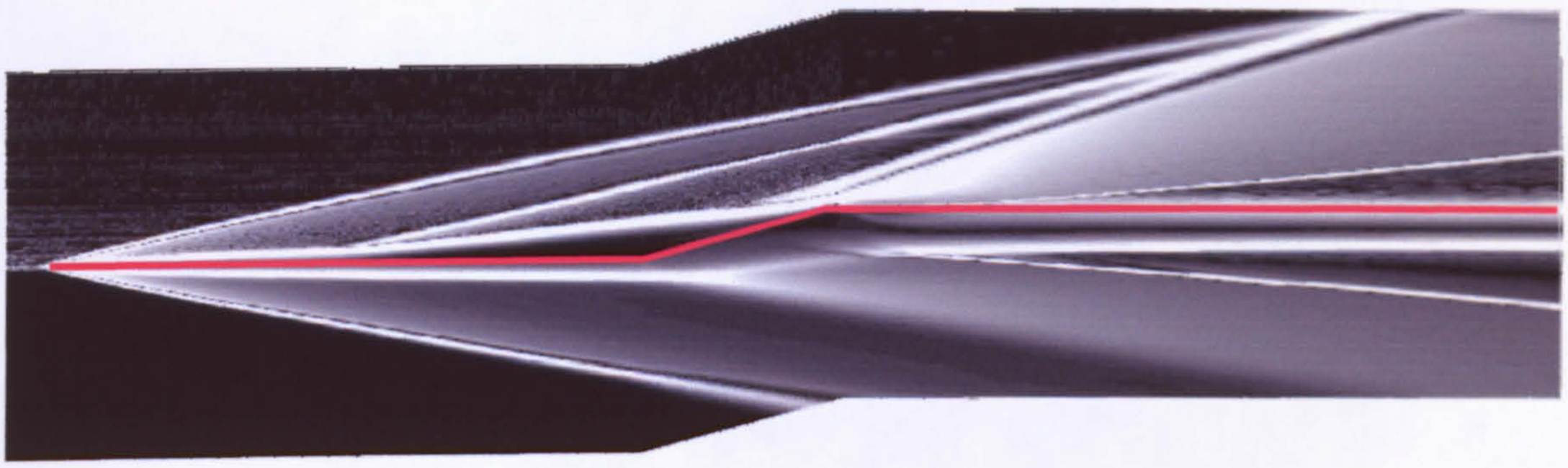

Figure 4.43 Density Gradient Plot - 25° Ramp Flow

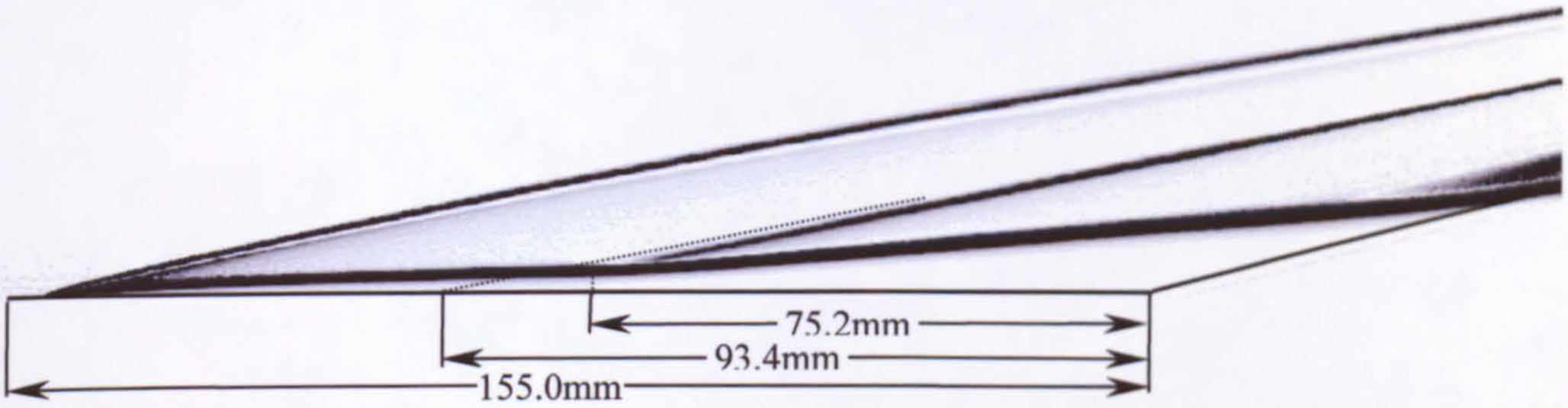

Figure 4.44. Computational Density Gradient (15° flap deployment)

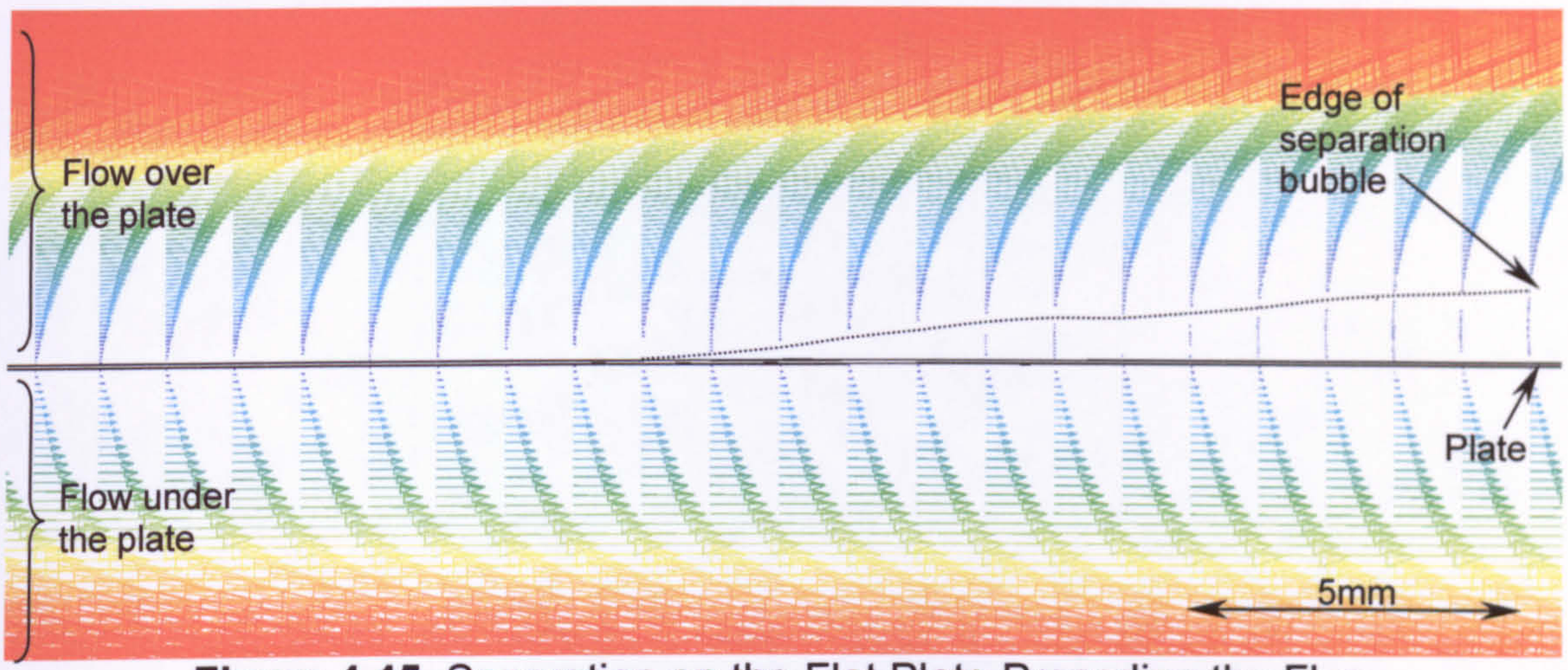

Figure 4.45. Separation on the Flat Plate Preceding the Flap

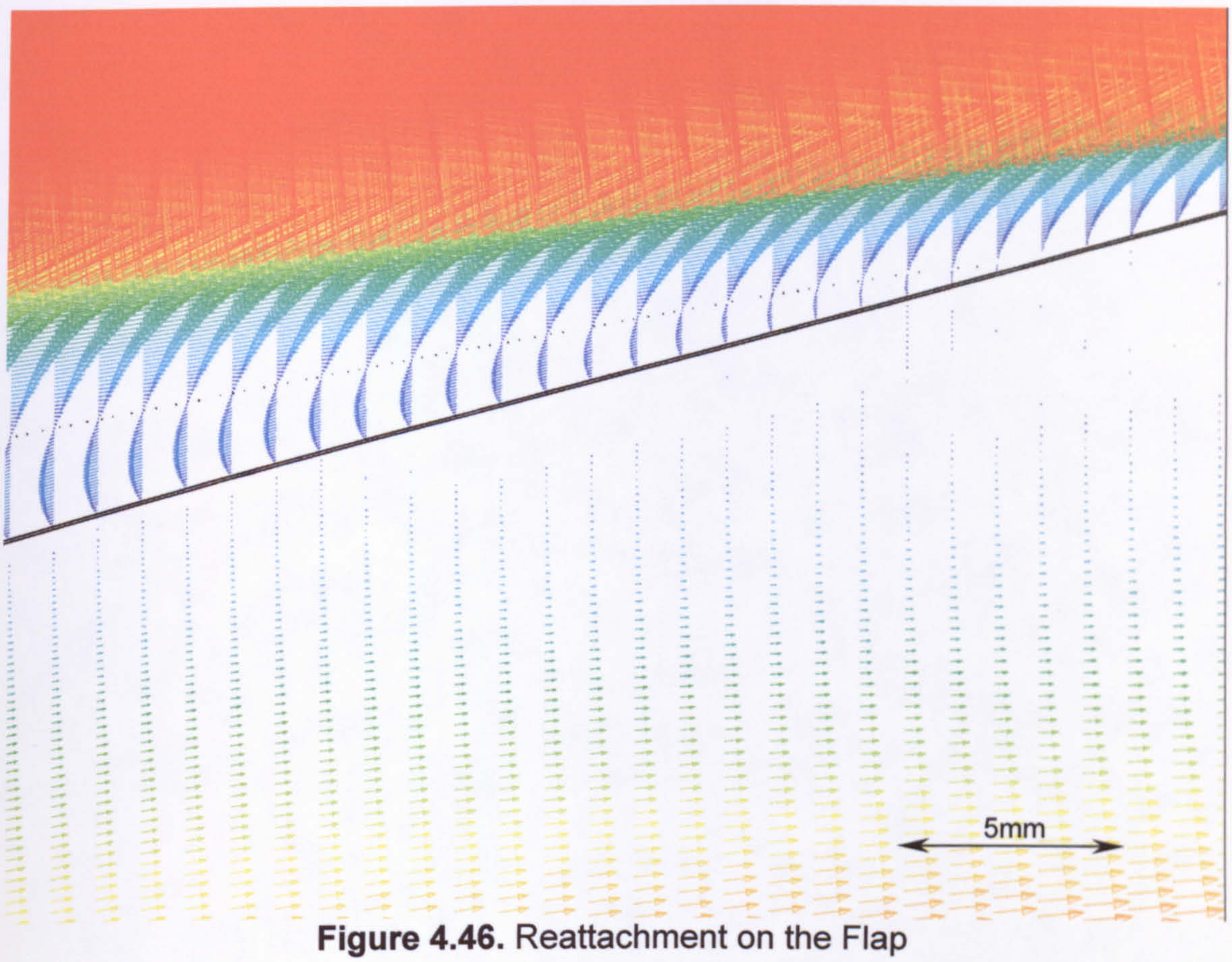

Figure 4.46. Reattachment on the Flap

Figure 4.47a

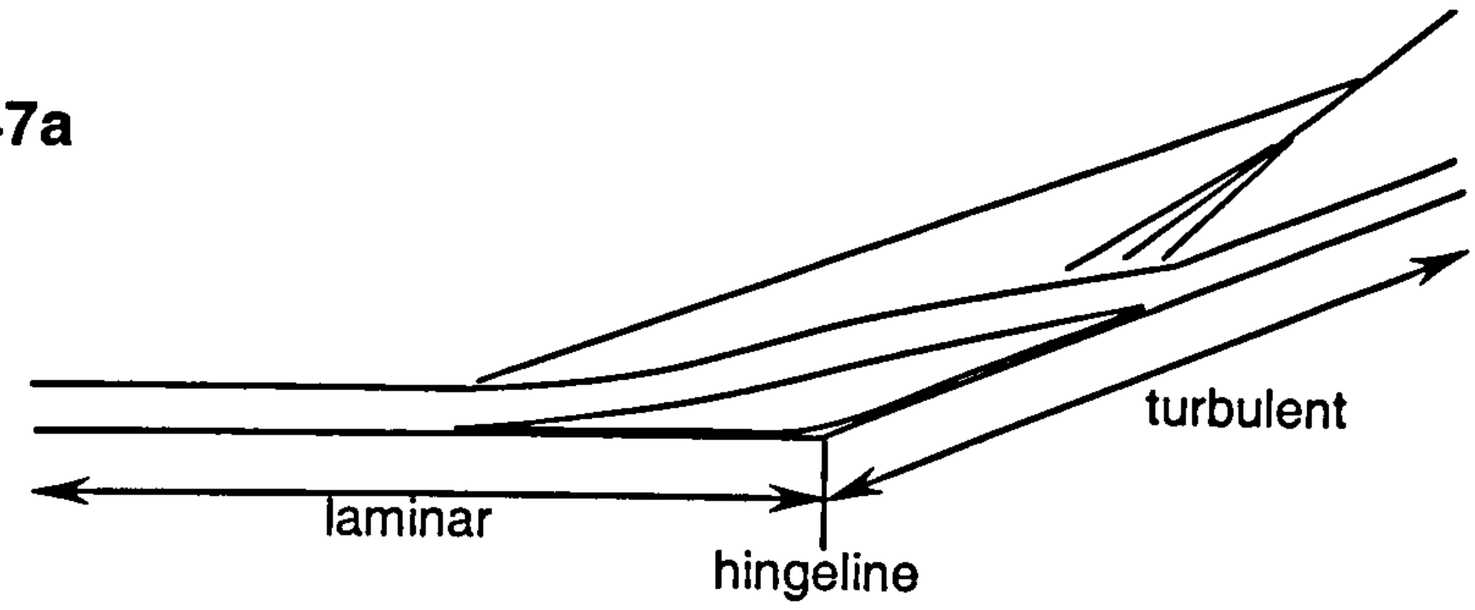

Figure 4.47b

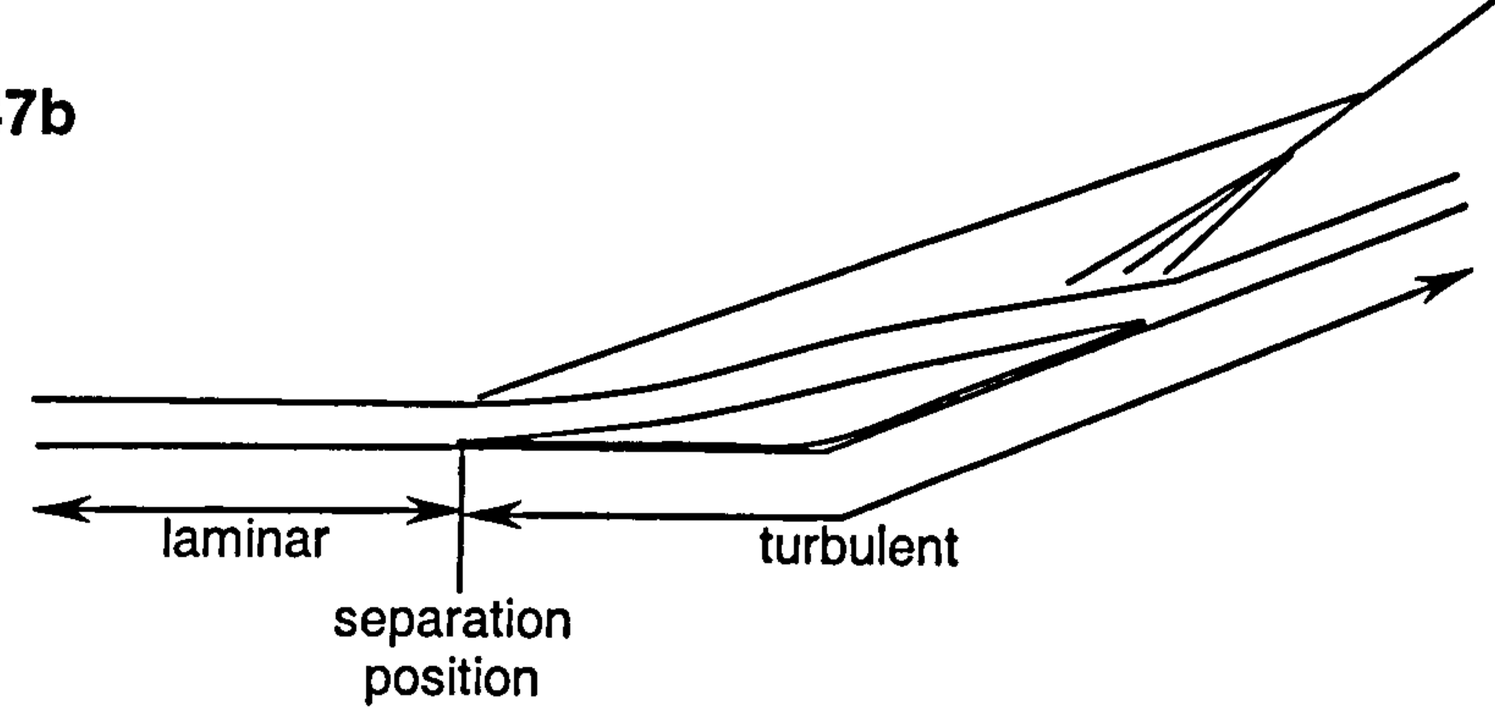

Figure 4.47c

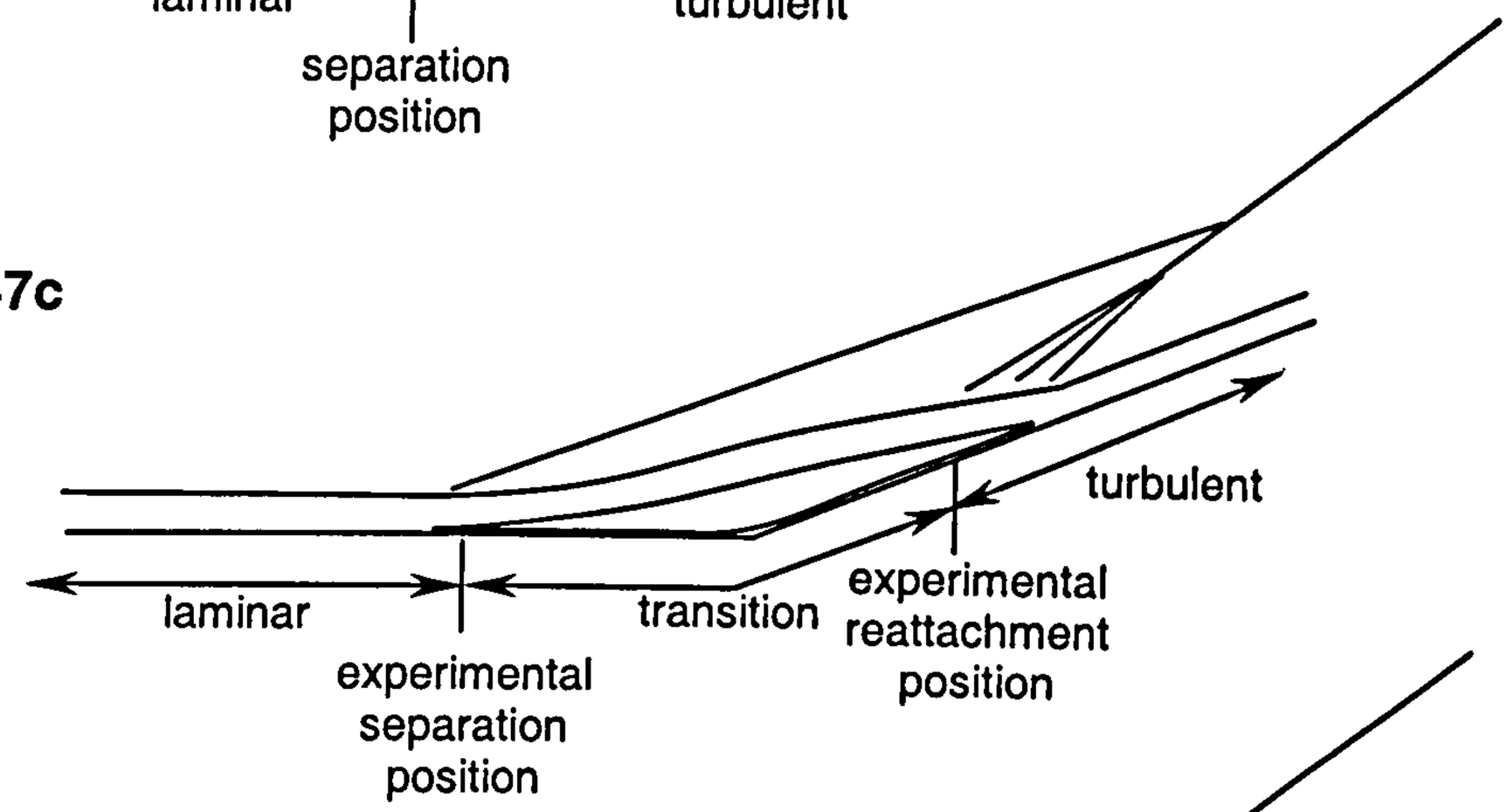

Figure 4.47d

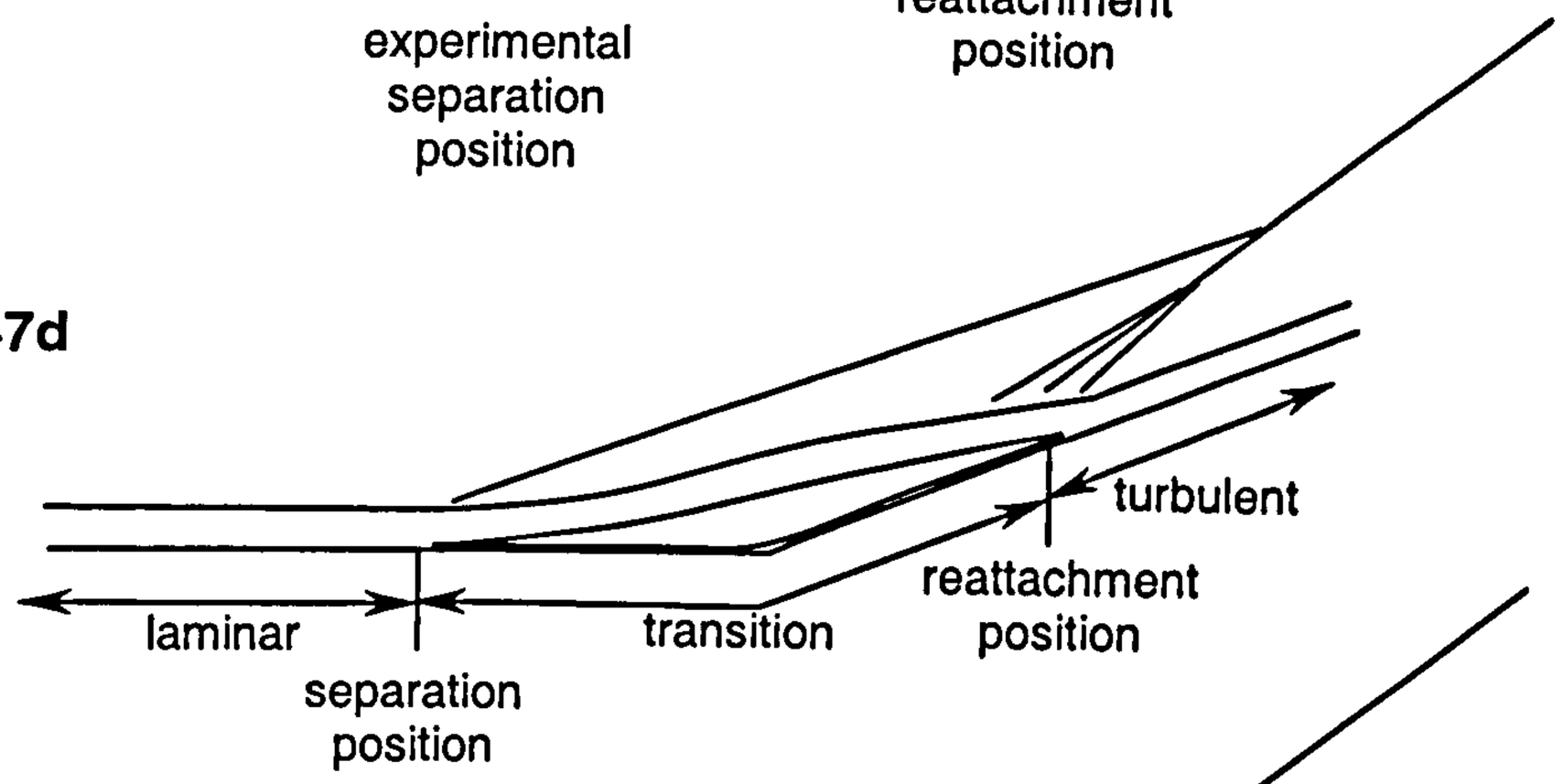

Figure 4.47e

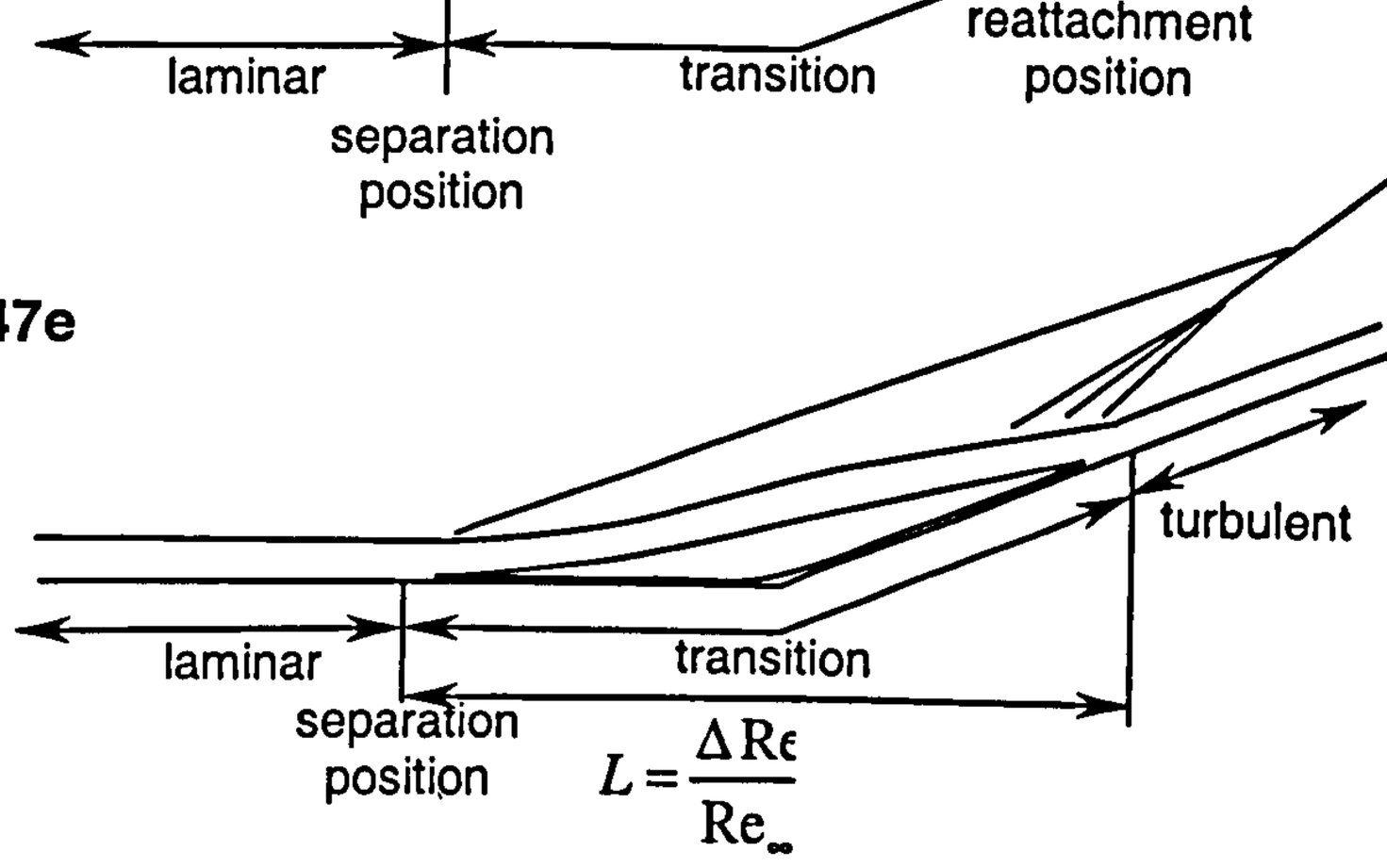

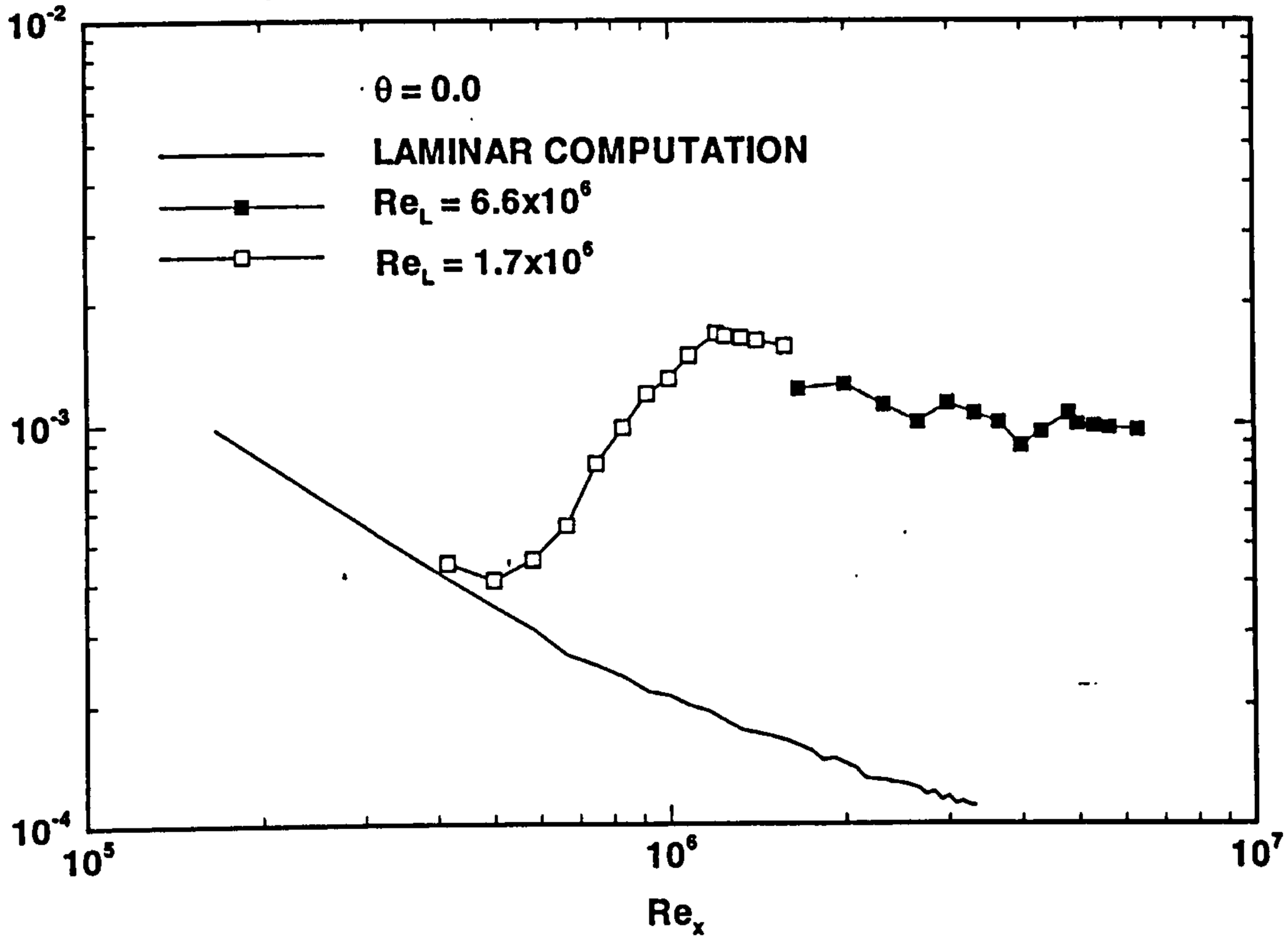

Figure 4.48. Variation in Stanton Number Over an Elliptic Cone With Reynolds Number [139]

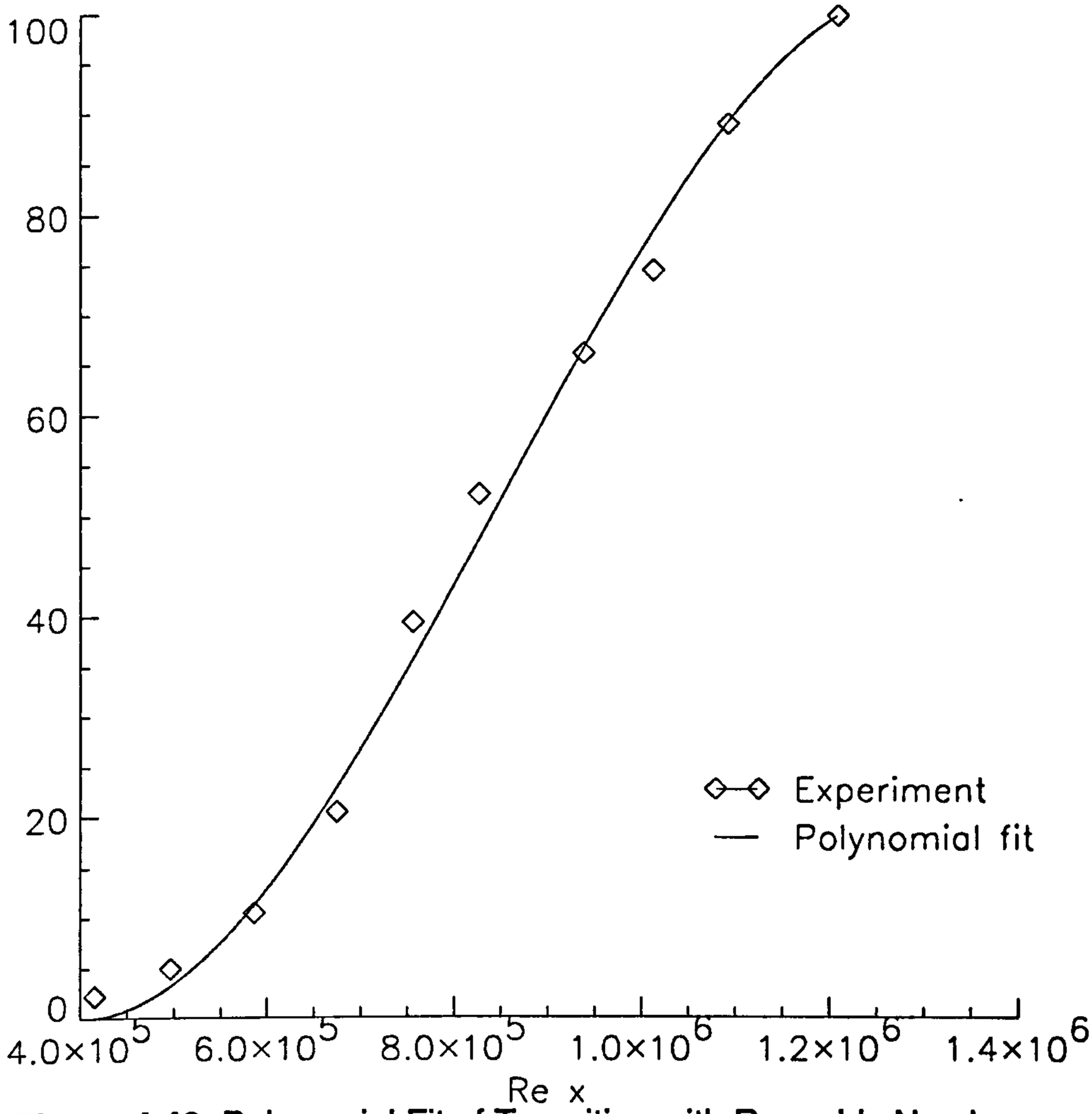

Figure 4.49. Polynomial Fit of Transition with Reynolds Number

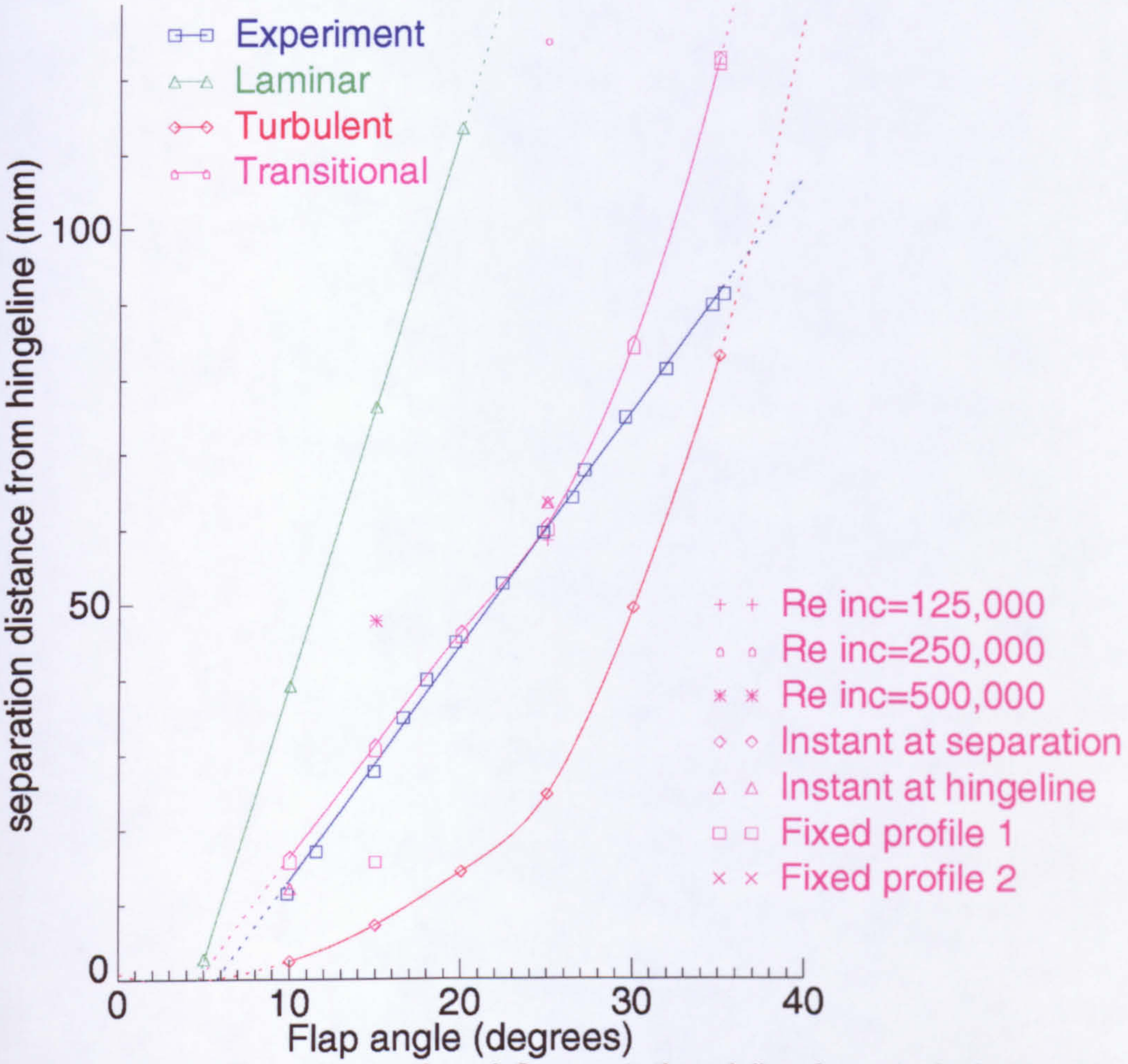

Figure 4.50. Experimental and Computational (laminar, turbulent and transitional) Variation in Separation Location with Flap Angle

Figure 4.51. An Example Flowfield Using Adaptive Body Capture (ΔRe=250,000, Flap Angle = 15°)

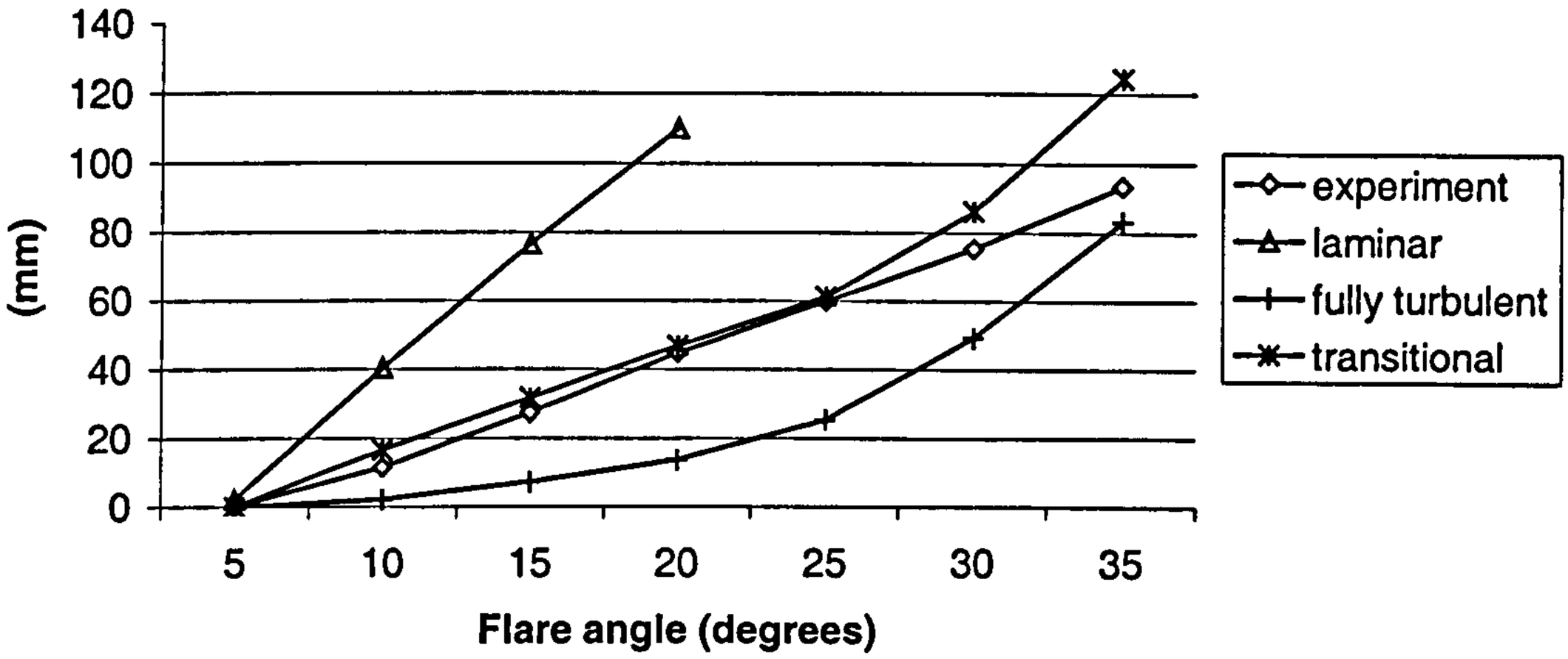

Figure 4.52. Experimental And Computational (Laminar, Turbulent And Selected Transitional) Variation In Separation Location With Flap Angle

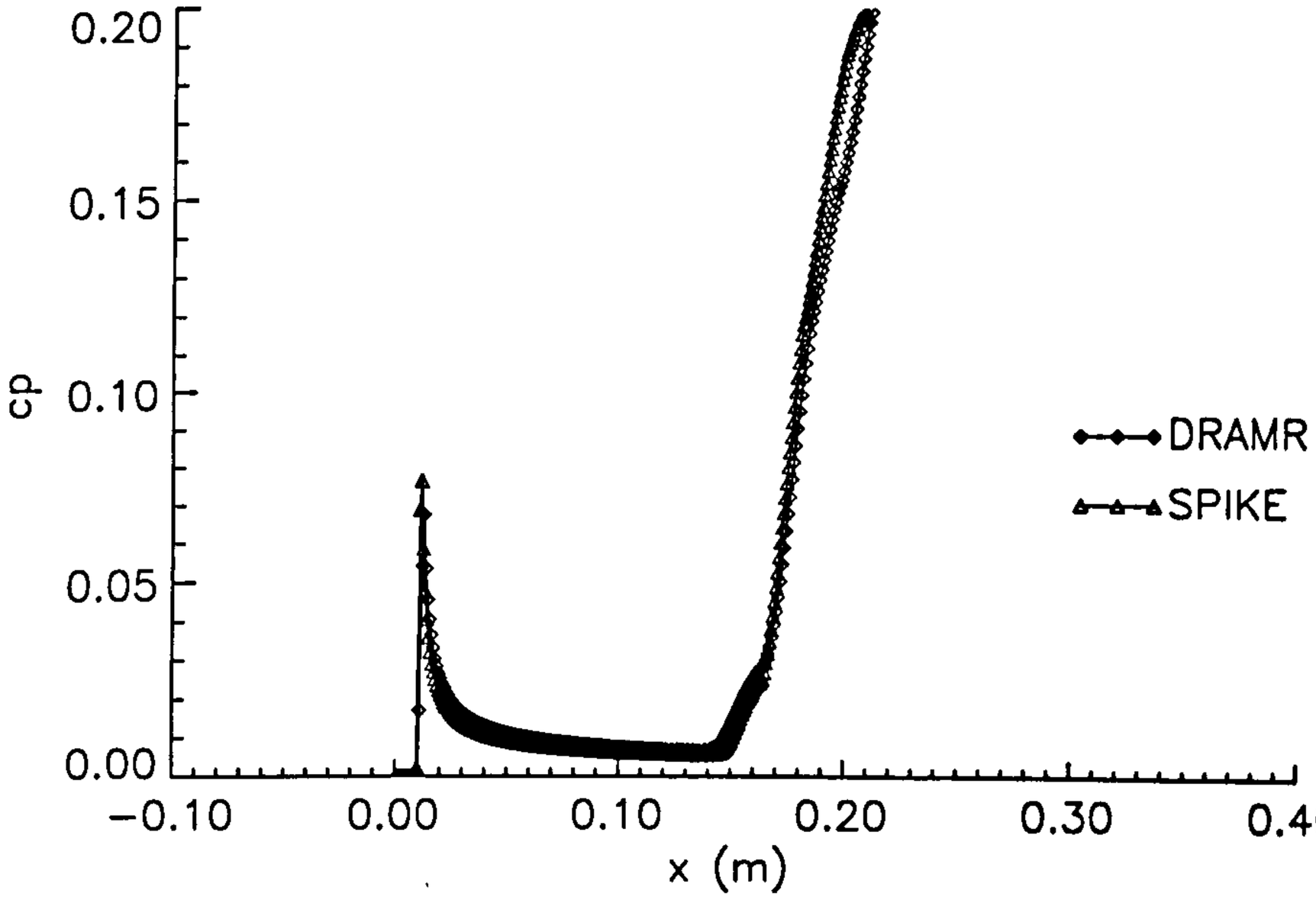

Figure 4.53. Comparison Of Surface Pressure Coefficients - 15° Flap, ΔRe=250,000 Transition Model

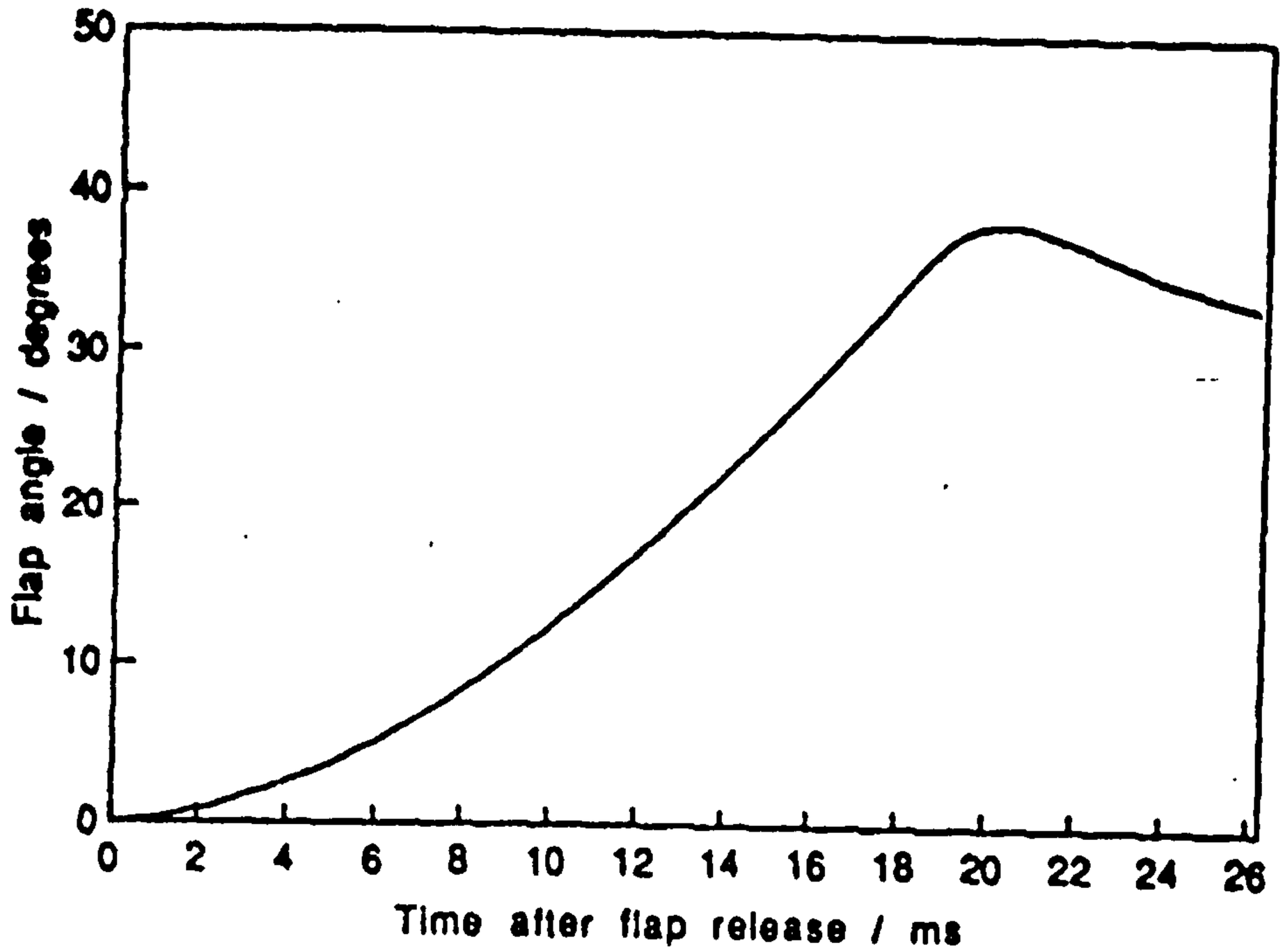

Figure 4.54. Experimental Variation in Flap Angle With Time [67]

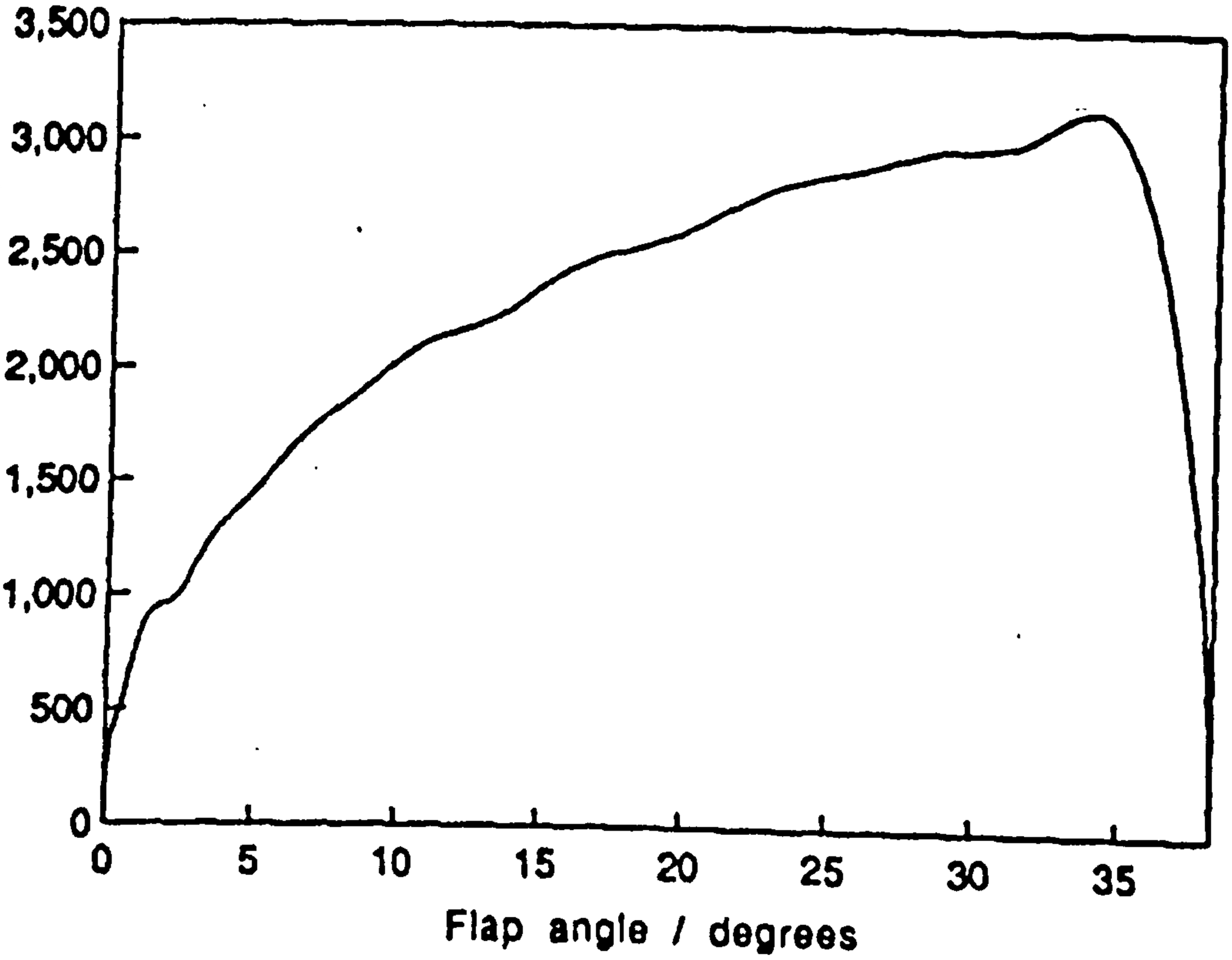

Figure 4.55. Experimental Variation in Flap Angular Velocity With Time [67]

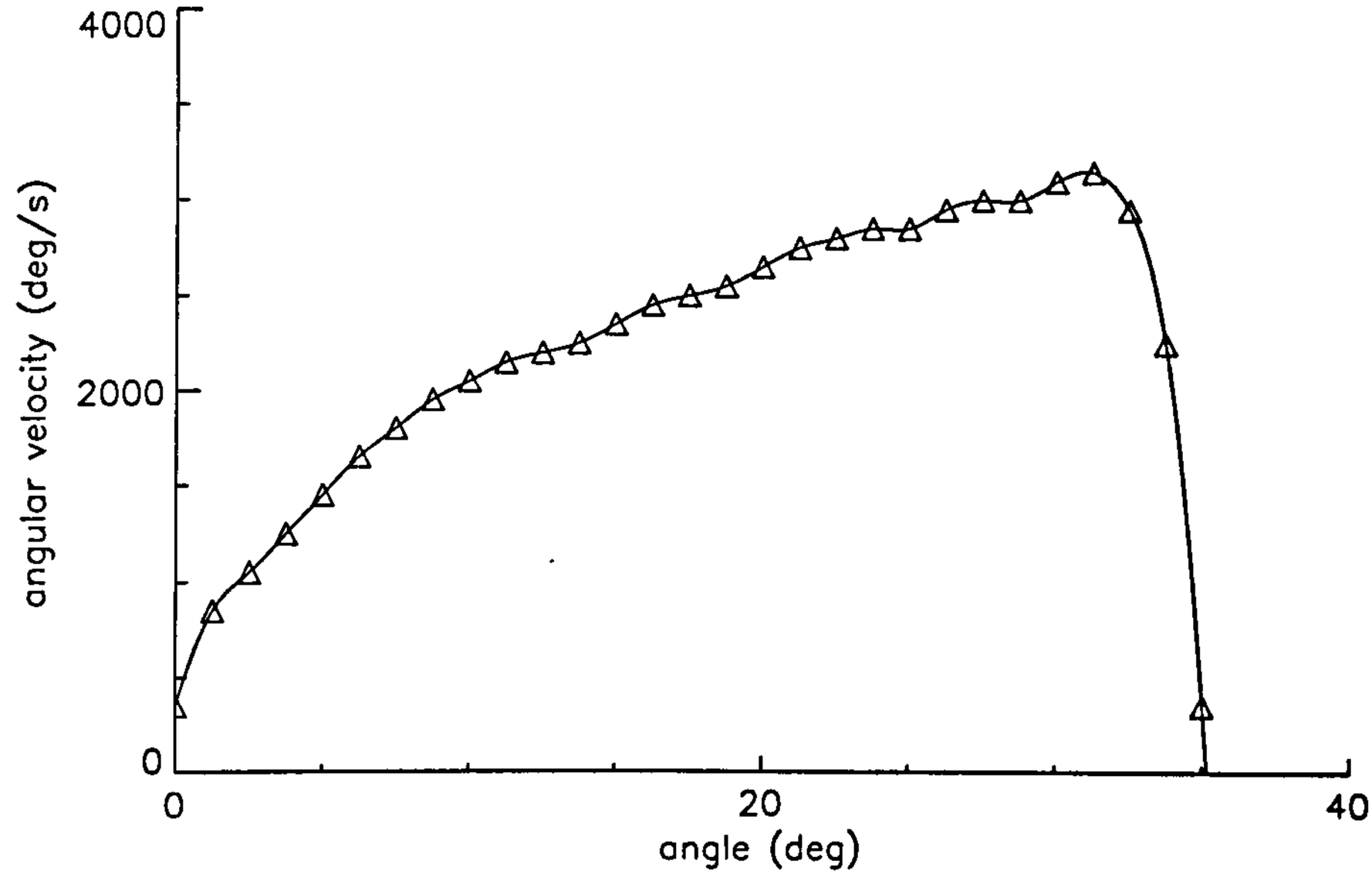

Figure 4.56. Sampled and Spline Fit of Experimental Variation in Flap Angular Velocity With Time

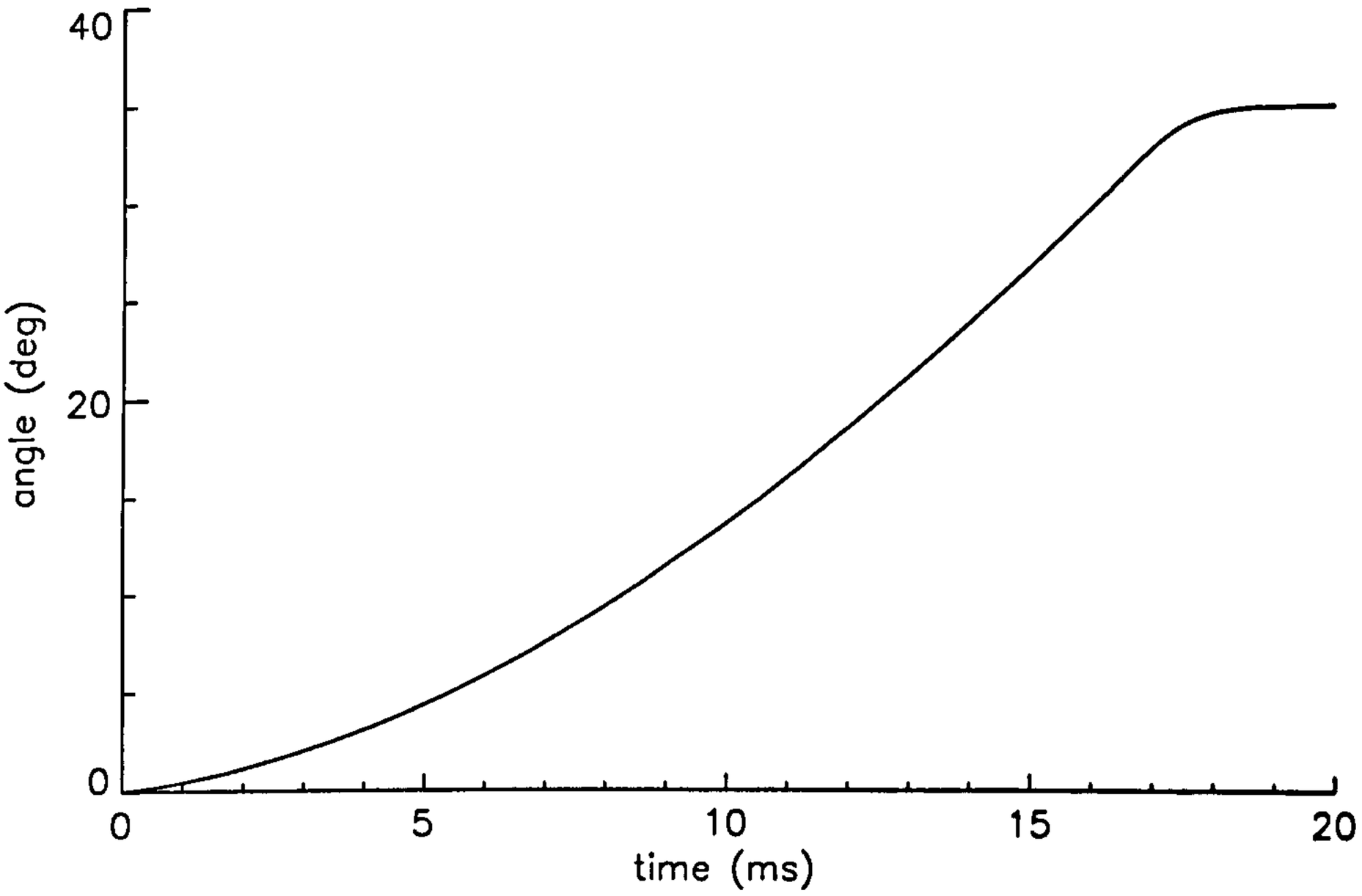

Figure 4.57. Flap Position Variation With Time (Integrated Flap Angular Velocity)

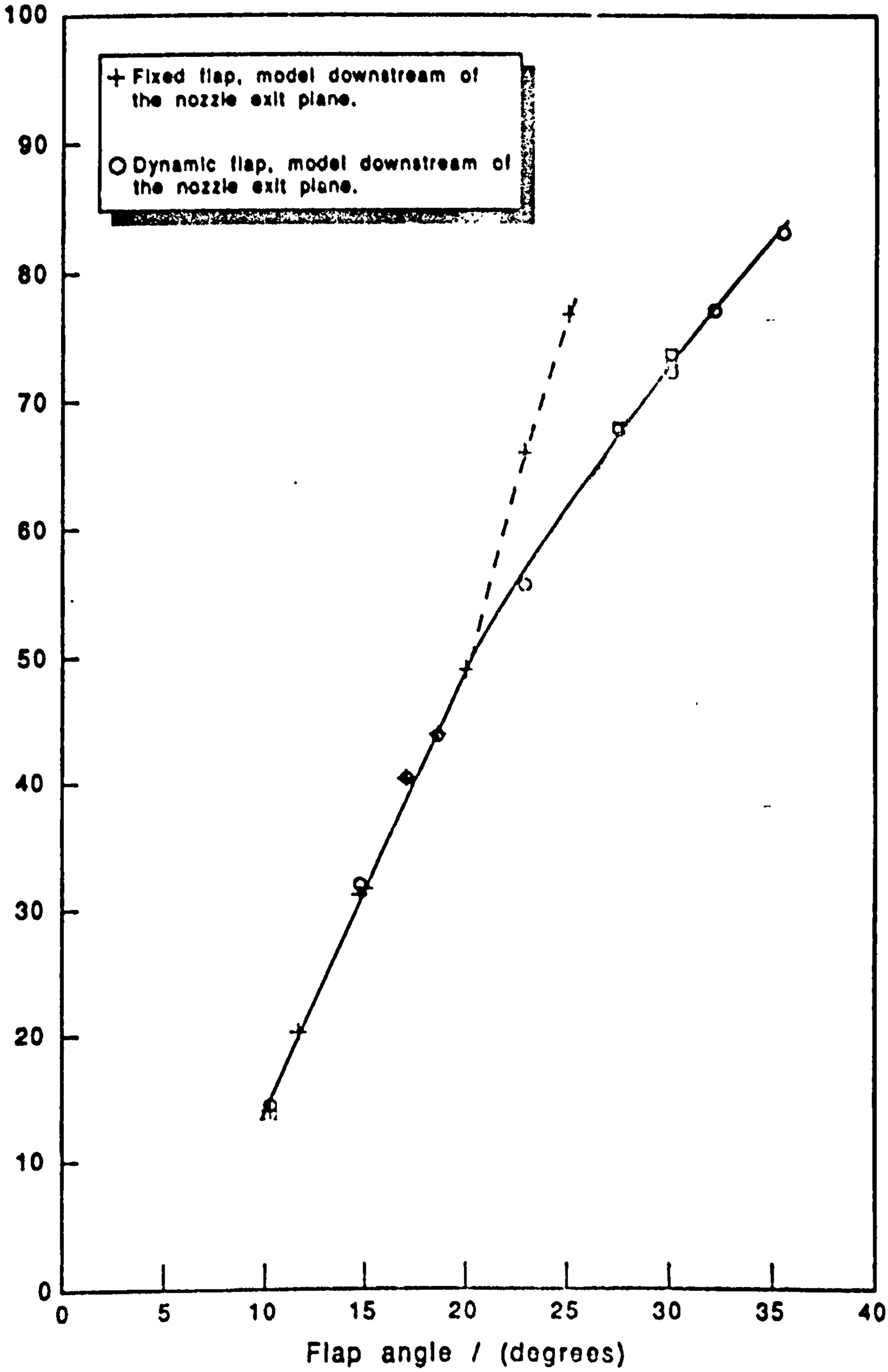

Figure 4.58. Experimentally Measured Dynamic and Static Separation Lengths [67]

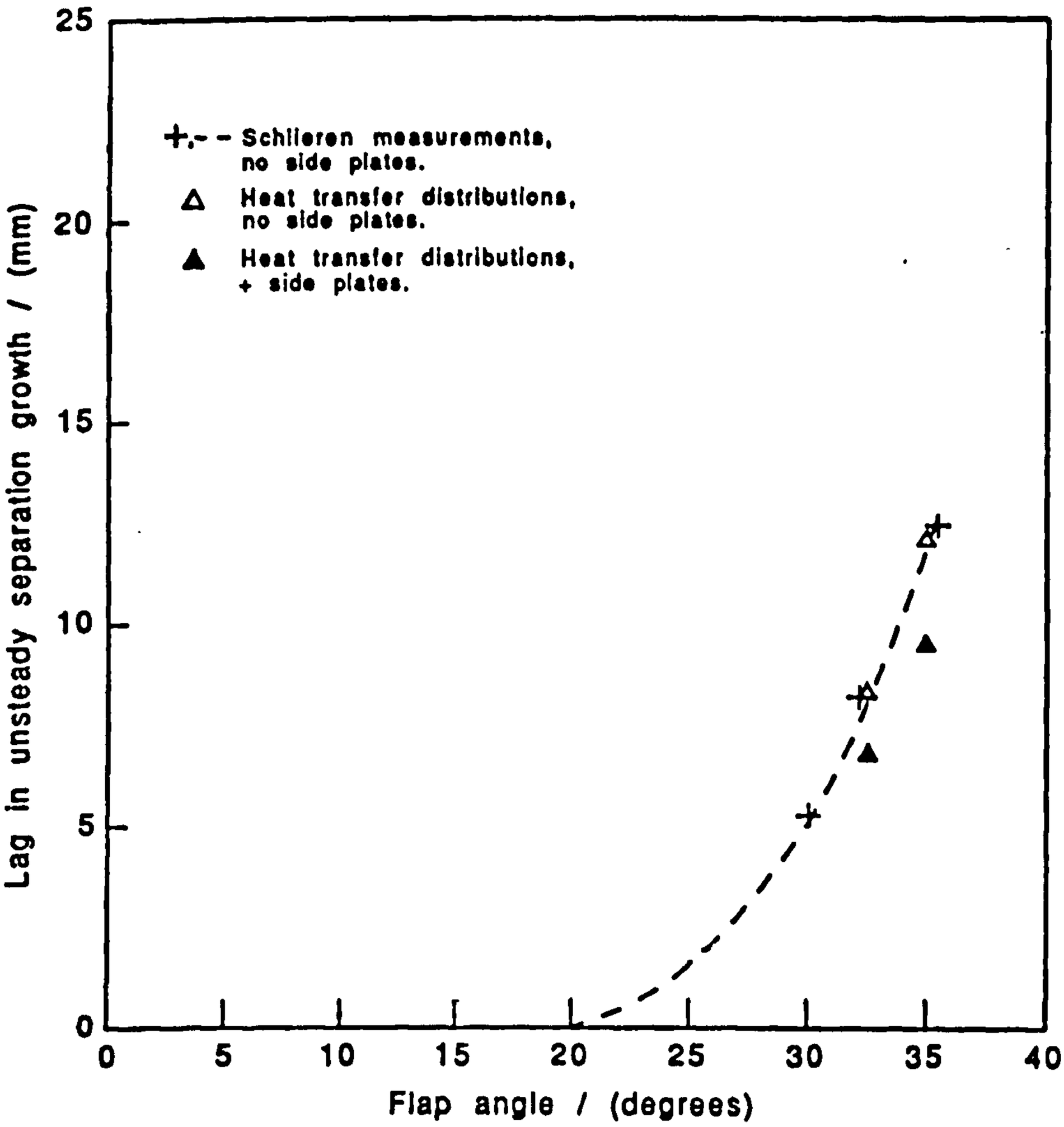

Figure 4.59. Dynamic Separation Position Lag [67]

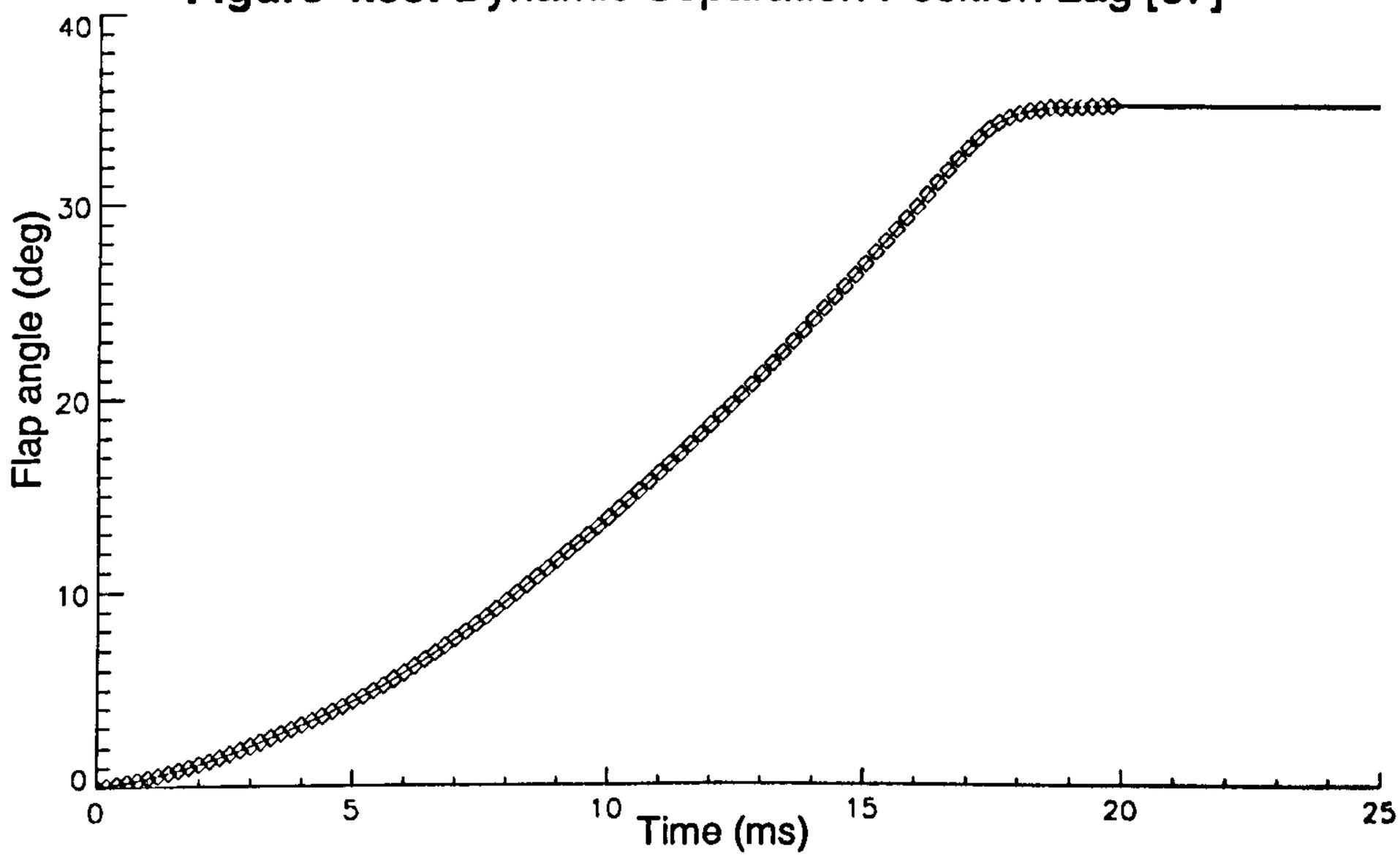

Figure 4.60. Computational and Experimental Flap Deployment Angle Variation With Time

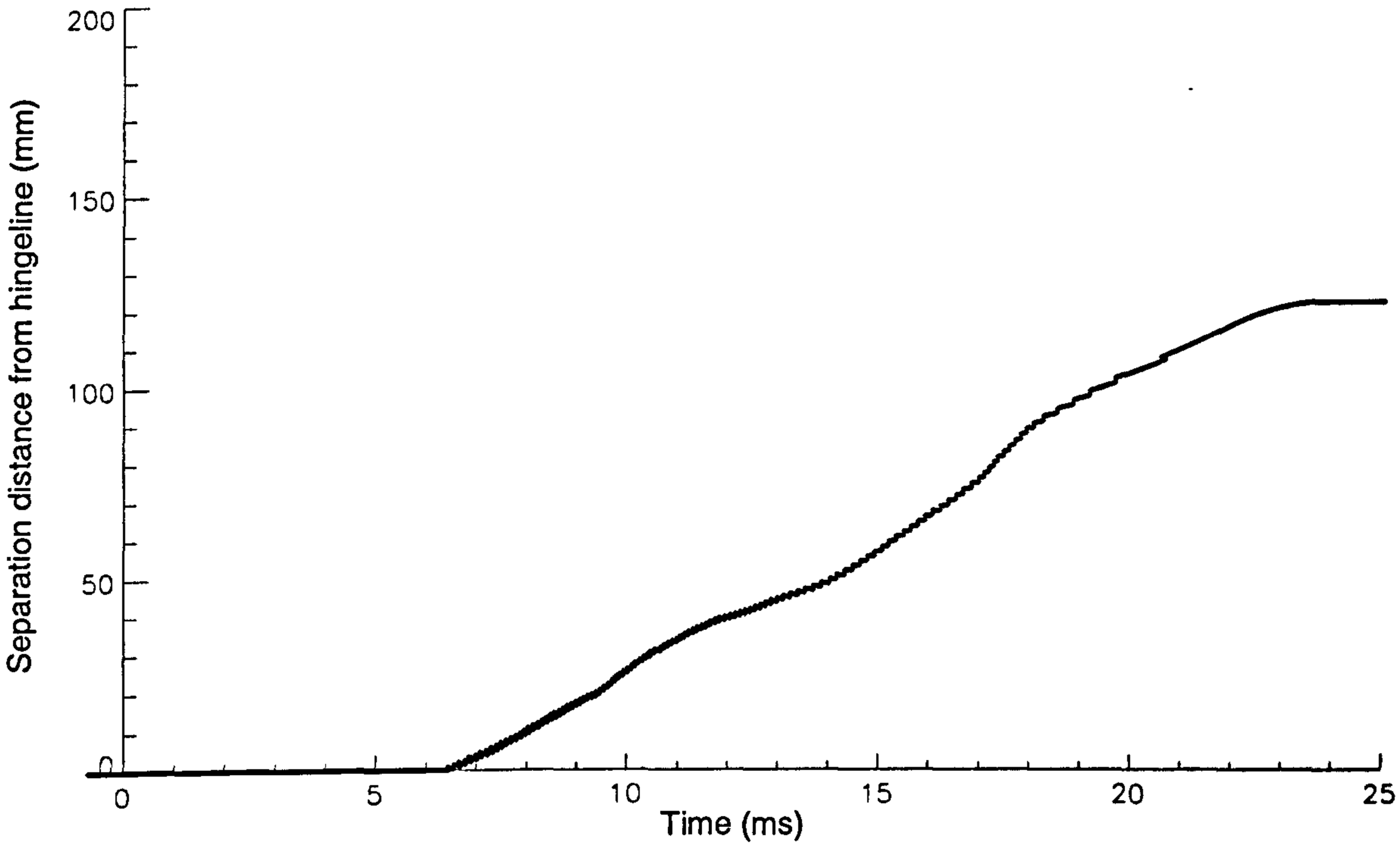

Figure 4.61. Dynamic Variation in Computed Separation Location With Time

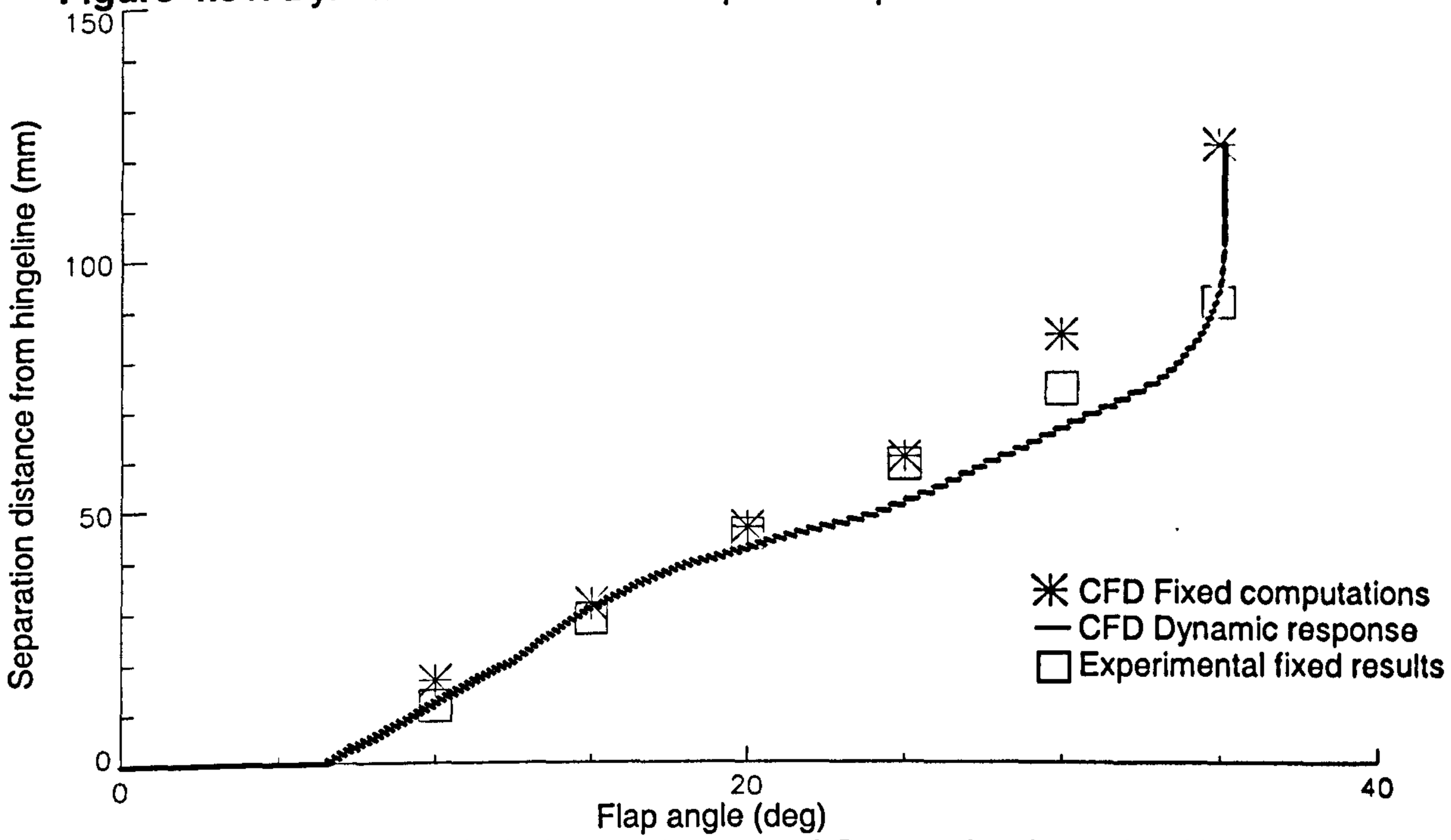

Figure 4.62. Dynamic Variation in Computed Separation Location With Flap Angle

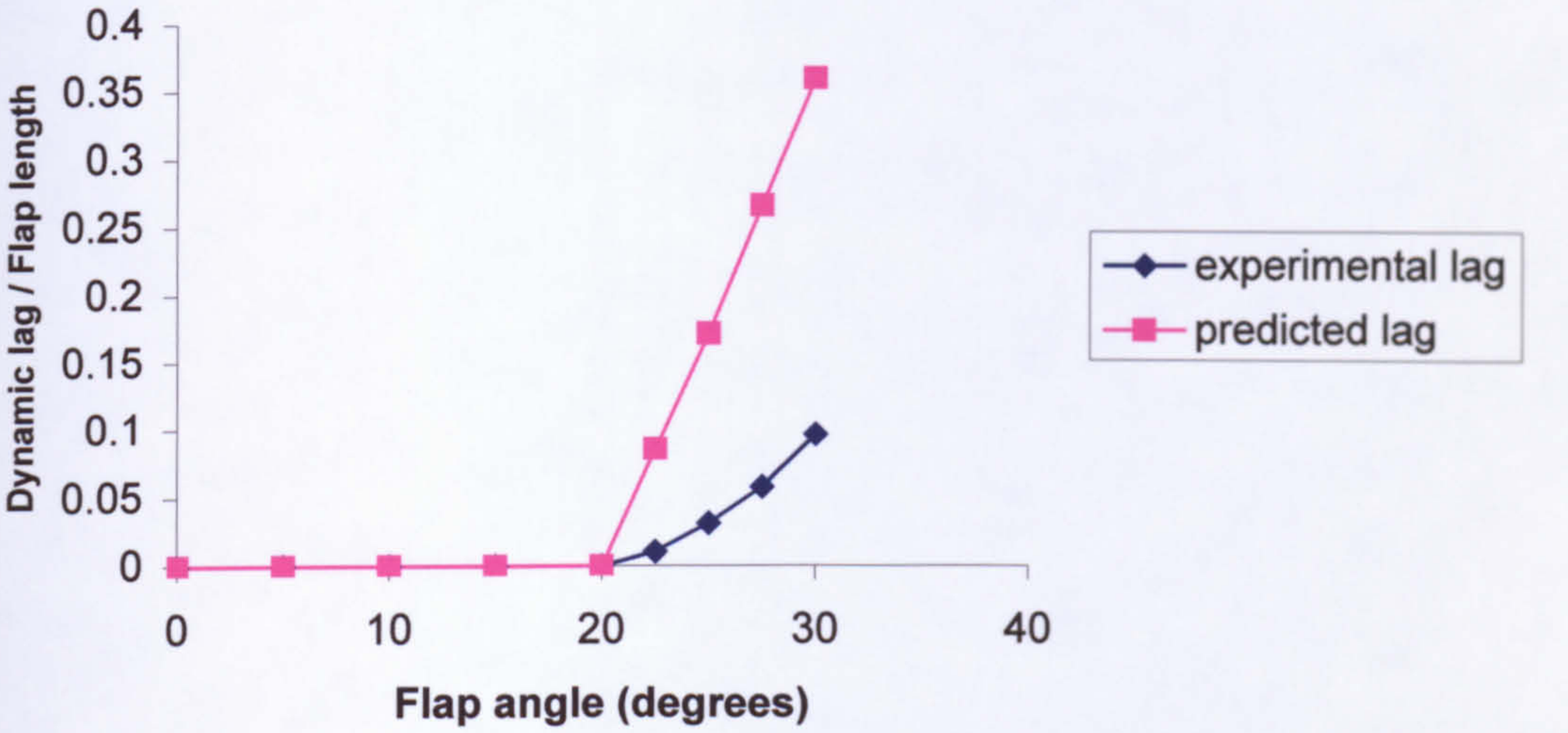

Figure 4.63. Experimental and Computational Dynamic Lag in mm With Flap Angle

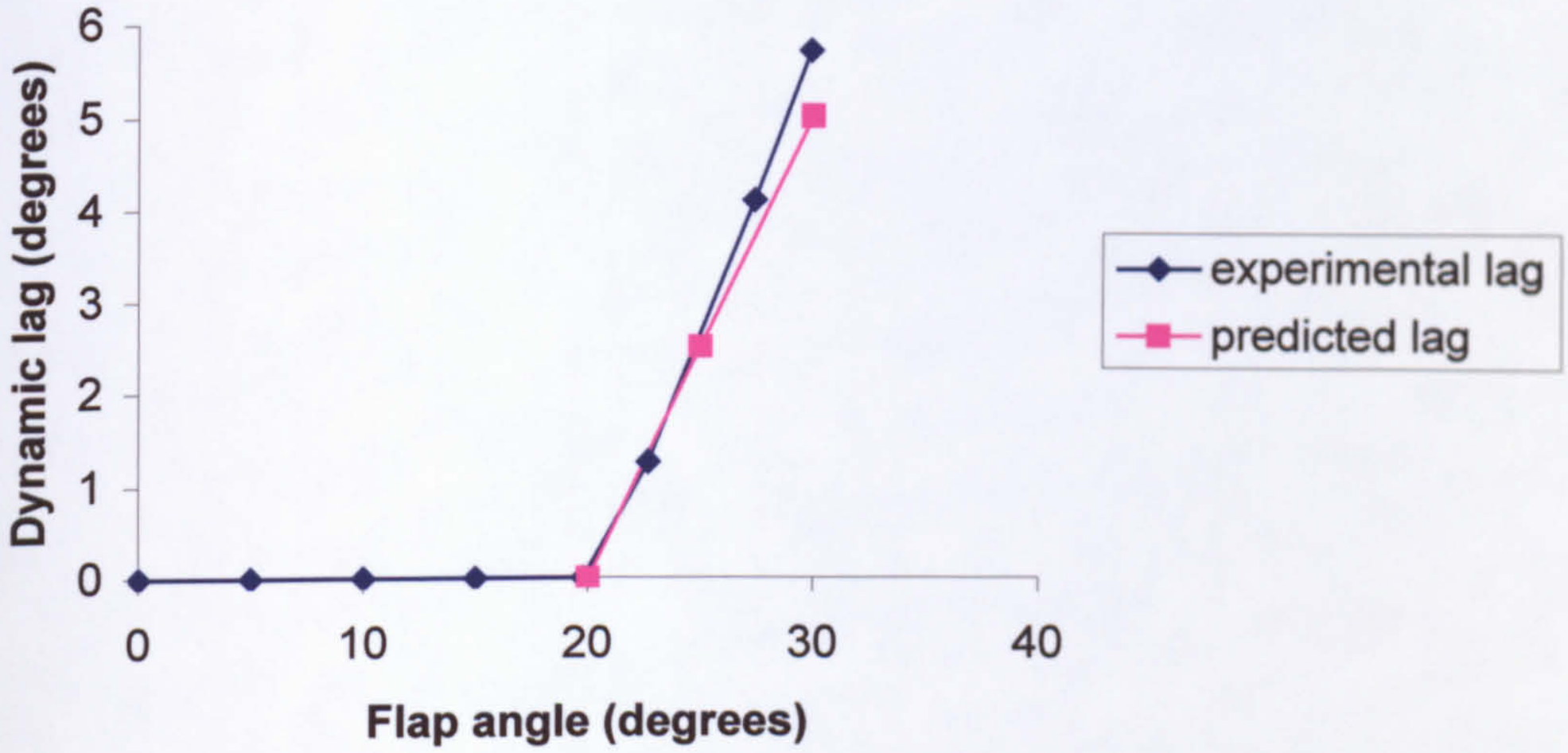

Figure 4.64. Experimental and Computational Dynamic Angular Lag With Flap Angle

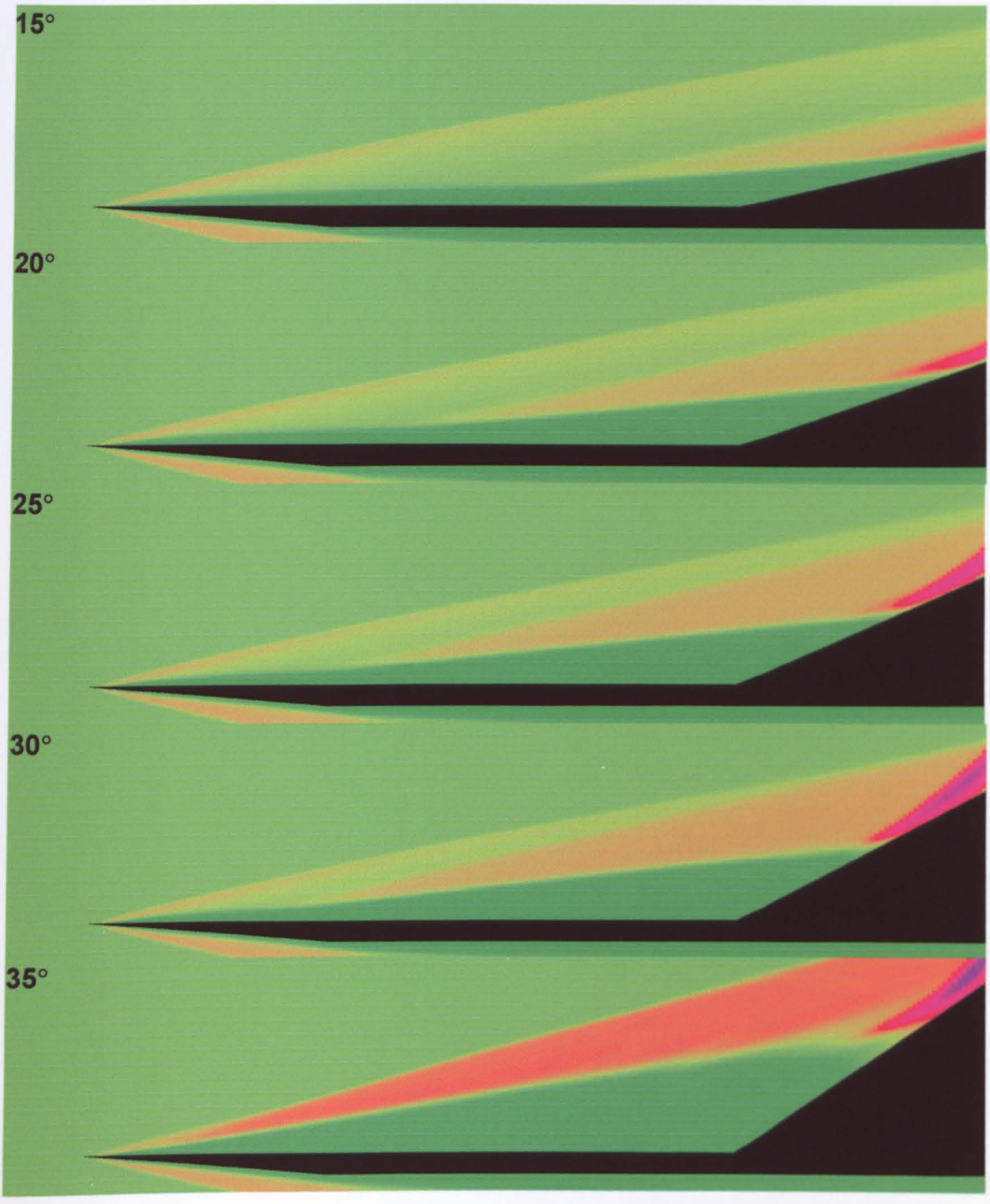

Figure 4.65. Instantaneous Density Plots During Dynamic Motion

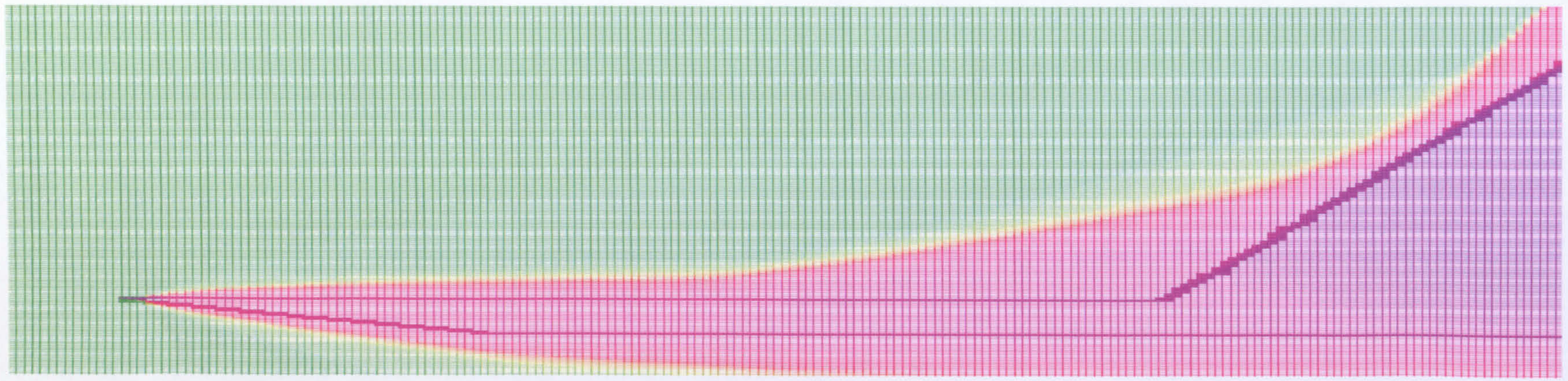

Figure 4.66. Instantaneous Mesh Plot (30° Flap Deployment – Coloured by Density)

5. Conclusions

Axisymmetric Mach 5 Cylinder Flare Flows.

Steady state axisymmetric computations of turbulent flow over a series of cylinder flare configurations were performed. Experimentally derived incoming boundary layers were found to be incompatible with both the Baldwin Lomax and k-ε turbulence models. By computing the evolution of the experimentally derived boundary layer along a cylinder in zero pressure gradient and extrapolating upstream provided a suitable inflow for subsequent computations. It was seen that this inflow differed only slightly from the original experimental profiles. This extrapolation technique was only effective with the Baldwin Lomax turbulence model. For the k-ε turbulence model, negative values of turbulent kinetic energy were produced, and hence the profiles could not be employed.

Quantitative agreement in terms of the incoming boundary layer profile (pitot pressure), surface pressure distribution and skin friction coefficient were good. Where separation occurred, the length of the separated region was over-predicted, although the correct trends with variation in separation angle were obtained.

Small separated regions were observed computationally with flare angles traditionally thought too small to induce separation, as reported experimentally [2][3][4][5]. Due to the over-prediction in separated length with flare angle, incipient separation was found at a lower flare angle than seen experimentally (7.5° and 15° respectively). Incipient separation, at the flow conditions examined here, on the basis of traditional empirical estimations, would have been expected at approximately 20°-30°.

For very small scale separations, embedded in the laminar sub-layer, the criteria for incipient separation of the turbulent boundary layer match those for a corresponding laminar boundary layer.

Although very small separated regions were being predicted, there was found to be a minimum angle, below which separation was not found to occur (7.5°). This is consistent with the cumulative momentum loss experienced by the boundary layer which induces flow retardation and separation [8]. The effects of flow retardation (for the attached flows) are visible in skin friction coefficient as a localised reduction in wall shear stress.

The small-scale separations have been shown to have very little effect on the surface pressure due to minimal disturbance of the external flow, and hence determining the presence of separation by examination of wall pressure distributions found to be difficult if not impossible.

A bi-modal variation in the height of the separated region was observed, whereby for small flow deflections, the height of the separated region varies little with flare angle. Above approximately twenty degrees (the angle at which incipient separation would typically be expected to occur) the height of the separated region increases rapidly with flare angle. This rapid growth in separation height with flare angle produces marked deflection of the external flow and hence significant perturbation of wall pressure distributions. The rapid increase in height of the separated region above twenty degrees produces marked effects in wall pressure which are likely to be seen experimentally (and hence the empirical prediction of incipient separation at approximately twenty degrees).

The variation in separated length with flare angle was found to closely follow an exponential curve of exponent 2.5 for these computations.

To examine the criteria for incipient separation, it was demonstrated that the momentum thickness of the boundary layer varies little over the region of interest and thus the boundary layer profiles, in momentum profile terms, could be regarded as quasi-one dimensional.

It was seen that the adverse pressure gradient distribution (responsible for inducing flow retardation and separation) upstream of separation is fixed, and thus invariant to flare shock pressure rise and flare flow deflection. Thus the integral of the adverse pressure gradient preceding separation is invariant with flow deflection and flare angle and hence the pressure rise necessary to induce separation is fixed for this particular cylinder flow. It was seen that a rise in Cp of 0.014 will result in separation of this boundary layer. The strength of the separation shock is independent of flare angle and the initial flow deflection of the boundary layer at the point of boundary layer separation is constant. The separation shock was found to be at an inclination of 20°±2° with initial flow deflection of 11° (this flow deflection is the flow deflection produced by the separation shock, not the flare). These angles, as expected, are consistent with the oblique shock equations. The rise in pressure coefficient resulting from the flow deflection of 11° induced by the separation shock was found to agree with the oblique shock relations, in that the 'plateau' in surface pressure coefficient (for the larger separated regions) was found to be at 0.12.

The qualitative, and to a limited extent, quantitative, agreement between experiment and computation was unexpected. To accurately predict shock boundary layer interactions, both the adverse pressure gradient and the incoming boundary layer momentum profiles must be accurately modelled. Since the Baldwin Lomax turbulence model has no mechanisms by which to reproduce the various regions of the boundary layer (sub-layer, log-layer, etc.), such agreement was surprising.

Self sustained, regular, pressure oscillations were produced for the flow over twenty and thirty degree flares.

No evidence of separation bubble motion was found. The magnitude of the unsteady oscillations was small, and hence the flowfields produced by the local time stepping implicit solver and the time accurate explicit solver were very similar.

Mach 5 Turbulent Flat Plate Ramp Flow.

Inflow boundary layers were grown over flat plates to produce profiles closely matching those reported experimentally.

A non-dimensionalised Baldwin Lomax turbulence model was derived and incorporated into an hierarchical adaptive meshing environment to provide affordable enhanced spatial resolution.

Both the Baldwin-Lomax and k-ε turbulence models replicated the structure of a typical turbulent boundary layer for this flat plate Mach 5 flow.

The results produced with the k-ε turbulence model were seen to be in very poor agreement with available experimental data.

The flows produced by the time averaged computations were found to be markedly different to those produced by the time accurate computations for the same inherently unsteady flow. The agreement in separation location for the time averaged computations with experimental data was significantly better than that for the time accurate computations (this is believed to be coincidental). The Baldwin Lomax turbulence model is known to over predict separation pressure rise and hence separation position. Since the separation shock is stationary, a larger pressure rise will be produced than that produced experimentally, which should also have resulted in computation separation further upstream than seen experimentally.

Oscillations in wall pressure were predicted with the Mach 5 flow over a 28° compression ramp which were in the range observed experimentally. The magnitude of these oscillations was larger than expected 55%P_∞ (this compares with the experimentally determined dominant oscillatory pressure fluctuations produced by the low frequency shock motion of 48%P_∞). This may be due to a proportionate fluctuation in wall pressure, where the wall pressure is over-predicted (as seen here), resulting in artificially large oscillations.

No motion of the separation shock and bubble were produced computationally, and it may be that this produced too strong a separation shock, resulting in the over-prediction of separated length, and under prediction of wall pressure fluctuations. This also explains the lack of large magnitude oscillations around 1kHz.

Large scale flow structures were seen to be created at separation and convected and distorted by the shock boundary layer interaction. The temporal extent of the structures was in good agreement with the experimental data (72μs computationally, 75μs-100μs experimentally), however due to differences in convective velocity, the physical extent of these structures differed from those seen experimentally (up to 1.7δ computationally, δ-4δ experimentally). The convective velocity was expected to be in error, due to the inaccurate prediction of the magnitude of the separated region – if the separated region is not correctly predicted, then the velocity profiles within the separated region must be in error.

The origin of these structures and perturbations was not clear and could either be due to amplification of numerical noise in the free shear layer, or an inherent oscillatory nature of the separated region.

Significant amplification of disturbances was seen around the location of separation.

Dynamic Flap Deployment.

A technique was developed to enable efficient computation (through the use of adaption, and by avoiding creating small cells) of laminar and turbulent flows around arbitrary moving and / or deforming bodies in an adaptive hierarchical environment.

Validation of the technique by comparison with a quasi-steady trajectory simulation of a moving aerofoil was effected. Agreement with experimental surface pressure data was similarly good.

Separated flows were successfully computed with the adaptive body capture code, with incipient separation in very good agreement with both experiment and theory.

Body surface geometry change was effected by recalculating the body surface at every iteration, which was accomplished at minimal computational expense.

Experimental static data for several flat plate flap flows were modelled using an under-relaxed Baldwin-Lomax turbulence model (to match experimental transitional flows – this was not intended as a model of the process of transition in the separated shear layer) and quantitative and qualitative agreement found to be consistent for flap angles between 0° and 25°.

Experimental flap deployment profiles were used in conjunction with a deforming body surface and the transitional adaptive body capture code to model the development of the separated region as the flap was rapidly deployed. Agreement between experimental and computational dynamic lag in length terms was found to be poor, however, this was expected due to

deficiencies in the turbulence model being used when predicting flows with large flap deflections. Comparing angular dynamic lag (which accommodates the over-prediction in separated length at the higher flap angles) shows good agreement between the computed dynamic lag and the experimentally recorded lag. The peak computed dynamic lag was 5° comparing favourably with the experimentally determined lag of 6°.

6. Future Work

Recommendations for future work fall into two categories: those regarding the flow physics and those regarding the computational techniques.

Unsteady Shock Boundary Layer Interactions.

Recomputing the 28° Mach 5 flat plate-ramp flow in three dimensions instead of two would be interesting, to see whether or not any computational spanwise ripple would be produced. This may not be possible until available computational resources become more powerful.

Modifying the flap angle used for comparison with Dolling et al's work, whilst retaining the same flow conditions, would be determine whether or not the frequency and form of the oscillations seen computationally are affected. If they are not affected then this suggest that amplification of numerical noise may be producing the oscillations (i.e. the oscillations are of Type I). If the characteristics are changed, it suggests that we may be modelling a phenomena associated with the separated region itself i.e. Type II or III oscillations (self sustaining or a conditioned response).

Computational boundary layer blowing á la Selig and Smits [23] could be modelled to introduce large scale disturbances upstream of the interaction to see whether or not control of the oscillatory frequencies could be effected. Similarly the addition of freestream noise may help to clarify its importance in the the underlying oscillatory mechanisms.

Recomputing, in a time accurate manner, other flare angles than the 20° and 30° flares examined here for the axisymmetric interactions, would determine whether or not the change in the nature of the oscillations were due to a change in flare angle or due to the formation of a secondary separation at 30°.

Three dimensional computations of Smith's configuration [67] would help to quantify the magnitude of edge effects such as lateral spillage with the larger flap angles for the static flap cases produced experimentally.

Computing a wider range of turbulent boundary layers with the Baldwin Lomax turbulence model would determine whether or not the model generally predicts the different regions comprising a turbulent boundary layer.

It has been seen that predicting unsteady flows with a local time stepping implicit solver produced reasonable results where small oscillations are known to be present, and poor results where large oscillations are known to be present. It would be useful to be able to generalise this by undertaking further time accurate explicit and local time stepping implicit computations of the same flows. If this is true, then we are necessarily precluded from using computationally less expensive local time stepping implicit solvers for flows of unknown steadiness.

Moving Body Computational Techniques.

The technique of adaptive body recovery should be extended to three dimensions so that the code can be employed with a broader range of problems. The minor extensions necessary to cater for multiple body flows should be included so that problems such as sabot separation can be attempted.

Assessing how often to remesh the body surface in terms of the overall body motion since the last time the body was remeshed would prove computationally advantageous. This is readily achieved by remeshing whenever any body surface vertex has moved a distance greater than half the minimum cell dimension.

Deriving moving body boundary conditions for other turbulence models, for example the k-ε and k-ω models, would help with computations of wake flows, etc. which are likely to be important when computing multiple body flows.

7. References

[1] Dupuis, A D, Edwards, J A, Normand, M, "Aerodynamic Characteristics and Aeroheating Aspects of Two Hypersonic Configurations From Free Flight Tests", DREV-R-9428, October 1995

[2] Babinsky, H "A Study of Roughness in Turbulent Hypersonic Boundary Layers", PhD Thesis, College of Aeronautics, Cranfield University, 1994

[3] Babinsky, H, Edwards, J A, "The Influence of Large Scale Roughness on a Turbulent Hypersonic Boundary Layer Approaching a Compression Corner", AIAA 95-0334, 1995

[4] Babinsky, H, Edwards, J A, "The Application and Analysis of Liquid Crystal Thermographs in Short Duration Hypersonic Flow", AIAA 93-0182, 1993

[5] Babinsky, H, Edwards, J A, "Automatic Liquid Crystal Thermography for Transient Heat Transfer Measurements in Hypersonic Flow", Experiment in Fluids, Vol. 21, pp227-236, 1996.

[6] Kuehn, D M, "Turbulent Boundary Layer Separation Induced by Flares on Cylinders at Zero Angle of Attack", TR R-117, 1961, NASA

[7] Kuehn, D M, "Experimental Investigation of the Pressure Rise Required for the Incipient Separation of Turbulent Boundary Layers in Two Dimensional Supersonic Flow", NASA Memo 1-21-59A, NASA, Washington, Feb. 1959

[8] Crocco, L, Lees, L, "A Mixing Theory for the Interaction Between Dissipative Flows and Nearly Isentropic Streams", Journal of Aerospace Science, Vol.19, No. 10, Oct. 1995, pp. 649-676

[9] Coleman, G T, Stollery, J L, "Incipient Separation of Axially Symmetric Hypersonic Turbulent Boundary Layers", AIAA Journal, Vol. 12, No. 1, January 1974, pp. 119-120

[10] Dolling, D S, "Fluctuating Loads in Shock Wave/Turbulent Boundary Layer Interaction: Tutorial and Update." AIAA 93-0284

[11] Kistler, A L, "Fluctuating Wall Pressure Under Separated Supersonic Flow", Journal of Acoustical Society of America, Volume 36, Mach 1964, pp. 543-550.

[12] Barter, J W, Dolling, D S, "Prediction Of Fluctuating Pressure Loads Produced By Shock Induced Turbulent Boundary Layer Separation"., AIAA 96-2043

[13] Pozefsky, P, Blevins, R D, Laganelli, A L, "Thermo- Vibro- Acoustic Loads and Fatigue of Hypersonic Flight Vehicle Structures", AFWAL, TR-89-3014, Feb. 1989

[14] Erengil, M E, Dolling, D S, "Physical Causes of Separation Shock Unsteadiness in Shock Wave / Turbulent Boundary-Layer Interactions", AIAA 93-3134, 1993

[15] Barter, J W, Dolling, D S, "Experimental Study To The Use Of Vortex

Generators To Reduce Fluctuating Pressure Loads In Shock Wave Turbulent Boundary Layer Interactions.", AIAA 93-4335

[16] Unalmis, O H, Dolling, D S, "Decay Of Wall Pressure Field And Structure Of A Mach 5 Adiabatic Turbulent Boundary Layer." AIAA 94-2363.

[17] Erengil, M E, Dolling, D S, "Correlation of Separation Shock Motion in a Compression Ramp Interaction with Pressure Fluctuations in the Incoming Boundary Layer", AIAA 90-1646, 21st Fluid Dynamics, Plasma Dynamics and Lasers Conference, Seattle, Washington, June 1990.

[18] Boitnott, T, "Video Visualisation Of Separation Shock Motion From Measured Wall Pressure Signals In Mach 5 Compression Ramp Interaction.", AIAA 90-0074

[19] McClure, W B, "An Experimental Study of the Driving Mechanism and Control of the Unsteady Shock Induced Turbulent Separation in a Mach 5 Compression Corner Flow", PhD Dissertation, Department of Aerospace Engineering and Engineering Mechanics, The University of Texas at Austin, August 1992.

[20] Gramman, R A, Dolling, D S, "Examination of Turbulent Structures Associated With Unsteady Shock Motion in a Mach 5 Interaction", AIAA Paper 92-0744, January 1992

[21] Kussoy, M L, Brown, J D, Lockman, W K, Horstmann, C C, "Fluctuations and Massive Separation in Three Dimensional Shock Wave / Boundary Layer Interactions", 2nd International Symposium of Transport Phenomena in Turbulent Flows, Tokyo, Japan, October 25-29, 1987

[22] Dolling, D S, Murphy M, " Wall Pressure Fluctuations in a Supersonic Separated Compression Ramp Flow Field", AIAA 82-0986, 1982

[23] Selig, M S, Smits, A J, "Effect of Periodic Blowing on Attached and Separated Supersonic Turbulent Boundary Layers", AIAA Journal, Vol. 29, No. 10, 1991, pp. 1651-1658

[24] Muck, K C, Bogdonoff, S M, Dussauge, J P, "Structure Of The Wall Pressure Fluctuations In A Shock-Induced Separated Turbulent Flow." AIAA 85-0179

[25] Dolling, D S, Smith, D R, "Separation Shock Dynamics in Mach 5 Turbulent Interactions Induced By Cylinders", AIAA Journal, Vol. 27, No. 12, 1988, pp. 1698-1706

[26] Tran, T T, "An Experimental Investigation of Unsteadiness in Swept Shock Wave / Turbulent Boundary Layer Interactions", PhD Dissertation, Mechanical and Aerospace Engineering Department, Princeton University, Princeton, NJ, October 1986.

[27] Erengil, M E, Dolling, D S, "Correlation of Separation Shock Motion and Pressure Fluctuations in the Incoming Boundary Layer", AIAA Journal, Vol. 29, No. 11, 1991, pp. 1868-1877

[28] Selig, M S, Andreopoulos, J, Muck, K C, Dussauge, J P, Smits, A J, "Simultaneous Wall Pressure And Mass Flux Measurements Downstream Of A Shock Wave/Turbulent Boundary Layer Interaction." AIAA 87-0550

[29] Dolling, D S, "Problems in the Validation of CFD Codes Through Comparison with Experiment", Paper 19, AGARD Symposium on Theoretical and Experimental Methods in Hypersonic Flows, Turin, Italy May 1992
[30] Wilcox, D C, "Turbulence Modelling For CFD", 1994, DCW Industries Inc, ISBN 0-9636051-0-0
[31] Baldwin, B S, Lomax, H, "Thin-Layer Approximation and Algebraic Model for Separated Turbulent Flows", AIAA 78-257, Huntsville, AL
[32] Menter, F R, "Performance of Popular Turbulence Models for Attached and Separated Adverse Pressure Gradient Flows", AIAA Journal, Vol. 30, No.8, pp. 2066-2072.
[33] Driver, D M, "Reynolds Shear Stress Measurements in a Separated Boundary Layer", AIAA 91-1787, Honolulu, HI
[34] Cebecci, T, Smith, A M O, "Analysis of Turbulent Boundary Layers", Ser. In Applied Mathematics and Mechanics, Vol. XV, Academic Press, 1974.
[35] Shang, J S, Hankey, W L, "Numerical Solution of the Navier-Stokes Equations for Compression Ramp", AIAA 75-4, Pasadena, CA
[36] Hung, C M, "Development of Relaxation Turbulence Models", NASA CR-2783, 1976
[37] Johnson, D A, King, L S, "A Mathematically Simple Turbulence Closure Model For Attached and Separated Turbulent Boundary Layers" AIAA Journal, Vol.23, No.11, pp. 1684-1692, 1985.
[38] Goldberg, U C, "Derivation and Testing of a One-Equation Model Based on Two Time Scales", AIAA Journal, Vol.29, No.8, pp.1337-1340.
[39] Baldwin, B S, Barth, T J, "A One Equation Turbulence Transport Model for High Reynolds Number Wall Bounded Flows", NASA, TM-102847, 1990
[40] Spalart, P R, Allmaras, S R, "A One Equation Turbulence Model for Aerodynamic Flows", AIAA 92-439, Reno, NV
[41] Wilcox, D C, "Reassessment of the Scale Determining Equation for Advanced Turbulence Models", AIAA Journal, Vol.26, No.11, pp. 1299-1310, 1988
[42] Dunagan, S E, Brown, J L. "Holographic Interferometry Study Of An Axisymmetric Shock-Wave/Boundary Layer Strong Interaction Flow." AIAA Jounral, Vol.25, No.2, Pp 294-297, 1986
[43] MacCormack, R W, "A Numerical Method for Solving the Equations of Compressible Viscous Flow", AIAA Journal, Vol.20, pp. 1275-1281, Sept. 1982
[44] Brown, J L, Kussoy, M I, Coakley, T J, "Turbulent Properties Of Axisymmetric Shock Wave/Boundary Layer Interaction Flows", Turbulent Shear Layer/Shock Wave Symposium IUTAM Symposium Palaiseau 1985
[45] Morkovin, M V, "Effects of Compressibility on Turbulent Flow", The Mechanics of Turbulence, Gordon and Breach, p. 367, 1962
[46] Favre, A, "Equations des Gaz Turbulents Compressibles", Journal de Mecanique, Vol.4, No.3, pp. 361-390, 1965.

[47] Marshall, T A, Dolling, D S, "Computation of Turbulent, Separated, Unswept Compression Ramp Interactions", AIAA Journal, Vol. 30, No.8, pp. 2056-2065, 1992.
[48] Horstman, C C, "Hypersonic Shock Wave Turbulent Boundary Layer Interaction Flows - Experiment and Computation". AIAA 91-1760
[49] Tennekes, H, Lumley, J L, "A First Course in Turbulence", MIT Press, Cambridge, MA, 1983.
[50] Speziale, C G, "Modelling of the Pressure Gradient Velocity Correlation of Turbulence", Physics of Fluids, Vol.28, pp.69-71
[51] Hunt, D, "A Very Large Eddy Simulation Of An Unsteady Shock Wave/ Turbulent Boundary Layer Interaction.", AIAA 95-2212
[52] Thomas, F O, Putnam, C M, Chu, H C, "Measurement Of The Nonlinear Spectral Dynamics Characterizing A Shock Wave/Turbulent Boundary Layer Interaction", AIAA 91-0653
[53] Hurdle, C V, "Calibration of the RARDE High Supersonic Intermittent Wind Tunnel", RARDE Memorandum 29/68, 1968
[54] Sale, N, "SPIKE User Manual", TN 7/93, Fluid Gravity Engineering Ltd., January 1993
[55] Sale, N, "Implementation, Validation and Verification of a Two Equation Turbulence Model", CR 134/92, Fluid Gravity Engineering Ltd., November 1992
[56] Sale, N M, "SPIKE v2 User Guide", TN 14/94, Fluid Gravity Engineering Ltd., February 1994
[57] Netterfield, M P, "Computation of the Aerodynamics of Spinning Bodies using a Point-Implicit Method", AIAA 91-0339
[58] Roper, J J, "A Computational Investigation of Unsteady Shock Boundary Layer Interaction", Cranfield University, MSc Thesis, Aug. 1995.
[59] Edwards, J A, Roper, J J, "A Computational Investigation of the Incipient Separation of a Hypersonic Turbulent Boundary Layer", AIAA 97-0769, 35th Aerospace Sciences Meeting and Exhibit, Jan, 1997, Reno, NV.
[60] Zhang, X, Edwards, J A, "Computational Analysis of Unsteady Cavity Flows Driven by Thick Shear Layers", The Aeronautical Journal, Vol. 92, No.919, November 1988, pp. 365-374
[61] Zhang, X, Edwards, J A, "Analysis of Unsteady Supersonic Cavity Flow Employing an Adaptive Meshing Algorithm", Computers and Fluids, Vol. 25, No. 4, pp.373-393, 1996. ISSN 0045-7930
[62] Wynn, D J,"INFEMS - Index Notation Finite Element Modeling System" Atomic Weapons Establishment, SDA Technical Note 1/88
[63] Lecture Series, Grid Generation, von Karman Institute for Fluid Dynamics. ISSN0377-8312
[64] Rose, W C, Page, R J, Childs, M E, "Incipient Separation Pressure Rise for a Mach 3.8 Turbulent Boundary Layer", AIAA Journal, Vol. 11, No. 5, May 1973, pp. 761-763
[65] Plotkin, K J, "Shock Wave Oscillation Driven by Turbulent Boundary Layer Fluctuations", AIAA Journal 13:1036, 1975
[66] Thomas, F O, Putnam, C M, Chu H C, "On The Mechanism Of

Unsteady Shock Oscillation In Shock Wave/Turbulent Boundary Layer Interactions." Experiments In Fluids Vol.18, 1994

[67] Smith, A J D, "The Dynamic Response of a Wedge Separated Hypersonic Flow and its Effects of Heat Transfer", PhD Thesis, Southampton University, 1993

[68] Berger, M J, "Adaptive mesh refinement for hyperbolic partial differential equations", PhD Thesis, Stanford University, 1982

[69] Quirk, J J, "An Adaptive Grid Algorithm For Computational Shock Hydrodynamics." Phd Thesis, Cranfield University , 1991

[70] Edwards, J A, Roper, J J, "Incorporation of Grid Generators Into DRAMR", DRA/WSS/WX5/CR97508, March 1997

[71] Wang, Z J, Yang, H Q, "Unsteady Flow Simulation Using A Zonal Multi-Grid Approach With Moving Boundaries", AIAA 94-0057, 32nd Aerospace Sciences Meeting and Exhibit, January 10-13, 1994, Reno, NV

[72] Quirk, J J, "A Cartesian Grid Approach with Hierarchical Refinement for Compressible Flows", ICASE, 1994

[73] Coirier, W J, "An Adaptively-Refined, Cartesian, Cell Based Scheme for the Euler and Navier-Stokes Equations", PhD Thesis, University of Michigan, 1994

[74] Wang, Z J, "An Automatic CFD Computing Environment with a Cartesian/Prism Grid Generator, Grid Adaptor and Flow Solver", Proceedings of the 4th International Meshing Roundtable, October 1995, Albuquerque, New Mexico.

[75] Coirier, W J, Powell, K G, "A Cartesian Cell Based Approach for Adaptively Refined Solutions of the Euler and Navier-Stokes, Equations", AIAA 1995

[76] Wilmoth, R G, LeBeau, G J, Carlson, A B, "DSMC Grid Methodologies for Computing Low-Density, Hypersonic Flows about Reusable Launch Vehicles", AIAA 1996

[77] Tuncer, I H, "A 2-D Unsteady Navier-Stokes Solution Method With Overlapping/Overset Moving Grids", AIAA 96-0822, 34th Aerospace Sciences Meeting and Exhibit, January 15-18, 1996, Reno, NV

[78] Wang, Z J, "A Conservative Overlapped (Chimera) Grid Algorithm For Multiple Moving Body Flows", AIAA 96-0823, 34th Aerospace Sciences Meeting and Exhibit, January 15-18, 1996, Reno, NV

[79] Wang, Z J, Bunning P, Benek, J, "Critical Evaluation of Conservative and Non-Conservative Interface Treatment for Chimera Grids", AIAA 95-0077, 33rd Aerospace Sciences Meeting and Exhibit, January 9-12, 1995, Reno, NV

[80] Hall, L H, Mitchell, C R, Parthasarathy, V, "An Unsteady Simulation Technique for Missile Guidance and Control Applications", AIAA 97-0636, 35th Aerospace Sciences Meeting and Exhibit, January 6-10, 1997, Reno, NV

[81] Yang, G, Causon, D M, Ingram, D M, Saunders, R, "A Cartesian Cut-Cell method for axisymmetric separating body flows", AIAA 96-1973, 27th Fluid Dynamics Conference, New Orleans, LA, June 1996

[82] Rainey, R W, "Pressure Measurement at Supersonic Speeds on a

Section of a Rectangular Wing Having an NACA 65-009 Profile", NACA RM L9L16, March 1950

[83] Babinsky, H, Edwards, J A, "On the Incipient Separation of a Turbulent Hypersonic Boundary Layer", The Aeronautical Journal, June 1996

[84] Bogdonoff, S M, "Some Experimental Studies of the Separation of Supersonic Turbulent Boundary Layers", Aeronautical Engineering Department Report 336, Princeton University, Princeton, NJ, June 1995

[85] Dolling, D S, Brusniak, L, "Separation Shock Motion in Fin, Cylinder, and Compression Ramp Induced Turbulent Interactions", AIAA Journal, Vol.27, No. 6, 1989, pp. 734-742

[86] Gramman, R A, "Dynamics of Separation and Reattachment in a Mach 5 Unswept Compression Ramp Flow", PhD Dissertation, Department of Aerospace Engineering and Engineering Mechanics, The University of Texas at Austin, December 1989

[87] Babinsky, H, "A Study of Roughness in Turbulent Hypersonic Boundary Layers" PhD Thesis, Cranfield University, 1994

[88] Thomas, P D, Middlecoff, J F,"Direct Control of the Grid Point Distribution in Meshes Generated by Elliptic Equations" June 1980, AIAA Volume 18, Number 6, Article number 79-1462R

[89] Erengil, M E, Dolling, D S, "Separation Shock Motion and Ensemble Averaged Wall Pressures in a Mach 5 Compression Ramp Interaction", AIAA 89-1853, 1989

[90] Dolling, D S, Or, C T, "Unsteadiness of the Shock Wave Structure in Attached and Separated Compression Ramp Flows", Experiments in Fluids 3:24-32, 1985

[91] Gramann, R A, Dolling D S, "Dynamics of Separation and Reattachment in a Mach 5 Unswept Compression Ramp Flow", AIAA 90-0380, 1990

[92] Gramann, R A, Dolling D S, "Dynamics of the Outgoing Turbulent Boundary Layer in a Mach 5 Compression Ramp Interaction", AIAA 90-1645, 1990

[93] Sale, N, "SPIKE User Manual", TN 7/93, Fluid Gravity Engineering Ltd., January 1993

[94] National Advisory Committee for Aeronautics, Report 1185

[95] Experiments in Fluids 18 (1994), 69-81

[96] Layer Blackwelder, R F, Kaplan, R E, "On The Wall Structure Of The Turbulent Boundary Journal Of Fluid Mechanics", Vol. 76, Part 1, Pp 89-112, 1976

[97] Dolling, D S, Murphy, M T, "Unsteadiness Of The Separation Shock Wave Structure In A Supersonic Compression Ramp Flowfield", Aiaa Journal Vol.21 No.12, 1982

[98] Hayakawa, K, Smits, A J, Bogdonoff, S M, "Hot Wire Investigation Of An Unseparated Shock Wave/Turbulent Boundary Layer Interaction", Aiaa 82-0985, 1982

[99] Dolling, D S, "On Upstream Influence In Shock Wave Turbulent Boundary Layer Interaction", Aeronautical Journal Oct 83, 1983

[100] Andreopoulos, J, Muck, K C. , "Some New Aspects of the Shock Wave

Boundary Layer Interaction in Compression Ramp Flows", AIAA 86-0342, 1986
[101] Tran, T T, Bogdonoff, S M, "A Study Of Unsteadiness Of Shock Wave/Turbulent Boundary Layer Interactions From Fluctuating Wall Pressure Measurements", Aiaa 87-0552, 1987
[102] Smits, A J, Muck, K C, "Experimental Study Of The Three Shock Wave Turbulent Boundary Layer Interactions", Journal Of Fluid Mechanics, Vol.182, Pp 291-314, 1987
[103] Spina, E F, Smits, A J, "Organized Structures In Compressible, Turbulent Boundary Layer", Journal Of Fluid Mechanics, Vol.182, Pp 85-109, 1987
[104] Marshall, T A, Dolling, D S. "Spanwise Properties Of The Unsteady Separation Shock In A Mach 5 Unswept Compression Ramp Interaction", AIAA 90-0377, 1990
[105] Smith, L G, Maurice, M S, Seibert, G L, Tyler, C "Laser Velocimetry Measurements Of Supersonic Vortex Flows On A Simple Razor-Edged Delta Wing", AIAA 91-1684, 1991
[106] Dodson, G S, Settles L J, "Hypersonic Shock/Boundary Layer Interaction Database", AIAA 91-1763, 1991
[107] Erengil, M E, Dolling, D S, "Effects Of Sweepback On Unsteady Separation In Mach 5 Compression Ramp Interactions", AIAA 92-0430, 1992
[108] Gramann, R A, Dolling, D S, "A Preliminary Study Of Turbulent Structures Associated With Unsteady Separation Shock Motion In A Mach 5 Compression Ramp Interaction". AIAA 92-0744, 1992
[109] Mcclure, W B, Dolling, D S, "An Experimental Examination Of The Effects Of Incoming Boundary Layer Modifications On The Dynamics Of A Turbulent Compression Corner Interaction", AIAA 92-3667, 1992
[110] Hytopoulos, E, Simpson, R L, "Critical Evalutation Of Recent Second-Order Closure Models", AIAA 93-0081, 1993
[111] Fan, S, Lakshminarayana, B, "A Simplified Reynolds Stress Model For Unsteady Turbulent Boundary Layers", AIAA 93-0204,1993
[112] Hamad, A, Shih, S H, Yeuan, J J, "A Parametric Study Of Bleed In Shock Boundary Layer Interactions", AIAA 93-0294 1993
[113] Lananelli, A L, "Prediction Of Fluctuating Pressure In Attached And Separated Compressible Flow", AIAA 93-0286. 1993
[114] Nixon, D, "The Effect Of Shock Motion On Entropy Production", AIAA 93-0665, 1993
[115] Gonsalez, J C, Dolling, D S, "Correlation Of Interaction Sweepback Effects On The Dynamics Of Shock Induced Turbulent Separation", AIAA 93-0776, 1993
[116] Grasso, F, Falconi, D, "On The High Speed Turbulence Modeling Of Shock-Wave Boundary Layer Interaction", AIAA 93-0778, 1993
[117] Park, S O, Chung, Y M, Sung, J, "A Numerical Study Of Unsteady Supersonic Compression Ramp Flows", AIAA 93-0883, 1993
[118] Stetson, K F, Kimmel, R L, "On The Breakdown Of A Hypersonic Laminar Boundary Layer", AIAA 93-0896, 1993
[119] Flanagan, M J, "Aerodynamic Heating In The Vicinity Of Hypersonic,

Axisymmetric, Shock Wave Boundary Layer Interactions", AIAA 93-2766 1993
[120] Brusniak, L, Dolling, D S, "Flowfield Dynamics In Blunt Fin Induced Shock Wave Turbulent Boundary Layer Interaction", AIAA 93-3133, 1993
[121] Yoon, B K, Chung, M K, Park, S O, "A Computational Study On Shock Wave/Turbulent Boundary Layer Interaction With Two-Equation Turbulence Models", AIAA 94-2276, 1994
[122] Steinthorsson, E, Modiano, D, "Computations Of Unsteady Viscous Compressible Flows Using Adaptive Mesh Refinement In Curvilinear Body-Fitted Grid Systems", AIAA 94-2330, 1994
[123] Luton, J A, Ragab, S A, Telionis, D P, "Interaction Of Spanwise Vortices With A Boundary Layer", AIAA 94-2377, 1994
[124] Bardina, J E "Three Dimensional Navier Stokes Method With Two Equation Turbulence Models For Efficient Numerical Simulation Of Hypersonic Flows", AIAA 94-2950, 1994
[125] Engblom, W A, Yuceil, B, Goldstein, D B, Dolling, D S, "Hypersonic Forward-Facing Cavity Flow:An Experimental And Numerical Study", AIAA 95-0293, 1995
[126] Erengil, M E, "The Aerodynamics Of Tandem Bodies At Mach 5, Part I: Preliminary Experimental Results", AIAA 95-0319, 1995
[127] Barter, J W, Dolling, D S, "Reduction Of Fluctuating Pressure Loads In Shock Wave Turbulent Boundary Layer Interactions", AIAA 95-0673, 1995
[128] X Zhang, "Turbulent Flow Simulation Using K-W Model. Department Of Aeronautics And Astronautics", 1996
[129] Perng, S W, Dolling, D S, "Passive Control Of Pressure Oscillations In Hypersonic Cavity Flow", AIAA 96-0444, 1996
[130] Unalmis, O H, Dolling, D S, "On The Possible Relationship Between Low Frequency Unsteadiness Of Shock Induced Separated Flow And Gortler Vortices", AIAA 96-2002, 1996
[131] Beresh,S J, Clemens, N T, "Investigation Of The Causes Of Large-Scale Unsteadiness Of Shock-Induced Separated Flow Using Planar Laser Imaging", AIAA 97-0064, 1997
[132] Meyer, M J, Buter, T A, Bowersox, R D W, "Compressible Turbulence Measurements In A Supersonic Boundary Layer With Impinging Shock Wave Interaction", AIAA 97-0427, 1997
[133] Sturek, W B, Danberg, J E, "Supersonic Turbulent Boundary Layer in Adverse Pressure Gradient. Part I: The experiment", AIAA Journal, Vol. 10, No.4, 1972.
[134] Coles, D E, Hirst, E A, "Computation of Turbulent Boundary Layers-1968- AFOSR-IFP-Stanford Conference, Volume II", Stanford University, CA, 1969
[135] Gerhart, P M, Gross, R J, "Fundamentals of Fluid Mechanics", Addison-Wesley Publishing Company, Menlo Park, California, 1985
[136] National Advisory Committee for Aeronautics, Technical Note 3271, "Thermodynamic Properties of Gaseous Nitrogen", Woolley, H W, March 1956

[137] Private communication. R East, Southampton University, December 1998.
[138] Private communication. R Buckland, DERA Fort Halstead, March 1999.
[139] Kimmel, R, Poggie, J, "Transition on an Elliptic Cone at Mach 8", Presented at 23rd TTCP WTP-2 Meeting, 27th April – 1st May 1998, DERA Bedford and DERA Fort Halstead.
[140] Shih, T H, Zhu, J, Lumley, J L, "A Realisable Reynolds Stress Algebraic Equation Model", NASA TM 105993, 1993.
[141] Feguson, H, Schaefer, J W, "Heat Transfer and Pressure Distribution on Cone-Cylinder-Flare Configurations with Boundary Layer Separation", NASA TN D-1436, 1962.
[142] Needham, D A, Stollery, J L, "Hypersonic Studies of Incipient Separation and Separated Flows", ARC 27752,1966.
[143] Duncan, W J, Thom, A S, Young, A D, "Mechanics of Fluids", 2nd Edition, Arnold, 1970.
[144] Kuehn, D M, "Laminar Boundary Layer Separation Induced by Flares on Cylinders with Highly Cooled Boundary Layers at a Mach Number of 15", NASA TN D-2610, 1965.
[145] Kuehn, D M, "Laminar Boundary Layer Separation Induced by Flares on Cylinders at Zero Angle of Attack", NASA TR-R-146, 1962.
[146] Gray, J, "Investigation of the Effect of Flare and Ramp Angle on the Upstream Influence of Laminar and Transitional Reattaching Flows from Mach 3 to 7", AEDC TR-66-190, 1967.
[147] Becker, J V, Korycinski, P F, "Heat Transfer and Pressure Distribution at a Mach Number of 6.8 on Bodies with Conical Flares and Extensive Flow Separation", NASA TN D-1260, 1956.
[148] Coleman, G T, Stollery, J L, "Incipient Separation of Axially Symmetric Hypersonic Turbulent Boundary Layers", AIAA Journal, Volume 12, Number 1, 1974.
[149] Ginoux, J J, "On Some Properties of Reattaching Laminar and Transitional High Speed Flows", VKI, TN-53, 1969.
[150] Granville, P S, "Baldwin Lomax Factors for Turbulent Boundary Layers in Pressure Gradients", AIAA Journal, Volume 25, Number 12, 1987.
[151] Granville, P S, "A Modified van Driest Formula for the Mixing Length of Turbulent Boundary Layers in Pressure Gradients", Journal of Fluid Engineering, Volume 111, 1989.
[152] Rodi, W, Scheuerer, G, "Scrutinizing the k-ε Turbulence Model Under Adverse Pressure Gradient Conditions", Transactions of the American Society of Mechanical Engineers, Vol. 108, June 1986, pp. 174-179.
[153] Wilcox, D C, "Reassessment of the Scale Determining Equation for Advanced Turbulent Models", AIAA Journal, Volume 26, Number 11, November 1988.
[154] Kumar, D, Stollery, J L, "Hypersonic Control Flap Effectiveness", The Aeronautical Journal, Volume 100, Number 996, 1996.
[155] Bloy, A W, "Hypersonic Laminar Boundary Layer Flow over Sharp Compression and Expansion Corners", PhD Thesis, University of London, 1973.

[156] Needham, D A, Stollery, J L, "Boundary Layer Separation in Hypersonic Flow", AIAA 78-1169, 1978.
[157] Holden, M S, "A Study of Flow Separation in Regions of Laminar Shockwave Boundary Layer Interactions in Hypersonic Flow", AIAA 78-1169, 1978
[158] Dhawan, S, Narasimha, R, "Some Properties of Boundary Layer Flow During Transition from Laminar to Turbulent Motion", Journal of Fluid Mechanics, Volume 3, 1958.
[159] Wilcox, D C, "Multiscale Model for Turbulent Flows", AIAA Journal, Volume 26, Number 11, November 1988
[160] Van Driest, E R, "Turbulent Boundary Layer in Compressible Fluids", Journal of Aeronautical Science, Volume 18, No. 3, Mach 1951.
[161] Anderson, J D, "Fundamentals of Aerodynamics", Published by McGraw-Hill International Editions, ISBN 0-07-100767-9

8. Appendix A – 3D Compressible Navier-Stokes Equations.

$$\frac{\partial}{\partial t}\begin{bmatrix}\rho\\ \rho u_x\\ \rho u_y\\ \rho u_z\\ e_t\end{bmatrix}+\frac{\partial}{\partial x}\begin{bmatrix}\rho u_x\\ \rho u_x^2+p\\ \rho u_x u_y\\ \rho u_x u_z\\ (e_t+p)u_x\end{bmatrix}+\frac{\partial}{\partial y}\begin{bmatrix}\rho u_y\\ \rho u_x u_y\\ \rho u_y^2+p\\ \rho u_y u_z\\ (e_t+p)u_y\end{bmatrix}+\frac{\partial}{\partial z}\begin{bmatrix}\rho u_z\\ \rho u_x u_z\\ \rho u_y u_z\\ \rho u_z^2+p\\ (e_t+p)u_z\end{bmatrix}=\frac{\partial}{\partial x}\begin{bmatrix}0\\ \tau_{xx}\\ \tau_{xy}\\ \tau_{xz}\\ u_x\tau_{xx}+u_y\tau_{xy}+u_z\tau_{xz}+\end{bmatrix}$$

$$+\frac{\partial}{\partial y}\begin{bmatrix}0\\ \tau_{xy}\\ \tau_{yy}\\ \tau_{yz}\\ u_x\tau_{xy}+u_y\tau_{yy}+u_z\tau_{yz}+q_y\end{bmatrix}+\frac{\partial}{\partial z}\begin{bmatrix}0\\ \tau_{xz}\\ \tau_{zy}\\ \tau_{zz}\\ u_x\tau_{zx}+u_y\tau_{zy}+u_z\tau_{zz}+q_z\end{bmatrix}$$

Where the stress tensors are given by:

$$\tau_{xy}=\frac{\mu_l+\mu_t}{\mathrm{Re}}\left[\frac{\partial u_x}{\partial y}+\frac{\partial u_y}{\partial x}\right] \qquad \tau_{xx}=\tfrac{2}{3}\frac{\mu_l+\mu_t}{\mathrm{Re}}\left[2\frac{\partial u_x}{\partial x}-\frac{\partial u_y}{\partial y}-\frac{\partial u_z}{\partial z}\right]$$

$$\tau_{xz}=\frac{\mu_l+\mu_t}{\mathrm{Re}}\left[\frac{\partial u_x}{\partial z}+\frac{\partial u_z}{\partial x}\right] \qquad \tau_{yy}=\tfrac{2}{3}\frac{\mu_l+\mu_t}{\mathrm{Re}}\left[2\frac{\partial u_y}{\partial y}-\frac{\partial u_x}{\partial x}-\frac{\partial u_z}{\partial z}\right]$$

$$\tau_{zy}=\frac{\mu_l+\mu_t}{\mathrm{Re}}\left[\frac{\partial u_y}{\partial z}+\frac{\partial u_z}{\partial y}\right] \qquad \tau_{zz}=\tfrac{2}{3}\frac{\mu_l+\mu_t}{\mathrm{Re}}\left[2\frac{\partial u_z}{\partial z}-\frac{\partial u_y}{\partial y}-\frac{\partial u_x}{\partial x}\right]$$

and the heat fluxes by:

$$q_x=\frac{1}{(\gamma-1)M_\infty^2\,\mathrm{Re}}\left[\frac{\mu_l}{\mathrm{Pr}}+\frac{\mu_t}{\mathrm{Pr}_t}\right]\frac{\partial T}{\partial x}$$

$$q_y=\frac{1}{(\gamma-1)M_\infty^2\,\mathrm{Re}}\left[\frac{\mu_l}{\mathrm{Pr}}+\frac{\mu_t}{\mathrm{Pr}_t}\right]\frac{\partial T}{\partial y}$$

$$q_z=\frac{1}{(\gamma-1)M_\infty^2\,\mathrm{Re}}\left[\frac{\mu_l}{\mathrm{Pr}}+\frac{\mu_t}{\mathrm{Pr}_t}\right]\frac{\partial T}{\partial z}$$

Internal energy is defined as :

$$e_t=\frac{p}{\gamma-1}+\frac{\rho}{2}(u_x^2+u_y^2+u_z^2)+\rho k$$

9. Appendix B - Non-Dimensional Baldwin-Lomax Turbulence Model

Sutherland's law:

$$\frac{\mu}{\mu_{ref}} = \left[\frac{T}{T_{ref}}\right]^{3/2} \frac{T_{ref} + 110}{T + 110}$$

Defining non-dimensional temperature as : $\bar{T} = \frac{T}{T_\infty}$, and non-dimensional viscosity as : $\bar{\mu} = \frac{\mu}{\mu_\infty}$, gives the non-dimensional form of Sutherland's law as:

$$\bar{\mu} = \bar{T}^{3/2} \frac{1 + \frac{110}{T_\infty}}{\bar{T} + \frac{110}{T_\infty}}$$

Using non-dimensionalisations employed throughout DRAMR i.e.:

$$\bar{x} = \frac{x}{L}, \bar{y} = \frac{y}{L}, \bar{u} = \frac{u}{u_\infty}, \bar{v} = \frac{v}{u_\infty}, \bar{\rho} = \frac{\rho}{\rho_\infty}, \bar{E}_t = \frac{E_t}{\rho_\infty u_\infty^2}, \bar{p} = \frac{p}{\rho_\infty u_\infty^2}$$

<u>Physical</u>

$$\underline{\xi}_{2D} = -\left\{\frac{\partial u}{\partial y} - \frac{\partial v}{\partial x}\right\}\underline{\hat{k}}$$

$$\tau_w = \mu_w \frac{\partial V_t}{\partial y}$$

$$u_\tau = \sqrt{\frac{\tau_w}{\rho_w}}$$

$$\nu_w = \frac{\mu_w}{\rho_w}$$

$$y^+ = \frac{u_\tau y}{\nu_w}$$

<u>Non-Dimensional</u>

$$\bar{\underline{\xi}}_{2D} = -\left\{\frac{\partial \bar{u}}{\partial \bar{y}} - \frac{\partial \bar{v}}{\partial \bar{x}}\right\}\underline{\hat{k}}$$

$$\Rightarrow \bar{\underline{\xi}}_{2D} = \frac{L\underline{\xi}}{u_\infty}$$

$$\bar{\tau}_w = \bar{\mu}_w \frac{\partial \bar{V}_t}{\partial \bar{y}}$$

$$\Rightarrow \bar{\tau}_w = \frac{\tau_w L}{\mu_\infty u_\infty}$$

$$\bar{u}_\tau = \sqrt{\frac{\bar{\tau}_w}{\bar{\rho}_w}} = u_\tau \sqrt{\frac{L\rho_\infty}{\mu_\infty u_\infty}}$$

$$\bar{\nu}_w = \frac{\bar{\mu}_w}{\bar{\rho}_w} = \nu_w \frac{\rho_\infty}{\mu_\infty}$$

$$\bar{y}^+ = \frac{\bar{u}_\tau \bar{y}}{\bar{\nu}_w} = y^+ \sqrt{\frac{L\rho_\infty}{\mu_\infty u_\infty}} \frac{1}{L} \frac{\mu_\infty}{\rho_\infty}$$

$$\Rightarrow \bar{y}^+ = y^+ \sqrt{\frac{\mu_\infty}{L u_\infty \rho_\infty}}$$

$$\Rightarrow \bar{y}^+ = y^+ \sqrt{\frac{1}{Re}}$$

$$\Rightarrow y^+ = \bar{y}^+ Re^{1/2}$$

$$l_{mix} = \kappa y\left[1 - e^{\frac{y^+}{A_0^+}}\right]$$

$$\mu_{t,inner} = \rho l_{mix}^2 \left|\underline{\xi}\right|$$

$$\bar{l}_{mix} = \kappa \bar{y}\left[1 - e^{\frac{y^+}{A_0^+}}\right]$$

$$\Rightarrow \bar{l}_{mix} = \frac{l_{mix}}{L}$$

$$\bar{\bar{\mu}}_{t,inner} = \bar{\rho}\bar{l}_{mix}^2 \left|\underline{\xi}\right|$$

$$\Rightarrow \bar{\bar{\mu}}_{t,inner} = \frac{\mu_{t,inner}}{L\rho_\infty u_\infty}$$

$$\Rightarrow \bar{\bar{\mu}}_{t,inner}\, Re = \frac{\mu_{t,inner}}{L\rho_\infty u_\infty} \cdot \frac{L\rho_\infty u_\infty}{\mu_\infty} = \frac{\mu_{t,inner}}{\mu_\infty}$$

$$\Rightarrow \bar{\mu}_{t,inner} = \bar{\bar{\mu}}_{t,inner}\, Re$$

$$F_{Kleb}(y) := \left[1 + 5.5\left(\frac{C_{KLEB}\, y}{Y_{MAX}}\right)^6\right]^{-1}$$

Since y and Y_{MAX} are both distances, both are normalised with respect to the same reference length, hence:

$$\bar{F}_{Kleb} = F_{Kleb}$$

$y_{max} = y$ where $l_{mix}\left|\underline{\xi}\right| = \max(l_{mix}\left|\underline{\xi}\right|)$ within a vertical strip of cells.

$\bar{y}_{max} = \bar{y}$ where $\bar{l}_{mix}\left|\underline{\xi}\right| = \max(\bar{l}_{mix}\left|\underline{\xi}\right|)$ i.e.

$$\bar{y}_{max} = \frac{y_{max}}{L}$$

$$F_{max} = \frac{1}{\kappa}\left[\max_{y}\left(l_{mix}\left|\underline{\xi}\right|\right)\right]$$

$$\bar{F}_{max} = \frac{1}{\kappa}\left[\max_{\bar{y}}\left(\bar{l}_{mix}\left|\underline{\xi}\right|\right)\right]$$

$$\Rightarrow \bar{\bar{F}}_{max} = \frac{1}{\kappa}\left[\max_{\bar{y}}\left(\frac{l_{mix}}{L}\frac{\left|\underline{\xi}\right|L}{U_\infty}\right)\right]$$

$$\Rightarrow \bar{F}_{max} = \frac{F_{max}}{u_\infty}$$

$$u_{diff} = u_{max} - u_{min}$$

$$\bar{u}_{diff} = \bar{u}_{max} - \bar{u}_{min}$$

$$\Rightarrow \bar{u}_{diff} = \frac{u_{diff}}{u_\infty}$$

$$F_{wake} = \min\left\{y_{max}F_{max}, \frac{C_{wk}\, y_{max}\, U_{diff}^2}{F_{max}}\right\}$$

$$\bar{F}_{wake} = \min\left\{\bar{y}_{max}\bar{F}_{max}, \frac{C_{wk}\,\bar{y}_{max}\,\bar{U}_{diff}^2}{\bar{\bar{F}}_{max}}\right\}$$

$$\bar{F}_{wake} = \min\left\{\frac{y_{max}}{L}\frac{F_{max}}{u_\infty}, \frac{C_{wk}\, y_{max}\, u_\infty U_{diff}^2}{LF_{max}u_\infty^2}\right\}$$

$$\Rightarrow \bar{F}_{wake} = \frac{F_{wake}}{Lu_\infty}$$

$$\mu_{t,outer} = \rho\alpha C_{cp} F_{wake} F_{Kleb} \left\{ y, \frac{y_{max}}{C_{Kleb}} \right\}$$

$$\bar{\mu}_{t,outer} = \bar{\rho}\alpha C_{cp} \bar{F}_{wake} \bar{F}_{Kleb} \left\{ \bar{y}, \frac{\bar{y}_{max}}{C_{Kleb}} \right\}$$

$$\Rightarrow \bar{\bar{\mu}}_{t,outer} = \frac{\mu_{t,outer}}{L\rho_\infty u_\infty}$$

$$\Rightarrow \bar{\bar{\mu}}_{t,outer} Re = \frac{\mu_{t,outer}}{L\rho_\infty u_\infty} \cdot \frac{L\rho_\infty u_\infty}{\mu_\infty} = \frac{\mu_{t,outer}}{\mu_\infty}$$

$$\Rightarrow \bar{\mu}_{t,outer} = \bar{\bar{\mu}}_{t,outer} Re$$

Closure coefficients:

$$\kappa = 0.4$$

$$C_{cp} = 1.6$$

$$\alpha = 0.0168$$

$$C_{Kleb} = 0.3$$

$$A_0^+ = 26.0$$

$$C_{wk} = 1.0$$

10. Appendix C - K-ε Turbulence Model

The k-ε turbulence model implemented in SPIKE is based on the model of Huang and Coakley. This model is essentially incompressible with compressibility effects implemented in the form of variable density using the mass weighted or Favre averaging approach.

The k-ε employs the Kolmogorov-Prandtl relation to produce the turbulent eddy viscosity μt:

$$\mu_t = C_\mu \rho \frac{\kappa^2}{\varepsilon}$$

The turbulent kinetic energy transport equation in two dimensions is given by:

$$\frac{\partial(\rho\kappa)}{\partial t} + \frac{\partial}{\partial x_i}(\rho u_i \kappa) = \frac{\mu_t}{\sigma_k}\frac{\partial \kappa}{\partial x_i} + \mu_t\left(\frac{\partial u_i}{\partial x_j} + \frac{\partial u_j}{\partial x_i} - \tfrac{2}{3}\rho\kappa\delta_{i,j}\right)\frac{\partial u_i}{\partial x_j} - \varepsilon$$

and the turbulent dissipation transport equation by:

$$\frac{\partial(\rho\varepsilon)}{\partial t} + \frac{\partial}{\partial x_i}(\rho u_i \varepsilon) = \frac{\partial}{\partial x_i}\left(\frac{\mu_t}{\sigma_\varepsilon}\frac{\partial \varepsilon}{\partial x_i}\right) + c_{1,\varepsilon}\frac{\varepsilon}{\kappa}\left[\mu_t\left(\frac{\partial u_i}{\partial x_j} + \frac{\partial u_j}{\partial x_i}\right)\frac{\partial u_i}{\partial x_j}\right] - c_{2,\varepsilon}\frac{\rho\varepsilon^2}{\kappa}$$

The empirical constants are: c_μ=0.09, $c_{1,\varepsilon}$=1.44, $c_{2,\varepsilon}$=1.92, σ_k=1.0 and σ_ε=1.3.

SPIKE computes the inviscid κ and ε fluxes to first order accuracy whilst the five remaining fluxes are computed to second order accuracy. In the interests of code simplicity the κ and ε equations are solved in an uncoupled time lagged manner.

At viscous 'no-slip' boundary conditions the κ and ε equations are closed with the following:

$$\kappa_{WALL} = 0$$

$$\varepsilon_{WALL} = 2\nu\left(\frac{\partial\sqrt{\kappa}}{\partial y}\right)^2$$

The commonly employed trivial dissipation rate boundary condition of ε_{WALL} =0 is avoided in order to prevent the length scale from becoming unrealistically large.

Near wall functions of Jones and Launder are employed:

The freestream values for κ and ε are given by:

$$\omega_\infty \geq 10\frac{u_\infty}{L}$$

$$\frac{\mu_{T_\infty}}{\mu_\infty} = \frac{0.09\kappa_\infty}{\nu_\infty\omega_\infty} \leq 1$$

11. Appendix D - K-ω Turbulence Model

Eddy viscosity:

$$\mu_t = \frac{\rho\kappa}{\omega}$$

Turbulent kinetic energy transport equation:

$$\rho\frac{\partial\kappa}{\partial t} + \rho u_j\frac{\partial\kappa}{dx_j} = \tau_{ij}\frac{\partial u_i}{\partial x_j} - \beta^*\rho\kappa\omega + \frac{\partial}{\partial x_j}\left[(\mu + \sigma^*\mu_t)\frac{\partial\kappa}{\partial x_j}\right]$$

Specific turbulent dissipation rate transport equation:

$$\rho\frac{\partial\omega}{\partial t} + \rho u_j\frac{\partial\omega}{dx_j} = \alpha\frac{\omega}{\kappa}\tau_{ij}\frac{\partial u_i}{\partial x_j} - \beta\rho\omega^2 + \frac{\partial}{\partial x_j}\left[(\mu + \sigma\mu_t)\frac{\partial\omega}{\partial x_j}\right]$$

With closure coefficients:

$$\alpha = 5/9, \beta = 3/40, \beta^* = 9/100, \sigma = 1/2, \sigma^* = 1/2$$

Auxiliary equations:

$$\varepsilon = \beta^*\omega\kappa$$

$$l = \frac{\kappa^{1/2}}{\omega}$$

12. Appendix E - Eigenvalue Limiting within SPIKE

The general formulation for the fluxes in the approximate Riemann solver by Roe is given by:

$$F_{i+\frac{1}{2}}^{Roe} = \tfrac{1}{2}\left[F_i^n + F_{i+1}^n\right] - \tfrac{1}{2}\sum_k \tilde{\alpha}_k \left|\tilde{\lambda}_k\right| \tilde{R}_k$$

Where $\tilde{\alpha}_k$ are the wave strengths, $\tilde{\lambda}_k$ are the eigenvalues and $\tilde{R}_k$ are the eigenvectors.

To maintain the monotonicity and hence convergence of the solution the eigenvalues require limiting. SPIKE uses the eigenvalue limiter ξ_0 in the following manner:

$$\xi_{limit} = \xi_0 (c + |u| + |v| + |w|)$$

$$\left|\tilde{\lambda}'\right| = \tfrac{1}{2}\left(\frac{\tilde{\lambda}^2}{\xi_{limit}} + \xi_{limit}\right) \quad when \quad \left|\tilde{\lambda}\right| < \xi_{limit}$$

13. Appendix F - Dynamic Flap Deployment History.

Time (ms)	Flap angle (°)
0	0.000
1	0.362
2	0.725
3	1.630
4	2.599
5	3.623
6	5.072
7	6.522
8	8.333
9	10.370
10	12.319
11	14.493
12	16.667
13	19.565
14	22.464
15	25.638
16	28.986
17	31.435
18	34.058
19	36.232
20	38.043

Flap angle (°)	Angular rate (°/s)
0.00	350
1.25	850
2.50	1050
3.75	1250
5.00	1450
6.25	1650
7.50	1800
8.75	1950
10.00	2050
11.25	2150
12.50	2200
13.75	2250
15.00	2350
16.25	2450
17.50	2500
18.75	2550
20.00	2650
21.25	2750
22.50	2800
23.75	2850
25.00	2950
26.25	2900
27.50	2950
28.75	2950
30.00	3000
31.25	3000
32.50	3100
33.75	3150
35.00	2950
36.25	2250
37.50	350